A független citációs paraméterre vonatkozó követelményeket teljesítő közlemények listája és in extenso változata

(10 db olyan közlemény, amelyek mindegyike legalább 20 db független citációt kapott és melyeknek a pályázó első vagy vezető (levelező vagy utolsó) szerzője)

Sor-szám	**Cím**	**Szerző(k)**	**A pályázó szerzői szerepe (egyedüli/első/ utolsó/levelező)**	**Szakfolyóirat**		**n (citációs paraméter)**	**Független hivatkozások száma (Cit.)**
				neve	**besorolása a publikálás évében (pl. Q1)**		
1.	Complex formation between water-soluble sulfonated calixarenes and C-60 fullerene	Kunsagi, Mate S; Szabo, K ; Bitter, I ; Nagy, G ; Kollar, L	**első és levelező**	TETRAHEDRON LETTERS 45 (2004) 1387	Q1	10	43
2.	Structural properties of methanol - water binary mixtures within the quantum cluster equilibrium model	Gergely, Matisz ; Anne-Marie, Kelterer; Walter, Fabian ; Sándor, Kunsági-Máté	**utolsó**	PHYSICAL CHEMISTRY CHEMICAL PHYSICS 17 (2015) 8467	Q1(D1)	10	44
3.	Host-guest interaction between water-soluble calix[6]arene hexasulfonate and p-nitrophenol	Kunsagi, Mate S; Szabo, K ; Lemli, B ; Bitter, I ; Nagy, G ; Kollar, L	**első és levelező**	THERMOCHIMICA ACTA 425 (2005) 121	Q1	10	29
4.	Interaction of citrinin with human serum albumin	Poór, Miklós ; Lemli, Beáta ; Bálint, Mónika ; Hetényi, Csaba ; Sali, Nikolett ; Kőszegi, Tamás; Kunsági-Máté, Sándor	**utolsó**	TOXINS 7 (2015) 5155	Q1	10	24
5.	Some Unexpected Behavior of the Adsorption of Alkali Metal Ions onto the Graphene Surface under the E□ect of External Electric Field	Beáta, Peles-Lemli ; Dániel, Kánnár ; Jia, Cai Nie ; Heng, Li ; Sándor, Kunsági-Máté	**utolsó és levelező**	JOURNAL OF PHYSICAL CHEMISTRY C 117 (2013) 21509	Q1(D1)	10	37
6.	Determination of the thermodynamic parameters of the complex formation between malvidin-3-O-glucoside and polyphenols. Copigmentation effect in red wines	Kunsagi, Mate S; Szabó, K ; Nikfardjam, MP ; Kollár, L	**első és levelező**	JOURNAL OF BIOCHEMICAL AND BIOPHYSICAL METHODS 69 (2006) 113	Q2	10	27

7.	Host-guest interaction of calixarene molecules with neutral benzotrifluorides: Comparison of luminescence spectral data with results of model calculations relating to complex formation	Kunsagi, Mate S ; Nagy, G; Kollar, L	**első**	ANALYTICA CHIMICA ACTA 428 (2001) 301	Q1	10	21
8.	Effect of exposure time and pre-heating on the conversion degree of conventional, bulk-fill, fiber reinforced and polyacid-modified resin composites	Lempel, Edina ; Őri, Zsuzsanna ; Szalma, József ; Lovász, Bálint Viktor ; Kiss, Adél ; Tóth, Ákos ; Kunsági-Máté, Sándor	**utolsó**	DENTAL MATERIALS 35 (2019) 217	Q1(D1)	10	30
9.	Weinhold's QCE model – A modified parameter fit. Model study of liquid methanol based on MP2 cluster geometries	Gergely, Matisz ; Walter, M F Fabian ; Anne-Marie, Kelterer ; Sándor, Kunsági-Máté	**utolsó és levelező**	JOURNAL OF MOLECULAR STRUCTURE: THEOCHEM 956 (2010) 103	Q2	10	21
10	Coordination of Methanol Clusters to Benzene: A Computational Study	Matisz, G ; Kelterer, AM ; Fabian, WMF ; Kunsagi-Mate, S	**utolsó és levelező**	JOURNAL OF PHYSICAL CHEMISTRY A 115 (2011) 10556	Q1(D1)	10	22

Available online at www.sciencedirect.com
SCIENCE DIRECT®
Tetrahedron Letters 45 (2004) 1387–1390
Tetrahedron Letters

Complex formation between water-soluble sulfonated calixarenes and C_{60} fullerene

Sándor Kunsági-Máté,[a,*] Kornélia Szabó,[a] István Bitter,[b] Géza Nagy[a,d] and László Kollár[c,d]

[a]*Department of General and Physical Chemistry, University of Pécs, Pécs H-7624, Hungary*
[b]*Department of Organic Chemical Technology, Budapest University of Technology and Economics, Budapest H-1521, Hungary*
[c]*Department of Inorganic Chemistry, University of Pécs, Pécs H-7624, Hungary*
[d]*MTA-PTE Research Group for Chemical Sensors, Pécs H-7624, Hungary*

Received 22 October 2003; revised 3 December 2003; accepted 11 December 2003

Abstract—The inclusion complexes of sulfonated thiacalix[4]arene **1** and calix[6]arene **2** sodium salts with C_{60} fullerene were investigated by photoluminescence (PL) and quantum-chemical methods. The stoichiometries of calixarene/C_{60} complexes were found to be 2:1 for **1** and 1:1 for **2**. Related quantum-chemical investigations show that C_{60} fullerene is included in a cavity composed of two half-bowl molecules of **1**. The C_{60} fullerene ball is located deep within the cavity of **2** and the negatively charged sulfonate arms probably inhibit the formation of the bowl-shaped capsule that was observed in the case of **1**.
© 2003 Elsevier Ltd. All rights reserved.

The electron accepting ability of the fullerenes is known to inhibit the activity of redox enzymes[1–3] (e.g., nitric oxide synthase, thus providing a therapeutic approach for some neurodegenerative disorders[4]) and a large number of fullerene derivatives are competitive inhibitors of the human immunodeficiency virus (HIV) protease.[5] However, the very low solubility of fullerenes in aqueous solvents is a major difficulty hindering their application in clinical practice. Several strategies have been developed to increase the water solubility of fullerene derivatives.[6] One of them is the inclusion of C_{60} within water-soluble hosts such as cyclodextrins[7,8] and calixarenes.[9,10] Other approaches such as covalent functionalization of C_{60} with hydrophilic, ionic,[11,12] or nonionic[13,14] organic moieties or electrochemical/chemical reduction of C_{60} to a water-soluble anion[15] have also been utilized to overcome the natural water repulsion of C_{60} fullerene.

Williams et al. first used water-soluble calixarenes to include C_{60},[9] then two independent investigations showed that *p-tert*-butylcalix[8]arene selectively includes the C_{60} fullerene with 1:1 stoichiometry.[16,17] Subsequently efforts were made to study the supramolecular complexes of fullerenes with calixarenes.[6] It turned out that most calixarene–fullerene complexes exist only in the solid state, whereas in solvents they frequently dissociate or precipitate after formation. Therefore the existence of these complexes is difficult to prove by spectroscopic methods.[18]

In our recent papers,[19–21] the complexation behavior and the factors controlling the thermodynamic and kinetic stability or selectivity of some calixarene derivatives towards neutral π-electron deficient species were reported. A paper on the interaction of a water-soluble calixarene with iron ions has been published recently.[22]

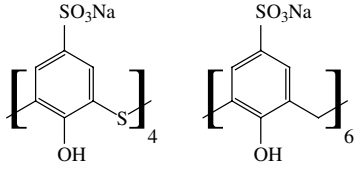

1 **2**

Figure 1. Sulfonated thiacalix[4]arene **1** and calix[6]arene **2** investigated in this work.

Herein, we report our results on the inclusion complexes of two sulfonated calixarene derivatives (Fig. 1, the

Keywords: Calixarene; Fullerene; Host–guest complex.
* Corresponding author. Tel.: +36-72-503600; fax: +36-72-501518; e-mail: kunsagi@ttk.pte.hu

0040-4039/$ - see front matter © 2003 Elsevier Ltd. All rights reserved.
doi:10.1016/j.tetlet.2003.12.076

sodium salts of thiacalix[4]arene tetrasulfonate **1** and calix[6]arene hexasulfonate **2**) with C_{60} fullerene. In this investigation our earlier developed methodology, based on PL measurements and on Job's method, is used.

In order to investigate the interaction, 10^{-4} M aqueous solutions of **1** or **2** at pH = 7, buffered by TRIS and a 10^{-4} M toluene solution of fullerene were prepared. For the application of Job's method, these solutions were mixed at different molar ratios and the PL spectra of the aqueous phases were recorded. The peaks at 310 nm were used for data evaluation. Both calixarene derivatives showed higher PL intensity in the presence of C_{60} fullerene (Fig. 2). No considerable emission of C_{60} fullerene was observed in the absence of calixarenes. According to our earlier results[19–22] it was concluded that the spectral changes were induced by a weak interaction between the calixarene hosts and the C_{60} guest.

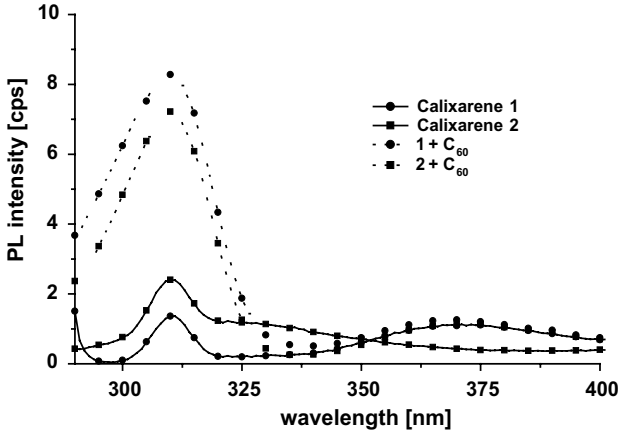

Figure 2. Spectral changes of calixarene derivatives **1** or **2** in the absence and in the presence of 10^{-4} M C_{60} fullerene.

For the experimental determination of thermodynamic properties, Job's method was applied at four different temperatures in the range of 20–35 °C with a step size of 5 °C. The Jobs's curves obtained (Fig. 3) suggest that **1** and **2** form complexes with C_{60} fullerene with 2:1 and 1:1 stoichiometry, respectively. For quantitative evaluation of the Job's curves (where C refers to the calixarene host **1** or **2**; G is the C_{60} fullerene guest; CG and C_2G are the individual types of complexes formed in the studied systems; K_1 and K_2 denote the formation constants of the individual complexes, respectively) the following considerations apply. Assuming that the observed PL signal varies linearly with the concentrations, ΔF in such a system is described by Eq. 1

$$\Delta F = f_{CG}[CG] + f_{C_2G}[C_2G], \tag{1}$$

wherein $\Delta F = F - F_0$ is the difference between the PL intensity obtained with the calixarene–C_{60} system and the PL intensity of the calixarene with the same concentration. The measures of the PL signals, f_{CG} and f_{C_2G} could be observed for the individual C_iG ($i = 1, 2$) species relative to the PL signal of pure calixarene at the same concentrations. By definition,

$$f_{C_iG} = \left.\frac{F([C]) - F([C_iG])}{F([C])}\right|_{[C_iG]=[C]} \quad (i = 1, 2). \tag{2}$$

Using the expressions for the total concentration of the calixarene (Eqs. 3 and 4), the theoretical change of the PL signal in the system studied can be obtained by Eq. 5,

$$C_0 = [C] + K_1[C][G] + 2K_1K_2[C]^2[G], \tag{3}$$

$$G_0 = [G] + K_1[C][G] + K_1K_2[C]^2[G], \tag{4}$$

$$F - F_0 = \frac{G_0\{f_{CG}K_1[C] + f_{C_2G}K_1K_2[C]^2\}}{1 + K_1[C] + K_1K_2[C]^2}, \tag{5}$$

wherein C_0 is the analytical concentration of calixarene, [C] is the equilibrium concentration of calixarene, G_0 and [G] are the analytical and equilibrium concentrations of the C_{60} fullerene, respectively, K_i ($i = 1,2$) is the complex formation constant. Using Eq. 5 the values of K_1 and K_2 as well as f_{CG} and f_{C_2G} could be optimized iteratively: First, Eqs. 3 and 4 are solved numerically for given values of the formation constants and the f_{CG}, f_{C_2G} coefficients. Then, using the equilibrium concentration of the C_{60} fullerene for the given parameters, the theoretical change in the PL signal can be calculated.

We note here, that the K_i values are extraction constants rather than association constants (K_{ass}), which are related by the equation

$$K_{ass} = K_i \cdot K_d, \tag{6}$$

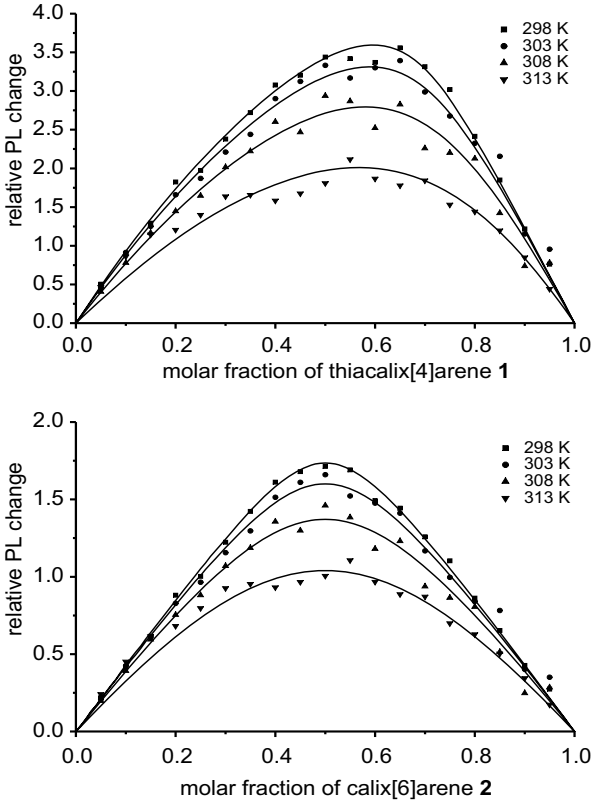

Figure 3. Job's plot of **1**–C_{60} (top) and **2**–C_{60} (bottom) complexes at different temperatures.

where K_d is the distribution coefficient of C_{60} from toluene to water.

However, it is known that the equilibrium in similar systems strongly depends on the temperature.[14] The thermodynamic parameters for the individual complexes formed in the calixarene–C_{60} system can be determined from the van't Hoff equation:

$$\ln K_i = -\frac{\Delta G_i}{RT} = -\frac{\Delta H_i}{RT} + \frac{\Delta S_i}{R} \quad (i = 1, 2), \qquad (7)$$

where ΔG_i is the Gibbs free energy change, ΔS_i the entropy change and ΔH_i the enthalpy change associated with complex formation.

Using Eq. 7, inserting this expression for the formation constants into the Eqs. 3–5, the fluorescence change in Eq. 5 can be expressed as a function of the ΔH_i, ΔS_i values and the f_{CG}, f_{C_2G} coefficients.

The thermodynamic parameters associated with the K_i values were determined from the Job's curves by an iterative solution of Eqs. 1–5 using the expression of K_i values from the van't Hoff equation (Eq. 7). In the case of host **1** (Fig. 3 top, Table 1), the enthalpy, entropy, and also the Gibbs free energy changes for both complexation steps are nearly the same. The complexation of **2** with the fullerene guest shows higher energy changes (Fig. 3 bottom, Table 2), however, with 1:1 calixarene–fullerene stoichiometry.

Table 1. Thermodynamic parameters of complexation of calixarene **1** with C_{60} fullerene

Coord. step	Log K_i	Log β_i	ΔG^0 (kJ mol^{-1})	ΔH^0 (kJ mol^{-1})	ΔS^0 (J K^{-1} mol^{-1})
1	5.08 (5)	5.08	−28.97 (8)	−37.11 (5)	−27.32 (3)
2	4.98 (5)	10.06	−28.43 (8)	−38.41 (5)	−33.46 (3)

Table 2. Thermodynamic parameters of complexation of calixarene **2** with C_{60} fullerene

Coord. step	Log K_i	Log β_i	ΔG^0 (kJ mol^{-1})	ΔH^0 (kJ mol^{-1})	ΔS^0 (J K^{-1} mol^{-1})
1	5.48 (4)	5.48	−31.29 (8)	−42.37 (5)	−37.17 (3)

Our related quantum-chemical calculations show that C_{60} fullerene is included in a cavity composed of two half-bowl molecules of **1** (Fig. 4). Interestingly, the C_{60} fullerene ball lies much more deeply in the cavity of **2**. The close proximity of the negatively charged sulfonate arms probably inhibits the formation of the bowl-shaped capsule found in the case of **1**.

In summary, we can conclude that water-soluble tetrasulfonated thiacalix[4]arene and hexasulfonated calix[6]arene form complexes with C_{60} fullerene exhibiting 2:1 and 1:1 stoichiometry, respectively. This observation makes these compounds promising candidates to overcome the natural water-repulsive character of C_{60} fullerene.

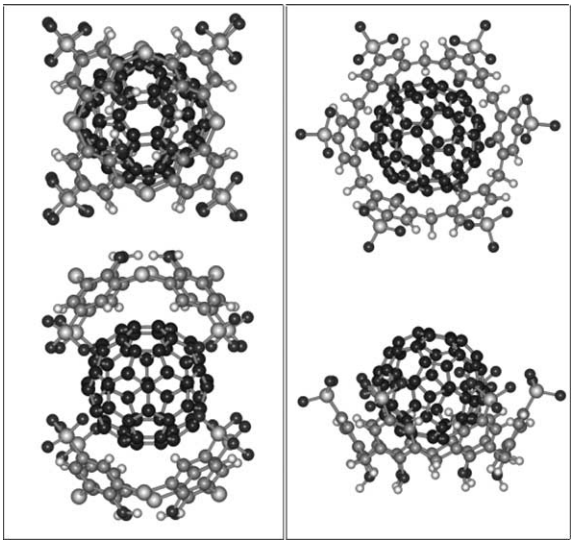

Figure 4. Top and side views of the equilibrium conformations of **1**–C_{60} (left) and **2**–C_{60} (right) complexes calculated by quantum-chemical methods.

Experimental

Both hosts were synthesized as described in the literature. Thus, thiacalix[4]arene-tetrasulfonate salt **1** was obtained by the *ipso* sulfonation of *p-tert*-butylthiacalix[4]arene,[23] while calix[6]arene-hexasulfonate salt **2** was prepared by direct sulfonation of the parent calix[6]-arene with concentrated sulfuric acid.[24] A highly sensitive Fluorolog τ3 spectrofluorometric system (Jobin-Yvon/SPEX) was used to investigate the photoluminescence (PL) spectra of the different solutions. For data collection a photon counting method with 0.4 s integration time was used. Excitation and emission bandwidths were set to 1 nm. A 1 mm layer thickness of the fluorescent probes with front face detection was used to eliminate the inner filter effect. The fluorometric experiments were carried out at pH = 7.0 using TRIS, Tris(hydroxymethyl)aminomethane (Merck) buffer. The exact pH value was reached by the addition of 0.1 M HCl. The equilibrium conformations of calixarene derivatives and their complexes with C_{60} fullerene were studied with semi-empirical AM1 (Austin Model) method, followed by ab initio HF/6-31G* calculations. The Fletcher–Reeves geometry optimization method was used for the investigation of the conformers. All calculations were carried out with the HyperChem Professional 7 program package.[25]

Acknowledgements

The financial support of the Hungarian Scientific Research Fund (OTKA T035047, OTKA T037403), the Hungarian National Committee of Technological Development (OMFB 97-20-MU0086) and Francelab Co. (France) are highly appreciated.

References and notes

1. Jensen, A. W.; Wilson, S. R.; Schuster, D. I. *Bioorg. Med. Chem.* **1996**, *4*, 767–779.
2. Da Ros, T.; Prato, M. *Chem. Commun.* **1999**, 663–669.
3. Wilson, L. J. *Interface* **1999**, *8*, 24–28.
4. Wolf, D. J.; Mialkowski, K.; Richardson, C. F.; Wilson, S. R. *Biochemistry* **2001**, *40*, 37–45.
5. Friedman, S. H.; Ganapathi, P. S.; Rubin, Y.; Kenyon, G. L. *J. Med. Chem.* **1998**, *41*, 2424–2429.
6. Zhong, Z.-L.; Ikeda, A.; Shinkai, S. Calixarenes 2001. In *Complexation of Fullerenes*; Asfari, Z., Böhmer, V., Harrowfield, J., Vicens, J., Eds.; Kluwer: Dordrecht, 2001; pp 476–495.
7. Andersson, T.; Nilsson, K.; Sundahl, M.; Westman, G.; Wennerstrom, O. *J. Chem. Soc., Chem. Commun.* **1992**, 604–606.
8. Priyadarsini, K. I.; Mohan, H.; Tyagi, A. K.; Mittal, J. P. *J. Phys. Chem.* **1994**, *98*, 4756–4759.
9. Williams, R. M.; Verhoeven, J. M. *Recl. Trav. Chim. Pays-Bas.* **1992**, *111*, 531–532.
10. Ikeda, A.; Hatano, T.; Kawaguchi, M.; Suenaga, H.; Shinkai, S. *Chem. Commun.* **1999**, 1403–1404.
11. Richardson, C. F.; Schuster, D. I.; Wilson, S. R. *Org. Lett.* **2000**, *2*, 1011–1014.
12. Okamura, H.; Miyazono, K.; Minoda, M.; Komatsu, K.; Fukuda, T.; Miyamoto, T. *J. Polym. Sci., Part. A: Polym. Chem.* **2000**, *38*, 3578–3585.
13. Samal, S.; Geckeler, K. E. *Chem. Commun.* **2000**, *23*, 1101–1102.
14. Wharton, T.; Kini, V. U.; Mortis, R. A.; Wilson, L. J. *Tetrahedron Lett.* **2001**, *42*, 5159–5162.
15. Wei, X.; Migfei, W.; Qi, L.; Xu, Z. *J. Chem. Soc., Perkin Trans. 2* **1997**, 1389–1393.
16. Suzuki, T.; Nakashima, K.; Shinkai, S. *Chem. Lett.* **1994**, 699–702.
17. Atwood, J. L.; Koutsantonis, G. A.; Raston, C. L. *Nature* **1994**, *368*, 229–231.
18. Shinkai, S. *Chem. Lett.* **2000**, 78–79.
19. Kunsági-Máté, S.; Nagy, G.; Kollár, L. *Sensors Actuators B: Chem.* **2001**, *76*, 545–550.
20. Kunsági-Máté, S.; Nagy, G.; Jurecka, P.; Kollár, L. *Tetrahedron* **2002**, *58*, 5119–5124, and references cited therein.
21. Kunsági-Máté, S.; Bitter, I.; Grün, A.; Nagy, G.; Kollár, L. *Anal. Chim. Acta* **2002**, *461*, 273–279.
22. Kunsági-Máté, S.; Nagy, L.; Nagy, G.; Bitter, I.; Kollár, L. *J. Phys. Chem. B* **2003**, *107*, 4727–4731, and references cited therein.
23. Iki, N.; Suzuki, T.; Koyama, K.; Kabuto, C.; Miyano, S. *Org. Lett.* **2002**, *4*, 509–512.
24. Shinkai, S.; Mori, T.; Tsubaki, T.; Sone, T.; Manabe, O. *Tetrahedron Lett.* **1984**, *25*, 5315–5318.
25. HyperChem Professional 7, HyperCube, 2002.

PCCP

PAPER

View Article Online
View Journal | View Issue

Open Access Article. Published on 30 January 2015. Downloaded on 11/24/2022 8:06:22 AM.
This article is licensed under a Creative Commons Attribution-NonCommercial 3.0 Unported Licence.

Cite this: *Phys. Chem. Chem. Phys.*, 2015, **17**, 8467

Structural properties of methanol–water binary mixtures within the quantum cluster equilibrium model†

G. Matisz,[ab] A.-M. Kelterer,*[c] W. M. F. Fabian[d] and S. Kunsági-Máté[ab]

Received 12th December 2014,
Accepted 27th January 2015

DOI: 10.1039/c4cp05836d

www.rsc.org/pccp

Density functional theory (B3LYP-D3, M06-2X) has been used to calculate the structures, interaction energies and vibrational frequencies of a set of 93 methanol–water clusters of different type (cubic, ring, spiro, lasso, bicyclic), size and composition. These interaction energies have been used within the framework of the Quantum Cluster Equilibrium Theory (QCE) to calculate cluster populations as well as thermodynamic properties of binary methanol–water mixtures spanning the whole range from pure water to pure methanol. The necessary parameters a_{mf} and b_{xv} of the QCE model were obtained by fitting to experimental isobars of MeOH–H_2O mixtures with different MeOH content. The cubic and spiro motifs dominate the distribution of methanol–water clusters in the mixtures with a maximum of mixed clusters at x(MeOH) = 0.365. Reasonable agreement with experimental data as well as earlier molecular dynamics simulations was found for excess enthalpies H^E, entropies S^E as well as Gibbs free energies of mixing G^E. In contrast, heat capacities C_p and C_p^E showed only poor agreement with experimental data.

Introduction

Preferential or selective solvation[1–4] of a solute in binary solvent mixtures, where the composition of the solvation shell differs from the composition of the bulk solvent phase, can have significant effects on the physicochemical properties of the solution. The observable differences are obviously in connection with the molecular associations present in the binary solvent mixtures. Several studies can be found in the literature addressing the investigation of binary liquids regarding structural aspects. For instance, in a recent study, Wakisaka published a summary of experimental results[5–8] related to the cluster structures possible in binary liquid mixtures of water–MeOH, water–EtOH, water–*n*-PrOH and water–*n*-BuOH using fragmentation of liquid droplets and mass spectrometric detection of the ionized clusters.[9,10] Solvent relaxation time measurements in mixtures of *n*-BuOH with MeOH, EtOH, and PrOH indicated a substantial change of the solvation shell at a specific molar fraction of *n*-BuOH.[11] Similarly, measurement of the solvent relaxation time by phase fluorimetry of phenols in binary EtOH–water mixtures resulted in a change from mono- to bi-exponential when the EtOH content exceeded a critical value.[12] In view of the importance of such solvent mixtures a detailed understanding of this selective/preferential solvation at an atomic level is essential. Besides experimental investigations quantum chemical calculations also have been used to determine the properties of such clusters formed by different solvent molecules, including *e.g.* methanol–water clusters up to four-membered rings[13] or methanol–benzene clusters.[14] Of particular importance for the present investigation are those dealing with water[15–17] and/or methanol[18–21] clusters addressing mainly the structural properties, binding energies and electronic properties of these clusters. Specifically, rather comprehensive calculations of $(MeOH)_n$ clusters with n up to n = 15 using a variety of computational procedures have been carried out by Thakkar and coworkers.[21] In addition to methanol clusters those of higher primary alcohols (up to *n*-hexanol) were treated by Golub *et al.*[19]

A powerful tool for the description and theoretical modelling of structure and properties of liquids is the quantum cluster equilibrium (QCE) theory[22] which is based on quantum chemically calculated cluster/molecular properties and the application of statistical thermodynamics. So far this procedure almost

[a] *Department of General and Physical Chemistry, University of Pécs, Ifjúság 6, 7624 Pécs, Hungary*
[b] *János Szentágothai Research Center, Ifjúság 20, 7624 Pécs, Hungary*
[c] *Institute of Physical and Theoretical Chemistry, Graz University of Technology, NAWI Graz, Stremayrgasse 9/I, 8010 Graz, Austria. E-mail: kelterer@tugraz.at*
[d] *Institute of Chemistry, University of Graz, NAWI Graz, Heinrichstr. 28, 8010 Graz, Austria*

† Electronic supplementary information (ESI) available: Fitting parameters a_{mf}, b_{xv} see Tables S1 (with *c8* clusters) and S2 (without *c8* clusters). Table S3 ΔG^{298}/H-bond and populations at different molar fraction. Fig. S1 Number of clusters for specific x(MeOH); Fig. S2 Benchmark of methods against MP2 for ring clusters; M06-2X data are shown in Fig. S3 (E_{int}), S4 (cluster populations), S5 (cluster distributions), S6 (H^E, S^E, G^E), S8 (C_p, C_p^E), and Fig. S7 (C_p^E for B3LYP-D3). Cartesian coordinates of all 93 clusters for B3LYP-D3 and M06-2X method as zip file. See DOI: 10.1039/c4cp05836d

Open Access Article. Published on 30 January 2015. Downloaded on 11/24/2022 8:06:22 AM.
This article is licensed under a Creative Commons Attribution-NonCommercial 3.0 Unported Licence.

exclusively has been applied to neat liquids, like water,[23–34] methanol,[28,35–38] ethanol,[28,38–41] propan-1-ol,[38] butan-1-ol,[38] benzyl alcohol,[39] 2,2-dimethyl-3-ethyl-3-pentanol,[39,42] formic acid,[43,44] liquid ammonia,[27,45,46] phosphine,[27] hydrogen sulfide,[27] *N*-methylacetamide,[47–49] liquid sulfur,[50] and liquid hydrogen-fluoride.[34,51–53] Recently, in addition to the static thermodynamic description by the QCE model, the kinetics of the hydrogen bond formation and proton transfer in water clusters has been studied by Weinhold.[54] To the best of our knowledge, the only binary system for which the QCE model has been applied until now is the water–dimethyl-sulfoxide (DMSO)[55] binary mixture. Evidently the reason is not limited interest in binary (or ternary) systems, but rather arise from technical difficulties for a proper description of such mixtures. These include both the approximations inherent in the QCE model, as well as the more complex structure of liquids consisting of more than one component. While in the binary system treated so far by the QCE model one component acts as a hydrogen bond acceptor (DMSO) and the other (water) as donor, in binary mixtures of alcohols or alcohol–water, as used in our previous experimental investigations,[11,12] both components can act as hydrogen bond acceptors as well as hydrogen bond donors.

As a first step to a detailed understanding of such binary solvent mixtures in this study we want to present a quantum cluster equilibrium study of the MeOH–water system with different composition ranging from pure water to pure MeOH. We have chosen this system not only as it represents the prototype of binary mixture used in our previous investigations but also since several theoretical modeling studies, mainly by molecular dynamics,[56–64] as well as experimental investigations,[65–68] have been published.

Moreover, since apparently the QCE model has for the first time been applied to a binary liquid mixture where both components can act as hydrogen bond acceptors and also as hydrogen bond donors, the MeOH–water system presents an important test case for the quantum cluster equilibrium model of such mixtures.

Computational methods

The methanol–water cluster structures have been optimized using the B3LYP density functional[69–72] augmented with the D3 dispersion correction[73] of Grimme *et al.* as implemented in the ORCA 2.9.1 program.[74] The TZVP basis set[75] has been used both for the optimizations and for the vibrational analysis. The intracluster interaction energies (E_{int}) were determined using the QZVP basis set[76] according to eqn (1) and are corrected for the basis set superposition error (BSSE)[77]

$$E_{int} = E_{cluster} - \sum E_{monomers} = E_{cluster} - i{\cdot}E_{MeOH} - j{\cdot}E_{H_2O} \quad (1)$$

where i, j are the numbers of monomers of methanol and water, respectively, participating in forming the cluster, while E is the electronic energy.

Gibbs free energies of interaction ΔG_{int} were obtained from the BSSE-corrected B3LYP-D3/QZVP interaction energies combined with non-thermal (ZPE) and thermal corrections dG^{corr} resulting from the TZVP frequency analysis at T = 298.15 K and p = 1 atm. For the rotational partition function the appropriate symmetry numbers (σ = 2 for *w1*, *m2w2r*, *w4r*, *m4r*, *m2w6*; σ = 3 for *m6r*; σ = 4 for *w8c* and *m4w4c*; for all other clusters σ = 1) were used.

$$\Delta G_{int} = E_{int}(\text{BSSE-QZVP}) + [dG^{corr}_{cluster} - \sum dG^{corr}_{monomers}](\text{TZVP}) \quad (2)$$

All calculations were done with a very tight SCF cutoff and integration grid size of 5, together with tight geometry optimization criteria. In addition to B3LYP-D3 the M06-2X density functional[78–80] as implemented in Gaussian 09 program[81] in combination with the aug-cc-pVTZ basis set[82] was also used. The motivation for choosing these two functional was mainly based on the works of Thakkar[21] and Golub[19] as well as our previous experience.[14]

The QCE calculations have been performed using the developer version of the PEACEMAKER 2.0 program (rev. 572) of the research group of Kirchner.[33] The extension of the program for binary systems is described in detail in ref. 55. Besides the electronic energy, interaction energy, principal moments of inertia and harmonic vibrational frequencies of clusters, to obtain the statistical thermodynamics data *via* partition functions, two fitting parameters a_{mf} and b_{xv} are used in the QCE theory. The recently developed one-parameter QCE variant so far has only been applied to neat liquids.[34]

Based on the parameter a_{mf}, the interaction energies of each cluster with the surrounding particles/clusters can be defined as an additive term (u_{int}) to the intracluster interaction energies (E_{int}). The parameter b_{xv} gives the correction for the calculation of the excluded volume V_{excl}.

The mean field potential u_{int} in the case of the binary mixture is given by eqn (3), for each cluster individually:

$$u^{int} = -a_{mf}\frac{i+j}{V_m} \quad (3)$$

The excluded volume for the total system is defined as

$$V_{excl} = b_{xv}{\cdot}V_{vdw} \quad (4)$$

where i, j denote the number of molecules of methanol and water, respectively, which are participating in forming a given cluster, and V_{vdw} denotes total volumes of the clusters. The sum of all cluster volumes V_{vdw} compose 1 mol of monomers.

In the PEACEMAKER program the aforementioned two parameters are sampled with the aims to make agreement between the experimental and the calculated isobars while searching for the phase with the lowest Gibbs energy at the given pressure and temperature. Since only the liquid phase was considered, the mean absolute deviation function was selected in the program for comparison of the calculated and experimental isobars during the sampling process. The experimental isobars were obtained from the Landolt–Börnstein database.[68] Both a_{mf} and b_{xv} were kept constant over the whole temperature range since there is no provision for a temperature dependence of these two parameters in the PEACEMAKER program.

Open Access Article. Published on 30 January 2015. Downloaded on 11/24/2022 8:06:22 AM.
This article is licensed under a Creative Commons Attribution-NonCommercial 3.0 Unported Licence.

Table 1 The clusters included in the cluster set describing the methanol–water binary liquid mixture[a]

			B3LYP-D3/QZVP			M06-2X/aug-cc-pVTZ		
Cluster class	Cluster structure	Number of H-bonds	E_{int}	ΔG_{int}^{298}	ΔG_{int}^{298}/monomer	E_{int}	ΔG_{int}^{298}	ΔG_{int}^{298}/monomer
mon	*m1*	0	0.00	0.00	0.00	0.00	0.00	0.00
	w1	0	0.00	0.00	0.00	0.00	0.00	0.00
dim	*m2*	1	−24.69	16.89	8.44	−24.44	14.98	7.49
	m1w1	1	−21.77	12.06	6.03	−20.90	13.90	6.95
	w1m1	1	−24.39	11.67	5.84	−23.83	12.92	6.46
	w2	1	−21.87	11.06	5.53	−21.31	13.65	6.83
r3	*m3r*	3	−75.08	19.72	6.57	−72.00	15.42	5.14
	m2w1r	3	−73.16	16.48	5.49	−71.60	17.07	5.69
	m1w2r	3	−71.16	17.29	5.76	−70.96	15.62	5.21
	w3r	3	−69.07	17.96	5.99	−70.39	17.83	5.94
r4	*m4r*	4	−133.08	17.94	4.48	−121.90	1.25	0.31
	m3w1r	4	−130.20	13.33	3.33	−121.27	6.68	1.67
	m2w2r	4	−127.46	16.78	4.19	−120.71	9.98	2.49
	m1w3r	4	−124.89	11.29	2.82	−119.68	13.07	3.27
	w4r	4	−122.36	14.70	3.68	−118.77	17.15	4.29
r5	*m5r*	5	−176.80	21.49	4.30	−163.32	14.30	2.86
	m4w1r	5	−173.36	19.23	3.85	−159.68	8.05	1.61
	m3w2r	5	−169.81	21.25	4.25	−157.59	11.13	2.23
	m2w3r	5	−165.96	22.54	4.51	−155.94	18.27	3.65
	m1w4r	5	−163.26	22.90	4.58	−155.59	18.62	3.72
	w5r	5	−160.58	20.76	4.15	−154.13	22.93	4.59
r6	*m6r*	6	−217.84	35.91	5.98	−200.47	0.60	0.10
	m5w1r	6	−214.21	35.51	5.92	−198.91	6.39	1.07
	m4w2r	6	−210.60	33.30	5.55	−197.35	15.34	2.56
	m3w3r	6	−207.21	30.58	5.10	−195.72	18.73	3.12
	m2w4r	6	−203.84	32.73	5.45	−194.11	24.65	4.11
	m1w5r	6	−200.76	29.77	4.96	−192.28	27.35	4.56
	w6r	6	−197.78	30.39	5.07	−190.47	31.31	5.22
r7	*m7r*	7	−261.88	42.60	6.09	−242.00	29.90	4.27
	m6w1r	7	−257.54	40.59	5.80	−240.49	34.72	4.96
	m5w2r	7	−253.78	43.01	6.14	−238.75	40.97	5.85
	m4w3r	7	−250.44	40.53	5.79	−237.95	44.14	6.31
	m3w4r	7	−245.83	42.51	6.07	−234.13	48.37	6.91
	m2w5r	7	−239.41	45.81	6.54	−230.56	39.58	5.65
	m1w6r	7	−234.20	37.28	5.33	−226.72	43.78	6.25
	w7r	7	−227.96	49.45	7.06	−220.17	37.24	5.32
bc7(5-4)	*m6w1bc*	8	−263.59	42.38	6.05	−242.49	34.45	4.92
	m5w2bc	8	−260.87	37.81	5.40	−243.50	36.35	5.19
	m4w3bc	8	−255.85	37.44	5.35	−241.75	41.28	5.90
	m3w4bc	8	−250.83	41.43	5.92	−240.26	37.97	5.42
	m2w5bc	9	−255.42	39.40	5.63	−246.11	31.00	4.43
	m1w6bc	9	−251.33	36.66	5.24	−244.61	36.80	5.26
	w7bc	9	−247.39	34.26	4.89	−241.68	38.40	5.49
s5(3-3)	*m4w1s*	6	−145.57	52.10	10.42	−140.81	32.08	6.42
	m3w2s	6	−143.10	51.88	10.38	−140.26	34.73	6.95
	m2w3s	6	−140.95	47.91	9.58	−139.93	34.67	6.93
	m1w4s	6	−138.81	42.77	8.55	−139.29	35.73	7.15
	w5s	6	−136.99	42.51	8.50	−138.93	37.01	7.40
s6(3-4)	*m5w1s*	7	−203.39	48.52	8.09	−190.70	29.28	4.88
	m4w2s	7	−201.22	48.74	8.12	−190.35	32.49	5.41
	m3w3s	7	−198.04	41.48	6.91	−189.37	32.71	5.45
	m2w4s	7	−195.69	41.17	6.86	−188.49	30.42	5.07
	m1w5s	7	−192.80	42.76	7.13	−187.71	33.78	5.63
	w6s	7	−190.27	43.51	7.25	−186.73	38.60	6.43
s9(5-5)	*m8w1s*	10	−357.17	55.40	6.16	−327.91	46.11	5.12
	m7w2s	10	−352.89	57.28	6.36	−325.19	49.64	5.52
	m6w3s	10	−348.04	59.15	6.57	−328.16	39.34	4.37
	m5w4s	10	−342.96	61.85	6.87	−324.78	42.49	4.72
	m4w5s	10	−339.60	60.48	6.72	−319.22	37.37	4.15

Open Access Article. Published on 30 January 2015. Downloaded on 11/24/2022 8:06:22 AM.
This article is licensed under a Creative Commons Attribution-NonCommercial 3.0 Unported Licence.

Table 1 (*continued*)

Cluster class	Cluster structure	Number of H-bonds	B3LYP-D3/QZVP			M06-2X/aug-cc-pVTZ		
			E_{int}	ΔG_{int}^{298}	ΔG_{int}^{298}/monomer	E_{int}	ΔG_{int}^{298}	ΔG_{int}^{298}/monomer
	m3w6s	10	−334.50	60.68	6.74	−316.61	40.36	4.48
	m2w7s	10	−331.41	57.48	6.39	−315.10	43.19	4.80
	m1w8s	10	−328.49	53.80	5.98	−313.82	49.65	5.52
	w9s	10	−325.62	54.85	6.09	−312.61	50.78	5.64
s11(6-6)	*m10w1s*	12	−445.33	72.99	6.64	−412.86	64.48	5.86
	m9w2s	12	−429.57	90.54	8.23	−406.99	72.29	6.57
	m8w3s	12	−424.96	93.75	8.52	−395.11	52.32	4.76
	m7w4s	12	−421.45	90.79	8.25	−395.51	50.19	4.56
	m6w5s	12	−417.84	87.80	7.98	−393.85	48.42	4.40
	m5w6s	12	−413.08	88.83	8.08	−389.70	46.33	4.21
	m4w7s	12	−409.66	90.71	8.25	−388.05	54.69	4.97
	m3w8s	12	−406.37	86.19	7.84	−386.33	56.45	5.13
	m2w9s	12	−407.83	76.25	6.93	−391.44	57.29	5.21
	m1w10s	12	−404.44	73.24	6.66	−389.72	62.27	5.66
	w11s	12	−401.20	74.77	6.80	−388.26	66.66	6.06
l5(4-1)	*m3w1r-m1*	5	−160.57	33.92	6.78	−150.76	35.86	7.17
l6(5-1)	*m5r-w1*	6	−209.40	41.25	6.87	−193.96	33.10	5.52
l6(4-2)	*m3w1r-2m1(1,1)*	6	−195.04	56.63	9.44	−184.46	50.15	8.36
	m3w1r-2m1(1,3)	6	−189.89	60.69	10.11	−177.78	44.24	7.37
b6(4-4)	*m2mwm2*	7	−220.47	27.84	4.64	−204.74	21.47	3.58
	mwmwm2	7	−215.86	33.51	5.58	−201.60	18.49	3.08
	mwmwmw	7	−212.42	30.65	5.11	−200.34	22.54	3.76
	w2mwmw	7	−210.13	26.32	4.39	−199.51	23.86	3.98
	mww2mw	7	−208.13	33.47	5.58	−198.48	26.23	4.37
	w2mww2	7	−207.15	27.90	4.65	−198.26	26.78	4.46
	w2w2w2	7	−202.96	31.01	5.17	−196.48	31.91	5.32
	mww2w2	7	−205.30	30.21	5.03	−197.28	28.74	4.79
	m2w2mw	7	−211.51	36.48	6.07	−202.07	27.86	4.64
	m2w2m2	7	−216.05	31.16	5.19	−203.55	25.13	4.19
c8	*m5w3c*	11	−331.17	24.08	3.01	−307.14	30.56	3.82
	m4w4c	12	−341.18	17.11	2.14	−319.27	21.34	2.67
	m3w5c	12	−337.67	15.94	1.99	−318.44	23.83	2.98
	m2w6c	12	−333.81	20.12	2.51	−317.63	26.52	3.32
	m1w7c	12	−330.03	20.77	2.60	−316.91	28.57	3.57
	w8c	12	−326.18	27.15	3.39	−315.84	30.39	3.80
c8-lasso	*m4w4c-m1*	13	−369.71	38.44	4.27	−350.33	42.17	4.69

[a] Interaction energies E_{int} and Gibbs free energies of interaction ΔG_{int}^{298} in kJ mol^{-1}. The M06-2X values for the clusters *m8w1s*, *m8w3s*, *m9w2s*, and *m10w1s* are based on aug-cc-pVDZ geometries, ZPE, and thermal corrections to ΔG_{int}.

In these QCE calculations it is especially important to provide a representative and comprehensive set of cluster motifs as it has been shown earlier.[31] In this study 93 clusters like ring, spiro, book, bicyclic, lasso and cubic structures have been included. The full cluster set (95 including the two monomers) with the naming convention is provided in Table 1 and some representative structures illustrating the notation are presented in Fig. 1. The various structures of the clusters required by the QCE model are denoted as $m_x w_y t$ where m and w indicate the monomers MeOH (m) and water (w); x and y mean the numbers of the corresponding monomers, and t indicates the cluster type *i.e.* mon: monomer, dim: dimer, r: monocyclic ring, bc: bicyclic ring, s: spiro cluster[31] in which two rings are connected through a common water molecule which establishes four hydrogen-bonds (2 donor and 2 acceptor) towards the two rings; l: lasso, b: book, c: cubic. The ring size of monocyclic clusters (r-type clusters) equals $x + y$; for spiro cluster besides the total clusters size in parentheses also the numbers of molecules participating in the connected rings are given. For lasso structures in parentheses the numbers of molecules within the ring and of those connected to the ring as well as the points of attachment are given. In the case of seven-membered clusters besides monocyclic rings also bi- and polycyclic structures consisting of a five- and four-membered ring, denoted by *bc7(5-4)*, have been found. Because previously linear chain and lasso structures were found to be less important[35,37,38] in the cases of primary alcohols, especially MeOH, within the QCE model only a few of these type of clusters were included. The reason of their smaller contribution originates from the smaller increase (as absolute value) in the interaction energy with the cluster size compared with cyclic structures where the cooperativity effect[18,83,84] plays a key role.

Open Access Article. Published on 30 January 2015. Downloaded on 11/24/2022 8:06:22 AM.
This article is licensed under a Creative Commons Attribution-NonCommercial 3.0 Unported Licence.

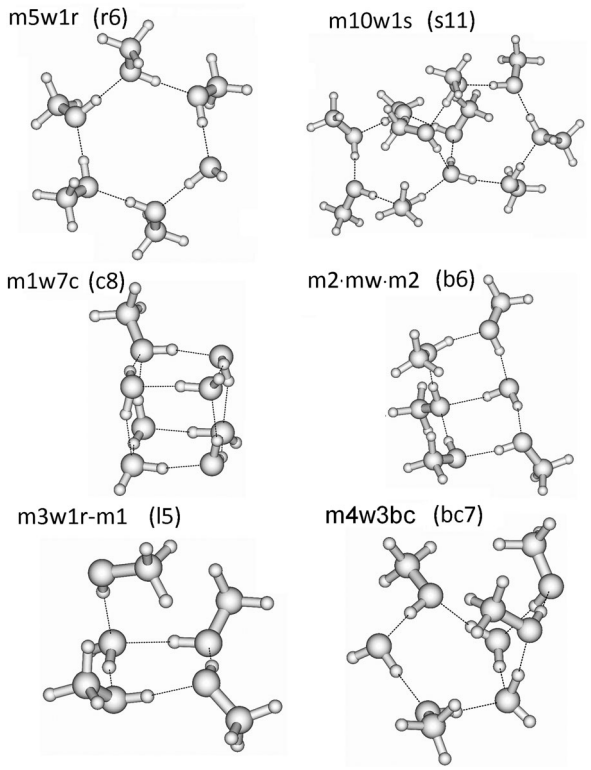

Fig. 1 Plot of the main cluster types (ring, spiro, cubic, book, lasso, and bicyclic).

Because not only the temperature but also the composition dependence of the cluster distribution were planned to be studied, the ring, spiro and cubic clusters were created with all the possible compositions. Hence, starting from pure water clusters, water molecules were successively replaced by methanol molecules with the restriction that the cluster motifs remain unchanged. Therefore, in the case of the spiro clusters one water molecule had to be retained; in the case of the cubic *c8* clusters four water molecules are needed to be kept; in case of the ring type clusters, no such restriction applies. The replacements have been carried out according to the previous findings:[37] in structures with adjacent MeOH molecules the methyl groups were oriented to different directions (*i.e.* up–down, respectively). Furthermore, the replacements have been done more or less randomly within the structures, keeping in mind that the appropriate selection of cluster motifs[31] (*i.e.* inclusion of the cubic, the ring and the spiro cluster classes) is more important than the strict placement of the methyl groups or using strictly the putative global minimum structure of a given cluster type. Cartesian coordinates of all clusters optimized with B3LYP-D3/TZVP and M06-2X/aug-cc-pVTZ methods are available as ESI.†

Results and discussion

Values of a_{mf} and b_{xv} obtained by fitting to experimental isobars for MeOH–water binary mixtures of different composition [molar fraction x(MeOH)] are summarized in ESI,† Table S1. With increasing methanol molar fraction, the a_{mf} value also increases, from 0.19 up to 0.41 J m^3 mol^{-1}. At the same time, the fitting becomes less accurate as shown by the increase of the mean absolute error (MAE). Importantly, the ratio of a_{mf}/b_{xv} is not constant but shows a parabolic shape. As a consequence, the application of the one-parameter variant of the QCE model to the methanol–water mixture might be problematic.

A similar dependence of the quality of the fitting on the composition has also been found for the DMSO–water binary system.[30] However, while in DMSO–water the deviation increases with increasing water content, in the MeOH–water mixture the quality of the fit becomes less satisfactory with increasing x(MeOH), *i.e.* with decreasing water content. For DMSO–water these deviations had been attributed to the rather small clusters used.[30] In the present case of MeOH–water not only larger clusters but also a more extensive cluster set has been used.

In the case of neat water the cubic *w8c* cluster has been shown to dominate at low temperatures,[31,32] although neglecting it led to slightly more accurate isobars. To check the importance of this cluster type in binary MeOH–water mixtures, the fitting to experimental isobars has been done with and without these *c8* clusters. Experimental isobars of neat water, neat MeOH, and of the 30, 60, 80 w% MeOH–water mixtures and those calculated by the QCE model using B3LYP-D3 results are shown in Fig. 2.

Compared with experiment a somewhat too small slope of the isobars – irrespective of the composition – is obtained. As ESI,† Table S2 shows, when cubic *c8* clusters are excluded, the values of a_{mf} and b_{xv} are only slightly changed. Isobars as well as the values of a_{mf} and b_{xv} obtained from M06-2X calculations differ only marginally from those based on B3LYP-D3 calculations (Tables S1 and S2, ESI†).

The quality of the fit only marginally depends on whether cubic clusters are included in the set or not (Fig. 2). The numbers of clusters corresponding to a specific x(MeOH) is shown in ESI,† Fig. S1. Although the number of clusters vary with x, overall the chosen cluster set should allow for a balanced description of the MeOH–water mixture over the whole range of MeOH content.

Based on these optimal parameters a_{mf} and b_{xv} in the following, first interaction energies and distribution of the individual clusters considered for the MeOH–water binary mixture will be presented. Second, thermodynamic properties (heat capacities C_p, excess enthalpies, entropies, Gibbs free energies, and volumes of mixing, H^E, S^E, G^E, and V^E) derived therefrom will be compared with the corresponding experimental data as well as those obtained from previous calculations (molecular dynamics and Monte Carlo simulations).

Cluster distribution in MeOH–H_2O binary mixture

B3LYP-D3 as well as M06-2X interaction energies E_{int} and Gibbs free energies of interaction ΔG_{int}^{298} for the whole cluster set used in the QCE procedure are presented in Table 1.

While interaction energies are strongly negative and approximately correlate with the number of hydrogen bonds, Gibbs free energies of interactions are invariably positive and do not show any correlation with the number of hydrogen bonds.

Open Access Article. Published on 30 January 2015. Downloaded on 11/24/2022 8:06:22 AM.
This article is licensed under a Creative Commons Attribution-NonCommercial 3.0 Unported Licence.

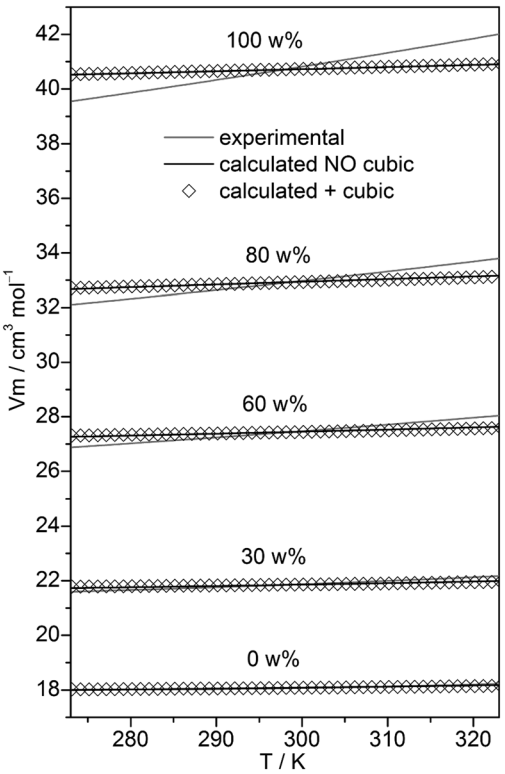

Fig. 2 Plot of experimental isobars[68] of neat water, neat MeOH and 10, 30, 60, 80 w% MeOH–water mixtures *versus* those obtained by the QCE model with and without inclusion of the cubic *c8* clusters.

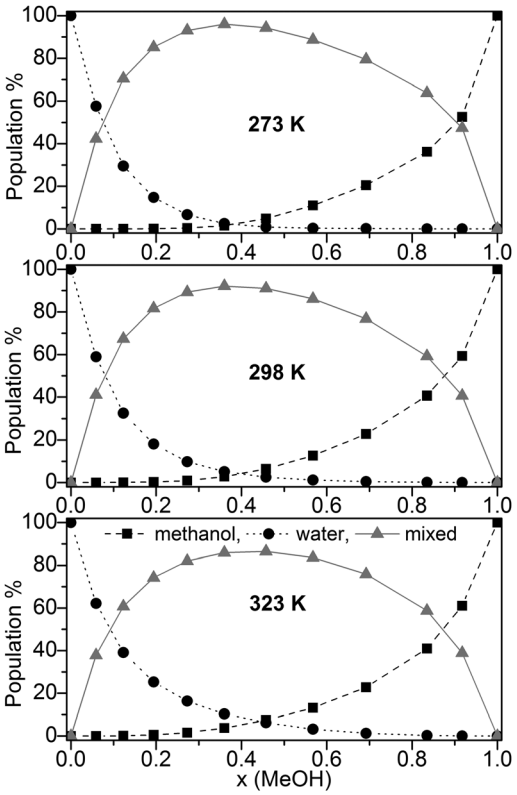

Fig. 3 Population (%) of ■ pure methanol clusters, ● pure water cluster, ▲ mixed MeOH–water clusters at 273 K, 298 K, and 323 K based on the B3LYP-D3 calculations.

According to the study of Thakkar *et al.*[21] dispersion-corrected density functionals work reasonably well for MeOH clusters compared with CCSD(T) results. Furthermore, M06-2X/aug-cc-pVDZ interaction energies per molecule of both linear as well as cyclic MeOH clusters were found to be nearly identical to those obtained by MP2/aug-cc-pVTZ calculations.[19] In contrast, B3LYP without dispersion corrections resulted in larger deviations.[19] Comparison of the present B3LYP-D3/QZVP//TZVP and M06-2X/aug-cc-pVTZ interaction energies with our previous MP2(fc)-CP/6-311++G(d,p) results indicate more negative E_{int} values but nearly identical trends for both density functionals (Fig. S2, ESI†). Moreover, B3LYP-D3 calculated interaction energies for the full cluster set considered in this paper (Table 1) are in close agreement with the corresponding M06-2X/aug-cc-pVTZ values (R^2 = 0.998, Fig. S3, ESI†). Thus, we are confident that the functionals used are appropriate for this study.

The population (based on the B3LYP-D3 calculations) of pure water, pure methanol as well as mixed clusters without further distinction of their composition at three different temperatures (273, 298, and 323 K) is displayed in Fig. 3.

Irrespective of the temperature mixed clusters dominate over a wide range of the composition of the binary MeOH-water system ($\geq$60% in the range x(MeOH) = 0.1 to 0.8). Only a slight decrease of the contribution of mixed clusters with increasing temperature is found (Fig. 3). It is interesting to note that NMR relaxation time measurements of MeOH–water mixtures have indicated that at low temperatures T_k < 245 K clusters between the same species prevail while above T_k mixed clusters are preferred.[85]

Since the lowest temperature considered here (T = 273 K) is well above T_k the predominance of mixed clusters in the intermediate molar fraction region is in line with these experimental findings. Although we have taken into account only clusters up to 11 molecules, our result obtained for the maximum population of mixed clusters at x = 0.365 (273 K) is in line with the mass spectroscopy experiments of Wakisaka.[5,8] From these experiments it had been concluded that above x(MeOH) = 0.375 the self-association of alcohol clusters becomes more preferred with increasing x(MeOH).[5,8] The gross populations of pure and mixed clusters based on M06-2X/aug-cc-pVTZ calculations are quite similar to those obtained by B3LYP-D3 (Fig. S4, ESI†). The most notable difference concerns mixed clusters which show lower populations over the whole range of x(MeOH) than those based on B3LYP-D3 calculations [<70% (M06-2X) at T = 298 K compared with up to 90% (B3LYP-D3, Fig. 3)]. For DMSO–water binary system a similar distribution of pure water, pure DMSO, and mixed clusters had been found.[30] However, the drop and/or rise of the pure clusters is less steep in DMSO–water than in MeOH–water.

For instance, ~60% pure water clusters at x(DMSO) = 0.2 and ~60% pure DMSO clusters at x(DMSO) = 0.8 had been calculated[30] compared with ~20% pure water clusters at x(MeOH) = 0.2 and ~40% pure MeOH clusters at x(MeOH) = 0.8 (Fig. 3). Consequently, the population of the mixed DMSO–water clusters is

Open Access Article. Published on 30 January 2015. Downloaded on 11/24/2022 8:06:22 AM.
This article is licensed under a Creative Commons Attribution-NonCommercial 3.0 Unported Licence.

significantly lower ($\leq$60%)[30] than that of mixed MeOH–water clusters.

The population of the various cluster classes irrespective of their composition (based on the B3LYP-D3 calculations) is presented in Fig. 4a (cubic *c8* clusters included) and Fig. 4b (populations with cubic *c8* clusters neglected).

The results in Fig. 4a show that only some of the used clusters are important to consider when including cubic clusters. These are the five- and six-membered monocyclic structures with only one ring, the 8-membered cubic clusters and the *s9* and *s11* spiro-type clusters. In line with previous findings for neat water[32,33] the population of cubic *c8* clusters decreases with increasing temperature. Nevertheless, this cluster type by far is dominating up to x(MeOH) = 0.7 (273 K), and x(MeOH) = 0.5 (323 K). Since these clusters contain at least 4 water molecules it is not surprising that at higher MeOH contents their population drops significantly while the populations of monocyclic clusters (*r5* and especially *r6*) where there is no such restriction with respect to the number of water molecules increase substantially at high x(MeOH). The presence of such cyclic structures in liquids capable of forming hydrogen bonds has been corroborated by experimental studies (soft X-ray emission[86] and X-ray absorption augmented by DFT calculations[87]). Especially at lower temperatures the spiro-type cluster *s11(6-6)* is quite important for mixtures with relatively high MeOH content (maximum of ~25% at x(MeOH) ~ 0.8 and T = 273 K, Fig. 4). The populations of *s9* spiro type clusters are fairly constant over the whole composition of the MeOH–water mixture at low temperatures; at T = 323 K this cluster type is also populated (10–20%) especially in the water-rich region.

If cubic clusters are neglected in the QCE model (Fig. 4b), the spiro-type clusters *s11(6-6)* and especially *s9(5-5)* dominate in the water-rich region at lower temperatures (up to x(MeOH) = 0.6 at T = 273 K); with increasing temperature their contribution decreases from ~50% (T = 273 K) to ~35% (T = 323 K) for neat water. Since at least one water molecule is required for the spiro motif, the population steadily decreases with increasing MeOH content. In contrast to spiro clusters, the populations of monocyclic rings (*r5* and *r6*) steadily increase with x(MeOH). As a consequence, neat MeOH is almost exclusively (>90%) composed of five- and six-membered ring clusters. Since cubic clusters require at least four water molecules, this result holds irrespective whether *c8* clusters are included or not in the cluster set used to describe the MeOH–water system. Interestingly, seven-membered monocyclic rings *r7* are not negligible at higher temperatures and low MeOH content (Fig. 4b).

Populations of individual clusters, *i.e.* distinguished by composition, are plotted in Fig. 5a (including cubic clusters) and Fig. 5b (neglecting cubic clusters). Dominating clusters are the cubic, spiro (*s9* and *s11*), and ring-type structures while

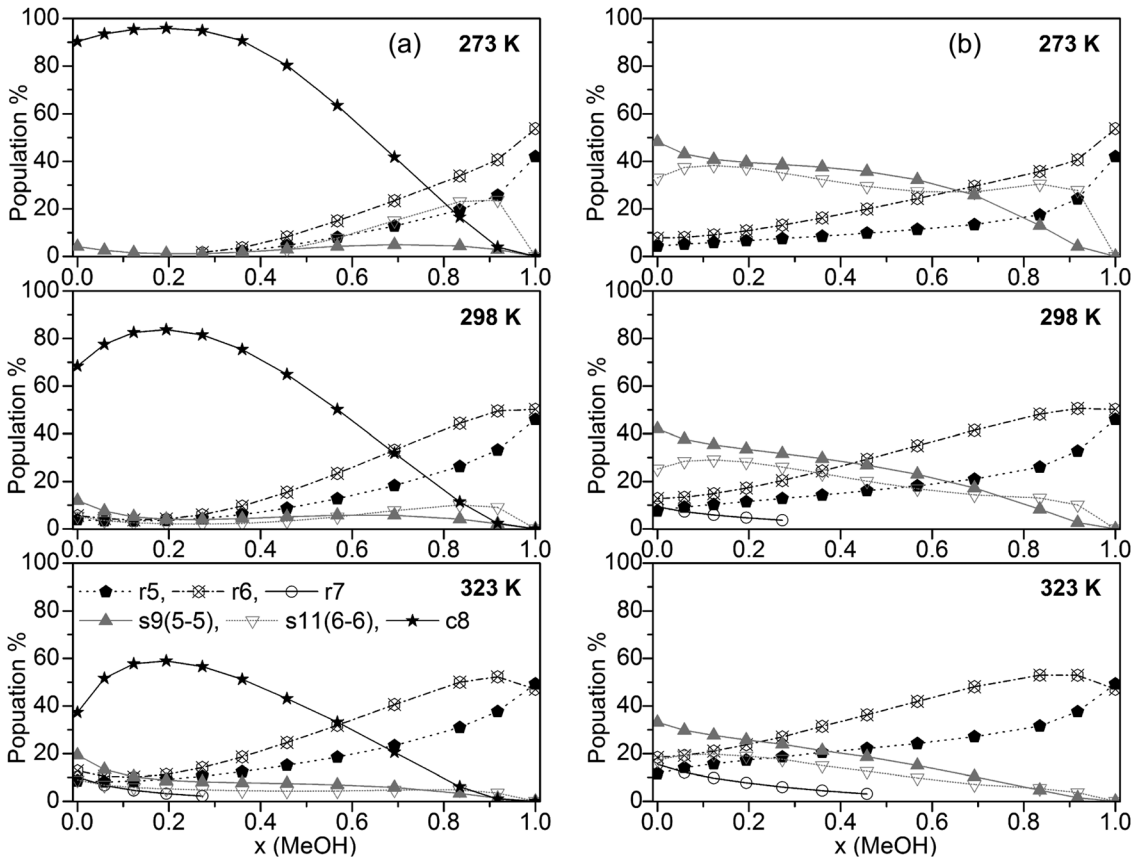

Fig. 4 Plot of the population of the cluster classes (a) including and (b) excluding cubic *c8* clusters (for clarity, only clusters with populations >10% are shown).

Open Access Article. Published on 30 January 2015. Downloaded on 11/24/2022 8:06:22 AM.
This article is licensed under a Creative Commons Attribution-NonCommercial 3.0 Unported Licence.

book, lasso and bicyclic clusters are of minor importance. Concerning cubic clusters, for neat water the *w8c* cluster is by far dominating, ~70% at T = 273 and 298 K, ~40% at T = 323 K. With increasing MeOH content the population of this cluster drops quite quickly (~10% for x(MeOH) = 0.2). In the water-rich region with x(MeOH) < 0.3 the *m1w7c* structure becomes the dominating cubic cluster with a relatively sharp maximum at x(MeOH) ~ 0.15. In the intermediate region, x(MeOH) = 0.2 to 0.7 the largest population is obtained for *m3w5c* and, to a lesser extent, for *m4w4c*. Especially at lower temperatures (T = 273 and 298 K) and low MeOH content (x(MeOH) = 0.1–0.4) the *m2w6c* cluster is significantly populated. An increase of the temperature results in a decrease of the populations of these cubic clusters. With respect to spiro-type clusters, in neat water and at very low MeOH content ($x \leq 0.15$) only *w9s* is significantly populated with the population increasing at higher temperatures at the expense of *w8c*. The only other spiro-type cluster is *m10w1s* at T = 273 K for x(MeOH) > 0.5 (maximum of 20% at x(MeOH) = ~0.9). While monocyclic ring structures consisting solely of water molecules (*w6r*, *w7r*) are of minor importance (<15% at T = 323 K and even less at lower temperatures), the analogous MeOH clusters *m5r* and *m6r* become increasingly important with increasing MeOH content. As mentioned above, neat MeOH can almost exclusively be described by these two cluster types. At T = 323 K the dominant cluster in the region x(MeOH) = 0.6–0.8 is *m5w1r*. The analogous plot obtained with M06-2X for T = 298 K is shown in Fig. S5 (ESI†). Similar to the B3LYP-D3 results, the dominating cluster types at low MeOH content are the cubic clusters *w8c* and *m1w7c* and at high MeOH content the *m6r* ring structure. In the range x(MeOH) = 0.6–0.9 the cyclic cluster *m5w1r* is already significantly populated (10–20%) at T = 298 K. Interestingly, in contrast to the B3LYP-D3 results, the five-membered cyclic *m5r* cluster does not show any substantial population at T = 298 K.

Fig. 5b presents cluster populations obtained when cubic clusters are excluded. In the MeOH – rich region (x(MeOH) > 0.8) where cubic clusters are of minor importance, the cluster distribution is quite similar to that obtained with cubic clusters included. The most important contributions are due to the five- and six-membered monocyclic rings *m5r*, *m6r*, and *m5w1r*. Of course, for neat MeOH the population of this latter cluster drops to 0 (Fig. 5b). For neat water and low MeOH content a significant increase of the spiro-type water clusters *w9s* and *w11s* can be seen. At higher temperatures the contributions of these clusters decrease in favor of monocyclic rings *w6r* and *w5r* (at T = 323 K). This is in agreement with Wakisaka's results,[8] that self-associated clusters are formed predominantly at low molar fraction (water clusters) and high molar fraction ($x \geq 0.375$, methanol clusters).

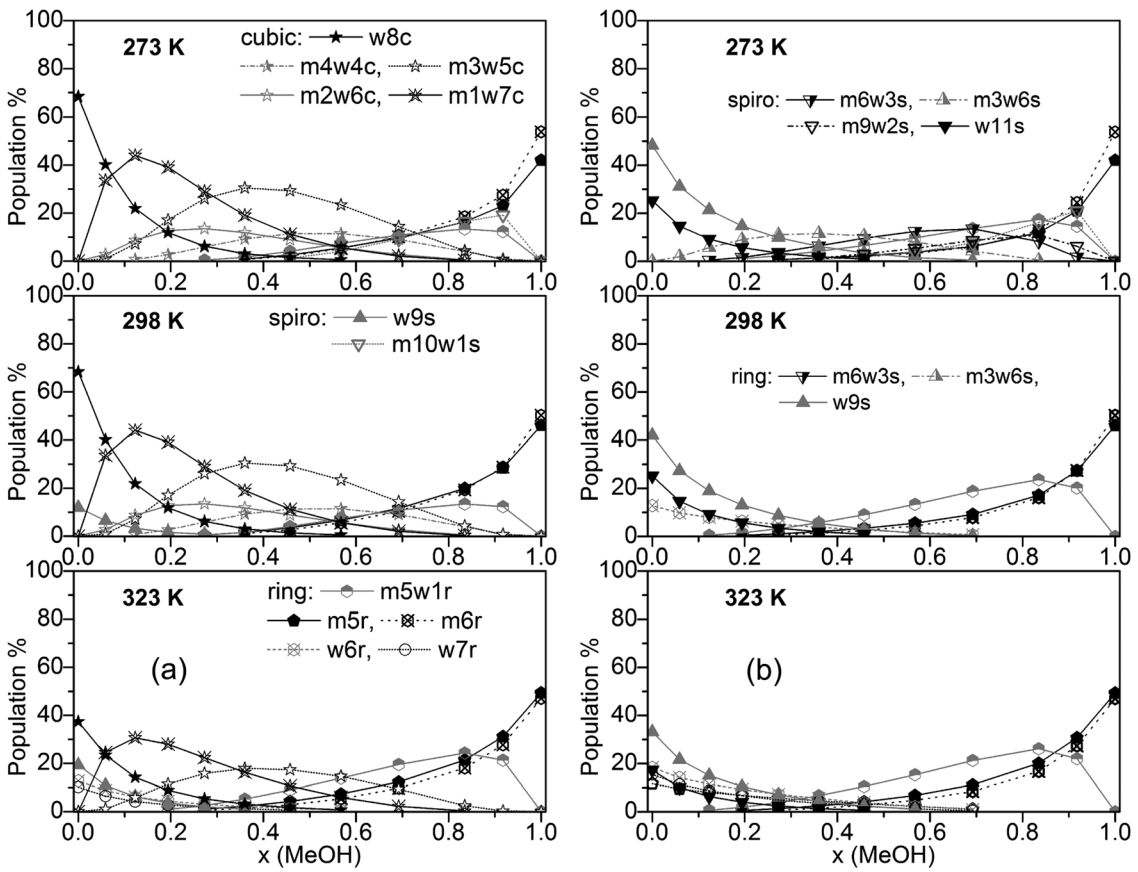

Fig. 5 Plot of individual cluster distributions (a) including and (b) excluding cubic *c8* clusters (for clarity, only clusters with populations >8% are shown).

 This journal is © the Owner Societies 2015

Open Access Article. Published on 30 January 2015. Downloaded on 11/24/2022 8:06:22 AM.
This article is licensed under a Creative Commons Attribution-NonCommercial 3.0 Unported Licence.

Table 2 Comparison of the calculated excess thermodynamic quantities (H^E, S^E, G^E) with data obtained from other experimental and theoretical studies. Units are kJ mol^{-1} and J K^{-1} mol^{-1}

x(MeOH)		Exp.[67,88, 91]	MD/2PT[56]	OPLS/TIP4P[64]	QCE B3LYP-D3	QCE M06-2X
0.05	H^E	−0.57	−0.18	−0.25	−0.81	−0.40
	S^E	−2.48	−0.70	−1.01	−2.91	−2.02
	G^E	0.17	0.06	0.05	0.11	0.20
0.27	H^E	−0.88	−0.66	−0.32	−2.18	−0.49
	S^E	−3.93	−3.31	−3.42	−8.44	−4.25
	G^E	0.29	0.37	0.70	0.42	0.78
0.54	H^E	−0.79	−0.82	−0.32	−1.67	−0.17
	S^E	−3.69	−3.93	−3.50	−7.45	−3.84
	G^E	0.31	0.42	0.72	0.63	0.97
0.70	H^E	−0.61	−0.73	−0.22	−1.06	0.16
	S^E	−2.89	−3.39	−2.77	−5.48	−2.99
	G^E	0.25	0.35	0.61	0.61	1.05

Calculated thermodynamic functions for methanol–water binary liquid mixtures

Based on the QCE calculations, the following thermodynamic functions are available from the canonical partition function according to eqn (22)–(29) in ref. 33 for the different temperatures and compositions: internal energy, enthalpy, entropy, Gibbs free energy, Helmholtz free energy as well as second derivatives of the partition function, like constant pressure and constant volume heat capacities.

In Table 2 we compare the experimental excess enthalpies, entropies, and Gibbs free energies of mixing[64,65,67,68,88–91] with those calculated by the QCE model as well as those obtained from a molecular dynamics simulation/two-phase thermodynamics (MD/2PT)[56] for different compositions of the MeOH–water system.

The excess enthalpies of mixing H^E (eqn (5)) (Fig. 6a) and the excess entropy of mixing S^E (eqn (6)) (Fig. 6b) obtained by the QCE calculations with and without inclusion of cubic clusters are plotted against experimental data.[89,90]

$$H^E(x) = H(x) - [H(H_2O_{liq}) \times (1 - x) + H(MeOH_{liq}) \times x] \quad (5)$$

The enthalpy values H are taken from the PEACEMAKER output, where $H(H_2O_{liq})$ and $H(MeOH_{liq})$ are the values for x = 0.0 and x = 100.0, respectively. Compared with experiment, the values of H^E are too negative but the minima of the curves occur approximately at the same molar fraction ($x \sim 0.36$). In contrast, MD/2PT[56] with the SPC/E model for water (which gave the best results) and even more so OPLS/TIP4P[64] calculations resulted in less negative H^E values than experiment (Table 2). Neglecting cubic clusters leads to considerably less negative excess enthalpies of mixing H^E, *i.e.* values closer to experiment but with a minimum shifted to much higher MeOH content, x(MeOH) $\sim$ 0.8 (Fig. 6a). The excess entropy of mixing S^E is computed according to eqn (6).

$$S^E(x) = S(x) - [S(H_2O_{liq}) \times (1 - x) + S(MeOH_{liq}) \times x] + R[x \ln(x) + (1 - x)\ln(1 - x)] \quad (6)$$

Similar to the excess enthalpies of mixing too negative values for S^E are obtained when cubic clusters are included. Without cubic clusters nearly perfect agreement with experiment is obtained (Fig. 6b). While OPLS/TIP4P[64] calculations resulted in less negative S^E values than experiment, MD/2PT S^E values

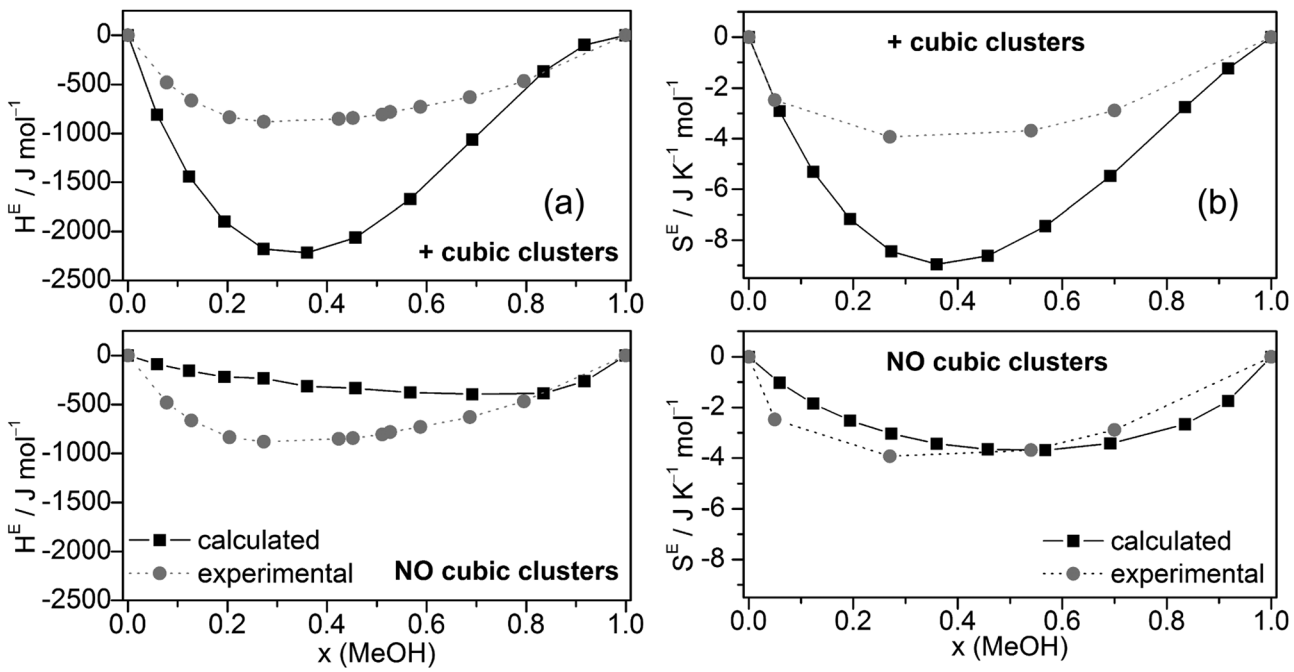

Fig. 6 Comparison of experimental and calculated excess enthalpies of mixing H^E (a),[89,90] excess entropies of mixing S^E (b)[56] for the full cluster set as well as the cluster set without the cubic *c8* clusters at different molar ratios.

Open Access Article. Published on 30 January 2015. Downloaded on 11/24/2022 8:06:22 AM.
This article is licensed under a Creative Commons Attribution-NonCommercial 3.0 Unported Licence.

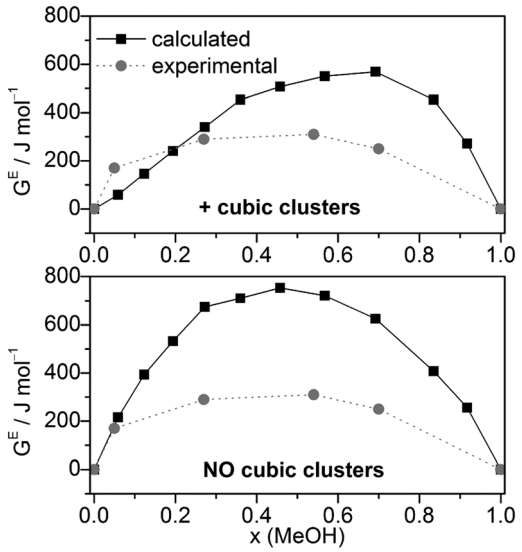

Fig. 7 Comparison of experimental[56] and calculated excess Gibbs free energies of mixing G^E for the full cluster set as well as the cluster set without the cubic *c8* clusters at different molar ratios (T = 298 K).

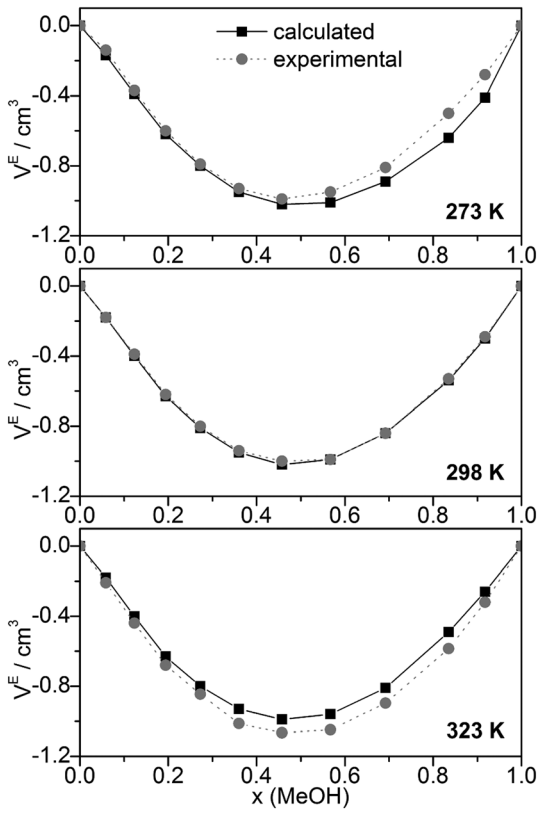

Fig. 8 Comparison of experimental[68] and calculated excess volumes of mixing V^E.

were less negative than experimental data at low and more negative at high x(MeOH), see Table 2.[56]

Combining H^E and S^E results to Gibbs free energies of mixing *via* $G^E = H^E - T{\cdot}S^E$. G^E values agree relatively well with the experimental data (Fig. 7), although more positive. Compared with the G^E values obtained by MD/2PT[56] or OPLS/TIP4P[64] the corresponding QCE data are more and less, respectively, positive except at x(MeOH) = 0.05 (Table 2).

Excess thermochemical quantities of mixing obtained by the QCE model using M06-2X interaction energies and vibrational frequencies show the following (Table 2 and Fig. S6, ESI†): the H^E values are less negative than those obtained with B3LYP-D3 or even positive in the methanol rich region ($x > 0.7$); S^E values are in quite good agreement with experimental values especially in the case of the full cluster set. As a consequence, the G^E values are more positive than the experimental ones or those calculated by the B3LYP-D3 functional.

The calculated dependence of the excess Gibbs free energy of mixing for the only other binary solvent system treated so far by the QCE model (DMSO–water) closely matches the experimental curve, especially the minimum at x(DMSO) $\sim$ 0.4. In contrast to MeOH–water, for DMSO–water G^E is negative over the whole range of x(DMSO). However, similar to the MeOH–water results, the QCE model yields for DMSO–water also too positive G^E values compared with experiment.[30]

Other quantities which can be compared with experiment are excess volumes of mixing V^E (Fig. 8), heat capacities C_p (Fig. 9), and excess heat capacities of mixing C_p^E (Fig. S7, ESI†). V^E and C_p^E were calculated in analogy to eqn (5). Since the parameter fits have been carried out to get good agreement between experimental and calculated molar volumes (V_m), the calculated V^E values agree nearly perfectly with the corresponding experimental data[68] as well as those obtained from a Monte Carlo simulation of TIP4P water and OPLS MeOH mixtures.[63]

The heat capacities C_p or the excess heat capacities of mixing C_p^E are the least satisfactorily reproduced quantities by the QCE calculations, irrespective of whether B3LYP-D3 or M06-2X results were used (Fig. 9, Fig. S7 and S8, ESI†). Such discrepancies

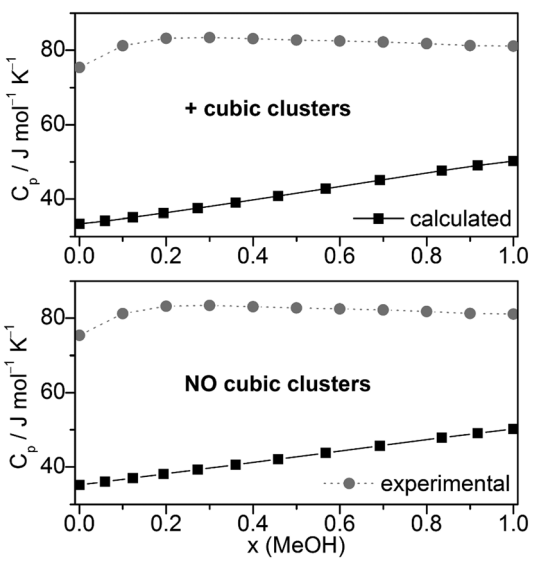

Fig. 9 Comparison of experimental[67,92,93] and calculated heat capacities C_p at T = 298.15 K.

Open Access Article. Published on 30 January 2015. Downloaded on 11/24/2022 8:06:22 AM.
This article is licensed under a Creative Commons Attribution-NonCommercial 3.0 Unported Licence.

had already been noticed in the original QCE publication.[23] One possible explanation of this deviation is the application of harmonic oscillator approximation even for the low frequency vibrations. In line with this, the vibrational contribution ($C_{p,vib}$) obtained from the vibrational partition function possess the largest amount of contribution to C_p, also in accordance with ref. 33.

Furthermore, it should be considered that the heat capacity is the second derivative of the partition function. Thus it is affected more by the applied approximations in the model than the other first derivative quantities.

Conclusions

The quantum cluster equilibrium model has been applied for the binary mixture of MeOH–water. Structures and interaction energies for a set of 93 clusters of different size, composition as well as class (chain, monocyclic rings, spiro, lasso, bicyclic, cubic) have been calculated by density functional theory (B3LYP-D3/QZVP and M06-2X/aug-cc-pVTZ including counterpoise BSSE corrections). B3LYP-D3 results in somewhat more negative interaction energies but the observed trend closely matches that obtained by M06-2X. The two fitting parameters a_{mf} and b_{xv} used in the QCE model were obtained by fitting to experimental isobars of MeOH–water binary mixtures with varying composition. Isobars based on B3LYP-D3 and M06-2X calculations were quite similar. With increasing MeOH content an increasing deviation between calculated and experimental isobars was found. Cluster distributions calculated by the QCE model using either B3LYP-D3 or M06-2X were quite similar with one notable exception: while the monocyclic ring-type clusters *m5r* and *m6r* both were found quite significant at high MeOH content with B3LYP-D3, only *m6r* showed a substantial population (50–100% in the range x(MeOH) = 0.7–1.0) based on M06-2X interaction energies and vibrational frequencies. Cubic *c8* cluster structures like *w8c* or *m1w7c* were found to dominate at low MeOH content whereas monocyclic ring structures, especially *m6r* were the most important clusters for x(MeOH) $>$ 0.8. In the intermediate region, x(MeOH) $\sim$ 0.4 to 0.7 the cubic cluster *m3w5c* is the dominant species. With increasing temperature the populations of these clusters decrease with a concomitant increase of other cluster populations, *e.g.* the monocyclic ring structure *m5w1r*.

Compared with experiment the calculated (B3LYP-D3) excess enthalpies of mixing H^E of methanol–water are somewhat too negative, those based on M06-2X are less negative and show larger overall deviations from the experimental curve in the methanol rich region. Excess entropies of mixing S^E are also too negative with B3LYP-D3 while those based on M06-2X nearly perfectly match the experimental S^E *vs.* x(MeOH) curve. Calculated excess Gibbs free energies of mixing G^E by either density functional are more positive than experimental values With respect to previous molecular dynamics simulations of the MeOH–water mixtures,[56,64] the QCE model based on B3LYP-D3 calculations consistently results in excess enthalpies H^E and especially entropies S^E of mixing which are more negative. Excess Gibbs free energies of mixing G^E are slightly more positive than the MD/2PT results of Pascal and Goddard[56] and slightly less positive than or even equal to the MD results of Tanaka and Gubbins.[64] The calculated excess volumes of mixing compare well with experiment. Significant deviations between calculated and experimental heat capacities C_p and excess heat capacity of mixing C_p^E were found.

Acknowledgements

The computations were run on the Hungarian HPC infrastructure (NIIF Institute, Hungary) and on computational facilities at Karl-Franzens University of Graz and at Graz University of Technology. The authors thank Prof. B. Kirchner and S.B.C. Lehmann for the discussions regarding the PEACEMAKER program. Financial support of the SROP-4.2.2.A-11/1/KONV-2012-0065 project is gratefully acknowledged. The work was also supported by the Scholarship program of the Aktion Österreich-Ungarn.

Notes and references

1 R. Mecke and H. Kempter, *Naturwissenschaften*, 1939, **27**, 583.
2 Y. Marcus, *Solvent Mixtures*, Properties and Selective Solvation, CRC Press, 2002.
3 A. Ben-Naim, *J. Phys. Chem. B*, 2007, **111**, 2896.
4 C. Reichardt, *Solvents and Solvent Effects in Organic Chemistry*, Wiley-VCH Verlag, Weinheim, 3rd edn, 2003.
5 A. Wakisaka and T. Iwakami, *J. Mol. Liq.*, 2014, **189**, 44.
6 A. Wakisaka and K. Matsuura, *J. Mol. Liq.*, 2006, **129**, 25.
7 A. Wakisaka, S. Mochizuki and H. Kobara, *J. Solution Chem.*, 2004, **33**, 721.
8 A. Wakisaka, S. Komatsu and Y. Usui, *J. Mol. Liq.*, 2001, **90**, 175.
9 A. Wakisaka and T. Ohki, *Faraday Discuss.*, 2005, **129**, 231.
10 A. Wakisaka and Y. Yamamoto, *J. Chem. Soc., Chem. Commun.*, 1994, 2105.
11 S. Kunsagi-Mate and K. Iwata, *Chem. Phys. Lett.*, 2009, **473**, 284.
12 S. Kunsagi-Mate and K. Iwata, *J. Solution Chem.*, 2013, **42**, 165.
13 A. Mandal, M. Prakash, R. M. Kumar, R. Parthasarathi and V. Subramanian, *J. Phys. Chem. A*, 2010, **114**, 2250.
14 G. Matisz, A.-M. Kelterer, W. M. F. Fabian and S. Kunsagi-Mate, *J. Phys. Chem. A*, 2011, **115**, 10556.
15 V. S. Bryantsev, M. S. Diallo, A. C. T. van Duin and W. A. Goddard, *J. Chem. Theory Comput.*, 2009, **5**, 1016.
16 R. Wieczorek, L. Haskamp and J. J. Dannenberg, *J. Phys. Chem. A*, 2004, **108**, 6713.
17 R. N. Barnett and U. Landman, *J. Phys. Chem. A*, 1997, **101**, 164.
18 S. L. Boyd and R. J. Boyd, *J. Chem. Theory Comput.*, 2007, **3**, 54.
19 P. Golub, I. Doroshenko and V. Pogorelov, *Phys. Lett. A*, 2014, **378**, 1937.

Open Access Article. Published on 30 January 2015. Downloaded on 11/24/2022 8:06:22 AM.
This article is licensed under a Creative Commons Attribution-NonCommercial 3.0 Unported Licence.

20 F. C. Hagemeister, C. J. Gruenloh and T. S. Zwier, *J. Phys. Chem. A*, 1998, **102**, 82.
21 S. Kazachenko, S. Bulusu and A. J. Thakkar, *J. Chem. Phys.*, 2013, **138**, 224303.
22 F. Weinhold, *J. Chem. Phys.*, 1998, **109**, 367.
23 F. Weinhold, *J. Chem. Phys.*, 1998, **109**, 373.
24 R. Ludwig and F. Weinhold, *J. Chem. Phys.*, 1999, **110**, 508.
25 R. Ludwig and F. Weinhold, *Phys. Chem. Chem. Phys.*, 2000, **2**, 1613.
26 R. Ludwig and F. Weinhold, *Z. Phys. Chem.*, 2002, **216**, 659.
27 R. Ludwig, *Phys. Chem. Chem. Phys.*, 2002, **4**, 5481.
28 P. Borowski, J. Jaroniec, T. Janowski and K. Wolinski, *Mol. Phys.*, 2003, **101**, 1413.
29 R. Ludwig, *ChemPhysChem*, 2007, **8**, 938.
30 A. Lenz and L. Ojamae, *J. Chem. Phys.*, 2009, **131**, 134302.
31 S. B. C. Lehmann, C. Spickermann and B. Kirchner, *J. Chem. Theory Comput.*, 2009, **5**, 1640.
32 S. B. C. Lehmann, C. Spickermann and B. Kirchner, *J. Chem. Theory Comput.*, 2009, **5**, 1650.
33 B. Kirchner, C. Spickermann, S. B. C. Lehmann, E. Perlt, J. Langner, M. von Domaros, P. Reuther, F. Uhlig, M. Kohagen and M. Brüssel, *Comput. Phys. Commun.*, 2011, **182**, 1428.
34 M. Brüssel, E. Perlt, M. von Domaros, M. Brehm and B. Kirchner, *J. Chem. Phys.*, 2012, **137**, 164107.
35 R. Ludwig, *ChemPhysChem*, 2005, **6**, 1369.
36 R. Ludwig, *ChemPhysChem*, 2005, **6**, 1376.
37 G. Matisz, W. M. F. Fabian, A.-M. Kelterer and S. Kunsagi-Mate, *THEOCHEM*, 2010, **956**, 103.
38 G. Matisz, A.-M. Kelterer, W. M. F. Fabian and S. Kunsagi-Mate, *J. Phys. Chem. B*, 2011, **115**, 3936.
39 M. Huelsekopf and R. Ludwig, *J. Mol. Liq.*, 2000, **85**, 105.
40 R. Ludwig, F. Weinhold and T. C. Farrar, *Mol. Phys.*, 1999, **97**, 465.
41 R. Ludwig, F. Weinhold and T. C. Farrar, *Mol. Phys.*, 1999, **97**, 479.
42 M. Huelsekopf and R. Ludwig, *J. Mol. Liq.*, 2002, **98**, 163.
43 M. A. Wendt, F. Weinhold and T. C. Farrar, *J. Chem. Phys.*, 1998, **109**, 5945.
44 M. J. Hansen, M. A. Wendt and F. Weinhold, *Mol. Phys.*, 2003, **101**, 1147.
45 R. Ludwig, F. Weinhold and T. C. Farrar, *Ber. Bunsen-Ges.*, 1998, **102**, 197.
46 R. Ludwig, F. Weinhold and T. C. Farrar, *Ber. Bunsen-Ges.*, 1998, **102**, 205.
47 R. Ludwig, F. Weinhold and T. C. Farrar, *J. Phys. Chem. A*, 1997, **101**, 8861.
48 R. Ludwig, O. Reis, R. Winter, F. Weinhold and T. C. Farrar, *J. Phys. Chem. B*, 1998, **102**, 9312.
49 M. Huelsekopf and R. Ludwig, *Magn. Reson. Chem.*, 2001, **39**, S127.
50 R. Ludwig, J. Behler, B. Klink and F. Weinhold, *Angew. Chem., Int. Ed.*, 2002, **41**, 3199.
51 J. Friedrich, E. Perlt, M. Roatsch, C. Spickermann and B. Kirchner, *J. Chem. Theory Comput.*, 2011, **7**, 843.
52 C. Spickermann, E. Perlt, M. von Domaros, M. Roatsch, J. Friedrich and B. Kirchner, *J. Chem. Theory Comput.*, 2011, **7**, 868.
53 E. Perlt, J. Friedrich, M. von Domaros and B. Kirchner, *ChemPhysChem*, 2011, **12**, 3474.
54 F. Weinhold, *J. Phys. Chem. B*, 2014, **118**, 7792.
55 M. Brüssel, E. Perlt, S. B. C. Lehmann, M. von Domaros and B. Kirchner, *J. Chem. Phys.*, 2011, **135**, 194113.
56 T. A. Pascal and W. A. Goddard, *J. Phys. Chem. B*, 2012, **116**, 13905.
57 L. Vlcek and I. Nezbeda, *J. Mol. Liq.*, 2007, **131**, 158.
58 B. Hribar-Lee and K. A. Dill, *Acta Chim. Slov.*, 2006, **53**, 257.
59 D. P. Geerke and W. F. van Gunsteren, *ChemPhysChem*, 2006, **7**, 671.
60 D. Gonzalez-Salgado and I. Nezbeda, *Fluid Phase Equilib.*, 2006, **240**, 161.
61 K. Liltorp, P. Westh and Y. Koga, *Can. J. Chem.*, 2005, **83**, 420.
62 E. J. W. Wensink, A. C. Hoffmann, P. J. van Maaren and D. van der Spoel, *J. Chem. Phys.*, 2003, **119**, 7308.
63 C. A. Koh, H. Tanaka, J. M. Walsh, K. E. Gubbins and J. A. Zollweg, *Fluid Phase Equilib.*, 1993, **83**, 51.
64 H. Tanaka and K. E. Gubbins, *J. Chem. Phys.*, 1992, **97**, 2626.
65 S. W. Cochran, J. C. Holste, K. N. Marsh, B. E. Gammon and K. R. Hall, *Fluid Phase Equilib.*, 1993, **88**, 171.
66 S. Z. Mikhail and W. R. Kimel, *J. Chem. Eng. Data*, 1961, **6**, 533.
67 J. M. Simonson, D. J. Bradley and R. H. Busey, *J. Chem. Thermodyn.*, 1987, **19**, 479.
68 C. Synowietz, in *1.1 Introduction*, Springer Materials - The Landolt–Börnstein Database, ed. K. Schäfer, http://www.springermaterials.com, DOI: 10.1007/10201852_1.
69 A. D. Becke, *J. Chem. Phys.*, 1993, **98**, 5648.
70 C. T. Lee, W. T. Yang and R. G. Parr, *Phys. Rev. B: Condens. Matter Mater. Phys.*, 1988, **37**, 785.
71 P. J. Stephens, F. J. Devlin, C. F. Chabalowski and M. J. Frisch, *J. Phys. Chem.*, 1994, **98**, 11623.
72 S. H. Vosko, L. Wilk and M. Nusair, *Can. J. Phys.*, 1980, **58**, 1200.
73 S. Grimme, J. Antony, S. Ehrlich and H. Krieg, *J. Chem. Phys.*, 2010, **132**, 154104.
74 F. Neese, The ORCA program system, *WIREs Comput. Mol. Sci.*, 2012, **2**, 73.
75 A. Schäfer, H. Horn and R. Ahlrichs, *J. Chem. Phys.*, 1992, **97**, 2571.
76 F. Weigend and R. Ahlrichs, *Phys. Chem. Chem. Phys.*, 2005, **7**, 3297.
77 S. F. Boys and F. Bernardi, *Mol. Phys.*, 2002, **100**, 65.
78 Y. Zhao and D. G. Truhlar, *J. Chem. Theory Comput.*, 2008, **4**, 1849.
79 Y. Zhao and D. G. Truhlar, *Acc. Chem. Res.*, 2008, **41**, 157.
80 Y. Zhao and D. G. Truhlar, *Theor. Chem. Acc.*, 2008, **120**, 215.
81 M. J. Frisch, G. W. Trucks, H. B. Schlegel, G. E. Scuseria, M. A. Robb, J. R. Cheeseman, G. Scalmani, V. Barone, B. Mennucci, G. A. Petersson, H. Nakatsuji, M. Caricato, X. Li, H. P. Hratchian, A. F. Izmaylov, J. Bloino, G. Zheng,

Open Access Article. Published on 30 January 2015. Downloaded on 11/24/2022 8:06:22 AM.
This article is licensed under a Creative Commons Attribution-NonCommercial 3.0 Unported Licence.

J. L. Sonnenberg, M. Hada, M. Ehara, K. Toyota, R. Fukuda, J. Hasegawa, M. Ishida, T. Nakajima, Y. Honda, O. Kitao, H. Nakai, T. Vreven, J. A. Montgomery Jr, J. E. Peralta, F. Ogliaro, M. Bearpark, J. J. Heyd, E. Brothers, K. N. Kudin, V. N. Staroverov, R. Kobayashi, J. Normand, K. Raghavachari, A. Rendell, J. C. Burant, S. S. Iyengar, J. Tomasi, M. Cossi, N. Rega, J. M. Millam, M. Klene, J. E. Knox, J. B. Cross, V. Bakken, C. Adamo, J. Jaramillo, R. Gomperts, R. E. Stratmann, O. Yazyev, A. J. Austin, R. Cammi, C. Pomelli, J. W. Ochterski, R. L. Martin, K. Morokuma, V. G. Zakrzewski, G. A. Voth, P. Salvador, J. J. Dannenberg, S. Dapprich, A. D. Daniels, Ö. Farkas, J. B. Foresman, J. V. Ortiz, J. Cioslowski and D. J. Fox, *Gaussian 09, Revision C.01*, Gaussian, Inc., Wallingford, CT, 2010.

82 T. H. Dunning, *J. Chem. Phys.*, 1989, **90**, 1007.

83 R. Ludwig, *Angew. Chem., Int. Ed.*, 2001, **40**, 1808–1827.

84 G. Z. Han, Y. L. Ding, P. Qian, C. Zhang and W. Song, *Int. J. Quantum Chem.*, 2013, **113**, 1511.

85 C. Corsaro, J. Spooren, C. Branca, N. Leone, M. Broccio, C. Kim, S. H. Chen, H. E. Stanley and F. Mallamace, *J. Phys. Chem. B*, 2008, **112**, 10449.

86 S. Kashtanov, A. Augustson, J. E. Rubensson, J. Nordgren, H. Agren, J. H. Guo and Y. Luo, *Phys. Rev. B: Condens. Matter Mater. Phys.*, 2005, **71**, 104205.

87 K. R. Wilson, M. Cavalleri, B. S. Rude, R. D. Schaller, T. Catalano, A. Nilsson, R. J. Saykally and L. G. M. Pettersson, *J. Phys. Chem. B*, 2005, **109**, 10194.

88 R. F. Lama and B. C. Y. Lu, *J. Chem. Eng. Data*, 1965, **10**, 216.

89 L. Abello, *J. Chim. Phys. Phys.-Chim. Biol.*, 1973, **70**, 1355.

90 I. Tomaszkiewicz, S. L. Randzio and P. Gierycz, *Thermochim. Acta*, 1986, **103**, 281.

91 J. A. V. Butler, D. W. Thomson and W. H. Maclennan, *J. Chem. Soc.*, 1933, **136**, 674.

92 M. W. Chase, NIST-JANAF Thermochemical Tables, J. Phys. Chem. Ref. Data, Monograph No. 9, 4th edn, 1998.

93 T. S. Khasanshin, T. B. Zykova and S. P. Bunko, *High Temp.*, 1997, **35**, 149.

Available online at www.sciencedirect.com
SCIENCE DIRECT®
Thermochimica Acta 425 (2005) 121–126
thermochimica acta
www.elsevier.com/locate/tca

Host–guest interaction between water-soluble calix[6]arene hexasulfonate and *p*-nitrophenol

Sándor Kunsági-Máté[a,*], Kornélia Szabó[a], Beáta Lemli[a], István Bitter[b], Géza Nagy[a,d], László Kollár[c,d]

[a] *Department of General and Physical Chemistry, University of Pécs, Ifjúság 6, H7624 Pécs, Hungary*
[b] *Department of Organic Chemical Technology, Budapest University of Technology and Economics, Budapest, Hungary*
[c] *Department of Inorganic Chemistry, University of Pécs, Pécs, Hungary*
[d] *MTA-PTE Research Group for Chemical Sensors, Pécs, Hungary*

Received 24 March 2004; received in revised form 17 June 2004; accepted 24 June 2004
Available online 5 August 2004

Abstract

The inclusion complexation of calix[6]arene hexasulfonate with *p*-nitrophenol has been studied by photoluminescence (PL), differential scanning calorimetry (DSC) and quantum-chemical methods in aqueous media. The results indicate 1:1 complex stoichiometry. The directly measured molar enthalpy of inclusion shows strong interaction between the host and the guest, however the entropy change of the complex formation is negative and quite high. Therefore, the Gibbs free enthalpy change of the complex formation is small resulting in a relatively low complex stability. This well-known enthalpy–entropy-compensation effect is probably due to the increased freedom of guest molecules relative to the host calixarenes and also due to the increased disorder of solvent molecules after the complex has been dissociated. The good correlation between the van't Hoff enthalpy determined by PL studies and the calorimetric enthalpy reflects the two-state character of complexation. Quantum-chemical investigation suggests π–π interaction between the host and the guest in agreement with earlier results.
© 2004 Elsevier B.V. All rights reserved.

Keywords: Inclusion compound; Host–guest complex; DSC; Enthalpy of inclusion; Calixarenes

1. Introduction

The recognition of neutral organic molecules by synthetic receptors is a topic of current interest in supramolecular- and also in analytical chemistry [1,2]. Calix[*n*]arenes (*n* = 4–6, 8) represent a fascinating class of macrocycles due to the simplicity of their well-defined skeleton, which is associated with versatile recognition properties towards metal or organic ions and neutral molecules [3,4]. Recent reviews summarize their thermodynamic [5] and redox properties [6], applications in analytical and separation science [7], modeling of their molecular dynamics [8–10] and the extent of their metal ion binding character in solution [11,12].

The selectivity of complexation with different species can be modified by changing the cavity size and by the incorporation of functional groups in the lower and/or upper rim of the calixarene molecule. In our recent papers [13–15] the complexation behavior and the factors controlling the thermodynamic and kinetic stability or selectivity of some calixarene derivatives towards neutral π-electron deficient aromatics were reported. In addition, the binding characteristics of water-soluble calixarenes with iron ions [16] and with C_{60} fullerene [17] have also been published.

The interactions of calixarenes with neutral species involve competition between complexation and solvation processes. Non-electrostatic forces arising from the interaction of the electronic systems of neutral hosts and guests are of primary importance. For example, calixarenes and electron-deficient aromatics can form complexes predominantly through π–π type interaction, whilst the inclusion of

* Corresponding author. Tel.: +36 72 503600x4208; fax: +36 72 501518.
E-mail address: kunsagi@ttk.pte.hu (S. Kunsági-Máté).

0040-6031/$ – see front matter © 2004 Elsevier B.V. All rights reserved.
doi:10.1016/j.tca.2004.06.015

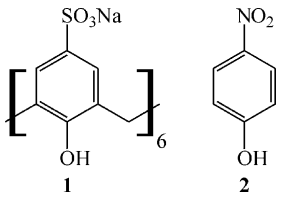

Fig. 1. Calix[6]arene-hexasulfonate sodium salt **1** as host and *p*-nitrophenol **2** as guest.

aliphatic guests into the hydrophobic cavity can be stabilized by CH–π contacts.

Calix[4]arene tetrasulfonate [18], and the thiacalix[4]arene counterpart [19] have been reported to bind small polar organic molecules (alcohols, carbonyl compounds, nitriles, acid derivatives, etc.) in aqueous solution and the complexation was monitored mostly by ^{1}H NMR spectroscopy. In these cases the importance of charge assistance of the sulfonate groups in apolar binding of the guests was confirmed. Because of the ^{1}HNMR is relatively seldom applied for identification of complexation, it may worth to note that this technique has been successfully used to identify the clathrate formation of 2,2′-bis(9-hydroxy-9-fluorenyl)biphenyl with small solvent molecules (acetone and methanol). This reaction has been also studied by means of simultaneous TG–DSC measurement using isothermal and scanning mode of operation [20].

In this paper, the interaction between calix[6]arene-hexasulfonate sodium salt **1** as a host and *p*-nitrophenol **2** as a guest (Fig. 1) in aqueous media was investigated by photoluminescence (PL), differential scanning calorimetry (DSC) and quantum-chemical methods. The stoichiometry and the van't Hoff enthalpy of the complex formation were determined by spectrofluorometric method. The calorimetric molar enthalpy of the inclusion was determined from the heat flow directly measured by DSC method. The fluorometrically determined van't Hoff enthalpy and the calorimetric enthalpy were compared to examine the two-state behavior of the formation of such a complex. Quantum-chemical investigations were carried out to determine the most stable conformation of the host–guest complex.

2. Experimental

Calix[6]arene-hexasulfonate salt **1** was prepared by the direct sulfonation of the parent calix[6]arene with concentrated sulfuric acid [21]. *p*-Nitrophenol (p.a. grade) was purchased (Merck, Germany) and used without further purification.

Calorimetric measurements were carried out with a highly sensitive nano-II-DSC 6100 (Setaram, France) instrument. The calorimeter is configurated with a platinum capillary cell (volume = 0.299 ml). The samples were pressurized to $3 \pm 0.02 \times 10^5$ Pa during all scans. Using oil rotation pump, standard degassing procedure for 15 min at about 15 Pa was applied before loading the samples into the capillary. The heat flow was scanned between 0 and 50 °C. A typical scanning rate of 0.5 K/min was applied, however it was varied from 0.1 up to 2 K/min for each sample to check the effect of diffusion of particles interacted and that of on the reaction rate of complexation. The experimental deviation of the calorimetric results were estimated to be ± 5 mJ.

To avoid any interaction other than the interaction related to the host – guest complex formation, the DSC curves of solutions of calixarene in buffer (i), calixarene in water (ii) and buffer by oneself (iii) were recorded against water. No significant differences between the curves of summed (ii) with (iii) and (i) were obtained, proving that no considerable interaction between the buffer and the host calixarene exists. Similar result was found for the guest *p*-nitrophenol species.

The PL spectra of the different solutions were investigated by means of Fluorolog τ3 spectrofluorometric system (Jobin-Yvon/SPEX). For data collection a photon counting method with 0.2 s integration time was used. Excitation and emission bandwidths were set to 1 nm. A 1 mm layer thickness of the fluorescent probes with front face detection was used to eliminate the inner filter effect.

The acid–base equilibria in the solutions of calixarene **1** was studied by potentiometry using a combined pH sensitive glass electrode (Triode pH electrode, ORION) and Orion 420 Aplus pH meter. The potentiometric measurements were carried out at 25 ± 0.1 °C. The protonation was studied in aqueous solution of **1** at concentration of 10^{-2} M with ionic strength of 0.1 M tetraethylammonium-perchlorate ($[Et_4N][ClO_4]$) background salt. The estimated error of the pH measurements was found to be about 0.02 pH unit. Values of the stepwise protonation constants K_i and the overall protonation constants β_i were computed with the HyperQuad 2000 (Protonic Software) computer program [22–24].

Both calorimetric and fluorometric experiments were carried out at pH 6.9 using phosphate buffer. 0.025 mol/kg disodium hydrogen phosphate (Merck) + 0.025 mol/kg potassium dihydrogen phosphate (Merck); pH 6.961, 6.912, 6.873, 6.843, 6.823, 6.814 at temperatures of 0, 10, 20, 30, 40, 50 °C, respectively.

The equilibrium conformations of calixarene **1** and their complexes with *p*-nitrophenol **2** were studied with semi-empirical AM1 (Austin Model) method, followed by ab initio HF/6-31G* calculations. The Fletcher-Reeves geometry optimization method was used for the investigation of the conformers. The interaction energy of the studied species was described at an ab initio level using HF/6-31G* calculation. TIP3P method [25] with extension to the solvent used [26] was applied for considering the solvent effect. All types of calculations were carried out with the HyperChem Professional 7 program package [27].

3. Results and discussion

Fig. 2 shows the distribution diagram of the differently protonated species of **1** derived from the acid–base titration

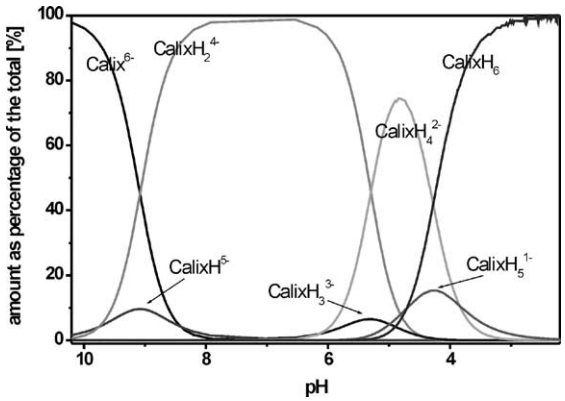

Fig. 2. Distribution diagram of the differently protonated calixarene **1** as a function of pH.

by adjusting ionic strength with 0.1 M tetraethylammonium-perchlorate background salt. Measurements were carried out under purified nitrogen atmosphere. It can be clearly seen that near pH 7, compound **1** exists in double protonated form. It has to be noted, that the distribution curve of $CalixH_2^{4-}$ has a wide maximum between pH 6 and pH 8.5 providing excellent conditions for the investigation of its host properties. Since no considerable abundance of other species has been observed at this pH range, therefore pH 6.9 was chosen for the further examinations. To minimize the effect of the temperature change on pH, phosphate buffer was used which keeps the pH constant at a wide range of temperature (see Section 2).

3.1. Effect of complexation on PL intensity

In order to investigate the interaction of **1** with **2**, 10^{-4} M solutions were prepared in phosphate buffer and the PL spectra were recorded. Their evaluation revealed that the guest molecule induced some changes in the spectra. The PL spectrum of **1** exhibits two peaks at 330 nm and at 495 nm, the intensities of which were decreased in the presence of **2** (Fig. 3). According to our earlier results [13–17] we supposed that the spectral changes were induced by the formation of an inclusion complex. Since *p*-nitrophenol **2** also shows considerable emission and its emission band overlaps with the 495 nm band of **1**, the 330 nm peak of calixarene was used for the determination of complex stability.

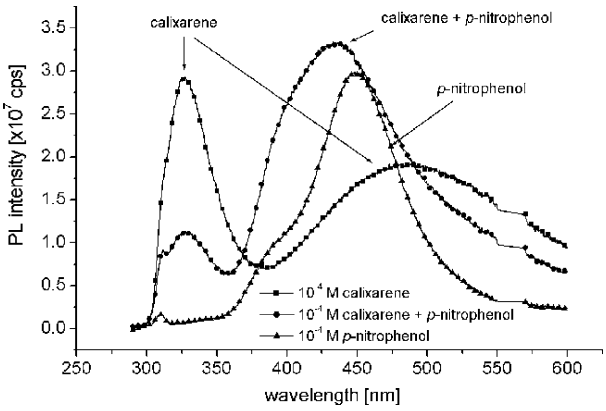

Fig. 3. The change of the PL spectra of calixarene derivative **1** obtained in the absence and in the presence of 10^{-4} M *p*-nitrophenol.

3.2. Determination of the complex stoichiometry and complex stability

Assuming a 1:1 stoichiometry, the complexation reaction can be written as follows ("H" refers to host while "G" means the guest):

$$H + G \overset{K_s}{\rightleftharpoons} HG \tag{1}$$

It is well known that in this particular case the concentration of the complex formed can be expressed as the function of the initial concentrations ($[H]_0$ and $[G]_0$):

$$[HG] = \frac{1}{2}\left\{\left([H]_0 + [G]_0 + \frac{1}{K_s}\right) \pm\sqrt{\left([H]_0 + [G]_0 + \frac{1}{K_s}\right)^2 - 4[H]_0[G]_0}\right\} \tag{2}$$

Assuming that the observed PL signal varies linearly with the concentration of the complex formed, ΔF is described by Eq. (3).

$$\Delta F = f_{HG}[HG] \tag{3}$$

wherein $\Delta F = F - F_0$ is a difference between the PL intensity obtained with the calixarene/*p*-nitrophenol system and that of the free calixarene with the same concentration. The measure of the PL signals, f_{HG} can be obtained for the individual HG species relative to the PL signal of pure calixarene species at the same concentrations. By definition,

$$f_{HG} = \left.\frac{F([G]) - F([HG])}{F([H])}\right|_{[HG]=[H]} \tag{4}$$

Job's method [28] is widely used for the spectroscopic determination of complex stability constants also in calixarene chemistry [29–33]. The stability constant of the inclusion complex can be determined by the curve fitting of Eq. (3) to the experimental data using the expression of [HG] from Eq. (2).

However, it is known that the equilibrium in similar systems strongly depends on the temperature [e.g. [34]]. The thermodynamic parameters for the individual complexes formed in the calixarene/*p*-nitrophenol system can be determined from the van't Hoff equation:

$$\ln K = -\frac{\Delta G}{RT} = -\frac{\Delta H}{RT} + \frac{\Delta S}{R} \tag{5}$$

where ΔG is the Gibbs energy change, ΔS the entropy change and ΔH the enthalpy change associated with complex formation.

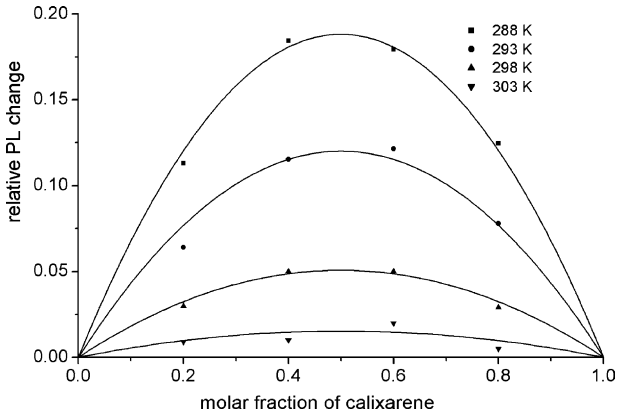

Fig. 4. Job's plot of calixarene **1**–*p*-nitrophenol system at different temperatures.

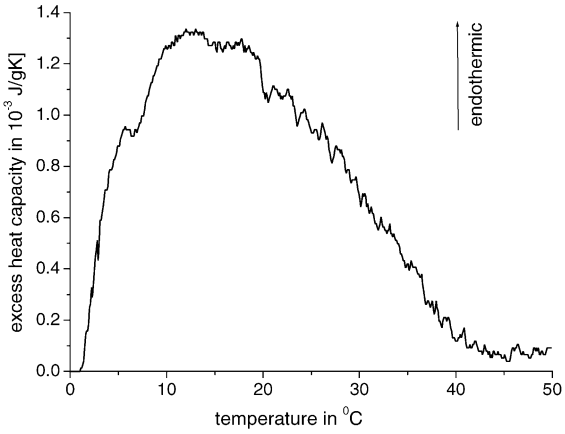

Fig. 5. The excess heat capacity of the equimolar (10^{-3} M) mixture of **1** and **2** recorded against the phosphate buffer. Scanning rate is 1 K/min.

Inserting Eq. (5) for the formation constants into the Eqs. (2) and (3), the fluorescence change in Eq. (3) can be expressed as a function of the ΔH, ΔS values and the f_{HG} coefficient.

The thermodynamic parameters associated with the K value were determined from the Job's curves by an iterative solution of Eqs. (2) and (3) using the expression of K value from the van't Hoff equation (Eq. (5)).

In order to determine the thermodynamic parameters mentioned above, 10^{-3} M stock solutions of **1** and **2** were mixed in four different [H]/([G] + [H]) ratio by stepwise addition of $n \times 300\,\mu l$ host to $(5 - n) \times 300\,\mu l$ guest solutions (n = 1–4) keeping 10^{-3} M total concentration ([G] + [H]). The measurements were carried out at four different temperatures and the iterative curve-fitting procedure was done simultaneously for the experimental data (Fig. 4). The plot of ΔF as a function of molar fraction of host gives an excellent fit, verifying the 1:1 complex stoichiometry assumed above. Table 1 summarizes the thermodynamic parameters determined from PL studies.

3.3. DSC measurements on the host–guest system

Fig. 5 shows a typical DSC scan of the mixture of equimolar (10^{-3} M) solutions of **1** and **2** recorded against the phosphate buffer with a scanning rate of 1 K/min. The excess heat capacity was calculated by substraction of the baseline (see later). The broad DSC curve reflects to fast dissociation process compared to the speed of change of concentration. This change is induced by the decreased complex stability at higher temperature, and therefore, its speed is determined by the scanning rate. This shape of the DSC curve is usual in case of weak host–guest complexes [20].

Fig. 6 shows the excess heat capacity of the equimolar mixture of **1** and **2** scanned by the rate of 0.5 K/min. Five different concentrations varying between 1×10^{-3} and 4.1×10^{-4} M were applied, keeping the same host–guest concentration ratio at each individual run. The more diluted solutions show lower excess heat capacities at each temperature. Furthermore, the curves display that the excess heat capacity decreases with increasing the temperature for each solution. This is consistent with the theoretical expectations: the amount of complexes, dissociated during the temperature changes in a temperature unit, decreases by increasing the temperature (see Eqs. (2) and (5)). Accordingly, the measured excess heat capacity decreases with increasing temperature. Overall, this shape of the DSC curves shows that the dissociation process is fast related to the speed of the change of complex concentration, which is induced by the change of temperature at a given scanning rate. Consequently, the system is in quasi-equilibrium state at each temperature. Therefore, the change of the host–guest complex concentration

Table 1
Thermodynamic parameters of complexation of **1** with **2**

Method	K_s (25 °C) (dm^3/mol)	ΔG (kJ/mol)	ΔH (kJ/mol)	ΔS (J/K mol)
DSC	192.6	−5.3 (5)	−68.2 (3)	−185 (9)
PL	145.4	−4.9 (4)	−66.4 (5)	−181.3 (3)

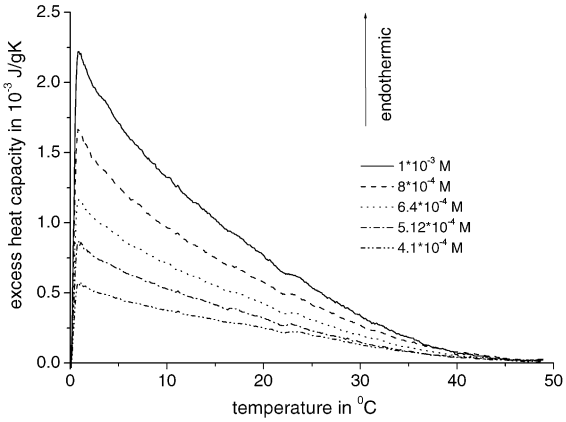

Fig. 6. Excess heat capacity of the equimolar solutions of **1** and **2** scanned with the rate of 0.5 K/min.

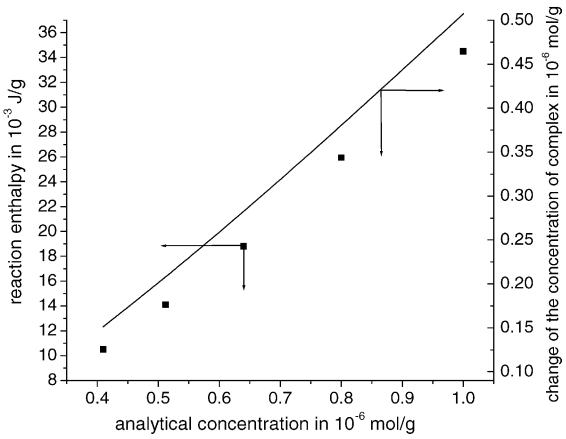

Fig. 7. The enthalpy change (■) of decomposition of the host–guest complexes (left axis) plotted against analytical concentration of equimolar solutions of **1** with **2**. The solid line shows the change of the concentration of the complex (right axis) while the temperature increases from 0 to 50 °C.

driven by the temperature change is reflected in the DSC curve.

The calculation of calorimetric enthalpies is based on the integration of the area under the excess heat capacity curve. The baseline for these calculations was generated using the software of the calorimeter: a polynomial baseline was generated by fitting it to the experimental baseline in the pre- and post-transition regions. Although this approximation of setting the baseline with a polynomial fitting was found to be widely used in such type of experiments, it is not free of an error, which is inversely proportional to the height to width ratio of the calorimetric peak. However, in our case this error was found below 0.5% of the total reaction enthalpy.

Fig. 7 shows the enthalpy changes of the dissociation plotted against the analytical concentration of equimolar solutions of **1** and **2**. The solid line shows the change of the complex concentration while the temperature increases from 0 to 50 °C. As it is well known, the concentration of a host–guest complex varies with the temperature as the complex stability constant is affected by the temperature during a DSC run. Therefore, we are unable to determine the concentration of the analyte and consequently, the thermodynamic parameters from a single DSC run.

However, using the expression of the stability constant K from the van't Hoff equation (Eq. (5)) the concentration of a 1:1 host–guest complex can be described as a function of the molar enthalpy, entropy change and of the temperature. The amount of the complex being dissociated while the temperature increases from 0 to 50 °C ($[HG]_{diss}$) can be expressed as the difference of concentrations of the complex at the two temperatures:

$$[HG]_{diss} = [HG\,(\Delta H, \Delta S, 0\,^{\circ}C)] - [HG\,(\Delta H, \Delta S, 50\,^{\circ}C)] \quad (6)$$

The reaction enthalpy measured by DSC is the product of the concentration of the complex dissociated and the molar enthalpy change of the reaction:

$$\begin{aligned}\Delta_R H &= \Delta H[HG]_{diss} \\ &= \Delta H\{[HG(\Delta H, \Delta S, 0\,^{\circ}C)] \\ &\quad -[HG\,(\Delta H, \Delta S, 50\,^{\circ}C)]\}\end{aligned} \quad (7)$$

After the measurements were carried out with five different, however equimolar concentrations of host and guest, iterative curve-fitting procedure by a variation of ΔH and ΔS was done for the experimental data plotted on Fig. 7. Table 1 summarizes the results determined by the procedure described above using the data of the DSC measurements. It has to be noted, that the enthalpy and entropy values in Table 1 are the averaged values over the temperature interval between 0 and 50 °C, where the complexation/decomplexation process is studied.

3.4. The stabilization energy of the inclusion complexes

The binding of *p*-nitrophenol **2** by calixarene **1** detected by PL and DSC studies, was examined by quantum-chemical method, too. The interaction energy between the host and the guest molecules was calculated by the procedure described earlier [15]. All energies were determined in the presence of solvent cage using TIP3P method [25,26], i.e. the solvation enthalpies of the interacting species were considered in this way. Only those conformations with the *p*-nitrophenol molecule located inside the calixarene cavity (i.e. interacts with calixarene from the side of the upper rim) were found

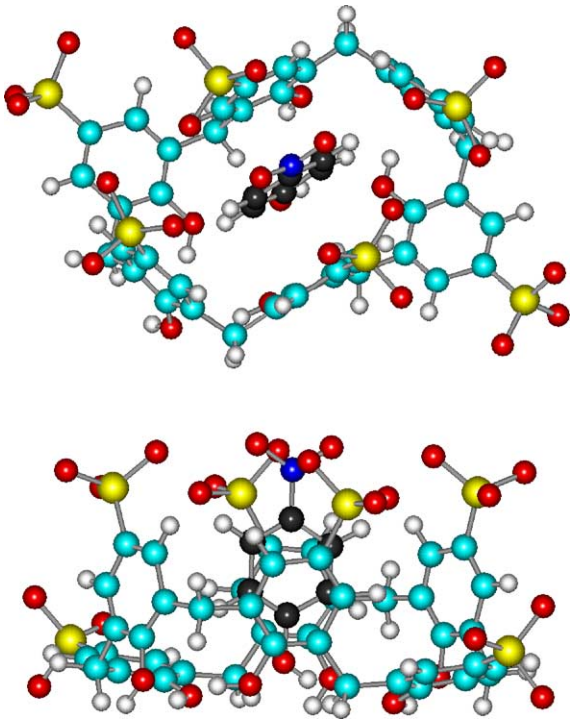

Fig. 8. Two views on the optimized structure of the inclusion complex of **1** with **2**.

stable. The stabilization energy of the complex was evaluated as the absolute value of the interaction energy, i.e. the difference between the total energy of the optimized structure of the complex and that of the separated host plus guest molecules. Fig. 8 shows the top and side view of the optimized structure of the host–guest complex. The stabilization energy was found to be 48.3 kJ/mol. This value can be compared with the enthalpy change of complexation since the entropy effect was not considered in the quantum chemical calculation. The ca. 30% deviation from the experimental value is probably due to the approximation used in the theory and also because this value is derived from the static calculation and relates to the temperature of 0 K.

4. Conclusion and summary

PL and DSC measurements have been successfully applied to study the inclusion complexation of calix[6]arene hexasulfonate with *p*-nitrophenol in aqueous solution. Both the PL and DSC signals indicate a 1:1 complex stoichiometry. The directly measured molar enthalpy of inclusion shows a strong interaction between the host and the guest. However, the entropy change during the complexation is a relatively high negative value, which decreases the Gibbs free enthalpy change of the reaction, thereby the complex stability. The highly exothermic complexation enthalpy parallel with the significant decrease of the entropy during complex formation reflects to the so-called enthalpy–entropy-compensation effect. It is probably due to the increased freedom of guest molecules relative to the host calixarenes and also due to the increased disorder of solvent molecules after the complex has been dissociated. Quantum-chemical investigation suggests that the *p*-nitrophenol guest resides in the calixarene cavity and the complex is stabilized by π–π interaction.

Acknowledgements

The financial support of the Hungarian Scientific Research Fund (OTKA TS044800), the Hungarian National Committee of Technological Development (OMFB 97-20-MU0086) and Francelab Co. (France) are highly appreciated.

References

[1] T. Kuwabara, H. Nakajima, M. Nanasawa, A. Ueno, A. Anal. Chem. 71 (1999) 2844–2849.
[2] P.D. Beer, P.A. Gale, G.Z. Chen, Coord. Chem. Rev. 186 (1999) 3–36.
[3] C.D. Gutsche, Monographs in Supramolecular Chemistry, vol. 1. Calixarenes, The Royal Society of Chemistry, Cambridge, 1989.
[4] C.D. Gutsche, Monographs in Supramolecular Chemistry, vol. 6. Calixarenes Revisited, The Royal Society of Chemistry, Cambridge, 1998.
[5] A.F. Danil de Namor, R.M. Cleverly, M.L. Zapata-Ormachea, Chem. Rev. 98 (1998) 2495–2525.
[6] P.D. Beer, P.A. Gale, G.Z. Chen, J. Chem. Soc., Dalton Trans. 12 (1999) 1897–1909.
[7] R. Ludwig, Fresenius J. Anal. Chem. 367 (2000) 103–128.
[8] A. Varnek, G. Wipff, J. Comput. Chem. 17 (1996) 1520–1531.
[9] M. Lauterbach, G. Wipff, in: L. Echegoyen, A. Kaifer (Eds.), Physical Supramolecular Chemistry, Kluwer Academic Publishers, Dordrecht, 1999, pp. 65–102.
[10] A. Varnek, G. Wipff, J. Mol. Struct. (THEOCHEM) 363 (1996) 67–85.
[11] A. Ikeda, S. Shinkai, Chem. Rev. 97 (1997) 1713–1734.
[12] A.T. Yordanov, D.M. Roundhill, Coord. Chem. Rev. 170 (1998) 93–124.
[13] S. Kunsági-Máté, G. Nagy, L. Kollár, Sens. Actuators B: Chem. 76 (2001) 545–550.
[14] S. Kunsági-Máté, G. Nagy, P. Jurecka, L. Kollár, Tetrahedron 58 (2002) 5119–5124, and references cited therein.
[15] S. Kunsági-Máté, I. Bitter, A. Grün, G. Nagy, L. Kollár, Anal. Chim. Acta 461 (2002) 273–279.
[16] S. Kunsági-Máté, L. Nagy, G. Nagy, I. Bitter, L. Kollár, J. Phys. Chem. B 107 (2003) 4727–4731, and references cited therein.
[17] S. Kunsági-Máté, K. Szabó, I. Bitter, G. Nagy, L. Kollár, Tetrahedron Lett. 45 (2004) 1387–1390.
[18] G. Arena, A. Contino, F.G. Guliano, A. Magri, D. Sciotto, R. Ungaro, Tetrahedron Lett. 41 (2000) 9327–9330.
[19] N. Iki, T. Suzuki, K. Koyama, C. Kabuto, S. Miyano, Org. Lett. 4 (2002) 509–512.
[20] J. Seidel, G. Wolf, E. Weber, Thermochim. Acta 271 (1996) 141–148.
[21] S. Shinkai, T. Mori, T. Tsubaki, T. Sone, O. Manabe, Tetrahedron Lett. 25 (1984) 5315–5318.
[22] HyperQuad 2000. Ver. 2.1. Protonic Software, 2002.
[23] P. Gans, A. Sabatini, A. Vacca, Talanta 43 (1996) 1739–1753.
[24] L. Alderighi, P. Gans, A. Ienco, D. Peters, A. Sabatini, A. Vacca, Coord. Chem. Rev. 184 (1999) 311–318.
[25] W.L. Jorgensen, J. Chandrasekhas, J.D. Madura, R.W. Impey, M.L. Klein, J. Chem. Phys. 79 (1983) 926–935.
[26] T. Bender, Solvent Cage, Excel Macros to HyperChem, Hypercube, www.hyper.com, 2000.
[27] HyperChem Professional 7, HyperCube, 2002.
[28] F.J.C. Rossotti, H. Rossotti, The determination of stability constants, McGraw-Hill, New York, 1961 (pp. 47–51).
[29] Y. Inoue, K. Yamamoto, T. Wada, S. Everitt, X.-M. Gao, Z.J. Hou, L.H. Tong, S.K. Jiang, H.M. Wu, J. Chem. Soc., Perkin Trans. 2 (1998) 1807.
[30] Y. Liu, L. Jin, S.-X. Sun, Microchem. J. 64 (2000) 59.
[31] Y. Liu, S.-Z. Kang, H.-Y. Zhang, Microchem. J. 70 (2001) 115.
[32] I. Mohammed-Ziegler, M. Kubinyi, A. Grofcsik, A. Grün, I. Bitter, J. Mol. Struct. 480–481 (1999) 289.
[33] Y. Okada, M. Mizutani, F. Ishii, Y. Kasai, J. Nishimura, Tetrahedron 57 (2001) 1219.
[34] T. Wharton, V.U. Kini, R.A. Mortis, L.J. Wilson, Tetrahedron Lett. 42 (2001) 5159–5162.

toxins

MDPI

Article

Interaction of Citrinin with Human Serum Albumin

Miklós Poór [1,*], Beáta Lemli [2,3], Mónika Bálint [4], Csaba Hetényi [5], Nikolett Sali [3,6], Tamás Kőszegi [3,6] and Sándor Kunsági-Máté [2,3]

Received: 19 October 2015; Accepted: 25 November 2015; Published: 1 December 2015
Academic Editor: HJ (Ine) van der Fels-Klerx

1 Department of Pharmacology and Pharmacotherapy, Toxicology Section, University of Pécs, Szigeti út 12, Pécs H-7624, Hungary
2 Department of General and Physical Chemistry, University of Pécs, Ifjúság útja 6, Pécs H-7624, Hungary; blemli@gamma.ttk.pte.hu (B.L.); kunsagi@gamma.ttk.pte.hu (S.K.-M.)
3 János Szentágothai Research Center, Ifjúság útja 20, Pécs H-7624, Hungary; niki26@gmail.hu (N.S.); koszegitam@gmail.com (T.K.)
4 Department of Biochemistry, Eötvös Loránd University, Pázmány sétány 1/C, Budapest 1117, Hungary; monibalint18@gmail.com
5 MTA-ELTE Molecular Biophysics Research Group, Hungarian Academy of Sciences, Pázmány sétány 1/C, Budapest 1117, Hungary; csabahete@yahoo.com
6 Department of Laboratory Medicine, University of Pécs, Ifjúság útja 13, Pécs H-7624, Hungary
* Correspondence: poor.miklos@pte.hu; Tel.: +36-72-536-000 (ext. 31646); Fax: +36-72-536-218

Abstract: Citrinin (CIT) is a mycotoxin produced by several *Aspergillus*, *Penicillium*, and *Monascus* species. CIT occurs worldwide in different foods and drinks and causes health problems for humans and animals. Human serum albumin (HSA) is the most abundant plasma protein in human circulation. Albumin forms stable complexes with many drugs and xenobiotics; therefore, HSA commonly plays important role in the pharmacokinetics or toxicokinetics of numerous compounds. However, the interaction of CIT with HSA is poorly characterized yet. In this study, the complex formation of CIT with HSA was investigated using fluorescence spectroscopy and ultrafiltration techniques. For the deeper understanding of the interaction, thermodynamic, and molecular modeling studies were performed as well. Our results suggest that CIT forms stable complex with HSA (log$K$ ~ 5.3) and its primary binding site is located in subdomain IIA (Sudlow's Site I). *In vitro* cell experiments also recommend that CIT-HSA interaction may have biological relevance. Finally, the complex formations of CIT with bovine, porcine, and rat serum albumin were investigated, in order to test the potential species differences of CIT-albumin interactions.

Keywords: citrinin; human serum albumin; fluorescence spectroscopy; ultrafiltration; species differences

1. Introduction

Mycotoxins are toxic secondary metabolites produced naturally by filamentous fungi. Due to their wide occurrence, mycotoxin contamination of various foods, drinks, and animal feed is unavoidable, causing serious health problems for humans and animals [1]. The nephrotoxic mycotoxin citrinin (CIT) is produced by *Aspergillus*, *Penicillium*, and *Monascus* fungi and appears mainly in various cereals (e.g., maize, rye, oat, barley, wheat, and rice); however, CIT occurs in other foodstuffs, as well (e.g., pomaceous fruits, black olive, spices, cheese, *etc.*) [2,3]. The wide occurrence of CIT is associated with a relatively high thermal stability making its removal from contaminated sources more difficult [4]. Recent studies suggest apoptosis induction and cell cycle arrest as its main toxic impacts; however, the exact mechanism of action of CIT is not clearly understood yet [5–7]. Relatively little information is available regarding the toxicokinetics of CIT. Some studies suggest that CIT is taken up by kidney cells through organic anion transporters [8,9]. Furthermore, recent

investigations highlighted that both CIT and its inactive metabolite dihydrocitrinone [10] are present in measurable levels in human blood and urine [11,12].

Human serum albumin (HSA) is the most abundant plasma protein in human circulation. In addition to its role in the maintenance of oncotic pressure and pH of the blood, it also has antioxidant and pseudo-enzymatic activities [13]. In addition, one of the most important functions of HSA is the binding (and in this route the transport) of numerous endogenous molecules, drugs, and xenobiotics; therefore, HSA can play a major role in their pharmacokinetics/toxicokinetics in many cases [13,14]. Very relevant interactions of HSA with mycotoxins occur, e.g., in the case of ochratoxin A which shows structural similarity with citrinin [15,16]. However, previous studies demonstrated the presence of interaction between CIT and some albumin species [17,18], the complex formation of CIT with human serum albumin is poorly characterized.

In this study the interaction of CIT with human serum albumin (HSA) was investigated using fluorescence spectroscopy, ultrafiltration, and molecular docking studies. Our main goals were to determine the stability of CIT-HSA complex, as well as to identify the primary binding site of CIT on the HSA molecule. For deeper understanding of CIT-HSA complex formation, thermodynamic studies were performed, as well. Furthermore, CIT-albumin interaction was tested on kidney cells applying an *in vitro* cell culture, in order to examine its potential relevance. Finally, interactions of CIT with bovine, porcine, and rat serum albumin were also investigated to explore the possible species differences regarding CIT-albumin complexes. Our results clearly demonstrate that CIT forms a stable complex with albumin suggesting the potential *in vivo* relevance of the interaction, which one should keep in mind in the future.

2. Results and Discussion

2.1. Binding Constant of Citrinin-HSA Complex

Citrinin shows fluorescence properties only under an acidic environment (below pH 5) [19]; therefore, fluorescence quenching of HSA by CIT was examined in order to investigate CIT-HSA interaction at physiological pH (pH 7.4; λ_{exc} = 280 nm, λ_{em} = 340 nm). Fluorescence emission spectra of HSA (2 μM) in the absence and in the presence of increasing CIT concentrations (0.25–5.0 μM) are plotted in Figure 1. Even the presence of CIT in nanomolar concentrations resulted in the significant fluorescence quenching of HSA. During these measurements 5.32 ± 0.01 was determined as log$K$ value at 25 °C (see details in Section 3.2.), suggesting a stable and relevant interaction between CIT and HSA. The determined binding constant is similar to that of described regarding warfarin-HSA interaction (log$K$ ~ 5.3), which results in approximately 99% bonding in plasma and, therefore, the long half-life of warfarin in human circulation [15,20]. Due to the blue shift of the fluorescence emission maximum of HSA in the presence of CIT, determination of a binding constant was repeated using different emission wavelengths (330–350 nm). No significant differences were observed compared to the stability constant determined at a wavelength of 340 nm. Our calculations strongly suggest 1:1 stoichiometry of the CIT-HSA complex, indicating the presence of one high-affinity binding site of CIT on the HSA molecule.

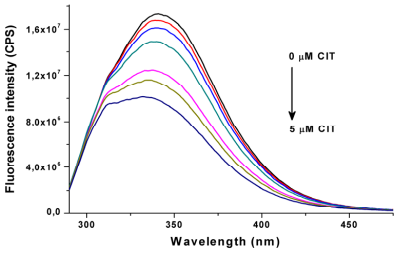

Figure 1. Fluorescence emission spectra of human serum albumin (2 μM) in the presence of increasing CIT concentrations (0, 0.25, 0.5, 1, 2, 3 and 5 μM) in PBS (pH 7.4) (λ_{exc} = 280 nm).

The impact of pH on CIT-HSA interaction was also tested. Since albumin presents in its N (neutral) form between pH 4.3–8.0 [13], during our experiments CIT-HSA complex formation was investigated at pH 6.0, 7.0 and 7.8 in PBS buffer (T = 25 °C). Under these circumstances, only slight changes of the stability of CIT-HSA complex was observed (pH 6.0 → log$K$ = 5.25 ± 0.01; pH 7.0 → log$K$ = 5.28 ± 0.01; pH 7.8 → log$K$ = 5.12 ± 0.01). However, at pH 7.8 a larger decrease of the log$K$ value was noticed compared to log$K$ values determined at pH 6.0 and 7.0.

2.2. Ultrafiltration Experiments

To confirm the presence of CIT-HSA interaction, as well as to identify the primary binding site of CIT on HSA molecule, ultrafiltration experiments were performed. Since ultrafiltration is a relatively long process (10 min in our experiments), this technique is not suitable to quantify the binding constant. However, ultrafiltration is highly suitable to clearly demonstrate the complex formation and to investigate different competitive interactions (and in this way to identify the binding site with specific site markers) [21,22]. As Figure 2A demonstrates, the presence of increasing HSA concentrations (1, 2.5, and 5 μM) led to the significant decrease of CIT in the filtrate. Since HSA is an approximately 67 kDa sized macromolecule [15], it is not able to pass through the filter unit with a 10 kDa molecular weight cut-off value. For this reason only the free (not albumin-bound) molecules will reach the filtrate. These results confirm the presence of a relevant interaction between CIT and HSA.

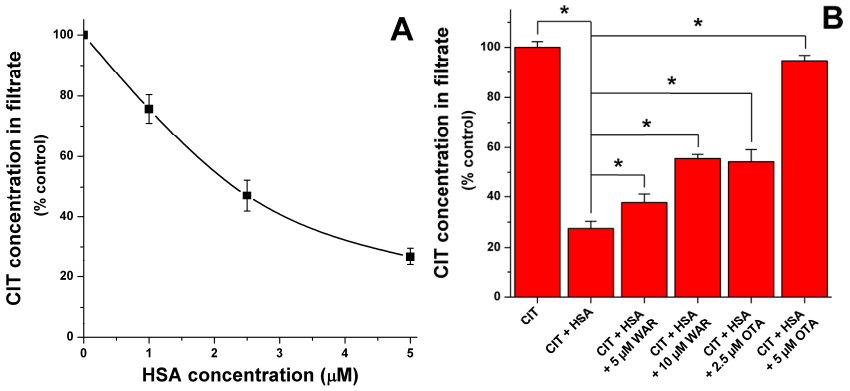

Figure 2. (**A**) Citrinin levels in ultrafiltrates (1 μM CIT) in absence and presence of increasing HSA concentrations; and (**B**) influence of warfarin and ochratoxin A (in the presence of 1 μM CIT + 5 μM HSA) on citrinin concentrations in filtrate (see further details in Section 3.4.) (* $p < 0.05$).

Thereafter, the influence of site markers on CIT-HSA interaction was tested. Warfarin and ibuprofen are commonly applied site markers of Sudlow's site I and II, respectively [13]. HSA contains three domains (I, II, and III) and each domain is built up from two subdomains (A and B). A large cavity in subdomain IIIA hosts Sudlow's site II (or drug binding site II); the typical ligands of this binding site are the non-steroidal anti-inflammatory drug ibuprofen and benzodiazepines (e.g., diazepam), and Sudlow's site II is preferred by several aromatic carboxylates, as well [13]. Sudlow's site I (or drug binding site I) is located in a cavity in subdomain IIA; however, it is smaller compared to the cavity in Sudlow's site II. The ligands of Sudlow's site I are mainly bulky heterocyclic anions and its typical ligand is warfarin. Tyr150 amino acid presumably plays a major role regarding drug-HSA interactions, because its hydroxyl group commonly forms hydrogen bond during the complex formation of HSA with different ligands [13]. Before ultrafiltration, samples contained 1 μM CIT and 5 μM HSA in absence and presence of warfarin or ibuprofen (5 or 10 μM). In presence of ibuprofen no significant changes of CIT concentrations were observed in the filtrate (data not shown). In contrast, the presence of warfarin caused considerable increase of CIT in the filtrate suggesting the significant displacement of CIT by warfarin (Figure 2B). It was plausible to hypothesize that CIT is a

Sudlow's site I ligand similarly to the other mycotoxin ochratoxin A (OTA) which shows structural similarity with CIT [23]. Furthermore, the molecular location of the binding site of OTA and warfarin is almost completely the same [24]. For this reason, molecular displacement of CIT by OTA was also investigated. As Figure 2B demonstrates, the presence of OTA resulted in the significant elevation of CIT in the filtrate, showing remarkable displacement of CIT even by 2.5 and 5 μM OTA. It is not surprising because OTA binds to HSA with much higher affinity (log$K$ = 7.4–7.6 at 25 °C) compared to warfarin (and to citrinin as well) [15,20,25,26]. Since equimolar amount of OTA is able to bind most of the HSA molecules [26] and because of the much higher affinity of OTA toward HSA, almost complete displacement of CIT (1 μM) was observed in the presence of 5 μM OTA.

The strong quenching of the fluorescence of HSA by CIT as well as the remarkable displacement of CIT from HSA in presence of Sudlow's site I ligands warfarin and ochratoxin A show a circumstantial evidence that the primary binding site of CIT is located in Sudlow's site I (subdomain IIA).

2.3. Fluorescence Investigation of Molecular Displacement of Warfarin and Ochratoxin A from HSA by Citrinin

To support further the binding site of CIT obtained and the quantified stability constant of CIT-HSA complex, competitive interaction of CIT with warfarin and ochratoxin A was investigated using our models published earlier [20,25,26].

Warfarin shows fluorescence excitation and emission maxima at 309 nm and 389 nm wavelengths, respectively. However, in presence of HSA warfarin exerts more than 15-fold higher fluorescence signal, while the excitation maximum of HSA-bound warfarin is shifted to 317 nm and providing the maximum fluorescence emission intensity at 379 nm [20]. In the presence of increasing CIT concentrations (0.25–5.0 μM) significant decrease of the fluorescence intensities of warfarin was observed (Figure 3), indicating the molecular displacement of warfarin from the surface of HSA molecule [20].

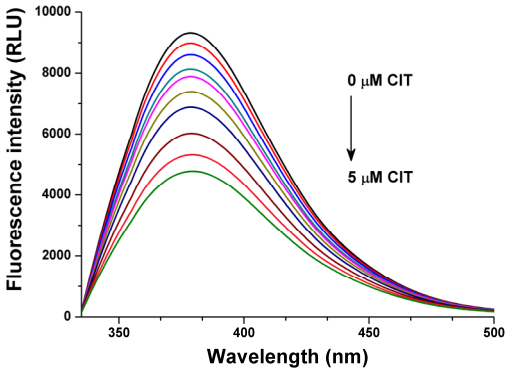

Figure 3. Fluorescence emission spectra of warfarin (1 μM) in the presence of HSA (3.5 μM) and increasing CIT concentrations (0, 0.25, 0.5, 0.75, 1, 1.5, 2, 3, 4 and 5 μM) in PBS (λ_{exc} = 317 nm).

As it was discussed previously (in Section 2.2.), ochratoxin A binds to HSA with very high affinity. Since OTA exerts strong fluorescence signal, the complex formation of OTA with HSA can be easily followed by fluorescence polarization technique [23,25,26]. Previous studies also highlighted that fluorescence polarization-based models are able to describe the molecular displacement of OTA by different drug molecules or other compounds [25,26]. Since the calculated binding constant of CIT-HSA complex was very similar compared to warfarin-HSA complex, fluorescence polarization (P) values of OTA (1 μM) in presence of HSA (1.4 μM) were determined in the absence and presence of CIT or warfarin (1–30 μM). Figure 4 shows that both CIT and warfarin result in the decrease of fluorescence polarization of OTA in a concentration dependent fashion. Since the rotational

freedom of free (not protein-bound) OTA is much higher (therefore its P value is substantially lower: P_{OTA} = 0.010–0.015, $P_{OTA-HSA}$ = 0.320–0.330) compared to its albumin-bound form, the decrease of fluorescence polarization values suggests the molecular displacement of OTA from HSA [25,26]. Furthermore, as it was demonstrated in previous studies, depending on the binding affinity of the competitor molecule the displacing ability could be higher or lower [25,26]. The very similar P values in presence of CIT and warfarin recommend that the displacing abilities of CIT and warfarin and therefore the binding constants of CIT-HSA and warfarin-HSA complexes are nearly the same; which is in a very good agreement with the results of fluorescence quenching experiments (see in Section 2.1.).

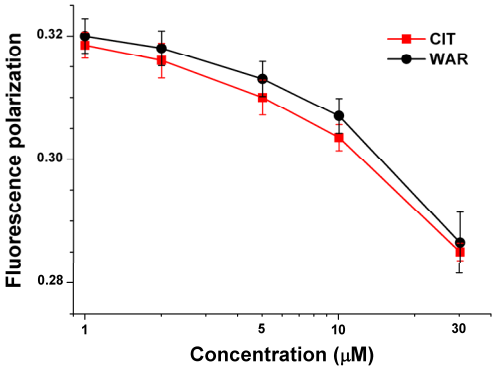

Figure 4. Fluorescence polarization data of OTA (1 μM) in the presence of HSA (1.4 μM) and increasing amounts of citrinin or warfarin in PBS (λ_{exc} = 393 nm, λ_{em} = 446 nm).

Based on steady-state fluorescence spectroscopic and fluorescence polarization studies, CIT is able to displace both warfarin and ochratoxin A form HSA. These results confirm further that CIT is a Sudlow's site I ligand, strongly supporting our observations regarding the ultrafiltration experiments (see in Section 2.2.).

2.4. Thermodynamic Studies

In order to investigate the temperature dependence of CIT-HSA interaction, binding constants were determined (using Equation (1)) between 25 and 40 °C. The measured log$K$ values of CIT-HSA complex at different temperatures are summarized in Table 1. Data show higher stability of the complexes at lower temperatures reflecting ground state complexes. Thermodynamic parameters were also determined (using Equation (2)) in order to get deeper insight regarding the nature of the binding forces. These interaction forces are usually van der Waals interactions, hydrophobic forces, multiple hydrogen bonds or electrostatic interactions. The calculated negative ΔG value (-29.96 kJ$\cdot$ mol^{-1}) suggests the spontaneous binding process between CIT and HSA; it is within the typical range of noncovalent interactions. ΔH and ΔS values of CIT-HSA complex formation were -24.15 kJ$\cdot$ mol^{-1} and +20.90 J$\cdot$ mol$^{-1}\cdot$ K^{-1}, respectively. These thermodynamic parameters are mostly analyzed from the point of view of Ross and Subramanian [27]. During the interactions between proteins and other molecules, the dominant role of van der Waals forces and hydrogen bond formation typically results in negative values of both enthalpy and entropy changes. From the point of view of the solvent molecules, positive value of the entropy change indicates hydrophobic interaction between the macromolecule and the ligand, supposing the decomposition of the solvation shells of the interacting molecules (or a part of them) leading to less ordered structure of water molecules. Furthermore, the negative enthalpy change in combination with the positive entropy change suggest the presence of specific electrostatic interaction. According to the calculated ΔH and ΔS values the interaction seems to be an enthalpy driven process therefore electrostatic forces may play a major role during the CIT-HSA complex formation.

Table 1. Temperature dependence of citrinin-HSA interaction compared to warfarin-HSA complex formation (log*K* values of warfarin-HSA complex are derived from the study of Oester *et al.* [28]).

T (°C)	25	30	35	40
log*K* (±SD) (CIT-HSA)	5.32 ± 0.01	5.26 ± 0.01	5.19 ± 0.01	5.11 ± 0.01
T (°C)	25	-	37	42
log*K* (warfarin-HSA)	5.38	-	5.31	5.28

2.5. Molecular Modeling Studies

A blind docking search was performed for the binding site(s) of citrinin on the entire surface of HSA. The search resulted in nine and ten representative binding positions for the o- and p-quinone forms of citrinin, respectively. For both forms, the best docked binding position with the lowest calculated Δ*G* found the well-known Sudlow's site I [13,29] located in the cavity of subdomain IIA that is composed by all six helices of the subdomain and a loop-helix feature (residues 148–154) from IB (Figure 5A). Analysis of the contacts between the best docked citrinin and HSA (Figure 5B) showed that both o- and p-quinone forms had H-bonds with R222, H242 and R257. Salt bridges were observed for both o-quinone (K199) and p-quinone (K199, H242) forms. Hydrophobic contacts also play an important role in binding of citrinin with L238, I264, I290 (o-quinone), and L260, I264, and A291 (p-quinone form) residues involved. The above mentioned interacting residues are known as part of Sudlow's site I (Figure 5A,B), and also as the binding site of warfarin (Figure 5A). For a direct comparison, the binding conformation of warfarin [30] was extracted from a previously determined warfarin-HSA complex structure (PDB code 1h9z) after superimposition of the HSA parts. A very good match was found between the bound conformations of warfarin and citrinin (Figure 5C). Thus, blind docking identified Sudlow's site I as a primary binding position of citrinin on the surface of HSA. Thermodynamic measurements also suggest an enthalpic binding process which is based on the interactions between electron rich citrinin and the positively charged residues (K195, K199, R218 and R222) of Sudows's site I. A good agreement between the measured Δ*G* of CIT (-30.0 kJ$\cdot$ mol^{-1}) and the calculated Δ*G* value of the p-quinone form of CIT (-31.5 kJ$\cdot$ mol^{-1}, Figure 5B,D) suggest that this tautomer is the most important in HSA binding. Previous studies also suggest that the p-quinone form may be the primary unbound tautomer (60%) in solution, as well [31].

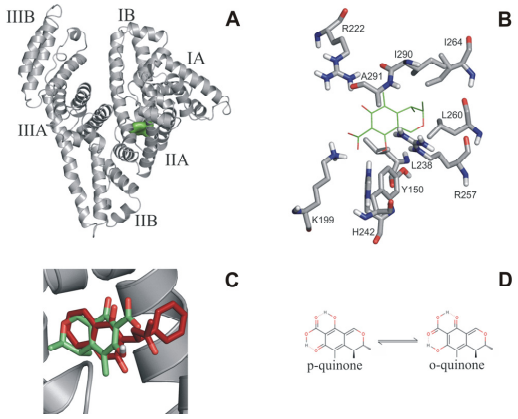

Figure 5. (**A**) Docked conformation of citrinin (green surface) in Sudlow's site I on HSA (grey cartoon); (**B**) Docked p-quinone is represented as green sticks and the interacting amino acids in grey; (**C**) Match between the bound conformations of warfarin (red sticks) and citrinin (green sticks) in Sudlow's site I. The binding conformation of warfarin was extracted from a previously determined warfarin-HSA complex structure (PDB code 1h9z) after superimposition of the HSA parts; (**D**) Lewis structure of tautomeric forms of citrinin.

2.6. *Influence of Albumin on the Citrinin-Induced Toxicity* in Vitro

In order to investigate the influence of albumin on the toxic impact of CIT, MDCK cells were treated with CIT in the absence and in the presence of FBS (fetal bovine serum) or HSA. To quantify the required CIT concentration which leads to serious viability loss, MDCK cells were exposed to increasing amounts of CIT (0–100 μM) in the absence of FBS for 24-h. Treatment of MDCK cells with 100 μM CIT caused approximately 50% decrease of cell viability (Figure S1); therefore, during the following experiments this concentration was applied. Presence of HSA (40 g/L) or FBS (10%) alone caused no or slight (but significant) changes of cell viability, respectively (compared to that of control); however, CIT-induced viability loss was considerably alleviated by both FBS and HSA (Figure 6). Aside from bovine serum albumin (BSA), FBS contains several further constituents (e.g., hormones and growth factors), and some of these factors enhance cell growth and cell division. It explains the positive effect of FBS even in the absence of CIT. Furthermore, the formation of stable complexes of different ligands with albumin results in the slower (and presumably incomplete) cellular uptake of the ligand molecules. Due to its toxic nature, CIT has negative effects on cell viability; therefore, the potential inhibition of its cellular uptake is beneficial. The CIT-induced viability loss was spectacularly alleviated by co-treatment of toxin-exposed cells with FBS (containing BSA) or HSA. This observation strongly suggests that the complex formation of CIT with albumin resulted in the decreased cellular uptake of CIT by MDCK cells. Furthermore, our results highlight that the presence of FBS in cell medium is important during *in vitro* experiments if one would like to mimic *in vivo* conditions.

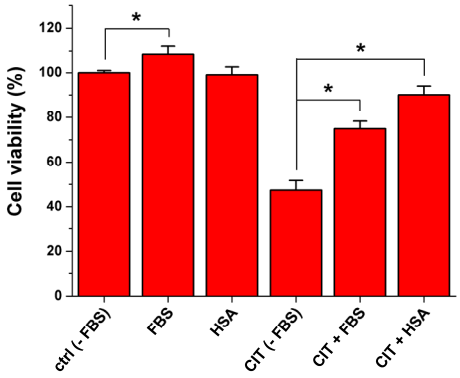

Figure 6. Influence of FBS (10%) and HSA (40 g/L) on viability of MDCK cells in the absence and in the presence of CIT (100 μM) after 24-h treatment (* $p < 0.05$).

2.7. *Interaction of Citrinin with Bovine, Porcine, and Rat Serum Albumin*

To test the potential species differences regarding CIT-albumin interactions, complex formations of CIT with bovine (BSA), porcine (PSA), and rat serum albumin (RSA) were also investigated. Despite of the structural differences of albumins (there is an approximately 25%–30% variability even in their amino acid sequences), their biological behavior (including their ligand binding properties) is usually very similar [15]. However, sometimes major differences occur: e.g., the complex stability of the mycotoxin ochratoxin A with HSA is 15-fold and 30-fold higher compared to its complexes with BSA and RSA, respectively [15]. Binding constants of CIT with albumins were determined with fluorescence quenching method under the same conditions than in Section 2.1. (using Equation (1)). Even if the binding constants of the four tested albumins with CIT show some differences (Table 2), we did not observe dramatic discrepancies, like in the case of ochratoxin A. The most stable complex of CIT is formed with RSA, followed by HSA, BSA, and PSA. These data suggest that albumin binding characteristics of CIT is similar in different species indicating that the albumin binding properties of CIT in humans may be modeled well by animal studies.

Table 2. Binding constants of CIT-albumin complexes in PBS (pH 7.4 at 25 °C).

Tested albumins	HSA	BSA	PSA	RSA
log*K* (±SD)	5.32 ± 0.01	5.05 ± 0.05	4.96 ± 0.05	5.50 ± 0.02

3. Experimental Section

3.1. Reagents

Citrinin (CIT), human serum albumin (HSA), bovine serum albumin (BSA), porcine serum albumin (PSA), rat serum albumin (RSA), warfarin (WAR), ochratoxin A (OTA), ibuprofen, DMEM (Dulbecco's Modified Eagle's Medium)—high glucose (4500 mg/L), fetal bovine serum (FBS), penicillin/streptomycin solution (all from Sigma-Aldrich, Saint Louis, MO, USA), calcein acetoxymethyl ester (CAM; from Thermo Fisher Scientific, Waltham, MA, USA) were used as received. All other reagents were of analytical or spectroscopic grade. 5000 μM stock solution of CIT was prepared in spectroscopic-grade ethanol (Reanal) and stored at −20 °C. In order to mimic extracellular physiological conditions, CIT-albumin interactions were investigated in phosphate-buffered saline (PBS, pH 7.4).

3.2. Fluorescence Spectroscopic Measurements

A Fluorolog τ3 spectrofluorometric system (Jobin-Yvon/SPEX) and Hitachi F-4500 fluorescence spectrophotometer were used for steady-state fluorescence and fluorescence polarization measurements. All analyses were performed at +25 °C except thermodynamic studies.

Binding constants (*K*) were determined using fluorescence quenching method, where increasing CIT concentrations (0–5 μM) were added to standard amount of albumin (2 μM). Fluorescence emission spectra were recorded in PBS buffer (pH 7.4; λ_{exc} = 280 nm). Similarly to our previous studies [15,16], *K* values of CIT-albumin complexes were quantified by non-linear fitting with Hyperquad2006 program package (Protonic Software) assuming 1:1 stoichiometry:

$$I = I_0 + \frac{I_{AC} - I_0}{2\,[A]_0}\left([A]_0 + [C]_0 + \frac{1}{K} - \sqrt{\left([A]_0 + [C]_0 + \frac{1}{K}\right)^2 - 4\,[A]_0\,[C]_0}\right) \quad (1)$$

where I denotes the fluorescence emission intensity of albumin in presence of CIT; I_0 denotes the fluorescence emission intensity of albumin in absence of CIT; I_{AC} denotes the fluorescence emission intensity of pure albumin-CIT complex (which is calculated by the Hyperquad2006 software); K denotes the binding constant; while $[A]_0$ and $[C]_0$ denote the total concentrations of albumin and CIT, respectively.

In order to investigate the potential displacement of warfarin (WAR) and ochratoxin A (OTA) from HSA in the presence of citrinin, our previously published models were applied with slight modifications: (1) increasing CIT concentrations (0–5 μM) were added to standard amounts of WAR (1 μM) and HSA (3.5 μM) in PBS (pH 7.4), then the fluorescence emission spectra were recorded (λ_{exc} = 317 nm) [20]; and (2) Increasing CIT or WAR concentrations (0–30 μM) were added to standard amounts of OTA (1 μM) and HSA (1.4 μM) in PBS (pH 7.4), then fluorescence polarization values of the samples were measured (λ_{exc} = 393 nm, λ_{em} = 446 nm) [25,26].

3.3. Thermodynamic Studies

To get deeper insight into the formation of CIT-HSA complex, quenching experiments were also performed at different temperatures (25, 30, 35, and 40 °C). Thermodynamic parameters were quantified applying the van't Hoff equation:

$$\ln K = -\frac{\Delta G}{RT} = -\frac{\Delta H}{RT} + \frac{\Delta S}{R} \quad (2)$$

where ΔG is the Gibbs free energy change, ΔS is the entropy change, while ΔH is the enthalpy change associated with the complex formation.

3.4. Ultrafiltration Studies

Before ultrafiltration samples contained 1 μM CIT with or without HSA (1, 2.5 or 5 μM), while displacement of CIT by WAR (5 and 10 μM) or OTA (2.5 and 5 μM) was investigated in the presence of 1 μM CIT and 5 μM HSA. During ultrafiltration experiments Amicon Ultra-4 centrifugal filter units (with 10 kDa molecular weight cut-off value; from Merck Millipore, Darmstadt, Germany) were applied. In order to remove glycerol from the filters, filter units were washed with 3 mL water and 3 mL PBS. Thereafter, 2.5 mL of the samples were transferred into the filter and Amicon tubes were centrifuged at 7500 g for 10 min at 25 °C (in Hettich Universal 32R centrifuge with fixed-angle rotor). Then 2 mL quantity of filtrate was transferred into 5-mL Eppendorf tube, after which 10 μL 6 M HCl solution was added to the sample in order to adjust the pH (to approximately 2). This step is necessary because CIT shows strong fluorescence properties only at highly acidic conditions [19]. Final CIT concentrations were determined (applying calibration curve at concentration range 0.1–2.0 μM) by Hitachi F-4500 fluorescence spectrophotometer with the measurement of the fluorescence signal of CIT itself, using 330 nm and 500 nm as excitation and emission wavelengths, respectively. No spectral interferences were observed during these experiments (data not shown). Regardless of the concentration used (tested between 0.1–2.0 μM CIT concentrations), constant recovery of CIT was determined after ultrafiltration (61.7% ± 1.8%).

3.5. Molecular Modeling Studies

Blind docking [32–34] calculations were performed using the AutoDock 4.2 [35] program package. Ligand molecules were built in Maestro [36]. It is known that two tautomeric form of citrinin exists in solution (p-quinone and o-quinone; Figure 5D) at room temperature [19,37], therefore both forms were studied in docking calculations. Both tautomeric forms were used in the carboxyl deprotonated state. Energy-minimization of the ligand molecules was performed by the semi-empirical quantum chemistry program package, MOPAC [38], performing a geometry optimization with a 0.001 gradient norm and subsequent force calculations with PM6 parameterization. In all cases, the force constant matrices were positive definite. The apo structure of human serum albumin (pdb code 1a06, Figure 5A) was used as a target of blind docking. Gasteiger-Marsilli partial charges were added to both ligand and target atoms and a united atom representation was applied for groups with non-polar bonds. ALamarckian genetic algorithm was used for search [32]. Docking box was centered on the center of mass of the target. A grid map with a box size of 250 × 250 × 250 points and 0.375 Å spacing was calculated by AutoGrid 4 [35]. The number of docking runs was set to 100, numbers of energy evaluations and generations were 20 million [34]. Ligand conformations resulted from the docking runs were ordered by the corresponding calculated ΔG values and clustered [34] using a tolerance of 1.75 Å root mean square deviation (RMSD) between cluster members. Conformations with the lowest binding energy within a cluster were selected as cluster representatives. In this way, blind docking resulted in a list of representative ligand positions and the corresponding calculated ΔG values. Ligand-protein contacts were listed and analyzed, within a 3.5 Å distance cut-off between heavy atoms of docked ligands and the target.

3.6. Tissue Culture and Cell Viability Measurements

MDCK (immortalized, epithelial-kidney, ATCC: CCL 34) cells were cultured in DMEM containing FBS (10%), penicillin (100 U/mL) and streptomycin (100 μg/mL), in 25 cm^2 sterile plastic flasks (VWR) and in 24-well sterile plastic plates (VWR). In order to test the effect of CIT on cell viability in absence and presence of albumin, cell media with and without 10% FBS or 40 g/L HSA were also prepared. After 24-h treatment of MDCK cells (in 24-well plates) with CIT (0–100 μM) in absence and presence of FBS (10%) or HSA (40 g/L), cells were washed three times with 500 μL PBS. Then PBS was replaced with 500 μL Hanks + glucose buffer containing 1.6 μM calcein acetoxymethyl ester and cells were incubated for 40 min at 37 °C in the dark. Thereafter, wells were washed again with 500 μL ice-cold PBS and the emptied wells were filled with 500 μL of 5% perchloric acid (PCA) after which cells were incubated for 15 min at room temperature. 20 μL PCA extract was added to 180 μL of 1 M NaOH using black 96-well optical plates (VWR) for fluorescence measurement of the formed calcein (λ_{exc} = 490 nm, λ_{em} = 520 nm). Fluorescence intensities were measured with a microplate reader (Perkin Elmer EnSpire Multimode reader).

3.7. Statistics

Statistical analyses were performed by One-Way ANOVA test employing IBM SPSS Statistics 22.0 software. The level of significance was set as $p < 0.05$.

4. Conclusions

In summary, in our study the complex formation of citrinin with human serum albumin was investigated. The strong quenching of the fluorescence of HSA by CIT as well as the spectroscopic and ultrafiltration experiments with site markers (warfarin and ochratoxin A) strongly suggest that the high-affinity binding site of CIT is located on Sudlow's site I (subdomain IIA). This experimental result was also confirmed by molecular modeling studies. Thermodynamic and modeling studies suggest that H-bonds, salt bridges, and hydrophobic interactions are involved as binding forces. Furthermore, based on our results CIT-HSA interaction is an enthalpy-driven process; therefore, electrostatic forces play a major role during the CIT-HSA complex formation. CIT forms a stable complex with HSA ($\log K \sim 5.3$); cell experiments indicated the high biological importance of the interaction as well. There are some differences between the complex stabilities of CIT complexes with albumins of other species (bovine, porcine, and rat albumins were tested); however, we did not observe dramatic differences, like in the case of ochratoxin A (which possesses a similar chemical structure to CIT).

Supplementary Materials: The following are available online at www.mdpi.com/2072-6651/7/12/4871/s1.

Acknowledgments: This work was financially supported by the University of Pécs, Medical School (PTE ÁOK-KA-2013/15). Financial support of the "Environmental industry related innovative trans- and interdisciplinary research team development in the University of Pécs knowledge base" (SROP-4.2.2.D-15/1/Konv-2015-0015) project is highly appreciated. The modeling work was supported by the Hungarian Scientific Research Fund (OTKA K112807). The support of the National Information Infrastructure Development Institute (NIIF, Budapest, Hungary) is acknowledged for computing resources. The present scientific contribution is dedicated to the 650th anniversary of the foundation of the University of Pécs, Hungary.

Author Contributions: Miklós Poór conceived the study, wrote the paper, and performed ultrafiltration and fluorescence competitive experiments. Beáta Lemli and Sándor Kunsági-Máté carried out thermodynamic studies. Mónika Bálint and Csaba Hetényi performed molecular modeling studies. Nikolett Sali and Tamás Kőszegi carried out *in vitro* cell experiments. All authors have read, edited, and approved the final version of the paper.

Conflicts of Interest: The authors declare no conflict of interest.

References

1. Da Rocha, M.E.B.; da Chagas Oliveira Freire, F.; Maia, F.E.F.; Guedes, M.I.F.; Rondina, D. Mycotoxins and their effects on human and animal health. *Food Contr.* **2014**, *36*, 159–165. [CrossRef]
2. Flajs, D.; Peraica, M. Toxicological properties of citrinin. *Arh. Hig. Rada Toksikol.* **2009**, *60*, 457–464. [CrossRef] [PubMed]
3. Ostry, V.; Malir, F.; Ruprich, J. Producers and important dietary sources of ochratoxin A and citrinin. *Toxins (Basel)* **2013**, *5*, 1574–1586. [CrossRef] [PubMed]
4. Kitabatake, N.; Trivedi, A.B.; Doi, E. Thermal decomposition and detoxification of citrinin under various moisture conditions. *J. Agric. Food Chem.* **1991**, *39*, 2240–2244. [CrossRef]
5. Chan, W.-H. Citrinin induces apoptosis via a mitochondria-dependent pathway and inhibition of survival signals in embryonic stem cells, and causes developmental injury in blastocysts. *Biochem. J.* **2007**, *404*, 317–326. [CrossRef] [PubMed]
6. Chang, C.-H.; Yu, F.-Y.; Wu, T.-S.; Wang, L.-T.; Liu, B.-H. Mycotoxin Citrinin Induced Cell Cycle G2/M arrest and numerical chromosomal aberration associated with disruption of microtubule formation in human cells. *Toxicol. Sci.* **2011**, *119*, 84–92. [CrossRef] [PubMed]
7. Kuroda, K.; Ishii, Y.; Takasu, S.; Kijima, A.; Matsushita, K.; Watanabe, M.; Takahashi, H.; Sugita-Konishi, Y.; Sakai, H.; Yanai, T.; *et al*. Cell cycle progression, but not genotoxic activity, mainly contributes to citrinin-induced renal carcinogenesis. *Toxicology* **2013**, *311*, 216–224. [CrossRef] [PubMed]
8. Berndt, W.O.; Hayes, A.W. The Effect of Probenecid on Citrinin-Induced Nephrotoxicity. *Toxicol. Appl. Pharmacol.* **1982**, *64*, 118–124. [CrossRef]
9. Berndt, W.O. Transport of citrinin by rat renal cortex. *Arch. Toxicol.* **1983**, *54*, 35–40. [CrossRef] [PubMed]
10. Föllmann, W.; Behm, C.; Degen, G.H. Toxicity of the mycotoxin citrinin and its metabolite dihydrocitrinone and of mixtures of citrinin and ochratoxin A *in vitro*. *Arch. Toxicol.* **2014**, *88*, 1097–1107. [CrossRef] [PubMed]
11. Blaszkewicz, M.; Munoz, K.; Degen, G.H. Methods for analysis of citrinin in human blood and urine. *Arch. Toxicol.* **2013**, *87*, 1087–1094. [CrossRef] [PubMed]
12. Ali, N.; Blaszkewicz, M.; Degen, G.H. Occurrence of the mycotoxin citrinin and its metabolite dihydrocitrinone in urines of German adults. *Arch. Toxicol.* **2015**, *89*, 573–578. [CrossRef] [PubMed]
13. Fanali, G.; Di Masi, A.; Trezza, V.; Marino, M.; Fasano, M.; Ascenzi, P. Human serum albumin: From bench to bedside. *Mol. Aspects Med.* **2012**, *33*, 209–290. [CrossRef] [PubMed]
14. Yamasaki, K.; Chuang, V.T.; Maruyama, T.; Otagiri, M. Albumin-drug interaction and its clinical implication. *Biochim. Biophys. Acta* **2013**, *1830*, 5435–5443. [CrossRef] [PubMed]
15. Poór, M.; Li, Y.; Matisz, G.; Kiss, L.; Kunsági-Máté, S.; Kőszegi, T. Quantitation of species differences in albumin-ligand interactions for bovine, human and rat serum albumins using fluorescence spectroscopy: A test case with some Sudlow's site I ligands. *J. Lumin.* **2014**, *145*, 767–773. [CrossRef]
16. Li, Y.; Czibulya, Z.; Poór, M.; Lecomte, S.; Kiss, L.; Harte, E.; Kőszegi, T.; Kunsági-Máté, S. Thermodynamic study of the effects of ethanol on the interaction of ochratoxin A with human serum albumin. *J. Lumin.* **2014**, *148*, 18–25. [CrossRef]
17. Damodaran, C. *In vitro* binding of citrinin to serum protein. *Experientia* **1977**, *33*, 598–599. [CrossRef] [PubMed]
18. Damodaran, C.; Shanmugasundaram, E. Distribution of radioactive citrinin in tissues and serum protein(s). *J. Radioanal. Chem.* **1978**, *46*, 373–377. [CrossRef]
19. Zhou, Y.; Chen, J.; Dong, L.; Lu, L.; Chen, F.; Hu, D.; Wang, X. A study of fluorescence properties of citrinin in β-cyclodextrin aqueous solution and different solvents. *J. Lumin.* **2012**, *132*, 1437–1445. [CrossRef]
20. Poór, M.; Li, Y.; Kunsági-Máté, S.; Petrik, J.; Vladimir-Knežević, S.; Kőszegi, T. Molecular displacement of warfarin from human serum albumin by flavonoid aglycones. *J. Lumin.* **2013**, *142*, 122–127. [CrossRef]
21. Li, X.; Wang, F.; Xu, B.; Yu, X.; Yang, Y.; Zhang, L.; Li, H. Determination of the free and total concentrations of vancomycin by two-dimensional liquid chromatography and its application in elderly patients. *J. Chromatogr. B* **2014**, *969*, 181–189. [CrossRef] [PubMed]
22. Tang, D.Q.; Li, Y.J.; Li, Z.; Bian, T.T.; Chen, K.; Zheng, X.X.; Yu, Y.Y.; Jiang, S.S. Study on the interaction of plasma protein binding rate between edaravone and taurine in human plasma based on HPLC analysis coupled with ultrafiltration technique. *Biomed. Chromatogr.* **2015**, *29*, 1137–1145. [CrossRef] [PubMed]

23. Il'ichev, Y.V.; Perry, J.L.; Rüker, F.; Dockal, M.; Simon, J.D. Interaction of ochratoxin A with human serum albumin. Binding sites localized by competitive interactions with the native protein and its recombinant fragments. *Chem. Biol. Interact.* **2002**, *141*, 275–293. [CrossRef]
24. Il'ichev, Y.V.; Perry, J.L.; Simon, J.D. Interaction of Ochratoxin A with Human Serum Albumin. A Common Binding Site of Ochratoxin A and Warfarin in Subdomain IIA. *J. Phys. Chem. B* **2002**, *106*, 460–465. [CrossRef]
25. Poór, M.; Kunsági-Máté, S.; Bencsik, T.; Petrik, J.; Vladimir-Knežević, S.; Kőszegi, T. Flavonoid aglycones can compete with Ochratoxin A for human serum albumin: A new possible mode of action. *Int. J. Biol. Macromol.* **2012**, *51*, 279–283. [CrossRef] [PubMed]
26. Poór, M.; Kunsági-Máté, S.; Czibulya, Z.; Li, Y.; Peles-Lemli, B.; Petrik, J.; Vladimir-Knežević, S.; Kőszegi, T. Fluorescence spectroscopic investigation of competitive interactions between ochratoxin A and 13 drug molecules for binding to human serum albumin. *Luminescence* **2013**, *28*, 726–733. [CrossRef] [PubMed]
27. Ross, P.D.; Subramanian, S. Thermodynamics of protein association reactions: Forces contributing to stability. *Biochemistry* **1981**, *20*, 3096–3102. [CrossRef] [PubMed]
28. Oester, Y.T.; Keresztes-Nagy, S.; Mais, R.F.; Becktel, J.; Zaroslinski, J.F. Effect of temperature on binding of warfarin by human serum albumin. *J. Pharm. Sci.* **1976**, *65*, 1673–1677. [CrossRef] [PubMed]
29. Abou-Zied, O.K.; Al-Shihi, O.I.K. Characterization of subdomain IIA binding site of human serum albumin in its native, unfolded, and refolded states using small molecular probes. *J. Am. Chem. Soc.* **2008**, *130*, 10793–10801. [CrossRef] [PubMed]
30. Petitpas, I.; Bhattacharya, A.A.; Twine, S.; East, M.; Curry, S. Crystal structure analysis of warfarin binding to human serum albumin anatomy of drug site I. *J. Biol. Chem.* **2001**, *276*, 22804–22809. [CrossRef] [PubMed]
31. Destro, R.; Marsh, R.E. Temperature dependence of tautomeric equilibria in the solid state: The case of citrinin. *J. Am. Chem. Soc.* **1984**, *106*, 7269–7271. [CrossRef]
32. Hetényi, C.; van der Spoel, D. Efficient docking of peptides to proteins without prior knowledge of the binding site. *Protein Sci.* **2002**, *11*, 1729–1737. [CrossRef] [PubMed]
33. Hetényi, C.; van der Spoel, D. Blind docking of drug-sized compounds to proteins with up to a thousand residues. *FEBS Lett.* **2006**, *580*, 1447–1450. [CrossRef] [PubMed]
34. Hetényi, C.; van der Spoel, D. Toward prediction of functional protein pockets using blind docking and pocket search algorithms. *Protein Sci.* **2011**, *20*, 880–893. [CrossRef] [PubMed]
35. Morris, G.M.; Huey, R.; Lindstrom, W.; Sanner, M.F.; Belew, R.K.; Goodsell, D.S.; Olson, A.J. AutoDock4 and AutoDockTools4: Automated docking with selective receptor flexibility. *J. Comput. Chem.* **2009**, *30*, 2785–2791. [CrossRef] [PubMed]
36. Schrödinger. Release, S. 2: Maestro, Schrödinger. LLC, New York, NY, USA, 2013.
37. Appell, M.; Moravec, D.; Bosma, W.B. Quantum chemical study of the structure and properties of citrinin. *Mol. Simul.* **2012**, *38*, 284–292. [CrossRef]
38. Stewart, J.J.P. MOPAC 2012, Stewart Computational Chemistry, Colorado Springs, CO, USA, 2012. Version 14.243L.

© 2015 by the authors; licensee MDPI, Basel, Switzerland. This article is an open access article distributed under the terms and conditions of the Creative Commons by Attribution (CC-BY) license (http://creativecommons.org/licenses/by/4.0/).

THE JOURNAL OF PHYSICAL CHEMISTRY C

Article

pubs.acs.org/JPCC

Some Unexpected Behavior of the Adsorption of Alkali Metal Ions onto the Graphene Surface under the Effect of External Electric Field

Beáta Peles-Lemli,[†,∥] Dániel Kánnár,[†] Jia Cai Nie,[‡] Heng Li,[§] and Sándor Kunsági-Máté*[,†,∥]

[†]Department of General and Physical Chemistry, University of Pécs, Ifjúság 6, Pécs, H-7624, Hungary

[‡]Department of Physics, Beijing Normal University, 100875 Beijing, People's Republic of China

[§]Department of Physics, Xiamen University, 361005 Xiamen, People's Republic of China

[∥]János Szentágothai Research Center, Ifjúság 20, Pécs H-7624, Hungary

ABSTRACT: In this work the interaction between alkali metal ions and a graphene surface with the absence and the presence of an external electric field applied perpendicular to the surface was investigated. M05-2X/6-31G(d) DFT calculations were performed to describe the adsorption properties. Results show that the electric field pushes the positively charged ion closer to the graphene, where the charge transfer between the alkali metal cations and the electron rich graphene surface increases. At a species-dependent certain strength of the electric field, the excess electrons cause negative charge on the alkali metal ion. This effect will promote the removal of the ion from the surface.

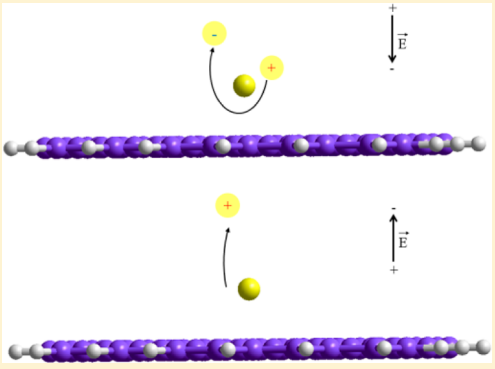

Downloaded via UNIV OF PECS on November 24, 2022 at 08:09:39 (UTC).
See https://pubs.acs.org/sharingguidelines for options on how to legitimately share published articles.

1. INTRODUCTION

Two-dimensional graphene, carbon nanotubes (CNTs), and graphene nanoribbons represent a novel class of low dimensional materials that could serve as building blocks for future carbon-based nanoelectronics. However, there are some wonderful properties of these nanomaterials (e.g., conductivity, flexibility, adsorptive behavior, and ability to form inclusion complexes) that are already known, and with much attention focused on these, the wide application still seems to be a big challenge.

It is well-known that the external electric field can modify the physical properties of carbon nanomaterials like CNTs[1] or graphene.[2] The application of the electric field as a reversible switch makes practical importance not only because of its easily controllable direction and intensity but also because it has the ability to control the surface properties for a short time such as seconds or less. In particular, the perpendicular electric field leads to a polarization of the charge density that could affect the adsorption properties of graphene, the importance of which has been widely recognized. Therefore, nowadays more and more studies investigate the atomic structures and adsorption property dependence of graphene under different strengths of external electric field. In this way, CO adsorption on graphene nanodots,[3] the interaction between O_2 and Au-doped graphene,[4] or the dissociative adsorption of H_2O on graphene[5] have been analyzed by taking the external electric field into account. These studies showed that the applied electric field can enhance or weaken the adsorption of different particles onto the graphene surface as well as provide possible new and/or energetically more favorable reaction pathways which can not be reached otherwise.

In our previous works noncovalent interactions between single-walled CNTs and aromatic "packer" molecules were analyzed with the aim to clarify the related solubilization processes.[6,7] Furthermore, the dispersion of hydroxylated multiwalled CNTs (MWCNTs) was modified in nonprotic acetonitrile solvent using a treatment by ethanol.[8] From this solution phase the MWCNTs were deposited onto the nanostructured CeO_2 films grown on sapphire substrate.[9,10] High resolution images by both transmission and scanning electron microscopy showed that the nanographite fractions existed in the solution and they were also reorganized on the surface. These graphene multilayers could be separated from the remaining MWCNTs by an entropy driven selective adsorption process.[11] On the nanostructured surface with specific morphology, the nanographite fractions are deposited into the valleys between the CeO_2 islands, and therefore a selective pattern of nanographite was formed. Molecular dynamics calculations highlighted that adsorption and reorganization properties of the nanographite layers have considerable dependence on the morphology of CeO_2 nanostructures.[12] Considering that the CeO_2 surface morphology is fully controlled by the experimental setup of growth, properties of the CNT layers are tunable toward the requirements of practical applications.

Received: April 18, 2013
Revised: August 22, 2013
Published: September 17, 2013

 © 2013 American Chemical Society

This generated graphene−CeO_2−sapphire layer with electrochemical modifications could be a potential surface of ion diffusion controlled by an external electric field. In this way, we might be able to get transported ions selectively by changing the applied perpendicular and parallel electric fields. To reach the practical benefits of this method, it is necessary to clarify the diffusion and adsorption mechanism of the ions on graphene layers. Therefore in this work the interaction between alkali ions and the graphene surface with the absence and the presence of external electric field applied perpendicular to the graphene surface was investigated using density functional theory (DFT) methods.

2. THEORETICAL METHODS

First, the model cluster with a molecular formula of $C_{54}H_{18}$ was constructed and fully optimized using the M05-2X hybrid meta-GGA functional[13,14] with the 6-31G(d) basis set. Then the alkali metal cation, namely a lithium, sodium, or potassium ion, was positioned above the surface. Three different orientations of the ion with respect to the graphene surface, namely, top, hollow, and bridge, were considered as starting structures (Figure 1). In the top site geometry the alkali metal ion located

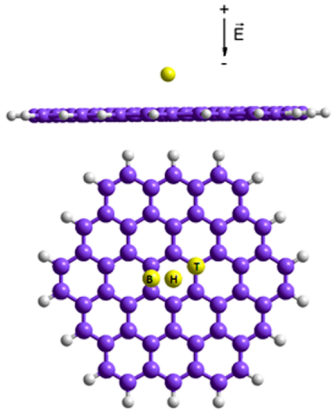

Figure 1. During the calculations the applied electric field was perpendicular to the graphene surface (up). The different orientations of the ion with respect to the graphene surface: (T) top, (H) hollow, and (B) bridge (down).

directly above the C atom, in the hollow site conformation the ion is above the center of a hexagon in the graphene layer and in the bridge site structure the ion is positioned above the center of a C−C bond. During the calculation the rigid model was used: the geometry of the cluster was frozen as it obtained in the first step and the optimized ion position was determined by varying the distance between the ion and the graphene plane until the most stable position is found. The site with the largest adsorption energy was referred to as the most stable one. The adsorption energy was calculated using the eq 1.

$$E_{ads} = E_{ion} + E_{graphene} - E_{ion/graphene} \quad (1)$$

In good agreement with the previous theoretical works (see, e.g., ref 15), we also found that the alkali metal ions are adsorbed preferably on top of the hollow site. Therefore in this work the hollow site adsorption of the ions in the middle of the $C_{54}H_{18}$ graphene cluster was analyzed in detail. The effect of homogeneous external electric field applied perpendicular to the graphene surface on the ion adsorption was analyzed (Figure 1). For the quantum chemical calculations the Gaussian 09 program package was used.[16] Preparation, manipulation, and visualization of coordinate files were done with HyperChem Professional 7.[17]

3. RESULTS AND DISCUSSION

3.1. Structures and Adsorption Energies under Neutral Field. Quantum chemistry is a fruitful testing technique for molecular-scale analysis; therefore, it is not surprising that a mass of computational or theoretical studies on carbon nanomaterials can be found in the literature. The adsorption of aromatic molecules such as benzene,[18] phenol,[19] dibenzothiophene,[20] cytosine,[21] or aniline[7] on single-walled carbon nanotubes has attracted increased attention in the past few years. Nowadays the synthesis[22] and characterizations[23] of graphene nanoribbons have been brought into focus. Furthermore, because of its practical applications in more efficient Li-ion batteries, the investigations of the interaction between alkali metal atoms and ions such as lithium and the graphitic surface have been also analyzed theoretically by several groups.[15,24−26] In the related theoretical works the first question always is how to describe the graphene and its interaction with different species: to model the surface one can use finite graphene clusters or two-dimensional periodic boundary conditions (PBC) applied on graphene unit cells. Furthermore, to obtain the adsorption energies the rigid model with frozen cluster is similarly popular as the fully relaxed approach. Uthaisar and Barone investigated the adsorption and diffusion properties of the Li atom on graphene and graphene nanoribbons.[27] Their results did not show significant difference between the structures determined by the rigid model or fully relaxed approach. Contrarily, Umadevy and Sastry found[24] that only in the case of small molecules is it possible to neglect the deformation of the graphene cluster. At the same time the metal atoms and ions induce considerable strain in the graphene cluster, although increasing the cluster size decreases the surface deformation. In this present work the cluster calculation combined with the rigid model was chosen to describe the alkali metal cation−graphene interaction under electric field. However, to take into account the possible effect of the cluster deformation, the fully optimized structures of the $Li^+C_{54}H_{18}$, $Na^+C_{54}H_{18}$, and $K^+C_{54}H_{18}$ systems were also determined at the M05-2X/6-31G(d) level of theory. Table 1 summarizes the calculated equilibrium distances (R_e) between the ion and the graphene, the adsorption energies (E_{ads}), and the Mulliken atomic charges (Z_{ion}) of the alkali ions. R_e was defined as the difference in the z coordinates where the graphene surface is located in the xy plane.

Table 1. Optimized Parameters of the Alkali Metal Ions on Graphene[a]

	R_e [Å]	E_{ads} [kJ mol^{-1}]	Z_{ion} [e]
$Li^+C_{54}H_{18}$ (rm)	1.835	220.20 (214.48)	0.548
$Li^+C_{54}H_{18}$ (fr)	1.826	222.14 (216.21)	0.542
$Na^+C_{54}H_{18}$ (rm)	2.289	163.50 (158.02)	0.740
$Na^+C_{54}H_{18}$ (fr)	2.285	164.63 (158.95)	0.737
$K^+C_{54}H_{18}$ (rm)	2.729	125.27 (120.56)	0.910
$K^+C_{54}H_{18}$ (fr)	2.723	126.03 (120.68)	0.909

[a]Adsorption energy (E_{ads}) with the BSSE-corrected value in parentheses, Mulliken atomic charge of the ion (Z_{ion}) and the equilibrium distance between the ion and the graphene (R_e). The use of a rigid model (rm) or fully relaxed (fr) approach are indicated.

dx.doi.org/10.1021/jp403856e | J. Phys. Chem. C 2013, 117, 21509−21515

The data show that the investigated parameters are slightly depending on the freezing of the graphene cluster. The calculated equilibrium distances between the Li^+ ion and graphene surface are 1.835 or 1.826 Å using the rigid model or fully relaxed approach, respectively. These distances are in good agreement not only with the calculated data by Umadevy and Sastry using the cluster model with fully relaxed approach at the same level of theory[17] but also with the data determined by Zheng et al. with the combination of the PBC calculation and the rigid model approach at GGA-PAW level.[15] However, the most popular B3LYP method results in a 17% larger adsorption distance[25] indicating that the choice of the DFT method can play an important role in describing the weak or nonbonding interactions.

It is not surprising that the Li^+ ion with the smallest ionic radius located the closest to the graphene surface and the K^+ ion the furthest. The adsorption energies indicate chemisorptions as the most pronounced role in the adsorption processes although it is well-known that the cation$-\pi$ interaction is a noncovalent interaction between an electron rich π-system and a positively charged ion. The strength of this weak interaction can be modulated by the molecular environment, e.g., the used solvent permittivity or by the characterics of the aromatic hydrocarbons determined by the number of the fused aromatic rings and the effect of substituent. Our calculated data are about 1 order magnitude larger than the average physisorption energy. The account for these large adsorption energy values is the size of the graphene cluster because the increasing size of the polycyclic aromatic hydrocarbons results in the increase of the cation$-\pi$ interaction energy.[24]

As it can be seen in Table 1 there is no significant difference between the data determined by the rigid model or the fully relaxed approach. However in the fully optimized structure the graphene surface slightly bends like a convex lens.

3.2. Electric Field Induced Deformation of the Graphene Cluster. In this work the homogeneous and directed electric field was generated by the 'Field' keyword of the Gaussian program code. The electric field induced bending of graphene nanoribbons was described by Wang;[28] therefore, first the geometry of the $C_{54}H_{28}$ cluster was analyzed under homogeneous external electric field applied perpendicular to the graphene plane. Our results also show the mechanical sensitivity of the graphene surface to the external electric field; the $C_{54}H_{28}$ cluster bends as if it would fit on the surface of a tube while the C−C distances increase by 0.5%.

However the question is still opened that how the geometry of the graphene will change when it is deposited onto a carrier surface, e.g., onto a nanostructured CeO_2 films grown on a sapphire substrate. Lee and co-workers studied the atomic and electronic structures of single-layer graphene on the Si-terminated surface of SiC.[29] They found that the atomic positions of the graphene layer on the SiC surface are insensitive to the electric field, although the electronic band structures of the layer depend strongly on the direction and strength of the applied electric fields. We can assume that it is not necessary to take into consideration the electric field induced change of the graphene geometry. Therefore to model the graphene layers formed on the CeO_2 surface, the atomic positions of the $C_{54}H_{28}$ cluster were kept frozen as they were obtained under neutral field.

3.3. Li^+ Ion Adsorption under External Electric Field. In this work the effect of a homogeneous external electric field on the ion adsorption properties on graphene was modeled. Because of its electrochemical aspects the electric field ($\vec{E}$) was applied perpendicular to the surface. The electric field is directed from the ion toward the graphene surface (Figure 1). During the calculations the $C_{54}H_{28}$ cluster was kept frozen with the aim to eliminate the electric field induced bend of the graphene plane and the strength of the applied field was changed.

First the changes of the equilibrium distance between the Li^+ ion and the graphene surface were investigated. At first when increasing the strength of the electric field the distance between the Li^+ ion and the graphene surface decreases because the positively charged ion moves to the negative direction of the electric field. It can be clearly seen in Figure 2a that the electric field pushes the Li^+ ion to the surface, and at a certain strength of the electric field, the system reaches the accessible lowest distance. Even after a little strengthening of the electric field, a large moving of the ion from the surface is induced. The minimum equilibrium distance between the graphene surface and the lithium particle was calculated to be 1.556 Å under the electric field strength of 0.041 au. Furthermore, the change of the adsorption energy as a function of the electric field was analyzed (Figure 2b). One can expect that the decrease of the equilibrium distance between the ion and the cluster results in an increase of the adsorption energy because of the increasing Coulomb attraction between the positively charged Li^+ ion and the negatively charged C atoms of the graphene located the closest to the alkali metal ion. However Figure 2b shows the opposite trend. The long-range electrostatic attraction is balanced by the repulsive interaction between the atoms and molecules at short distances. The repulsion between oppositely charged molecules is very weak but it increase rapidly at very small intermolecular distances. This phenomenon can explain why the shortest equilibrium distance results in the weakest interaction between the Li particle and the graphene cluster.

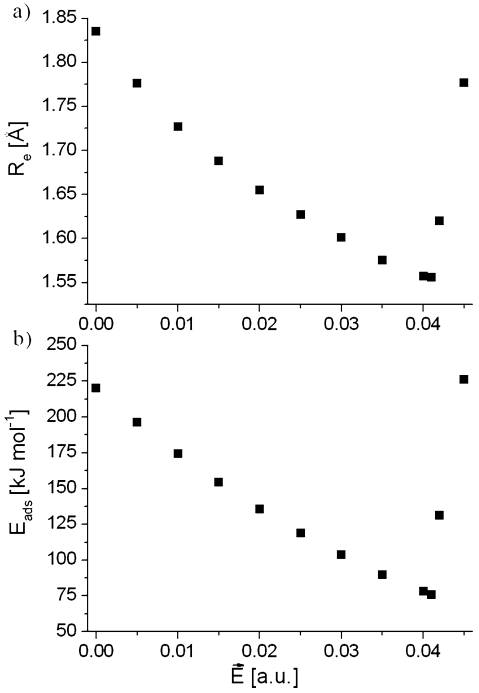

Figure 2. Equilibrium distance (R_e) between the Li^+ ion and graphene surface (a) and the adsorption energy (E_{ads}) (b) as a function of the applied electric field ($\vec{E}$). 1 au of electric field = 5.14×10^{11} V m^{-1}.

dx.doi.org/10.1021/jp403856e | J. Phys. Chem. C 2013, 117, 21509−21515

The calculated adsorption energy (BSSE corrected data in parentheses) is 75.98 (69.43) kJ mol^{-1}.

The molecule placed in an electric field undergoes deformation while the electric field partially polarizes the molecule, resulting in the separation of its charge. The polarizability is the measure of the change of the molecule to respond to an applied electric field. The polarizability determines the energy of the work done on electrons by the electric field to move along the direction of the field. The mean polarizabilty ($\langle\alpha\rangle$) was calculated

$$\langle\alpha\rangle = (\alpha_{xx} + \alpha_{yy} + \alpha_{zz})/3 \quad (2)$$

where the subscripts indicate the triangular orders. The values are calculated in atomic units (au); 1 au of polarizability = 1.65 × 10^{-41} C^2 m^2 J^{-1}. The polarizability of the $C_{54}H_{18}$ cluster is 268.06 au and almost independent of the strength of the applied electric field. Not surprisingly the interaction with the positively charged ion decreases the polarizability of the $Li^+C_{54}H_{18}$ system compared with the pure cluster containing electron rich aromatic rings. The mean polarizability of $Li^+C_{54}H_{18}$ monotonously decreases under electric field, and the determined values are 228.52, 226.01, and 213.81 au under the applied electric field strength of 0.000, 0.041, and 0.045 au, respectively. The data show that the change is about 1% until the system reaches the minimum equilibrium distance between the graphene surface and the lithium particle, and after that point the polarizabilty decreases more rapidly.

It is not surprising that the electrostatic repulsion between the nuclei stops the lithium from getting any closer to the graphene surface than the determined minimum equilibrium distance. However, a question arises as to why the lithium particle would remove from the surface after the system reaches the accessible lowest distance. After the system reached the minimum equilibrium distance, the intensive decrease of the polarizability of the $Li^+C_{54}H_{18}$ system and the movement of the originally positive ion to the positive direction of the electric field indicate the electric field induced change of the electron distribution of the $Li^+C_{54}H_{18}$ system.

To analyze the charge transfer between the ion and graphene surface the change of charge on the Li particle was analyzed. As it can seen in Table 1 there is an intensive charge transfer from the graphene surface to the Li^+ ion. According to these data the Li^+–graphene cluster interaction results in an almost 50% decrease of the positive charge of the Li^+ ion under neutral field of which the effect seems to be overestimated. Therefore to describe the charge transfer between the ion and graphene surface, Mulliken charge distribution and also natural bond orbitals (NBO) analysis[30] were performed. In both cases the charge transfer was described as the change of the atomic charge on the lithium particle. In a deeper view, one can see that the atomic charges calculated using NBO by summing the occupancy of the natural atomic orbitals (NPA) are different from Mulliken charges (Figure 3). However the differences in charge distribution barely depend on the methods and the two different analysis show similar trends: as the electric field pushes the positively charged ion closer to the surface the charge transfer from the graphene increases. Once the lithium reaches the shortest equilibrium distance it becomes a negatively charged ion. This effect results in an intensive removing of the lithium from the surface because the negative ion simply moves with the electric field. Furthermore, it is in good agreement with the change of the polarizability of the

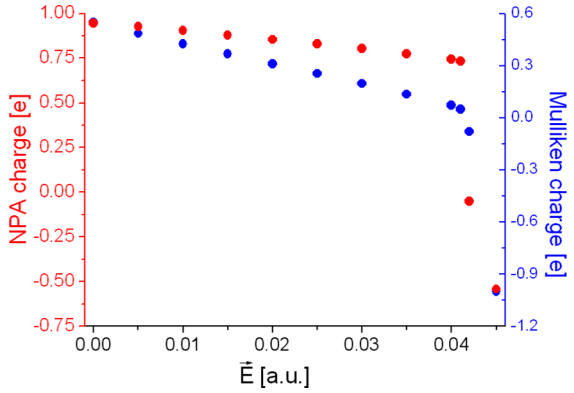

Figure 3. Charge of the lithium particle calculated by Mulliken charge distribution and NBO analysis.

$Li^+C_{54}H_{18}$ system and explains the intensive decrease of the polarizability while the Li ion is removed from the graphene surface.

The electron configuration of lithium particles in the $Li^+C_{54}H_{18}$ system is calculated to be $1s^2\ 2s^{0.01}\ 2p^{0.04}$, $1s^2\ 2s^{0.05}\ 2p^{0.20}\ 3s^{0.01}\ 3p^{0.01}$, and $1s^2\ 2s^{0.77}\ 2p^{0.75}\ 3p^{0.02}$ under the applied electric field strengths of 0.000, 0.041, and 0.045 au, respectively. The relatively high adsorption energy (220.20 kJ mol^{-1} under neutral field) shows that the electron donation from the 2p orbitals of the C atoms located in the middle of the cluster first promotes the binding of the Li^+ ion to the graphene. The strengthening of the electric field results that the 2sp and 3sp orbitals of the lithium particles occupied by slightly higher electron density.

Umadevy and Sastry found correlation between the strength of the Li^+ ion–graphene interaction and the pattern as well as the energy of the highest occupied molecular orbital (HOMO) of the graphene.[24] Tachikawa and co-workers showed that the Li^+ ion diffused along the HOMO of the graphene surface.[25] Furthermore, they found that the adsorption of the Li^+ ion induced almost no change on the pattern of the lowest unoccupied molecular orbital (LUMO) of the graphene.[31] However our results indicate that the LUMO was also affected by the Li^+ ion–graphene interaction. We have calculated the electric field effect on the energies of the HOMO and LUMO of $C_{54}H_{18}$ and $Li^+C_{54}H_{18}$ systems. Our results show (Figure 4) that under electric field both energies of the HOMO and LUMO decrease but at different rates. Hence the HOMO–

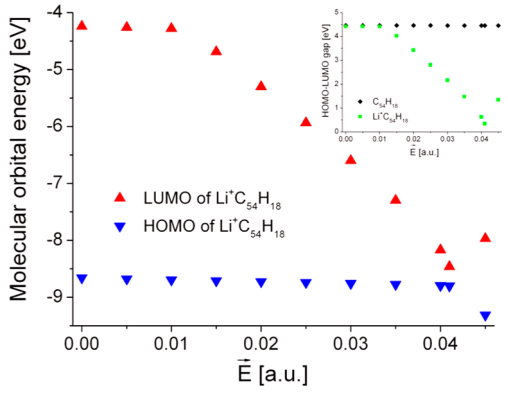

Figure 4. HOMO and LUMO energies of the $Li^+C_{54}H_{18}$ system and the HOMO–LUMO gap of $C_{54}H_{18}$ and $Li^+C_{54}H_{18}$ (inset) as a function of the electric field strength.

dx.doi.org/10.1021/jp403856e | J. Phys. Chem. C 2013, 117, 21509–21515

LUMO gap decreases, and it becomes the smallest when the electric filed pushes the closest of the Li^+ ions to the surface. Then the energy of the HOMO and LUMO decreases and increases, respectively. Therefore, it can be concluded that the change of the HOMO−LUMO gap and the energy of the LUMO show similar tendencies as the adsorption energy changes.

3.4. Adsorption and Diffusion of the Alkali Metal Ions.

The energetic and structural properties of the adsorption of sodium and potassium ions on graphene are similar to the properties of the adsorption of lithium ion described above. The minimum equilibrium distances are found to be 2.000 Å ($\bar{E}$ = 0.032 au) and 2.437 Å ($\bar{E}$ = 0.025 au) in the case of Na^+ and K^+ ions, respectively. The calculated minimum equilibrium distances depend on the ionic radius (Figure 5). Therefore particles with larger ionic radii reach the closest distance from the surface under weaker electric field, while in the case of smaller ions, it is necessary to apply a stronger field to push the particle as close as possible to the surface.

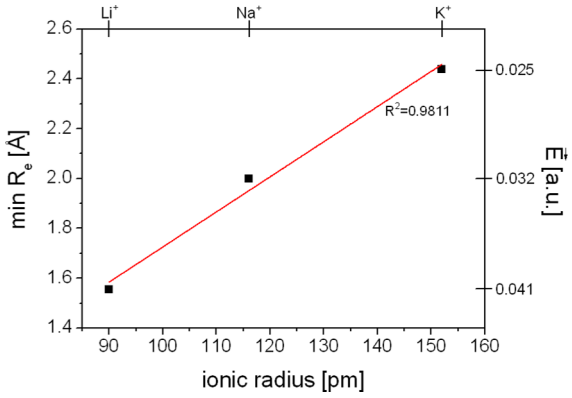

Figure 5. Minimum equilibrium distances between the alkali metal ions and the $C_{54}H_{18}$ graphene cluster.

In order to study the diffusion mechanism of Li^+, Na^+, and K^+ ions on the graphene surface, a larger graphene cluster ($C_{130}H_{28}$) was constructed to eliminate the edge effects. Because of the high symmetry of the cluster, we have studied two different diffusion paths (Figure 6): in both cases the starting position of the ion is the hollow position in the middle of the cluster (H_0) and the ion migrate through the middle of the bond (B) or on the top of the C atom (T), denoted as paths A or B, respectively. To eliminate the electric field induced bending of the graphene plane, the rigid model was used to determine the energies for different adsorption positions. Particle diffusion processes on a lattice can be analyzed as the particle elementary jumps between adsorption sites along the potential energy surface. The activation energies or energy barriers were calculated by the difference between the stable states and saddle points related to the rate of the diffusion. Therefore the relative adsorption energies (ΔE_{ads}) could be calculated with respect to the E_{ads} of starting point in hollow site adsorption (H_0) of the investigated ion.

Figure 6 shows that the determined potential minima and maximum of the $Li^+C_{54}H_{18}$, $Na^+C_{54}H_{18}$ and $K^+C_{54}H_{18}$ systems located in the same sites and the shape of the examined diffusion paths are not depending on the applied electric field. At the same time the heights of the activation barrier are considerably increased under electric field. The bigger energy barriers on the diffusion paths indicate slower diffusion of the investigated particle.

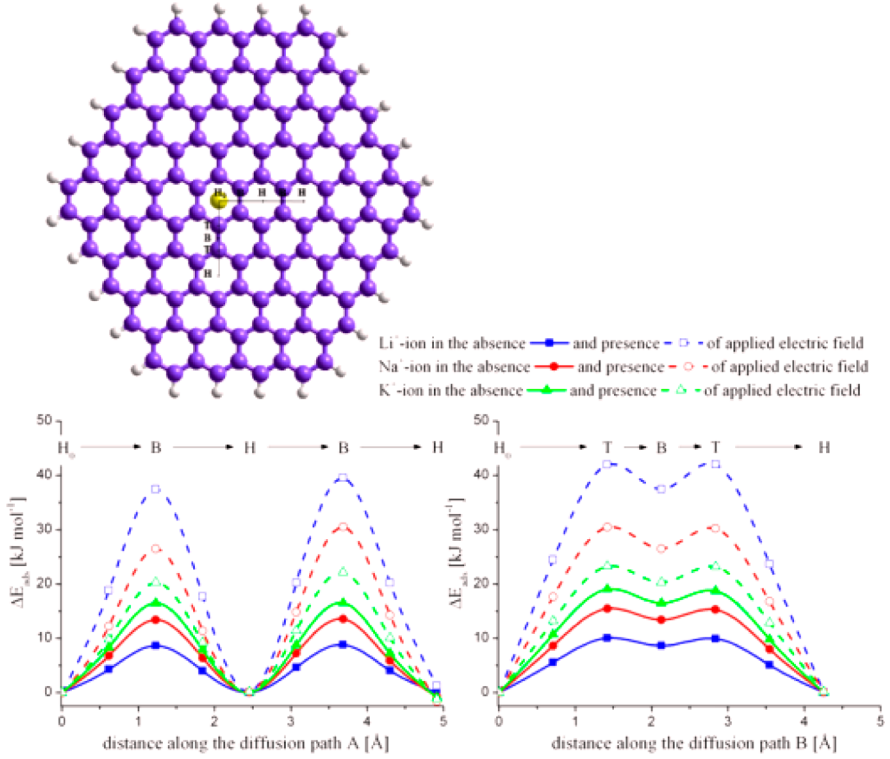

Figure 6. (a) Schematic representation of the $C_{130}H_{28}$ cluster used in the calculation. H, B, and T represent the ion adsorption position on the top of the hexagon, on the middle of the bond, and on the top of a C atom, respectively. (b) Energy barriers of the diffusion of Li^+, Na^+, and K^+ ions on paths A and B in the absence and presence of an applied electric field.

dx.doi.org/10.1021/jp403856e | J. Phys. Chem. C 2013, 117, 21509−21515

In the graphene cluster of $C_{130}H_{28}$ the two middle rings are equal, therefore the hollow site adsorption of the ions show no differences between these two rings (Figure 6). The diffusion of the ions between these middle rings along path A ($H_0 \rightarrow B \rightarrow H$) is capable to investigate the electric field effect with eliminating other conditions like the edge effect. The calculated energy barriers corresponding to the diffusion of Li, Na, and K ions are 8.65, 13.43, and 16.50 kJ mol^{-1} when the electric field is absent and 37.44, 26.52, and 20.31 kJ mol^{-1} when it is present, respectively. Accordingly, the diffusions of the ions are much slower under electric field than without it. Going along on path A, the next energy barriers related to the $H \rightarrow B \rightarrow H$ diffusion are slightly different from the previous case. The edge effect is hardly noticeable in the absence of an electric field. The difference between the energy barriers are smaller than 0.2 kJ mol^{-1}. At the same time, in the presence of electric field the second energy barriers on path A are at least 2 kJ mol^{-1} higher than the first one. These results indicate the importance of further investigations of the edge effect on the ion diffusion on graphitic surfaces like graphene nanoribbons under external electric field.

Previous studies[15,25] showed that in a neutral field on the graphene surface, the ion diffusion from the middle of the hexagon through the middle of the C−C bond is faster than through the top of the C atom. Therefore it is necessary to investigate how the preferred pathway changes under external electric field. The calculated barrier heights for path B are 10.06, 15.50, and 19.06 kJ mol^{-1} in the absence and 42.00, 30.48, and 23.28 kJ mol^{-1} in the presence of an electric field related to the diffusion of Li, Na, and K ions, respectively. This means that, even though the preferred pathway does not change in the absence or presence of electric field, the electric field induces higher differences between the energy barriers of the investigated two pathways.

The static calculations indicate that the Li^+ ion which has the smallest ionic radius diffuses fastest under neutral field. In contrast, the diffusion of the Li^+ ion is the slowest in the presence of an external electric field. On the diffusion path above the C−C bond (bridge site), the short-range repulsion between the particles is getting stronger, which causes a higher energy barrier if the particle is closer to the surface even as the Li^+ ion.

4. CONCLUSION

In this work the interaction between three kinds of alkali metal ions (namely Li^+, Na^+, and K^+) and the graphene surface in the cases of the absence and presence of the external electric field was investigated. An electric field perpendicular to the surface has been applied which pushes closer the positively charged ion to the graphene surface. Results show the importance of the charge transfer from the graphene surface to the alkali metal ion. At a species-dependent certain strength of the electric field the excess electrons cause negative charge on the alkali metal ion, promoting the shoving off of the ion from the surface. The static calculations indicate that the Li^+ ion which has the smallest ionic radius diffuses the fastest or the slowest under neutral or external electric field, respectively.

These findings may promote the more detailed exploration of the ions' adsorption and diffusion mechanism on graphene and graphene-like surfaces and facilitate the design of the experimental investigations and the applications in electrochemical devices and chemical sensors. Moreover, as we showed previously, the energy gap between the HOMO and LUMO orbitals of our systems decreases quite rapidly as the alkali metal ions approach the graphene surface and settle around 0.5−1 eV when the ions reached their lowest equilibrium distances. This low value predicts favorable holdings in photochemical studies at the range of visible light. With this property, the graphene−ion systems may open a new area besides sensor- and electrochemistry and play an important role in future developments of more efficient solar cells.

Although during the calculations the applied electric field strength is unrealistic for a larger device, it is achievable at the atomic level using a field ion microscope or atomic force microscope. Furthermore, the cluster model calculations are approximate, the size of the systems are limited, and in the present case, no surface defects or carrier surface like the nanostructured CeO_2 film have been taken into account. Even so we think that the present predictions and determined trends are applicable both in theoretical and experimental studies about how the electric field would affect ion−graphene interactions.

AUTHOR INFORMATION

Corresponding Author

*Tel: +36 72 503600. Fax: +36 72 501518. E-mail: kunsagi@gamma.ttk.pte.hu.

Notes

The authors declare no competing financial interest.

ACKNOWLEDGMENTS

This work was supported by the Hungarian research Project No. TÁMOP-4.2.2.A-11/1/KONV-2012-0065 and by the Chinese−Hungarian Intergovernmental S&T Cooperation Programme (Project Nos. CH-5-21/2010, TÉT_10-1-2011-0126, and TÉT_12_CN-1-2012-0040). The calculations are performed using the Gaussian 09, revision C.01 program package on SGI UltraViolet 1000 supercomputer of the Hungarian National Infrastructure Development Program Office located in the University of Pécs.

REFERENCES

(1) Kim, C.; Kim, B.; Lee, S. M.; Jo, C.; Lee, Y. H. Effect of Electric Field on the Electronic Structures of Carbon Nanotubes. *Appl. Phys. Lett.* **2001**, *79*, 1187−1189.

(2) Guo, Y.; Guo, W.; Chen, C. Tuning Field-induced Energy Gap of Bilayer Graphene via Interlayer Spacing. *Appl. Phys. Lett.* **2008**, *92*, 243101.

(3) Liu, H.; Lee, J. Y. Electric Field Effects on the Adsorption of CO on a Graphene Nanodot and the Healing Mechanism of a Vacancy in a Graphene Nanodot. *J. Phys. Chem. C* **2012**, *116*, 3034−3041.

(4) Zhang, T.; Xue, Q.; Shan, M.; Jiao, Z.; Zhou, X.; Ling, C.; Yan, Z. Adsorption and Catalytic Activation of O_2 Molecule on the Surface of Au-Doped Graphene under an External Electric Field. *J. Phys. Chem. C* **2012**, *116*, 19918−19924.

(5) Jiang, Q. G.; Ao, Z. M.; Chu, D. W.; Q. Jiang, Q. Reversible Transition of Graphene from Hydrophobic to Hydrophilic int he Presence of an Electric Field. *J. Phys. Chem. C* **2012**, *116*, 19321−19326.

(6) Peles-Lemli, B.; Kollár, L.; Kunsági-Máté, S. Thermodynamics of the Solvation of Carbon Nanotubes: Exchange of Aniline to Primary Alcohols on the Surface of Carbon Nanotubes. *Fullerenes, Nanotubes, Carbon Nanostruct.* **2010**, *18*, 207−215.

(7) Peles-Lemli, B.; Matisz, G.; Kelterer, A. M.; Fabian, W. M. F.; Kunsági-Máté, S. Noncovalent Interaction between Aniline and Carbon Nanotubes: Effect of Nanotube Diameter and the Hydro-

gen-Bonded Solvent Methanol on the Adsorption Energy and the Photophysics. *J. Phys. Chem. C* **2010**, *114*, 5898−5905.
(8) Li, H.; Nie, J. C.; Kunsági-Máté, S. Modified Dispersion of Functionalized Multi-Walled Carbon Nanotubes in Acetonitrile. *Chem. Phys. Lett.* **2010**, *492*, 258−262.
(9) Li, H.; Petz, A.; Yan, H.; Nie, J. C.; Kunsági-Máté, S. Morphology Dependence of Raman Properties of Carbon Nanotube Layers Formed on Nanostructured CeO_2 Films. *J. Phys. Chem. C* **2011**, *115*, 1480−1483.
(10) Li, H.; Nie, J. C.; Kunsági-Máté, S. EtOH Induced Formation of Nanographite Fractions and their Reorganization on Nanostructured CeO_2 Films. *Chem. Phys. Lett.* **2012**, *531*, 183−187.
(11) Li, H.; Nie, J. C.; Li, J. C.; Kunsági-Máté, S. Ethanol Induced Formation of Graphene Fractions Suspended in Acetonitrile. *Carbon* **2013**, *54*, 495−497.
(12) Kunsági-Máté, S.; Nie, J. C. Entropy-driven Adsorption of Carbon Nanotubes on (0 0 1) and (1 1 1) Surfaces of CeO_2 Islands Grown on Sapphire Substrate Surf. *Science* **2010**, *604*, 654−659.
(13) Zhao, Y.; Schultz, Y. E.; Truhlar, D. G. Design of Density Functionals by Combining the Method of Constraint Satisfaction with Parametrization for Thermochemistry, Thermochemical Kinetics, and Noncovalent Interactions. *J. Chem. Theory Comput.* **2006**, *2*, 364−382.
(14) Zhao, Y.; Truhlar, D. G. Density Functionals with Broad Applicability in Chemistry. *Acc. Chem. Res.* **2008**, *41*, 157−167.
(15) Zheng, J.; Ren, Z.; Gou, P.; Fang, L.; Fan, J. Diffusion of Li^+ ion on Graphene: A DFT Study. *Appl. Surf. Sci.* **2011**, *258*, 1651−1655.
(16) Frisch, M. J.; et al. *Gaussian 09*, revision C.01; Gaussian, Inc.: Wallingford, CT, 2009.
(17) *HyperChem Professional 7*; HyperCube: Gainesville, FL, 2002.
(18) Tournus, F.; Charlier, J. - C. Ab Initio Study of Benzene Adsorption on Carbon Nanotubes. *Phys. Rev. B* **2005**, *71*, 165421.
(19) Efremenko, I.; Sheintuch, M. Predicting Solute Adsorption on Activated Carbon: Phenol. *Langmuir* **2006**, *22*, 3614−3621.
(20) Gómez, B.; Martínez-Magadán, J. M. A Theoretical Study of Dibenzothiophene Absorbed on Open-Ended Carbon Nanotubes. *J. Phys. Chem. B* **2005**, *109*, 14868−14875.
(21) Wang, Y.; Bu, Y. Noncovalent Interactions between Cytosine and SWCNT: Curvature Dependence of Complexes via $\pi\cdots\pi$ Stacking and Cooperative CH$\cdots\pi$/NH$\cdots\pi$. *J. Phys. Chem. B* **2007**, *111*, 6520−6526.
(22) Ma, L.; Wang, J.; Ding, F. Recent Progress and Challenges in Graphene Nanoribbon Synthesis. *Chem. Phys. Chem.* **2013**, *14*, 47−54.
(23) Dai, Q. Q.; Zhu, Y. F.; Jiang, Q. Electronic and Magnetic Engineering in Zigzag Graphene Nanoribbons Having a Topological Line Defect at Different Positions with or without Strain. *J. Phys. Chem. C* **2013**, *117*, 4791−4799.
(24) Umadevi, D.; Sastry, G. N. Molecular and Ionic Interaction with Graphene Nanoflakes: A Computational Investigation of CO_2, H_2O, Li, Mg, Li^+, and Mg^{2+} Interaction with Polycyclic Aromatic Hydrocarbons. *J. Phys. Chem. C* **2011**, *115*, 9656−9667.
(25) Tachikawa, H.; Shimizu, A. Diffusion Dynamics of the Li+ Ion on a Model Surface of Amorphous Carbon: A Direct Molecular Orbital Dynamics Study. *J. Phys. Chem. B* **2005**, *109*, 13255−13262.
(26) Suzuki, T.; Hasegawa, T.; Mukai, S. R.; Tamon, H. A Theoretical Study on Storage States of Li Ions in Carbon Anodes of Li Ion Batteries using Molecular Orbital Calculations. *Carbon* **2003**, *41*, 1933−1939.
(27) Uthaisar, C.; Barone, V. Edge Effects on the Characteristics of Li Diffusion in Graphene. *Nano Lett.* **2010**, *10*, 2838−2842.
(28) Wang, Z. Alignment of Graphene Nanoribbons by an Electric Field. *Carbon* **2009**, *47*, 3050−3053.
(29) Lee, H.; Kim, S.; Ihm, J.; Son, Y. W.; Choi, H. J. Field-induced Recovery of Massless Dirac Fermions in Epitaxial Graphene on SiC. *Carbon* **2011**, *49*, 2300−2305.
(30) Glendening, E. D.; Reed, A. E.; Carpenter, J. E.; Weinhold, F. NBO, version 3.1; Gaussian, Inc.: Wallingford, CT, 2009.
(31) Tachikawa, H.; Shimizu, A. Density functional theory (DFT) study on the effects of Li^+ doping on electronic states of graphene. *J. Power Source* **2010**, *195*, 6148−6152.

Available online at www.sciencedirect.com
ScienceDirect
J. Biochem. Biophys. Methods 69 (2006) 113–119
JOURNAL OF biochemical and biophysical methods
www.elsevier.com/locate/jbbm

Determination of the thermodynamic parameters of the complex formation between malvidin-3-O-glucoside and polyphenols. Copigmentation effect in red wines

Sándor Kunsági-Máté [a,*], Kornélia Szabó [a], Martin P. Nikfardjam [b], László Kollár [c]

[a] Department of General and Physical Chemistry, University of Pécs, Ifjúság 6, H-7624, Pécs, Hungary
[b] State Research Institute for Viticulture and Pomiculture, Am Traubenplatz 5, D-74189, Weinsberg, Germany
[c] Department of Inorganic Chemistry, University of Pécs, Ifjúság 6, H-7624, Pécs, Hungary

Received 24 November 2005; received in revised form 16 March 2006; accepted 26 March 2006

Abstract

The thermodynamics of the molecular association process between the malvidin-3-O-glucoside and a series of polyphenol derivatives (called 'copigmentation' in food chemistry) were studied in aqueous media. The Gibbs free energy, enthalpy and entropy values were determined by the fluorometric method. A combination of the Job's method with the van't Hoff theory was applied for data evaluation. The results show the exothermic character of the copigmentation process. The change of the enthalpy seems to be the same in every complexation step. However, the decreasing of the entropy term is higher at higher stoichiometries. As a result, the Gibbs free energy changes and, thus, the complex stability decreases quickly with increasing stoichiometry. Quantum-chemical investigation reveals the complexity of molecular interactions between malvidin and polyphenols, which is preferably based on π–π and OH–π interaction moderated by repulsive Coulomb-type interactions.
© 2006 Elsevier B.V. All rights reserved.

Keywords: Polyphenols; Copigmentation; π–π interaction

1. Introduction

The color of red wine is one of the most important quality parameters, which determines the sensorial evaluation significantly. Furthermore, it plays a key role in the decision-

* Corresponding author. Tel.: +36 72 503 600 (-4208); fax: +36 72 503 635.
E-mail address: kunsagi@ttk.pte.hu (S. Kunsági-Máté).

0165-022X/$ - see front matter © 2006 Elsevier B.V. All rights reserved.
doi:10.1016/j.jbbm.2006.03.014

making process of the consumer, who usually prefers red wines of deeper hue. Therefore, loss of the original wine color during storage should be avoided as much as possible. The color of the wine is affected by many parameters, among them copigmentation is of overriding importance [1]. During copigmentation weak interactions are formed between the colored anthocyanins and colorless compounds (so-called copigments) resulting in a sandwich-type structure. During complex formation the equilibrium between the cromenol (colorless species) and the dark-red flavylium ion is shifted towards the latter one [2]. Consequently, the color of wine gets deeper [3–5]. Furthermore, red clover isoflavonoids were found to be anthocyanin color enhancing agents in muscadine wine and juice [6]. Due to their attractive colors, anthocyanins are the most known natural colorants, however they have stability problems [7,8]. The copigmentation is significantly affected by temperature and the complex equilibrium was also found to be sensitive to pH.

In the present work we examined the thermodynamics of the molecular association process between various polyphenols (**2a**–**2e**) and malvidin-3-O-glucoside (**1**) (Fig 1). Our investigations were focused on the determination of the thermodynamic properties of the copigmentation process, i.e. on Gibbs free energy, enthalpy and entropy values. These were measured by means of methods already applied in our lab [9,10]. Photoluminescence (PL) and quantum-chemical investigations were performed and a combination of the Job's method with the van't Hoff theory was applied for data evaluation.

2. Materials and methods

2.1. Chemicals

Anthocyanin: malvidin-3-O-glucoside: 1 MW = 494.87.

Colorless polyphenols: **2a**: caffeic acid, MW = 180.16; **2b**: catechin, MW = 290.28; **2c**: ellagic acid, MW=302.20; 2d: rutin (quercetin-3-O-rutinosid), MW = 610.53 and **2e**: procyanidin B2 (epicatechin–(4β-8)–epicatechin, MW = 610.53).

All polyphenol standards were purchased from Extrasynthese (Genay, France) and used without further purification.

2.2. Experimental method

In order to investigate the interaction of compound **1** with compounds **2a**–**2e**, 1 g/dm^3 stock solutions were prepared in a model wine solution at pH 3.2 and the PL spectra were recorded. To determine the stoichiometry of the complexes and the thermodynamic parameters of the complex formation, 1 g/dm^3 stock solutions of malvidin-3-O-glucoside and the stock solutions of one of the polyphenols from the series **2** were mixed at five different molar ratios. Concentration range is chosen according to the concentration of these materials found in natural grapes [11,12]. The measurements were carried out at three different temperatures (15, 25, and 35 °C) and the ratios of the change obtained in the PL peak of **1** under the effect of one of the polyphenols were plotted against the molar fraction of malvidin-3-O-glucoside (Fig. 2).

The PL measurements were performed on a Fluorolog τ3 spectrofluorometric system (Jobin–Yvon/SPEX). For data collection a photon counting method with 0.1 s integration-time was used. A 1 mm layer thickness of the fluorescent probes with right angle detection was used to eliminate the inner filter effect.

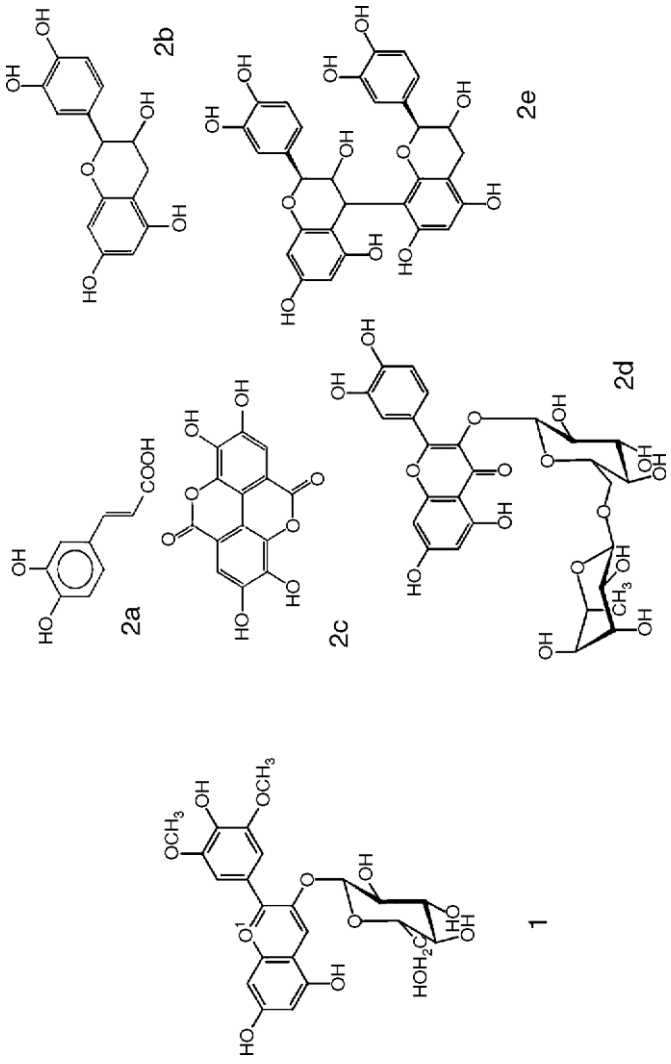

Fig. 1. Interaction of malvidin-3-O-glucoside (**1**) and various polyphenols (**2a–2e**) were investigated in this work.

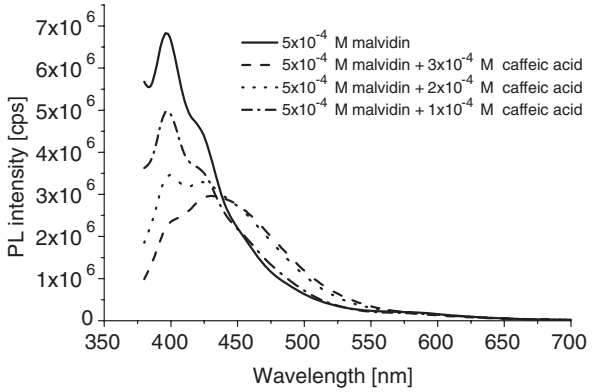

Fig. 2. Change of the fluorescence spectra of **1** in the presence of 2e.

2.3. Data evaluation

To experimentally determine the thermodynamic properties, the Job's method was applied [5,6]. The thermodynamic parameters associated to the individual complexation steps were determined from the Job's curves by an iterative solution of Eq. (1) using the expression of K_i values from Eq. (2).

$$\begin{aligned}
[P]_0 &= [P] + K_1[P][M] \\
&\quad + 2K_1K_2[P]^2[M] + K_1K_2'[P][M]^2 \\
&\quad + 2K_1K_2'K_3[P]^2[M]^2 + 2K_1K_2K_3'[P]^2[M]^2 \\
&\quad + 2K_1K_2'K_3K_4'[P]^2[M]^3 + 3K_1K_2K_3'K_4[P]^3[M]^2 + \ldots \\
[M]_0 &= [M] + K_1[P][M] \\
&\quad + K_1K_2[P]^2[M] + 2K_1K_2'[P][M]^2 \\
&\quad + 2K_1K_2'K_3[P]^2[M]^2 + 2K_1K_2K_3'[P]^2[M]^2 \\
&\quad + 3K_1K_2'K_3K_4'[P]^2[M]^3 + 2K_1K_2K_3'K_4[P]^3[M]^2 + \ldots
\end{aligned} \tag{1}$$

$$\ln K = -\frac{\Delta G}{RT} = -\frac{\Delta H}{RT} + \frac{\Delta S}{R} \tag{2}$$

2.4. Theoretical calculations

The equilibrium conformations of **1** and its complexes with polyphenol derivatives (**2a–2e**) were studied at DFT/B3LYP/6-31++G level by using the GAUSSIAN 03 package. The PCM (Polarizable Continuum Model) method was used to consider the solvent effect. The Fletcher–Reeves geometry optimization method was used for the investigation of the conformers. The temperature-dependent molecular dynamic simulations were performed with AMBER forcefield using the HyperChem Professional 7 code.

Table 1
Thermodynamic parameters of complexation of **1** with **2a–2e**

Stability constant (see Eq. (1))	Stoichiometry	Polyphenol interacting with malvidin (data for ΔH and ΔG are given in kJ/mol, ΔS is given in J/K^{-1} mol^{-1}, precision of ΔG is around ±0.7 kJ/mol)														
		Caffeic acid			Catechin			Ellagic acid			Procyanidin B_2			Rutin		
		ΔH	ΔS	ΔG	ΔH	ΔS	ΔG	ΔH	ΔS	ΔG	ΔH	ΔS	ΔG	ΔH	ΔS	ΔG
K_1	1:1	−57.3	−87	−31.9	−52.3	−112	−19.7	−55.4	−131	−17.3	−44.6	−111	−12.3	−47.2	−63	−28.9
K_2	2:2	−48.3	−102	−18.6	−49.6	−117	−15.6	−51.3	−138	−11.1	−42.3	−114	−9.1	−44.6	−70	−24.2
K_3	3:3	−48.2	−120	−13.2	−49.7	−123	−13.9	−51.5	−146	−9.0	−42.1	−117	−8.0	−44.4	−78	−21.7
K_4	4:4	−48	−137	−8.1	−49.6	−128	−12.4	−51.2	−154	−6.4	−42	−121	−6.8	−44.3	−86	−19.3
K_5	5:5	−48.1	−149	−4.7	−49.4	−135	−10.1	−51	−161	−4.2	−41.8	−124	−5.7	−44.1	−93	−17.0
K_6	6:6				−49.2	−140	−8.5	−50.8	−170	−1.3	−41.6	−128	−4.4	−43.9	−101	−14.5
K_7	7:7				−49.5	−146	−7.0				−41.6	−131	−3.5	−43.9	−110	−11.9
K_8	8:8				−49.7	−151	−5.8							−43.7	−121	−8.5
K_9	9:9				−49.2	−156	−3.8							−43.6	−131	−5.5
K_{10}	10:10													−43.6	−140	−2.9

Only parameters for stoichiometric complexes are listed for clarity.

3. Results

Table 1 summarizes the thermodynamic parameters of the complex formation of **1** with **2a–2e**. It can be clearly seen that the Gibbs free energy changes, therefore the stability of the complexes are different when different polyphenol molecules associate with the malvidin-3-O-glucoside. In all examined cases, the enthalpy decreased in the second coordination step compared to the first coordination step. At all higher coordination steps the changes in enthalpy are nearly the same. However, the entropy value is negative showing a more ordered structure after the complex was formed, which ultimately decreases the Gibbs free energy.

4. Discussion

To understand the consequences raised from the decrease of the Gibbs free energy at higher coordination steps we have to consider the following: using the equipartition theorem, about 3.5 kJ/mol kinetic energy can be assumed for the molecules at 289 K, which is a typical temperature for wine storage. As a consequence, the decrease of the Gibbs free energy compared to the kinetic energy of the particle limits the size of the particles formed during the copigmentation effect.

The entropy of the complexation decreases the stability of the complex. Furthermore, our experiments show that the entropy was on the rise with increasing number of the coordination steps showing formation of more and more ordered structures. This is probably the most important characteristic limiting the size of the complex being formed.

We explain these characteristics as follows: the degree of freedom of the molecules during complexation decreases mainly because of the inhibited rotation of these molecules when they attach to an already existing complex. This inhibition gains weight with increasing size of the complex. Thus, the change of order of the total system slightly increases with the size of the complex formed. As a result, the change in entropy slightly increases. Among several known interactions between flavanol and anthocyanin molecules [12,13], our quantum-chemical investigations highlight the importance of a π-electron rich character of the colorless copigments for a successful association with the malvidin-3-O-glucoside molecule. This property suggests that the complex formation between malvidin and family of polyphenols investigated here is preferably based on a π–π interaction [4].

Furthermore, the results show that mainly completely planar polyphenols, such as rutin, are better copigments due to the complete overlapping of the π-bonds between malvidin and the copigment. Non-planar copigments, such as catechin or procyanidin B_2, despite their large size are not able to stabilize the positive charge of the flavylium ion of the malvidin in the same magnitude like rutin due to their sterical arrangement. In the case of smaller, yet still planar phenols, such as caffeic acid, the size of the copigment plays the crucial role. Due to its smaller size, caffeic acid cannot completely stabilize the positive charge on the flavylium ion and, thus, shows a weaker copigmentation than rutin or the flavan-3ols catechin and procyanidin B_2. We can, thus, conclude that sterical arrangement and size of the copigment play an important role in the stabilization of the flavylium ion.

5. Conclusion

The thermodynamics of the molecular association process between polyphenols and malvidin-3-O-glucoside were investigated by fluorometric and quantum-chemical methods. The higher the

number of associated molecules, the smaller the interaction and, hitherto, the change in enthalpy between each individual malvidin-3-O-glucoside and polyphenol molecule. Our results show that the increased change in entropy is responsible for the decreased stability of the complexes formed with higher stoichiometry. This property limits the size of the complex. The efficiency of the copigmentation effect depends mainly on the size and the sterical arrangement of the copigment. Our method provides useful means to select those phenols, which possess the most pronounced copigmentation effect. These results can hopefully be exploited in winemaking to extract the most efficient copigments (phenols) from grape berry skin. Beyond that, application of the results during the fining process, i.e. avoiding harmful influence of fining agents on color stabilization and on undesired changes in color hue, are possible.

References

[1] Boulton R. The copigmentation of anthocyanins and its role in the color of red wine: a critical review. Am J Enol Vitic 2001;52:67–87.
[2] Borkowski T, Szymusiak H, Gliszczyjska-Swigio A, Tyrakowska B. The effect of 3-O-β-glucosylation on structural transformations of anthocyanidins. Food Res Int 2005;38:1031–7.
[3] Markovic JMD, Petranovic NA, Baranac JM. The copigmentation effect of sinapic acid on malvin: a spectroscopic investigation on colour enhancement. J Photochem Photobiol B Biol 2005;78:223–8.
[4] Berké B, de Freitas AP. Influence of procyanidin structures on their ability to complex with oenin. Food Chem 2005;90:453–60.
[5] Bloomfield DG, Heatherbell DA, Pour Nikfardjam MS. Effect of p-coumaric acid on the color in red wine. Mitt Klosterneuburg 2003;53:195–8.
[6] Talcott ST, Peele JE, Brenes CH. Red clover isoflavonoids as anthocyanin color enhancing agents in muscadine wine and juice. Food Res Int 2005;38:1205–12.
[7] Giusti MM, Wrolstad RE. Acylated anthocyanins from edible sources and their applications in food systems. Biochem Eng J 2003;14:217–25.
[8] Pazmino-Duran AE, Giusti M, Wrolstad RE, Gloria MB. Anthocyanins from oxalis triangularis as potential food colorants. Food Chem 2001;75:211–6.
[9] Kunsági-Máté S, Szabó K, Lemli B, Bitter I, Nagy G, Kollár L. Host–guest interaction between water-soluble calix[6]arene hexasulfonate and *p*-nitrophenol. Thermochim Acta 2005;425:121–6.
[10] Kunsági-Máté S, Szabó K, Bitter I, Nagy G, Kollár L. Unexpected effect of charge density of the aromatic guests on the stability of calix[6]arene phenol host guests complexes. J Phys Chem A 2005;109(23):5237–42.
[11] Jeong ST, Goto-Yamamoto N, Hashizume K, Esaka M. Expression of the flavonoid 3′-hydroxylase and flavonoid 3′,5′-hydroxylase genes and flavonoid composition in grape (*Vitis vinifera*). Plant Sci 2006;170:61–9.
[12] Gómez-Plaza E, Minano A, López-Roca JM. Comparison of chromatic properties, stability and antioxidant capacity of anthocyanin-based aqueous extracts from grape pomace obtained from different vinification methods. Food Chem 2006;97:87–94.
[13] Salas E, Le Guernevé C, Fulcrand H, Poncet-Legrand C, Cheynier V. Structure determination and colour properties of a new directly linked flavanol–anthocyanin dimer. Tetrahedron Lett 2004;45:8725–9.

ELSEVIER

Analytica Chimica Acta 428 (2001) 301–307

ANALYTICA CHIMICA ACTA

www.elsevier.com/locate/aca

Host–guest interaction of calixarene molecules with neutral benzotrifluorides Comparison of luminescence spectral data with results of model calculations relating to complex formation

Sándor Kunsági-Máté [a], Géza Nagy [a,c,*], László Kollár [b,c]

[a] *Department of General and Physical Chemistry, University of Pécs, 7624 Pécs, Ifjúság 6, Hungary*
[b] *Department of Inorganic Chemistry, Faculty of Sciences, University of Pécs, 7624 Pécs, Ifjúság 6, Hungary*
[c] *MTA-PTE Research Group for Chemical Sensors, 7624 Pécs, Ifjúság 6, Hungary*

Received 26 April 2000; received in revised form 2 October 2000; accepted 9 October 2000

Abstract

The 'host' properties of calix[4]arene and 4-*tert*-butyl-calix[6]arene molecules under the effect of different neutral pesticide related trifluoromethyl-benzene molecules as 'guests' have been investigated by spectrofluorometric method. Significant dependence of the photoluminescence behaviour of calixarene derivatives on the structure of interactive molecules was detected in chloroform and dimethylformamide solvent. The formation of stable host–guest complexes was checked by quantum-chemical method. The results show that the photoluminescence signal reflects the supramolecular interaction. This makes calixarenes promising candidates as host molecules to be used in chemical sensors measuring neutral organic molecules.
© 2001 Elsevier Science B.V. All rights reserved.

Keywords: Calixarenes; Organic guests; Photoluminescence; Chemical sensors

1. Introduction

It is a common sense that the function of a selective chemical sensor is based on two equally important steps, on the selective recognition and on the signal transduction. Supramolecular interactions between host molecules incorporated in a sensor and an analyte acting as guest could be used successfully in sensor research.

Calixarenes because of their well defined frame and chemically stable intermolecular cavity of tunable size and co-ordination selectivity are frequently selected as host molecules in sensor research [1,2] or in separation sciences [3–5].

Calix[4]arene ester was successfully used as active ionophore incorporated in elasticised PVC membrane preparing cesium-selective potentiometric electrodes [6]. Kimura and co-workers prepared sodium selective electrode [7] and ion selective field effect transistors [8] with calix[4]arene ionophore. Calixarene based solid state sodium ion selective electrode was also reported [9]. Calix[4]arene containing PVC membrane showed amine and alkaline ion selectivity [10].

* Corresponding author. Tel.: +36-72-327622 (-4681); fax: +36-72-327622 (-4680).
E-mail address: g-nagy@ttk.pte.hu (G. Nagy).

0003-2670/01/$ – see front matter © 2001 Elsevier Science B.V. All rights reserved.
PII: S0003-2670(00)01237-X

The application of calixarenes in electroanalysis was reviewed by O'Connor et al. [11].

For an ionic species measuring chemical sensors — as it can be seen — often potentiometric signal transduction is used. However, considerable interest has been focused to prepare calixarene ionophore based optodes [12–14].

Lynch and co-workers investigated the interactions of calixarene ionophore derivatives with metal ions in solution using fluorescence and absorption spectroscopy [15]. On the other hand, Schierbaum and co-workers studied the interaction of calixarene derivative containing layers with organic molecules using experimental techniques and force field calculations [16].

Since calixarene derivatives can form host–guest type complexes with neutral organic molecules, it is likely that they can be used for selective molecular recognition in chemical sensors measuring neutral species, too. Therefore, it was obvious to investigate the possible signal transduction mechanisms. Since fluorescence generation is a very sensitive signal forming technique, in our laboratories studies have been carried out with different calixarene derivatives and organic guest molecules to collect data about the influence of the supramolecular interaction on the fluorescence signal. It was hoped that comparing the fluorescence spectroscopic data with interaction energy values obtained by model calculation can be used in designing selective host molecules. As model guest molecules different trifluoromethylbenzene derivatives possessing electron-withdrawing groups-EWG-were selected. It could be expected that the electron-deficiency in their aromatic ring might give a chance for the interaction with the relatively electron-rich calixarene aromatic moieties. However, the analysis of these neutral molecules can be of practical importance because of their pesticides relating structure [17]. In this short paper presented here, our preliminary results are summarised.

2. Chemicals, apparatus and methods

Calixarenes (calix[4]arene, MW = 424.8, 99% and 4-*tert*-butyl-calix[6]arene, MW = 973.39, 99%) were obtained from Aldrich Chemical Co. and were used as received. Benzotrifluoride derivatives were obtained from Budapest Chemical works Co. Ltd. Dimethylformamide (Reanal, Hungary) and chloroform (Fluka) solvents were distilled freshly before the measurements.

Highly sensitive Fluorolog τ3 spectrofluorometric system was used to investigate the photoluminescence (PL) spectral behaviour of the different solutions prepared. For data collection photon counting method with 0.2 s integration time was used. Excitation and emission bandwidths were set to 2 nm. All measurements were carried out at 20°C.

The equilibrium conformation of calixarenes and benzotrifluoride derivatives and the interaction energy of the studied species were described at *ab initio* level using HyperChem Professional 5.1 program package.

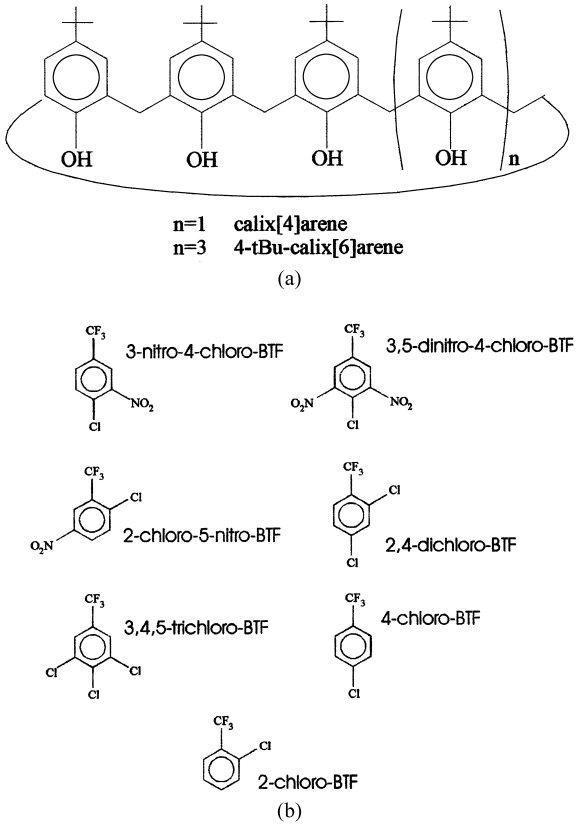

Fig. 1. Calixarenes (a) as host and benzotrifluoride derivatives (b) as guests were chosen for this model studies (BTF stands for benzotrifluoride).

For the calculations 6–31 G Gaussian-type basis set with Fletcher–Reeves geometry optimisation method were used. The solvent effect of chloroform and DMF was described by TIP3P method (HyperChem package) and by Onsager method (Gaussian 94 package), respectively.

3. Results and discussion

Since the aromatic ring of calixarenes can be considered electron rich due to the slightly positive inductive effects of *tert*-butyl and methylene groups, electron deficient neutral aromatics as guest

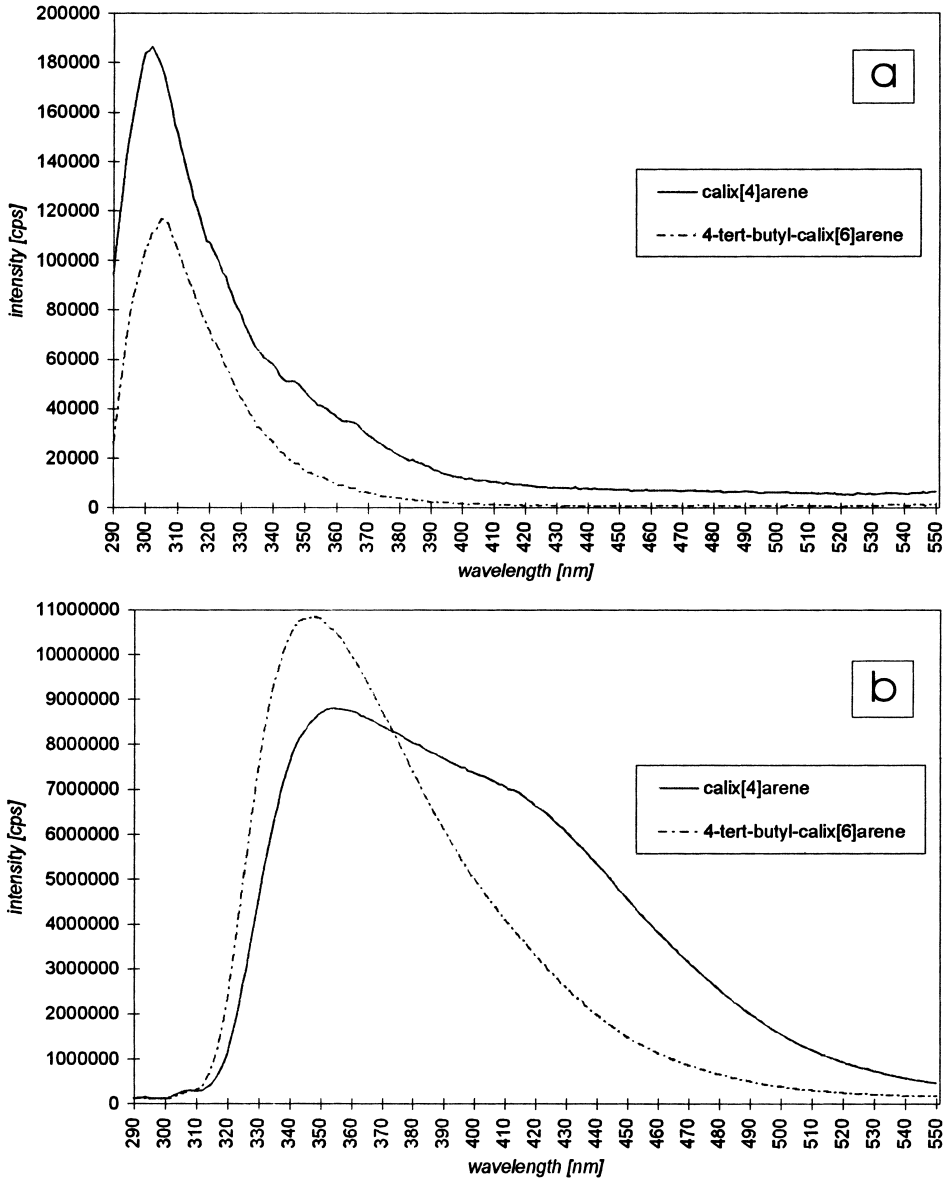

Fig. 2. PL spectra of calix[4]arene and 4-*tert*-butyl-calix[6]arene dissolved in chloroform (a) and dimethylformamide (b) solvents using 280 nm for excitation.

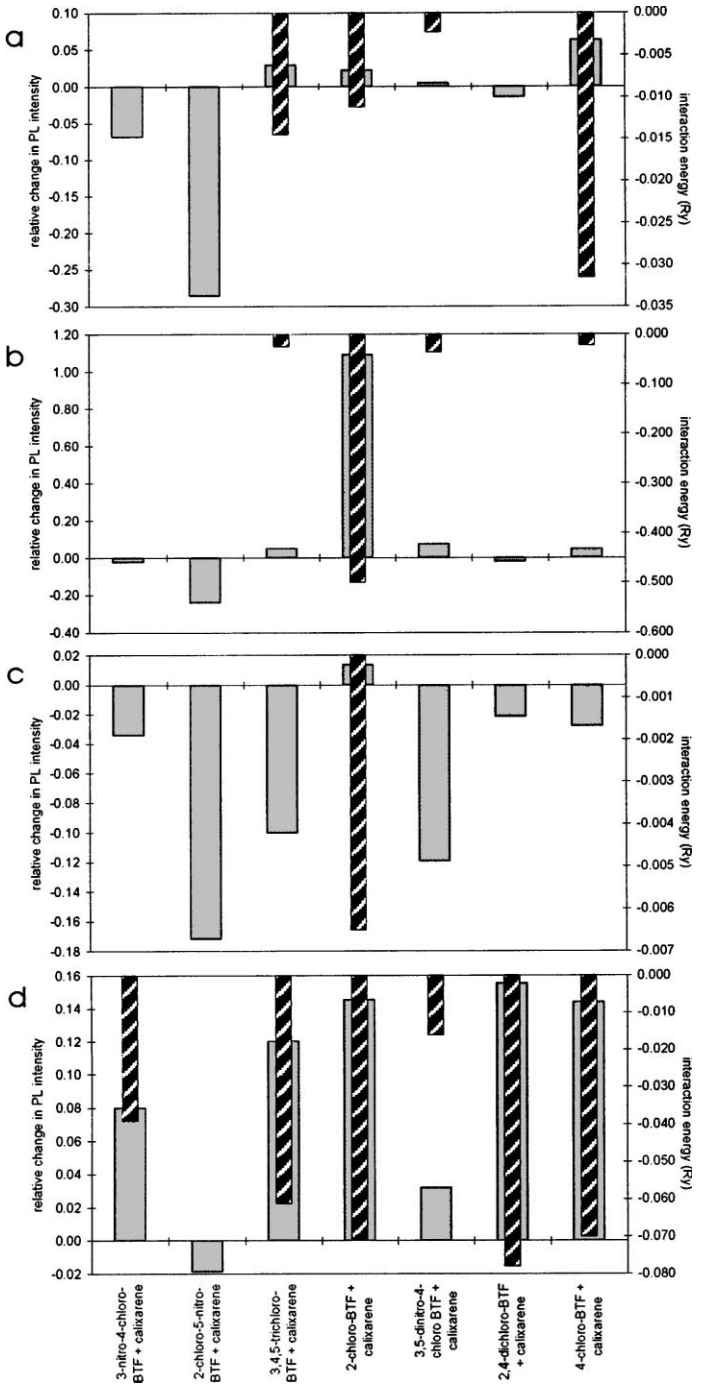

Fig. 3. Relative changes in PL intensity of the 1:1 calixarene:benzotrifluoride mixtures and the interaction energy of the corresponding stable complexes. (a) Calix[4]arene + BTF in chloroform; (b) 4-*tert*-butyl-calix[6]arene + BTF in chloroform; (c) calix[4]arene + BTF in dimethylformamide; (d) 4-*tert*-butyl-calix[6]arene + BTF in dimethylformamide.

molecules were chosen for model studies. The structures of molecules investigated are shown in Fig. 1. Preliminary experiments indicated that nitro- and chloro-substitued benzotrifluorides (3-nitro-4-chloro-benzotrifluoride (**1**), 2-chloro-5-nitro-benzotrifluoride (**2**), 3,4,5-trichloro-benzotrifluoride (**3**), 2-chloro-benzotrifluoride (**4**), 3,5-dinitro-4-chloro-benzotrifluoride (**5**), 2,4-dichloro-benzotrifluoride (**6**), 4-chloro-benzotrifluoride (**7**)) interact with calix[4]arene and 4-*tert*-butyl-calix[6]arene according to photoluminescence spectra.

Fig. 2 shows the PL spectra of calix[4]arene and 4-*tert*-butyl-calix[6]arene dissolved in chloroform (a) and dimethylformamide (b) solvents using 280 nm for excitation. In the case of dimethylformamide solvent, the peaks of spectra are shifted to the longer wavelength by about 40 nm. The calix[4]arene shows the higher light emission in chloroform and 4-*tert*-butyl-calix[6]arene shows the higher emission in DMF. On the other hand, the intensity of the emitted light is higher in case at both molecules in DMF. Most likely the difference between the permittivities of the two solvents is responsible for the changes of the band shape of the spectra.

In order to investigate the effect of interaction of the different benzotrifluoride derivatives 1:1 calixarene:benzotrifluoride solution of 10^{-4} M of the different species was prepared with the two different solvents and the PL spectra were recorded. Evaluating them it could be seen that the presence of the different benzotrifluorides induced some changes in the spectra. The shapes of the PL spectra of the mixtures were very similar to those of the PL spectra of the pure corresponding calixarene solution, however, significant changes of the intensities appeared in each cases. For certain benzotrifluorides, the intensity increased while in other cases it decreased. Since no light emission could be observed from 10^{-4} M solutions of the benzotrifluoride molecules using the same condition, it could be expected that the obtained spectral changes were induced by the changes of the optical properties of the calixarene species.

Fig. 3 shows the relative changes found in the PL intensity of calixarenes included by the effect of the different benzotrifluoride molecules studied. The relative change of PL intensity (ΔI_{rel}) shown in the bar graph were calculated by the following form:

$$\Delta I_{rel} = \frac{I_{mix} - I_{pure}}{I_{pure}}$$

where I_{mix} is the intensity maximum of the PL spectra of calixarene–benzotrifluoride mixture and I_{pure} is the intensity maximum of the spectra of pure calixarene solutions. The ΔI_{rel} values clearly indicate that the PL signal of the studied calixarenes is influenced by the molecular structures of benzotrifluoride derivatives being present. It also can be seen that the effect of uncharged benzotrifluoride molecules on the PL behaviour of calixarenes depends on the properties of the solvent.

The interaction between the calixarene and benzotrifluoride molecules proposed by PL studies, was examined by quantum-chemical method using the

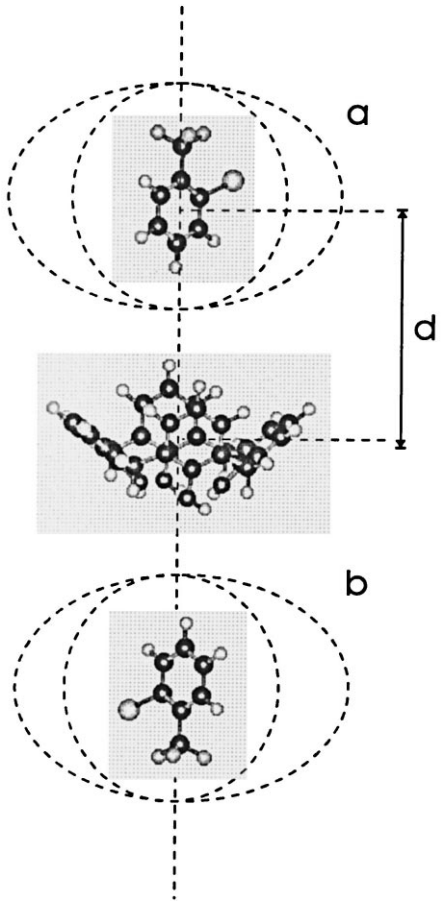

Fig. 4. The model for the calculation of interaction energy. *d* is the distance between the centres of gravity of the molecules.

HyperChem and Gaussian 94 packages. Doing so the interaction energy between the host calixarene and the guest benzotrifluoride molecules were calculated using the following procedure (for illustration see Fig. 4). The benzotrifluoride molecule was fixed with its centre of gravity on the symmetry axis C above (a) or below (b) of calixarene molecule, Fig. 4. Beginning from these initial conditions, the free rotation of benzotrifluoride molecules around its centre of gravity was allowed. In this model, the reaction path is given by the minimal total energy positions of the calixarene–benzotrifluoride system and it can be described by the distance between the centres of gravity of the two molecules. The total energies of the system are determined by *ab initio* calculations as mentioned above. When the stable conformation of calixarene–benzotrifluoride system found, full geometry optimisation were done for the complex and the total energy of the unforced state was used to determine the interaction energy E_{inter} using the following equation:

$$E_{\text{inter}} = E_{\text{syst}} - E_{\text{tot,calix}} - E_{\text{tot,BTF}}$$

where E_{syst} is the total energy of the calixarene–benzotrifluoride system, $E_{\text{tot, calix}}$ and $E_{\text{tot, BTF}}$ is the total energy of the separated calixarene and benzotrifluoride molecules, respectively.

Fig. 3 and Table 1 summarize the PL and quantum-chemical results. It can be seen clearly that the interaction energy (E_{inter}) shows negative values (indicating stable conformations) only in those cases when the relative change (ΔI_{rel}) in PL intensity are positive ($I_{\text{mix}} > I_{\text{pure}}$). The change in the PL intensity corresponds to the absolute value of the interaction energy. Model calculations did not find stable calixarene–benzotrifluoride complex for $I_{\text{mix}} > I_{\text{pure}}$ cases.

It turned out that calix[4]arene forms stable complexes with higher number of the BTF molecules studied in chloroform (**3**, **4**, **5** and **7**) than in dimethylformamide (**4**). It has been found also previously [18] that the solvent polarity has a great influence on the rate of conformational inversion and therefore on the predominating conformer under given conditions. In less polar solvents such as $CHCl_3$ the interconversion of the cone conformer was found very slow at low temperature. The hole of the cone conformer of calix[4]arene seems to be appropriate for the inclusion of benzotrifluorides of smaller sizes (**3**, **4**, **5**) with the exeption of **7**. We can postulate that in dimethylformamide the disruption of 'circular hydrogen bonding' takes place. This intramolecular hydrogen bonding at the 'low rim' is a contributing force in maintaining the calixarene in cone conformation. In the lack of the hydrogen bonding the aromatic rings become nearly

Table 1
The relative change (I_{rel}) in PL intensity of calixarene molecules in presence of benzotrifluoride derivatives and the interaction energy (E_{inter}) of calixarene–benzotrifluoride complexes

Calixarene	Benzotrifluoride	Chloroform solvent			Dimethylformamide solvent		
		Complex	ΔI_{rel}	E_{inter} (Ry)	Complex	ΔI_{rel}	E_{inter} (Ry)
Calix[4]rene	3-Nitro-4-chloro-BTF	No	−0.068390	>0	No	−0.034230	>0
	2-Chloro-5-nitro-BTF	No	−0.285670	>0	No	−0.171790	>0
	3,4,5-Trichloro-BTF	Yes	0.029294	−0.0145	No	−0.100320	>0
	2-Chloro-BTF	Yes	0.022640	−0.0112	Yes	0.013598	−0.0065
	3,5-Dinitro-4-chloro-BTF	Yes	0.004693	−0.0023	No	−0.119320	>0
	2,4-Dichloro-BTF	No	−0.013970	>0	No	−0.021720	>0
	4-Chloro-BTF	Yes	0.063336	−0.0316	No	−0.027970	>0
4-*Tert*-butyl-calix[6]arene	3-Nitro-4-chloro-BTF	No	−0.024840	>0	Yes	0.079852	−0.0391
	2-Chloro-5-nitro-BTF	No	−0.240240	>0	No	−0.018820	>0
	3,4,5-Trichloro-BTF	Yes	0.049012	−0.0251	Yes	0.120170	−0.0611
	2-Chloro-BTF	Yes	0.073883	−0.0361	Yes	0.145255	−0.0712
	3,5-Dinitro-4-chloro-BTF	No	−0.021500	>0	Yes	0.031662	−0.0161
	2,4-Dichloro-BTF	Yes	0.046391	−0.0231	Yes	0.155336	−0.0782
	4-Chloro-BTF	Yes	0.070868	−0.0352	Yes	0.143638	−0.0711

parallel, i.e. the size of the hole becomes smaller, and also the interconversion barrier decreases. As a consequence of that, the sterically more favoured **4** shows some effects only.

It is well-known from the temperature dependent NMR studies that 4-*tert*-butyl-calix[6]arene is more flexible than the cyclic tetramers even in less polar solvents [18]. Surprisingly, the same benzotrifluoride derivatives show interactions as in case of calix[4]-arene. Even more suprising is the fact, that practically all benzotrifluoride guest molecules seem to form inclusion complex with 4-*tert*-butyl-calix[6]arene in dimethylformamide. It validates that a 'plated loop' conformer must be stabilised by the interaction with the benzotrifluoride. Similarly, the interaction of phenolic OH groups with the solvent and the complexation of benzotrifluorides from the side of the 'upper rim' might result in a calixarene conformer which resembles much more to a basket-like hole than that obtained in $CHCl_3$.

4. Conclusion

The preliminary experimental results clearly indicate that the photoluminescence signal reflects the supramolecular host–guest interaction. It validates that calixarenes can be used as host molecules to gain sensor response detecting neutral substituted aromatics possessing electron-withdrawing groups (EWG). In the present stage, about 25% luminescence intensity change as signal has been observed. The high sensitivity of the luminescence detection can accurately measure relative intensity changes of this size. Further molecular engineering needed to develop practical sensors may result also in improved signal to noise ratio.

Acknowledgements

The financial support of Hungarian Scientific Research Fund (OTKA T023525, F020181), Hungarian National Committee of Technological Development (OMFB 97-20 MU0086) and Francelab Co. (France) are highly appreciated.

References

[1] P.L.H.M. Cobben, R.J.M. Egbernik, J.G. Bomer, P. Bergveld, W. Verboom, D.N. Reinhoudt, J. Am. Chem. Soc. 114 (1992) 10573.
[2] D.N. Reinhoudt, Sens. Actuators B 6 (1992) 179.
[3] J.-C. Bunzli, J.A. Harrowfield, in: J. Vicens, V. Bohmer (Eds.), Calixarenes: A Versatile Class of Macrocyclic Compounds, Kluwer, Boston, 1991.
[4] P. Munk, L.J. Feltl, Chromatography A 696 (1) (1995) 101.
[5] D. Shohat, E. Grushka, Anal. Chem. 66 (1994) 747.
[6] A. Cadogan, D. Diamond, M.R. Smyth, G. Svehla, M.A. McKervey, E.M. Seward, S.J. Harris, Analyst 115 (9) (1990) 1207.
[7] K. Kimura, T. Miura, M. Matsuo, T. Shono, Anal. Chem. 62 (14) (1990) 1510.
[8] K. Kimura, T. Matsuba, Y. Tsujimura, M. Yokoyama, Anal. Chem. 64 (1992) 2508.
[9] A. Gao, Z.Q. Cadogan, A. Lewenstam, A. Ivaska, D. Diamond, Anal. Chem. 64 (1992) 2496.
[10] K. Odashima, K. Yagi, K. Tahda, Y. Umezava, Anal. Chem. 65 (1993) 1074.
[11] K.M. O'Connor, D.W.M. Arrigan, G. Svehla, Electroanalysis 7 (1995) 205.
[12] Y. Kawabota, T. Mashiro, Y. Kitazaki, T. Imasaka, Sens. Actuators B B29 (1995) 135.
[13] M. Carrick, S.J. Harris, D. Diamond, Analyst 118 (9) (1993) 1127.
[14] W.H. Chan, A.W. Lee, D.W. Kwong, W.L. Tam, K.M. Wang, Analyst 121 (4) (1996) 531.
[15] B.M. Lynch, M.M. Ryan, B.S. Creaven, G. Barrett, M.A. McKervey, S.J. Harris, Anal. Proc. (London) 30 (1993) 150.
[16] K.D. Schierbaum, A. Gerlach, W. Goepel, W.M. Mueller, F. Voegtle, A. Dominik, H.J. Roth, Fresenius' J. Anal. Chem. 349 (1994) 372.
[17] E. Wegler, Chemie der Pflanzenschutz und Schädlingsbekämpfungsmittel, Band 5, Springer, Berlin, Heidelberg, New York, 1977, Pages 73–80 and 401–407.
[18] C.D. Gutsche, in: J.F. Stoddart (Ed.), Calixarenes: Monographs in Supramolecular Chemistry, Royal Society of Chemistry, Cambridge, 1989, pp. 90–97.

DENTAL MATERIALS 35 (2019) 217–228

Available online at www.sciencedirect.com

ScienceDirect

journal homepage: www.intl.elsevierhealth.com/journals/dema

Effect of exposure time and pre-heating on the conversion degree of conventional, bulk-fill, fiber reinforced and polyacid-modified resin composites

Edina Lempel[a,*], *Zsuzsanna Őri*[b,c], *József Szalma*[d], *Bálint Viktor Lovász*[a], *Adél Kiss*[a], *Ákos Tóth*[e], *Sándor Kunsági-Máté*[b,c]

[a] *Department of Restorative Dentistry and Periodontology, University of Pécs, Pécs, Hungary*
[b] *Department of General and Physical Chemistry, University of Pécs, 6 Ifjúság Street, Pécs, H-7624, Hungary*
[c] *János Szentágothai Research Center, 20 Ifjúság Street, Pécs, H-7624, Hungary*
[d] *Department of Oral and Maxillofacial Surgery, University of Pécs, Pécs, Hungary*
[e] *Faculty of Sciences, University of Pécs Pécs, Hungary*

ARTICLE INFO

Article history:
Received 19 May 2018
Received in revised form
3 October 2018
Accepted 14 November 2018

Keywords:
Resin based composite
Degree of conversion
Pre-heating
Exposure time

ABSTRACT

Objective. To determine the degree of conversion (DC) of different type of resin-based composites (RBC) in eight-millimeter-deep clinically relevant molds, and investigate the influence of exposure time and pre-heating on DC.

Methods. Two-millimeter-thick samples of conventional sculptable [FiltekZ250 (FZ)], flowable [Filtek Ultimate Flow (FUF)] and polyacid-modified [Twinky Star Flow (TS)] RBCs, and four-millimeter-thick samples of flowable bulk-fill [Filtek Bulk Fill Flow (FBF), Surefil SDR (SDR)] and sculptable fibre-reinforced [EverX Posterior (EX)] RBCs were prepared in an eight-millimeter-deep mold. The RBCs temperature was pre-set to 25, 35 and 55 °C. The RBCs were photopolymerized with the recommended and its double exposure time. The DC at the top and bottom was measured with micro-Raman spectroscopy. Data were analyzed with ANOVA and Scheffe post-hoc test ($p < 0.05$).

Results. The differences in DC% between the top/bottom and the recommended/extended exposure time were significant for the materials, except SDR (64.5/63.0% and 67.4/63.0%). FUF (69.0% and 53.4%) and TS (64.9% and 60.9%) in 2 mm provided higher DC% at the top and bottom with the recommended curing time, compared to the other materials, except SDR. Pre-heating had negative effect on DC at the bottom in flowable RBCs (FUF: 48.9%, FBF: 36.7%, SDR: 43%, TS: 54.7%). Pre-heating to 55 °C significantly increased the DC% in fibre-reinforced RBC (75.0% at the top, 64.7% at the bottom).

Significance. Increased exposure time improves the DC for each material. Among bulk-fills, only SDR performed similarly, compared to the two-millimeter-thick flowable RBCs. Pre-heating of low-viscosity RBCs decreased the DC% at the bottom. Pre-heating of fibre-reinforced RBC to 55 °C increased the DC% at a higher rate than the extended curing time.

© 2018 The Academy of Dental Materials. Published by Elsevier Inc. All rights reserved.

* *Corresponding author at*: Department of Restorative Dentistry and Periodontology, University of Pécs, 5. Dischka Gy Street, Pécs, H-7621 Hungary.
E-mail address: lempel.edina@pte.hu (E. Lempel).

https://doi.org/10.1016/j.dental.2018.11.017

0109-5641/© 2018 The Academy of Dental Materials. Published by Elsevier Inc. All rights reserved.

1. Introduction

The marginal seal is an essential factor in the longevity of a dental restoration. Leakage at the deep gingival margin can lead to secondary caries development resulting in the failure of the restoration and compromising the health of the vital pulp tissue [1]. In root canal treated teeth the penetration of microorganisms through the coronal orifice of the root canal may also cause recontamination and subsequent failure of the endodontic treatment [2].

Resin-based composite restorative materials (RBC) are widely used among dentists as the most common restorative material. Evolution in both filler and polymer technology led to a wide selection of materials that provide the adequate characteristics required for each clinical situation [3]. Besides the conventional RBCs, bulk-fill and fiber reinforced RBCs are also available in the market as improved materials. Low and high viscosity bulk filling composites usually have higher translucency, and sometimes a modified initiator system to ensure better curing in depth, as compared to conventional composites. These materials are recommended to use in 4 mm or even 5 mm in thickness without stratification [4], and promise adequate curing depth, physical and mechanical properties. Many bulk-fill composite resins have been investigated regarding different parameters like mechanical features, degree of conversion, polymerization stress or microleakage. On the one hand, such studies have shown that bulk-fill composite resins have similar physical and chemical properties as conventional RBCs [5–8], on the other hand, bulk filling RBCs were found to have lower mechanical properties, higher shrinkage rate and lower degree of conversion in the recommended 4 mm thickness compared to 2 mm of the conventional RBC's [9–11].

Fiber reinforcement of conventional dental composites were also introduced with the aim of enhancing their physical properties [12]. The enhancement was due to the stress transfer from the matrix to the fibers depending on the fibers length and diameter, leading to high resistance to fracture [13,14]. Besides the above mentioned developments, manufacturers are looking for continuous improvements to eliminate disadvantageous properties, like the polymerization shrinkage and the inadequate rate of polymerization. The presence of the aforementioned drawbacks adversely affects the marginal or coronal leakage. To avoid it, flowable RBCs could be used at the gingival margins of a proximal cavity or as a barrier to seal the orifices of the root canals [15]. Flowable RBCs have better adaptation to the cavity walls owing to their high tooth surface wetting ability, ensuring penetration into all irregularities [16].

Pre-heating of RBC can also decrease microleakage. Increasing the polymerization temperature leads to lower viscosity thus increasing the fluidity and improving the adaptation of the RBC material to the cavity [17,18]. Pre-heating in turn results in greater mobility of monomer molecules within the resin matrix, enhances free radical formation, which results in a higher value of the DC and shorten curing time [19,20]. The increased mobility of monomers at elevated temperature can lead to delayed autodeceleration stage of the polymerization reaction thus contribute to increased monomer conversion [21]. In addition, pre-heating significantly reduces the generation of shrinkage forces in both high-viscosity bulk-fill and conventional resin composites [22].

Clinical restoring procedures meet complex cavity shapes which could be challenging. Occasionally, cavity preparations that are 7–10 mm deep with a narrow orifice, as well as the angulation of the light curing tip may influence the polymerization rate of RBCs. Incomplete curing can lead to the early degradation, wear of the RBC restoration and also affect the functional durability, eventually leading to failure [23]. Light-curing an RBC is a complex process, as the depth of cure is affected by material composition, layer thickness, irradiance, curing time and variety of other factors [24]. For adequate polymerization the conventional RBC should receive a radiant exposure within the 16–24 J/cm^2 range [25]. This radiant exposure or energy density is calculated by multiplying the irradiance level coming from the light curing unit (LCU) by its duration [25]. Curing time is set depending of the irradiance level of the LCU. The "exposure reciprocity low" proposes reciprocity between the irradiance level and exposure duration to achieve equivalent DC of RBCs. This low has been evaluated in the literature and found not to apply, as it depends on the photoinitiator- and monomer-system of the RBC, the spectral radiant power of the LCU and is even time-dependent [26–28]. Selig et al. showed that an exposure time of only 10 s and above gave a sufficient DC [29], thus increasing the light exposure time results in higher radiant exposure reaching the RBC increment, especially with conservative cavity preparation (small orifice) and increased distance between the LCU tip and the RBC surface [30].

Selecting the proper material from the wide range available in the market is also a hard decision. In deep, occasionally irregular cavities the RBC should be easy to handle – if it is possible without the conventional layering – well adaptable and must be converted at an acceptable degree to provide good sealing and mechanical properties with low solubility. When sealing the orifices in root canal treated teeth, the use of a well distinguished material could be also advisable supposing a possible future re-treatment.

The purpose of this study was to measure the conversion degree with micro-Raman spectroscopy at the top and bottom of the first layer of a conventional sculptable and flowable, two flowable bulk-fill, a fibre-reinforced high-viscosity bulk-fill and a low-viscosity, coloured polyacid-modified RBC applied in a clinically relevant *in vitro* model, where an 8 mm distance from the light guide tip to the bottom side of the cavity was compiled. Further aim was to determine the effect of the recommended and the doubled curing time, as well as the RBC's pre-heating to 35 °C or 55 °C on the polymerization rate of the investigated materials.

2. Materials and methods

2.1. Preparation of the composite resin specimens

During this *in vitro* study six brands of resin composite material – a conventional sculptable microhybrid, a flowable nanofill, two flowable bulk-fill RBC, a fibre-reinforced bulk-fill material and a polyacid-modified RBC – were analyzed.

Table 1 – Materials, manufactures and composition.

Group	Material layer thickness	Code	Manufacturer	Shade	Organic matrix	Filler	Filler loading
Conventional RBC	Filtek Z250 2 mm	FZ	3M ESPE, St. Paul, MN, USA	A2	Bis-GMA, UDMA, Bis-EMA, TEGDMA	0.6 μm zirconia-silica	78 wt%
Conventional flowable RBC	Filtek Ultimate Flow 2 mm	FUF	3M ESPE, St. Paul, MN, USA	A2	BisGMA, TEGDMA, Procrylat resin	Zirconia/silica, ytterbium trifluoride	65 wt%
Bulk-fill RBC	Filtek Bulk Fill 4 mm	FBF	3M ESPE, St. Paul, MN, USA	U	BisGMA, UDMA, BisEMA, Procrylat resin	Zirconia/silica, ytterbium trifluoride	64.5 wt%
	SureFil SDR Flow 4 mm	SDR	Dentsply, Milford, DE, USA	U	Modified UDMA, EBPADMA, TEGDMA	Ba-Al-F-B silicate glass, Sr-Al-F silicate glass	68 wt%
Short glass fiber-reinforced RBC	EverX Posterior 4 mm	EX	GC Europe, Leuven, Belgium	U	BisGMA, TEGDMA, PMMA	Barium glass, short E-glass fibers	74.2 wt%
Polyacid-modified RBC	Twinky Star Flow Blue 2 mm	TS	VOCO GMBH, Cuxhaven, Germany	Blue	BisGMA, TEGDMA, UDMA, carboxylic acid modified methacrylate	Ba-Al-F-B silicate glass, silicon dioxide, glimmer	65 wt%

Abbreviation: RBC: resin-based composite; U: universal; UDMA: urethane dimethacrylate; EBPADMA: ethoxylated Bisphenol A dimethacrylate; TEGDMA: triethylene glycol dimethacrylate; BisEMA: Bisphenol A polyethylene glycol diether dimethacrylate; BisGMA: Bisphenol A diglycidil ether dimethacrylate; PMMA: polymethyl methacrylate.

The brand, the chemical composition and the manufacturer are presented in Table 1. According to the sample preparation and polymerization method, four experimental groups of specimens were divided. In each group, from each material, 5 specimens were prepared. Table 2 shows the experimental groups according to the method of polymerization and the abbreviations of the investigated materials.

Cylindrical Teflon molds with 5 mm internal diameter and 8 mm in height (representing a pulp chamber or deep proximal cavity) were constructed from two parts stacked on top of one another, according to the recommended thickness of the investigated materials. The schematic figure of sample preparation is presented in Fig. 1. For conventional sculptable and flowable RBCs and for the polyacid-modified resin composite the mold was built up from a 2 and a 6 mm high parts. For the bulk-fill RBCs the mold was constructed from two 4 mm high parts. Specimen preparation was performed inside a temperature-controlled chamber set at 25 °C. Materials with recommended 2 mm layer thickness were condensed or filled with a canula into the 2 mm high mold part, which was positioned on a glass slide. Thereafter, the uncured RBC was covered with a polyester (Mylar) strip in order to avoid contact with oxygen, which is an inhibitor of the polymerization. Immediately after that the 6 mm mold was positioned on top of the 2 mm mold filled with the investigated material providing the distance between the light curing guide and the material. The specimen was irradiated with a Light Emitting Diode (LED) curing unit (λ = 420–480 nm; LED.D, Woodpecker, Guilin, China) in standard mode, at an average tip irradiance of 1450 mW/cm^2 with an 8 mm diameter fiberglass light guide. The irradiance of the LED source was monitored before and after curing with a radiometer (Cure Rite, Dentsply, Milford, DE, USA). The curing light guide was centrally positioned directly on the mold entrance and the tip of the light guide was ensured to be parallel to the sample. Recommended curing time was applied for Group 1 (control), whereas double exposure time for group 4 (Table 2). For the bulk-fill RBCs the 4 mm high mold was positioned on the glass slide and was filled with the material in the recommended 4 mm thickness. The top of the sample was covered with a Mylar strip and the second 4 mm high mold was positioned on top of the first one, then the specimen was irradiated as mentioned above. In case of pre-heated groups, the RBC preheating was performed using a resin composite heating device (Ena Heat, Micerium, Avegno, Italy) preset to 35 °C (Group 2) and 55 °C (Group 3). The attained RBC's temperature was measured with a thermocouple probe (Type K thermocouple device; Ø = 0.5 mm; Cu/CuNi; TC Direct, Budapest, Hungary) which was coupled to a digital thermometer (EL-EnviroPad-TC, Lascar Electronics Ltd., Salisbury, UK), with a resolution of 0.1 per 1 °C and a data sampling frequency of 1 measurement per second. The preparation for the pre-heated specimens followed the above described protocol and was photoactivated with the recommended irradiation time for each material, respectively.

Additionally, the irradiance which reached the top of the 2 mm conventional and the 4 mm bulk-fill RBC, was measured with the radiometer. The 6 mm high mold part with 5 mm internal diameter was positioned at the center of the radiometer sensor and the incident irradiance was recorded, representing the radiant power which reaches the top of the conventional sculptable and flowable, or polyacid-modified RBC sample, filled into the 2 mm high mold. Then the procedure was repeated with the 4 mm high mold to indicate the irradiance, that reached the top of the bulk-fill RBC, filled into the 4 mm high mold part. According to this information the radiant exposure (J/cm^2) could be calculated with the product of the irradiance (mW/cm^2) and the exposure time (s).

Table 2 – Methods of polymerization and abbreviations of the investigated materials.

Methods of polymerization		Material temperature	Materials, exposure time, abbreviations, calculated radiant exposure					
			Filtek Z250	Filtek Ultimate Flow	Filtek Bulk Fill Flow	Surefil SDR	EverX Posterior	Twinky Star Blue
Group1	Exposure time recommended by the manufacturer	25 °C	20 s FZ_20 9 J/cm^2	20 s FUF_20 9 J/cm^2	10 s FBF_10 5.1 J/cm^2	20 s SDR_20 10.2 J/cm^2	10 s EX_10 5.1 J/cm^2	40 s TS_40 18 J/cm^2
Group2	Pre-heating to 35 °C and recommended exposure time	35 °C	20 s FZ_35_20 9 J/cm^2	20 s FUF_35_20 9 J/cm^2	10 s FBF_35_10 5.1 J/cm^2	20 s SDR_35_20 10.2 J/cm^2	10 s EX_35_10 5.1 J/cm^2	40 s TS_35_40 18 J/cm^2
Group3	Pre-heating to 55 °C and recommended exposure time	55 °C	20 s FZ_55_20 9 J/cm^2	20 s FUF_55_20 9 J/cm^2	10 s FBF_55_10 5.1 J/cm^2	20 s SDR_55_20 10.2 J/cm^2	10 s EX_55_10 5.1 J/cm^2	40 s TS_55_40 18 J/cm^2
Group4	Double exposure time	25 °C	40 s FZ_40 18 J/cm^2	40 s FUF_40 18 J/cm^2	20 s FBF_20 10.2 J/cm^2	40 s SDR_40 20.4 J/cm^2	20 s EX_20 10.2 J/cm^2	80 s TS_80 36 J/cm^2

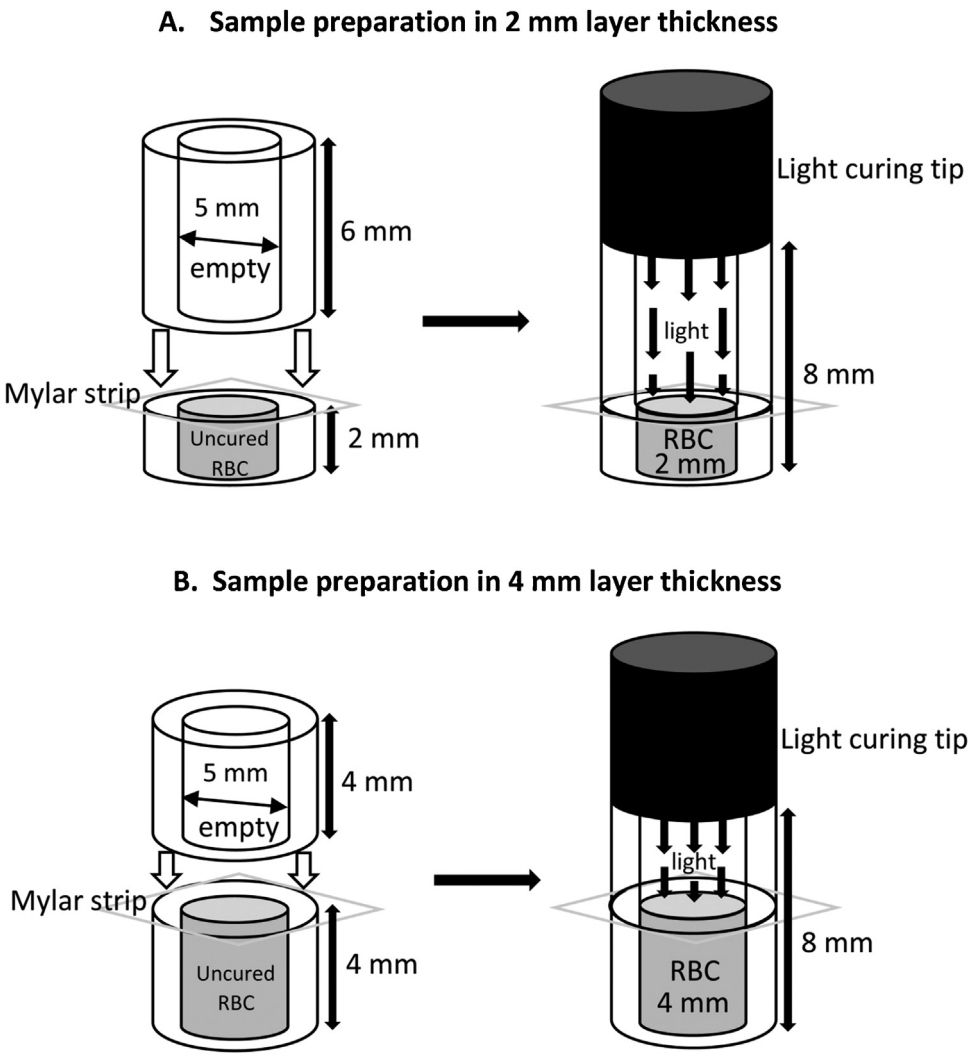

Fig. 1 – Schematic figure of the 2 mm thick (A) and the 4 mm thick (B) sample preparation.

2.2. *Micro-Raman spectroscopy measurement*

The 24 h post-cure DC values of the polymerized composite resin samples were examined using Labram HR 800 Confocal Raman spectrometer (HORIBA Jobin Yvon S.A.S., Longjumeau Cedex, France). The following sets of parameters were applied during the micro-Raman measurements: 20 mW He–Ne laser with 632.817 nm wavelength, spatial resolution ~1.5 μm, spectral resolution ~2.5 cm^{-1}, magnification x 100 (Olympus UK Ltd., London, UK). The spectra were taken on the top surface of the composite specimens at three random locations with 10 s integration time and ten acquisitions were averaged for each geometrical point. Spectra of uncured composite were taken as reference. Post-processing of spectra was performed using the dedicated software LabSpec 5.0 (HORIBA Jobin Yvon S.A.S., Longjumeau Cedex, France). The ratio of double-bond content of monomer to polymer in the composite resin was calculated according to the following equation:

$$DC\% = (1 - (R_{cured}/R_{uncured})) \times 100$$

where R is the ratio of peak intensities at 1639 cm^{-1} and 1609 cm^{-1} associated to the aliphatic and aromatic (unconjugated and conjugated) C–C stretching in cured and uncured composite resins, respectively.

2.3. *Statistical analysis*

The statistical analysis was performed using the SPSS (Statistical Package for Social Science, SPSS Inc., Chicago, USA) software for Windows. The values for degree of conversion between the studied test groups and between each material were compared by one-way analysis of variance (ANOVA) test. For multiple comparisons the significance between the groups, materials and between the top and bottom surfaces was determined by Scheffe's post-hoc test at $\alpha = 0.05$ level.

3. Results

Fig. 2 shows the degree of conversion at the top of the investigated materials according to the method of polymerization.

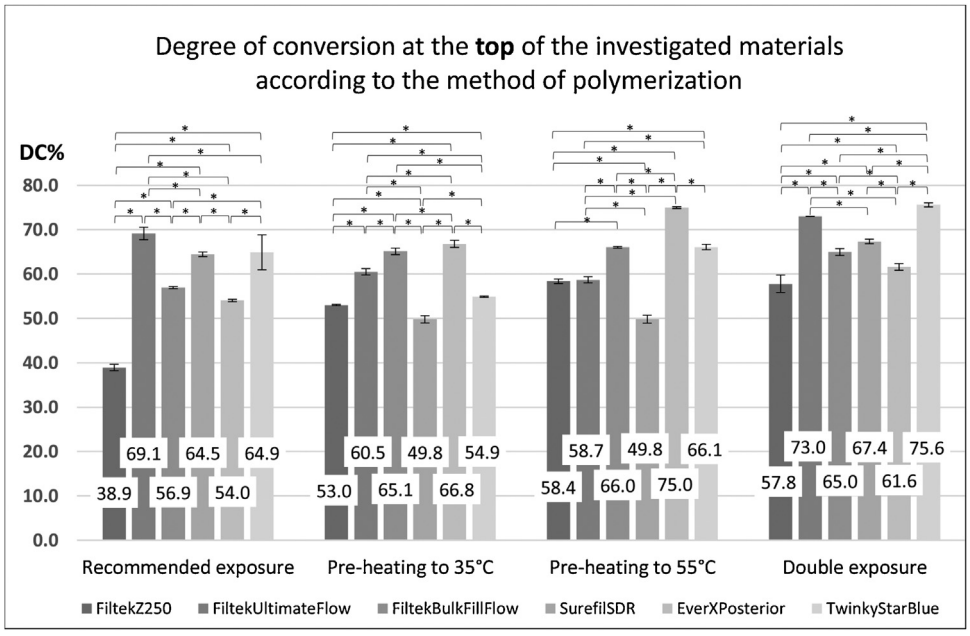

Fig. 2 – Degree of conversion at the top of the investigated materials according to the method of polymerization. The * mark indicates statistically significant difference between the investigated materials.

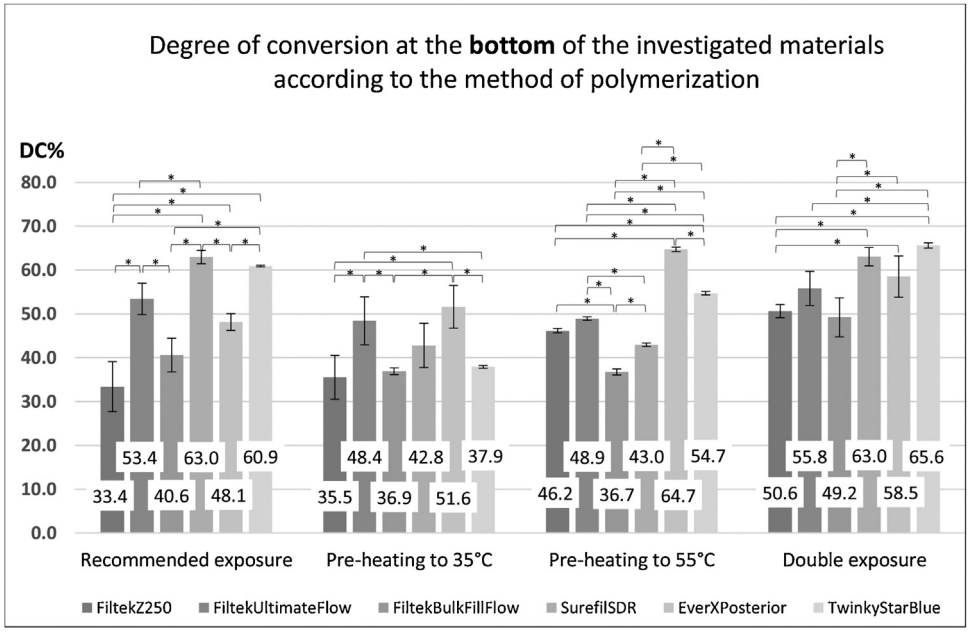

Fig. 3 – Degree of conversion at the bottom of the investigated materials according to the method of polymerization. The * mark indicates statistically significant difference between the investigated materials.

Regarding the top of the samples, conversion degree of the different materials ranged between 38.9% and 75.6%. The lowest value was measured in case of conventional sculptable microhybrid RBC (FZ_20) irradiated with the recommended exposure time at room temperature, meanwhile the highest DC% was detected in the case of the polyacid-modified resin composite (TS_80) with double exposure time at room temperature. In Group 1 the highest DC was measured in case of conventional flowable RBC (FUF_20) in 2 mm layer thickness. Similar values were detected on SDR_20 in 4 mm layer thickness and on TS_40 in 2 mm layer thickness. In Group 2 the effect of pre-heating to 35 °C was divisive. For FZ_35_20, FBF_35_10 and EX_35_10 there was a statistically significant increase in DC% on the top surface compared to the FZ_20, FBF_10 and EX_10 belong to Group 1. On the other hand, in most of the low viscosity materials (FUF_35_20, SDR_35_20 and TS_35_40) a statistically significant decrease was detected. In group 3. similar distribution in DC% was observed. In group 4. significantly higher DC

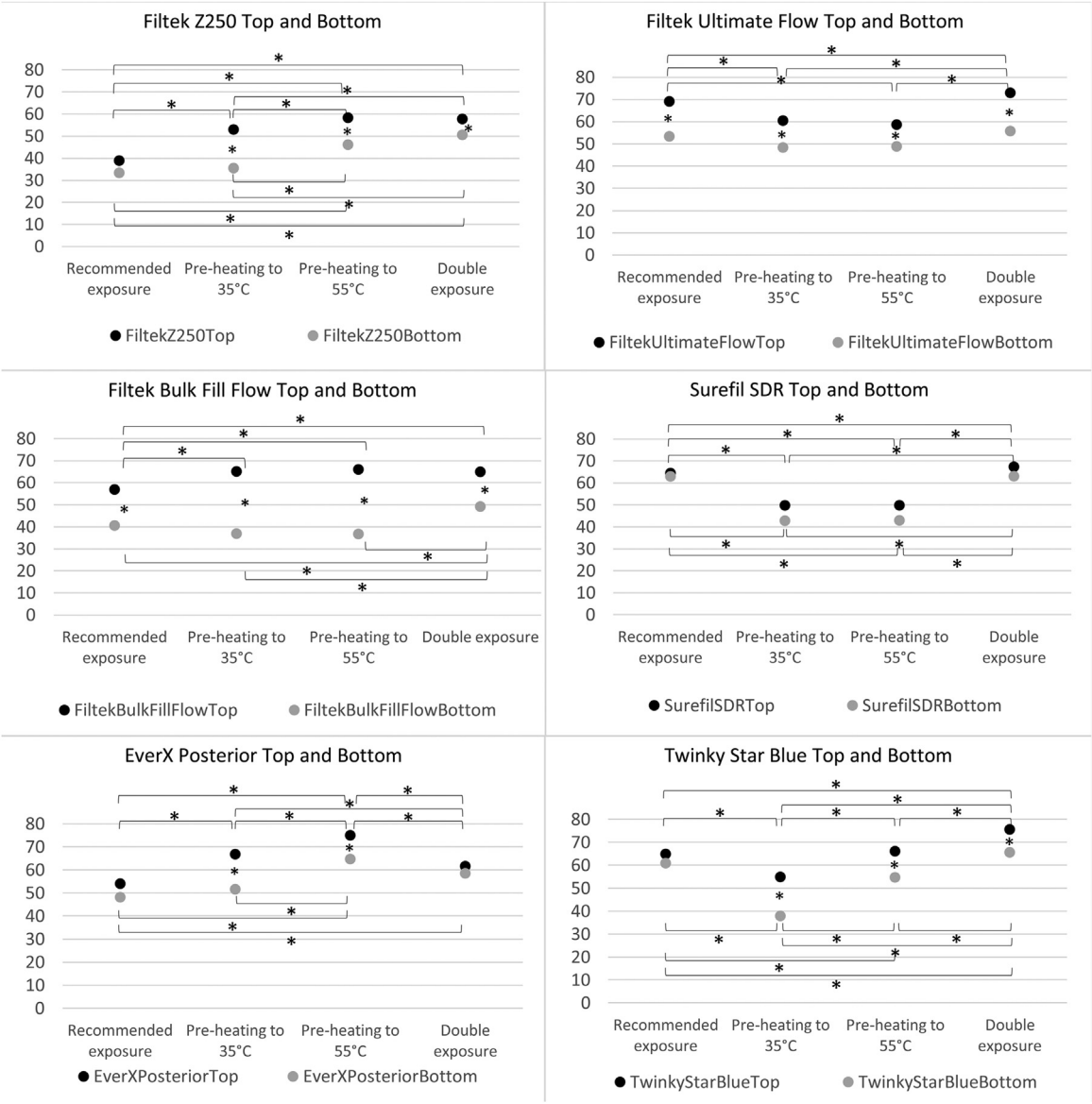

Fig. 4 – Degree of conversion at the top and the bottom of the investigated materials according to the polymerization methods. The * mark indicates a statistically significant difference between the investigated groups and as well as between top and bottom surfaces.

values (5–15% more) were measured compared to the single exposure at room temperature, except for SDR, which showed similar DC values both in Group 1 and 4. Double exposure time provided significantly higher DC for each material compared to the pre heated groups, except for EX, on which the effect of pre-heating to 55 °C dramatically improved the rate of polymerization. Fig. 3 demonstrates the degree of conversion at the bottom of the investigated materials according to the method of polymerization. Focusing on the bottom of the samples, the conversion degree of the different materials ranged between 33.4 and 65.6%. Similarly to the results of the top DC%, the lowest value was measured in case of FZ_20 and the highest was detected on TS_80. In general, at the bottom of the samples, in all cases, a lower value (5–15% less) could be measured than at the top. However, the decrease in DC was not statistically significant in any of the materials. Fig. 4 shows the degree of conversion and the statistical significance at the top and the bottom of the investigated RBCs according to the polymerization methods. In the case of FZ_20, EX_10, TS_40 (Group 1) and in EX_20 (Group 4) the difference was not statistically significant between the top and bottom DCs. In the case of SDR the DC of the top and bottom surfaces was similar in all groups. In the low viscosity materials pre-heating to 35 °C inhibited the DC level at the bottom to reach the DC values of Group 1(FUF_35_20, FBF_35_10, SDR_35_20, TS_35_40) and had no statistically significant effect on the high viscosity materials (FZ_35_20, EX_35_10). In Group 3, the same result was observed in almost all low viscosity materials and a significant increase was detected in the high viscosity RBCs (FZ_55_20, EX_55_10). Double exposure unequivocally increased the DC values at the

bottom of the samples compared to Group 1, 2 and 3, except EX_20, where the highest DC was observed in Group 3, when the material was pre-heated to 55 °C.

The irradiance decreased from 1450 mW/cm^2 to 510 mW/cm^2 in the 4 mm deep mold, while in the case of the 6 mm deep mold with 5 mm internal diameter, it decreased to 450 mW/cm^2. The calculated radiant energy delivered to the samples is presented in Table 2.

4. Discussion

In this study a clinically relevant 8 mm deep, 5 mm wide mold was filled with six different RBCs in the recommended layer thicknesses, irradiated with the recommended and its doubled exposure time as well as pre-heated to 35 and 55 °C. The degree of conversion at the top and bottom surfaces was assessed using micro-Raman spectroscopy. Different type of RBC materials were included in this investigation: a commercial sculptable microhybrid RBC (FZ), a conventional flowable nanofill RBC (FUF), a nanofill flowable bulk-fill RBC (FBF), another flowable bulk-fill RBC (SDR), a short glass-fiber reinforced bulk-fill RBC (EX) and a colored polyacid- modified RBC (TS).

The polymerization process has a major influence on the mechanical and biological properties of light cured RBCs [3]. Resin composite polymerization depends on the chemical structure of the monomer, filler particle characteristics, the photoinitiator concentration and the polymerization conditions, such as the spectral irradiance, exposure duration, distance between the curing guide and the material, layer thickness, just to mention a few of them [31,32]. An increment thickness of 2 mm is the gold standard for composite resin placement and curing [23]. It is technique sensitive and time consuming in cases of deeper posterior restorations or during coronal sealing of an endodontically treated tooth. To address these problems, various manufactures have recently introduced the newest type of resins, so called bulk-fill materials which claim to cure at a maximum increment thickness of 4 mm.

According to our results, with the recommended exposure time (Group 1) the commercial sculptable RBC in 2 mm layer thickness with 20 s irradiation showed the lowest DC% at the top and bottom surface of the samples. This RBC has the highest amount of filler content (78 wt%) among the investigated materials, which exhibited the highest light distribution. Halvorson et al. demonstrated, that increasing the filler-matrix ratio progressively decreases conversion, because an increased amount of filler particles is an obstacle for polymeric chain propagation [33]. To provide acceptable depth of cure in 4 mm or more layer thickness, the manufacturers of bulk-fill RBCs were able to improve polymerization depth by the use of potent photoinitiator systems along with an increased translucency [34]. However, with the recommended exposure time, bulk-fill RBCs (except SDR) did not reach the DC level of the 2 mm thick commercial as well as the polyacid-modified flowable RBC's DC value at the top of the samples in our investigation. Each RBC product revealed an inverse correlation between DC and depth. The monomer to polymer conversions showed 5–15% lower values at the bottom, except for SDR, where the DC % reached the value measured at the top. It also exceeded the polymerization rate of the materials used in 2 mm layer thickness. The unique combination of glass filler loading with SDR resin provides high depth of cure in the recommended 4 mm thickness [35]. Besides the filler-matrix ratio, the DC is affected by the viscosity and reactivity of the monomers, as well [36,37]. In our study, only the SDR monomer system does not contain BisGMA, which is considered the most viscous, thus the less mobile monomer. SDR is a UDMA/EBPADMA-based bulk-fill flowable composite with additional TEGDMA, which has a synergistic effect on the rate of polymerization. Thus, the DC value of this monomer is significantly higher than that of the other investigated bulk-fill materials [38]. In addition, a photo-active modulator – embedded in the polymerizable resin backbone of the SDR resin monomer – may cooperate with camphorquinone (CQ), thereby facilitating polymerization.

In Group 4 with double exposure, the materials showed almost the same order, but with a 5–15% higher DC level on the top of the samples. It has been concluded by Zorzin et al., that extended curing time (30 s) had a positive effect on polymerization properties, so enhanced light curing of bulk-fills in deep cavities is recommended [39]. It is well-documented that radiant exposure (irradiance x exposure duration) of the light cure influences the DC and DOC of RBCs, thus a given radiant exposure can be delivered with different combinations of irradiance and exposure duration [25–27,40] Daugherty et al. concluded that the polymerization kinetics have been found to be highly complex, and a simple reciprocal relationship between radiant exposure and exposure time does not exist since irradiance and exposure can independently affect DC and DOC [41]. Increased depth of the cavity implies a radiant exposure reduction, whereas the irradiance of the light exponentially decreases with distance. Rueggeberg et al. and Emami and Söderholm concluded, that in order for a 2 mm thick conventional RBC increment to have adequate polymerization, it should receive a radiant exposure within the 16–24 J/cm^2 range [25,26]. In our study, an 8 mm deep cavity was simulated, where the distance between the light curing tip and the material top surface is increased, thus a decreased irradiance could initiate the polymerization. At 2 mm layer thickness (FZ, FUF, TS) the photons travel through 6 mm to reach the material's surface. This distance decreased the 1450 mW/cm^2 irradiance provided by the LED curing unit to ~740 mW/cm^2, however the small – 5 mm in diameter – orifice of the cavity further decreased the irradiance to 450 mW/cm^2. At 4 mm layer thickness (FBF, SDR, EX) in the 8 mm deep simulated cavity the photons travel through 4 mm distance, which decreases their radiant power to 930 mW/cm^2, and the shuttering effect of the narrow orifice resulted in 510 mW/cm^2 irradiance. The beneficial effect of the longer exposure duration is evident in group 4 in these conditions, however the DC of the different materials was not in correlation with the radiant exposure. The exception was TS, where the doubled exposure time increased the radiant exposure to 36 J/cm^2, resulted in 75.6% DC at the top surface and 65.6% at the bottom of the sample, which was the highest rate of polymerization among the investigated materials. The conventional flowable RBC (FUF) in also 2 mm layer thickness received 18 J/cm^2 radiant exposure and performed well with its 73% DC level at the top surface. The

bulk-fill materials failed to reach the DC value of the 2 mm thick flowable RBC's, but exceeded the polymerization rate of the sculptable FZ. At the bottom of the specimens, however, the bulk-fill RBCs performed better than the conventional RBCs used in 2 mm thickness, except FBF. The composition and initiator system of SDR and EX provided a convincing DC% through its 4 mm layer thickness without significant difference between the top and the bottom surfaces, cured in an 8 mm deep simulated cavity. Although, the highest DC was provided by TS (received 36 J/cm^2), there was no significant difference found between TS and SDR (received 20.4 J/cm^2), or TS and EX (received 10.2 J/cm^2) at the bottom surface in Group 4. According to our results, SDR was unique among the investigated materials with its 63% degree of conversion at the bottom of the samples, both in Group 1 and 4. It means, the rate of polymerization was the same (63%) with the recommended (20 s) and its double (40 s) exposure time in an 8 mm deep simulated cavity with 4 mm layer thickness.

Considering EX, in spite of the fact, that the 4 mm thick EX sample received less energy density (10.2 J/cm^2) compared to the 2 mm thick conventional one (18 J/cm^2), provided higher DC% at the bottom of the 4 mm thick sample. In fact, did not differ significantly from the highest values of TS and SDR, which received greater radiant exposure, 36 J/cm^2 and 20.4 J/cm^2, respectively. Certainly the short glass fibers have great significance in providing high depth of cure with the extended curing time (20 s) at the bottom of the samples. Similarity between the fiber/matrix refractive indices may allow light penetration into the deeper parts of the material. Goracci et al. concluded in their experiment, that EX exhibited DOC over 4 mm, the maximum thickness recommended for bulk placement [42]. From the available bulk-fill RBCs, besides SDR and EX, FBF was also investigated in this study. A universal shade was selected for all three brands. The absence or low amount of pigments in universal shaded, more translucent composite resin materials also have a beneficial effect on DC or depth of cure because pigments are opaque particles that will limit light penetration and reduce the degree of polymerization at greater depths [43] Although, Ilie found no correlation among DC and light transmittance. It was concluded, that light transmission changes during polymerization do not alter polymerization kinetics in modern bulk-fill RBCs [44]. Among bulk-fill materials in the present study, FBF has the lowest filler loading and the highest translucency parameter [45]. Despite of these advantageous parameters, FBF failed to reach the DC of the other investigated materials, especially at the bottom of the 8 mm deep simulated cavity in Group 1 and 4, except for FZ. In accordance with previous studies, the DC values for FBF were lower compared to the conventional flowable RBCs or to the other investigated bulk-fill materials [6,44]. Considering the chemical composition of FBF, it has the same filler content than the conventional flowable RBC (FUF) from the same manufacturer, however the matrix composition is different. FUF contains highly viscous BisGMA, low molecular weight, highly mobile and reactive TEGDMA as a diluting monomer and a Procrylate monomer. In case of FBF, besides Procrylate resin, BisGMA was combined with UDMA and BisEMA, instead of TEGDMA. Although the viscosity of UDMA is much lower than that of BisGMA, when it is mixed with the high molecular weight BisEMA, it can significantly restrict the mobility of UDMA monomers and decrease their reactivity and conversion value [6,46]. The other influencing factor of DC is the radiant exposure delivered to the material. With the recommended 10 s curing time and 1450 mW/cm^2 irradiance, the delivered energy density was only 5.1 J/cm^2, which increased to 10.2 J/cm^2 with the extended irradiation time.

In Group 2 and 3 the effect of pre-heating on degree of conversion was investigated. Increasing the temperature of the RBC before application, decreases their viscosity, therefore enhances the marginal adaptation, reduces microleakage [17], and significantly reduces shrinkage force formation [22], while maintaining or increasing the degree of conversion and crosslinking by enhancing free radical and monomer mobility and increasing collisions among molecules [20,21]. The restoration of deep cavities with a narrow orifice – *i.e.* pulp chamber – could be difficult, considering the decreased irradiance of the curing light, that can reach the surface of the first RBC layer. Based on these considerations, the aim of increasing the temperature of the investigated materials was to determine the influence on degree of conversion in 8 mm deep – clinically relevant – simulated cavities. Two temperature values were used, 35 °C and 55 °C. As Fig. 3 shows, both in Group 2 and 3 two main effect was detected. In case of sculptable conventional RBC (FZ) and sculptable glass-fibre reinforced bulk-fill RBC (EX) a significant increase in DC% was found as a positive influence of pre-heating. In Group 2, the increase was remarkable at the top and less, but significant, at the bottom of the samples. In Group 3 the pre-heating to 55 °C increased the DC level by 20% at the top and around 15% at the bottom. This increase at the top of FZ and EX exceeded the DC values found in group 4, however, the DC% was higher at the bottom only for EX, compared to the double exposure. On the other hand, in case of the flowable RBCs, a negative effect on DC% was detected both in Group 2 and 3, especially at the bottom of the samples, compared to Group 1. Interestingly, there was not significant difference in DC values of flowable RBCs at the bottom between Group 2 and 3. At the top, the results were not as homogenous than at the bottom: in case of FUF, SDR and TS_35_40 a significant decrease was detected, meanwhile FBF showed a significant increase. The unexpected decrease of DC level of pre-heated (both 35 °C and 55 °C) flowable RBCs from the top to the bottom may be caused by the rapid cooling process of materials with lower filler content [47]. In our study the material was placed in an 8 mm deep mold under a non-isothermal condition, where the composite temperature reached after pre-heating is not stabilized, in order to simulate a clinically realistic scenario. Plasmans et al. reported an intraoral temperature of 25.1 °C around the treatment area after rubber dam isolation [48]. Studies, that have shown improvement in monomer conversion upon pre-heating generally maintained the resin composite temperature constant during the experimentation [20,21]. Once RBC temperature is elevated, there is a time delay between removing it from the heating device, dispensing it from a canula or syringe, placing it into an occasionally deep cavity, contouring it, and subsequently light-curing it. Our preliminary investigations revealed that during the 40 s manipulation time interval between RBC removal from the heater and start of photoactivation with 20 s, the temperature of the 55 °C pre-heated flowable test materials decreased to 26.2 °C. Results

provided by Lohbauer et al. also confirm that RBC's temperature rapidly drops to the physiological level upon removal from the pre-heating device [18]. Polymerization is an exothermic process and the heat liberated tends to accelerate the curing reaction. Generated heat increases the system temperature leading to decrease of viscosity and improves molecular mobility, increasing collision frequency of reactive radicals and postponing diffusion-controlled propagation, also known as autodeceleration, thus increasing final conversion [21]. However, during cooling the polymer formation has an excess heat loss. It deprives energy from the system, which is necessary for polymer chain propagation. The gel-phase interval may be decreased, autodeceleration takes place and leads to early vitrification, decreasing the degree of conversion. The polymerization as an exothermic process is influenced by the environmental temperature, curing time, monomer and filler content and nature of the filler surface [49]. Our results show different effect of pre-heating thermal changes on RBCs, probably depending on their filler content. On highly filled RBCs (FZ, EX) the pre-heating had a positive effect, it could increase significantly the DC% at the top and bottom, however on RBCs with lower filler content, the pre-heating even resulted in a negative effect on the bottom of the samples. These results are contradictious to most of the previous experiments [20,21], however Tauböck et al. reported similar, non-isothermal, real scenario pre-heating experiments and among the five investigated materials, only one showed significant DC% increase resulted from the pre-heating and in case of three materials, a non-significant DC% decrease was presented [22]. The observed DC% values and changes reflect overall result of the temperature dependent complex processes. It is speculated, that, on one hand, the higher volume content of inorganic fillers kept more energy and allowed for a delayed autodeceleration. According to another aspect, Plueddemann stated, that organofunctional silane coupling agents are hybrid organic-inorganic compounds which act as an interface between inorganic filler and organic polymer matrix and can help overcome the obstacle resulting from the mismatch of thermal coefficient [50]. In sculptable RBCs the filler content, thus the filler/matrix interface is higher. The dynamic equilibrium created at the silane interface between the filler and the polymer may provide higher exotherm reaction and dense bond formation at the deeper regions as well. This effect is stronger when the temperature increased to a higher level. On the other hand, in case of the less-filled RBCs, the highest DC% values were resulted on room temperature and most of them showed a negative effect of the pre-heating, indicating that, some part of the exothermic polymerization reaction is shifted towards the reactants, or the chain propagation is inhibited. Itś worth to mention here also, that in most cases of polymerization the entropy change associated with the building of one new segment into the chain continuously decreases since the rotational freedom of the chain decreases with an increasing length of the chain. The large negative entropy change inhibits the spontaneous growth of the chain due to the very small or positive free enthalpy (Gibbs free energy). Due to its complexity, further investigations are necessary to clarify this phenomenon. Preliminary testing of FZ and FUF in 8 mm deep cavity at isothermic (55 °C) condition resulted in 65 DC% and 63 DC% at the top and 59 DC% and 60.5 DC% at the bottom, respectively. These are higher DC values, compared to the results observed in this present study under clinically relevant conditions, therefore supporting the results that were concluded in previous experiments [20,21]. However, the above mentioned measurements are under work, supplemented with continuous testing of thermal changes during the restorative procedures. In some cases of flowable RBCs (FUF and TS_55_40) the pre-heating provided enough energy to reach higher DC level at the top, however the sudden drop of temperature decreased the diffusion-controlled propagation towards the bottom of the samples leading to lower DC, compared to the control group (Group 1).

The minimum DC% for clinically acceptable restoration has not yet been exactly recognized [51]. Soares et al. reported that, for occlusal restorative layers, DC values should be at least 55% [52]. In our investigation the samples represented the first layer of light-cured RBC, which are covered with more subsequent layers in clinical situation. However, the adequate degree of monomer conversion is also essential at the bottom of the cavity close to the pulp space or at the proximal gingival margin. According to our results in Group 1 only SDR and TS, only EX in Group 3 and FUF, SDR, EX and TS in group 4 provided this DC level at the bottom of the samples in an 8 mm deep and 5 mm wide simulated cavity.

Present study, however, has some limitations. Firstly, this is an *in vitro* study and the specimens were prepared in a teflon mold and irradiated from an "occlusal" direction. In case of *in vivo* circumstances there is a possibility to irradiate the composite resin specimen from a buccal or lingual aspect as well, to improve the DC. Although, indirect polymerization of the RBCs through a substance significantly reduces the radiant exposure delivered to the material, since the tooth absorbs the energy originated from the photocuring device [53]. Secondly, the DC measurements do not yield information about the mechanical properties or the development of contraction stress in the investigated materials in response to recommended or doubled duration exposures and pre-heating. Although, direct correlation existed between hardness and DC, further mechanical testing, like three-point bending is planned to get more information about the relation of DC and mechanical characteristics. Thirdly, a commercial handheld dental radiometer was used in this survey to measure the radiant exitance from the curing unit and to calculate the radiant exposure received by the RBC through the mold with 4 and 6 mm depth and 5 mm internal orifice diameter. Price et al. discourages the use of irradiance values derived from a dental radiometer to describe the real spectral radiant power from an LCU [32]. However, in our study only one type of LCU was used and all the specimens were prepared in molds with the same dimension in diameter and with standardized LCU tip positioning to the mold's orifice, thus the spectral radiant power was similar for all the investigated materials and the received energy density was influenced only by the distance between the light curing tip and the material. Although, the values of the calculated radiant exposure are not accurate due to the usage of a radiometer, it is presumed, that the comparison of resulted DC data for the investigated materials is relevant. Finally, further investigations are necessary to

clarify the negative effect of pre-heating on the DC of flowable RBCs.

5. Conclusion

Within the limitations of this *in vitro* study – simulating an eight mm deep clinically relevant simulated cavity – the following conclusions can be stated:

1) Significantly higher DC levels were measured at the top of the samples compared to the bottom in each investigated material, in each experimental group, except SDR in Group 1 and 4.
2) Doubling the exposure time had a significant effect on DC% except for SDR. It provided the highest DC% at the bottom of the samples in Group 1 and 4, regardless the exposure time, thus the radiant exposure.
3) Radiant exposure had no direct correlation with DC especially in bulk-fill RBCs.
4) Pre-heating had a positive effect on the DC% of the high-viscosity RBCs (especially 55 °C on the DC% of EX) and had negative effect on DC% of the low-viscosity RBCs at the bottom of the samples.

Acknowledgments

This work was supported by PTE-ÁOK-KA-2016/1 and GINOP-2.3.2.-15-2016-00022 Research Grant.

REFERENCES

[1] Demarco FF, Correa MB, Cenci MS, Moraes RR, Opdam NJM. Longevity of posterior composite restorations: not only a matter of materials. Dent Mater 2012;28:87–101.
[2] Mandke L. Importance of coronal seal: preventing coronal leakage in endodontics. J Res Dent 2016;4:71–5.
[3] Cramer NB, Stansbury JW, Bowman CN. Recent advances and developments in composite dental restorative materials. J Dent Res 2011;90:402–16.
[4] Ilie N, Stark K. Curing behavior of high-viscosity bulk-fill composites. J Dent 2014;42:977–85.
[5] Alshali RZ, Salim NA, Satterthwaite JD, Silikas N. Long-term sorption and solubility of bulk-fill and conventional resin-composites in water and artificial saliva. J Dent 2015;43:1511–8.
[6] Alshali RZ, Silikas N, Satterthwaite JD. Degree of conversion of bulk-fill compared to conventional resin-composites at two time intervals. Dent Mater 2013;29:e213–7.
[7] Van Ende A, De Munck J, Van Landuyt KL, Poitevin A, Peumans M, Van Meerbeek B. Bulk-filling of high C-factor posterior cavities: effect on adhesion to cavity-bottom dentin. Dent Mater 2013;29:269–77.
[8] Roggendorf MJ, Krämer N, Appelt A, Naumann M, Frankenberger R. Marginal quality of flowable 4-mm base vs. conventionally layered resin composite. J Dent 2011;39:643–7.
[9] Ilie N, Bucuta S, Draenert M. Bulk-fill resin-based composites: an in vitro assessment of their mechanical performance. Oper Dent 2013;38:618–25.
[10] Jang JH, Park SH, Hwang IN. Polymerization shrinkage and depth of cure of bulk-fill resin composites and highly filled flowable resin. Oper Dent 2015;40:172–80.
[11] Lempel E, Czibulya Z, Kovács B, Szalma J, Tóth Á, Kunsági-Máté S, et al. Degree of conversion and BisGMA, TEGDMA, UDMA elution from flowable bulk fill composites. Int J Mol Sci 2016;17:e732.
[12] Vallittu PK. An overview of development and status of fiber-reinforced composites as dental and medical biomaterials. Acta Biomater Odontol Scand 2018;4:44–55.
[13] Garoushi S, Säilynoja E, Vallittu PK, Lassila L. Physical properties and depth of cure of a new short fiber reinforced composite. Dent Mater 2013;29:835–41.
[14] Fráter M, Forster A, Keresztúri M, Braunitzer G, Nagy K. In vitro fracture resistance of molar teeth restored with a short fibre-reinforced composite material. J Dent 2014;42:1143–50.
[15] Majety KK, Pujar M. In vitro evaluation of microleakage of class II packable composite resin restorations using flowable composite and resin modified glass ionomers as intermediate layers. J Conserv Dent 2011;14:414–7.
[16] Baroudi K, Rodrigues JC. Flowable resin composites: a systematic review and clinical considerations. J Clin Diagn Res 2015;9:e18–24.
[17] Fróes-Salgado NR, Silva LM, Kawano Y, Francci C, Reis A, Loguercio AD. Composite pre-heating: effects on marginal adaptation, degree of conversion and mechanical properties. Dent Mater 2010;26:908–14.
[18] Lohbauer U, Zinelis S, Rahiotis C, Petschelt A, Eliades G. The effect of resin composite pre-heating on monomer conversion and polymerization shrinkage. Dent Mater 2009;25:514–9.
[19] AlShaafi MM. Effects of different temperatures and storage time on the degree of conversion and microhardness of resin-based composites. J Contemp Dent Pract 2016;17:217–23.
[20] Daronch M, Rueggeberg FA, De Goes MF. Monomer conversion of pre-heated composite. J Dent Res 2005;84:663–7.
[21] Daronch M, Rueggeberg FA, De Goes MF, Giudici R. Polymerization kinetics of pre-heated composite. J Dent Res 2006;85:38–43.
[22] Tauböck TT, Tarle Z, Marovic D, Attin T. Pre-heating of high-viscosity bulk-fill resin composites: effects on shrinkage force and monomer conversion. J Dent 2015;43:1358–64.
[23] Ferracane JL. Resin composite-state of the art. Dent Mater 2011;27:29–38.
[24] AlShaafi MM. Factors affecting polymerization of resin-based composites: a literature review. Saudi Dent J 2017;29:48–58.
[25] Rueggeberg FA, Caughman WF, Curtis Jr JW. Effect of light intensity and exposure duration on cure of resin composite. Oper Dent 1994;19:26–32.
[26] Emami N, Söderholm KJ. How light irradiance and curing time affect monomer conversion in light-cured resin composites. Eur J Oral Sci 2003;111:536–42.
[27] Halvorson RH, Erickson RL, Davidson CL. Energy dependent polymerization of resin-based composite. Dent Mater 2002;18:463–9.
[28] Wydra JW, Cramer NB, Stansbury FW, Bowman CN. The reciprocity low concerning light dose relationships applied to BisGMA/TEGDMA photopolymers: theoretical analysis and experimental characterization. Dent Mater 2014;30:605–12.
[29] Selig D, Haenel T, Hausnerova B, Moeginger B, Labrie D, Sullivan B, et al. Examining exposure reciprocity in a resin based composite using high irradiance levels and real-time

degree of conversion values. Dent Mater 2015;31:583–93.
[30] Erickson RL, Barkmeier WW. Curing characteristics of a composite. Part 2: the effect of curing configuration on depth and distribution of cure. Dent Mater 2014;30:e134–45.
[31] Leprince JG, Palin WM, Hadis MA, Devaux J, Leloup G. Progress in dimethacrylate-based dental composite technology and curing efficiency. Dent Mater 2013;29:139–56.
[32] Price RB, Ferracane JL, Shortall AC. Light-curing units: a review of what we need to know. J Dent Res 2015;94:1179–86.
[33] Halvorson RH, Erickson RL, Davidson CL. The effect of filler and silane content on conversion of resin-based composite. Dent Mater 2003;19:327–33.
[34] Bucuta S, Ilie N. Light transmittance and micro-mechanical properties of bulk fill vs. conventional resin based composites. Clin Oral Investig 2014;18:1991–2000.
[35] Ilie N, Hickel R. Investigations on a methacrylate-based flowable composite based on the SDR™ technology. Dent Mater 2011;27:348–55.
[36] Baroudi K, Saleh AM, Silikas N, Watts DC. Shrinkage behaviour of flowable resin-composites related to conversion and filler-fraction. J Dent 2007;35:651–5.
[37] Al-Ahdal K, Ilie N, Silikas N, Watts DC. Polymerization kinetics and impact of post polymerization on the degree of conversion of bulk-fill resin-composite at clinically relevant depth. Dent Mater 2015;31:1207–13.
[38] Sideridou ID, Karabela MM. Effect of the amount of 3-methacyloxypropyltrimethoxysilane coupling agent on physical properties of dental resin nanocomposites. Dent Mater 2009;25:1315–24.
[39] Zorzin J, Maier E, Harre S, Fey T, Belli R, Lohbauer U, et al. Bulk-fill resin composites: polymerization properties and extended light curing. Dent Mater 2015;31:293–301.
[40] Peutzfeldt A, Asmussen E. Resin composite properties and energy density of light cure. J Dent Res 2005;84:659–62.
[41] Dougherty MM, Lien W, Mansell MR, Risk DL, Savett DA, Wandewalle KS. Effect of high-intensity curing lights on the polymerization of bulk-fill composites. Dent Mater 2018;34:1531–41.
[42] Goracci C, Cadenaro M, Fontanive L, Giangrosso G, Juloski J, Vichi A, et al. Polymerization efficiency and flexural strength of low-stress restorative composites. Dent Mater 2014;30:688–94.
[43] Garcia D, Yaman P, Dennison J, Neiva G. Polymerization shrinkage and depth of cure of bulk fill flowable composite resins. Oper Dent 2014;39:441–8.
[44] Ilie N. Impact of light transmittance mode on polymerisation kinetics in bulk-fill resin-based composites. J Dent 2017;63:51–9.
[45] Miletic V, Pongprueksa P, De Munck J, Brooks NR, Van Meerbeek B. Curing characteristics of flowable and sculptable bulk-fill composites. Clin Oral Investig 2017;21:1201–12.
[46] Khatri CA, Stansbury JW, Schultheisz CR, Antonucci JM. Synthesis, characterization and evaluation of urethane derivatives of Bis-GMA. Dent Mater 2003;19:584–8.
[47] Daronch M, Rueggeberg FA, Moss L, de Goes MF. Clinically relevant issues related to preheating composites. J Esthet Restor Dent 2006;18:340–50.
[48] Plasmans PJ, Creugers NH, Hermsen RJ, Vrijhoef MM. Intraoral humidity during operative procedures. J Dent 1994;22:89–91.
[49] Mohsen NM, Craig RG, Filisko FE. Effects of curing time and filler concentration on curing and postcuring of urethane dimethacrylate composites: a microcalorimetric study. J Biomed Mater Res 1998;40:224–32.
[50] Plueddemann EP. Silane coupling agents. Plenum; 1982. p. 111.
[51] Galvao MR, Caldas SG, Bagnato VS, Rastelli AN, Andrade MF. Evaluation of degree of conversion and hardness of dental composites photoactivated with different light guide tips. Eur J Dent 2013;7:86–93.
[52] Soares LE, Liporoni PC, Martin AA. The effect of soft-start polymerization by second generation LEDs on the degree of conversion of resin composite. Oper Dent 2007;32:160–5.
[53] Watts DC, Cash AJ. Analysis of optical transmission by 400-500 nm visible light into aesthetic dental biomaterials. J Dent 1994;2:112–7.

Journal of Molecular Structure: THEOCHEM 956 (2010) 103–109

Contents lists available at ScienceDirect

Journal of Molecular Structure: THEOCHEM

journal homepage: www.elsevier.com/locate/theochem

Weinhold's QCE model – A modified parameter fit. Model study of liquid methanol based on MP2 cluster geometries

Gergely Matisz [a,b], Walter M.F. Fabian [b], Anne-Marie Kelterer [c], Sándor Kunsági-Máté [a,*]

[a] Department of General and Physical Chemistry, University of Pécs, Ifjúság 6, Pécs H-7624, Hungary
[b] Institute of Chemistry, Karl-Franzens University of Graz, Heinrichstr. 28, Graz A-8010, Austria
[c] Institute of Physical and Theoretical Chemistry, Graz University of Technology, Stremayrg. 9/I, Graz A-8010, Austria

ARTICLE INFO

Article history:
Received 3 June 2010
Accepted 2 July 2010
Available online 7 July 2010

Keywords:
Quantum cluster equilibrium theory
MP2 calculations
Heat capacity
Entropy
Structure
Liquid methanol

ABSTRACT

The quantum cluster equilibrium (QCE) theory was applied for liquid methanol using MP2(fc)/6-31+G(d,p) cluster geometries and MP2/6-311++G(d,p) energies. Three approaches for the determination of the empirical parameters inherent in the QCE model, a_{mf} and b_{xv}, were considered, while the molar volumes of both the liquid and the vapor were obtained from experiment. *Model 1*, in which a_{mf} and b_{xv} were optimized for the vapor and liquid phase, respectively, gave the best results for thermochemical parameters (constant pressure heat capacity C and entropy S) of methanol, especially for the liquid state. In line with Pauling's suggestions concerning the structure of liquid methanol, cyclic hexamers *cyclo*-$(MeOH)_6$ are the dominant species, even near the boiling point (~50%) increasing to ~90% at the freezing temperature.

© 2010 Elsevier B.V. All rights reserved.

1. Introduction

The most widely used approaches to describe liquid properties are molecular dynamics (MD) or Monte Carlo (MC) simulations [1–5]. Hydrogen bonding is the dominant factor responsible for the bulk properties of water [6–9]. In contrast to water, the structure of liquid alcohols, e.g. methanol, is not only determined by hydrogen bonding but hydrophobic interactions are also important. Pauling proposed that liquid methanol mainly is composed of cyclic clusters, mostly hexamers [10], whereas early MC and MD simulations all favor the existence of chains [11,12]. Recent simulations using polarizable force fields [13] and ab initio MD calculations on methanol [14] clearly show that the pairwise additive approximation is flawed for these hydrogen-bonded liquids. A summary of previous work on liquid methanol and methanol clusters is provided by Boyd [15] and Restrepo [16]. A comprehensive study on the methanol trimer has been done by Mó et al. [17] and Mandado et al. [18] and larger clusters (up to $n = 20$) were calculated by Pires and DeTuri [19].

Another possibility for the treatment of bulk liquids is to apply a static approach based on statistical thermodynamics, e.g. the quantum cluster equilibrium theory (QCE) of Weinhold [20,21]. This model has been successfully applied to describe structure and properties of liquids containing intermolecular hydrogen bonds like water or various alcohols [22–28], including methanol [29–31]. In these latter papers, cluster structures were obtained from geometry optimization by density functional theory [B3LYP/6-31+G(d) and B3LYP/6-311G(d,p), respectively]. Ludwig showed that the most important clusters are purely cyclic structures, whereas lasso and chain arrangements of the methanol molecules were found to be negligible in the liquid [30]. Borowski emphasized the need for a more careful fit onto more experimental data, e.g. a set for different temperatures, of the two empirical parameters (a_{mf} and b_{xv}) within the QCE model [29]. He also noted the discrepancy (1.5 ppm) between their calculated hydroxyl proton chemical shift and the experimental one. In contrast, Ludwig has found an excellent agreement between room temperature chemical shifts and those calculated for the $(MeOH)_5$ and $(MeOH)_6$ ring cluster structures [30].

The usefulness of the QCE model for the prediction of realistic liquid structures as well as thermochemistry is essentially determined by the reliability of calculated cluster structures, binding energies, and distribution. Besides the work of Borowski [29] and Ludwig [30,31], the B3LYP computational procedure has also been applied for the characterization of the $(MeOH)_4$ potential energy surface [16] as well as in a DFT investigation of methanol clusters up to dodecamers [15]. MP2/aug-cc-pVDZ calculations on selected methanol tetramers did not significantly change the structures but led to improved binding energies [16]. Frequently used density functionals have been shown to perform reasonably well for systems characterized by strong hydrogen bonds (dimers of HX,

* Corresponding author. Tel.: +36 72 503600/4208; fax: +36 72 501518.
E-mail address: kunsagi@gamma.ttk.pte.hu (S. Kunsági-Máté).

0166-1280/$ - see front matter © 2010 Elsevier B.V. All rights reserved.
doi:10.1016/j.theochem.2010.07.003

X = F, Cl, Br) [32]. Nevertheless, the reliability of DFT for describing such weak interactions, e.g. the CH...O interaction possible in methanol, might be questioned [33–35] and benchmarking by an alternative procedure appears to be worthwhile.

Consequently, in this paper we extend the study of Ludwig of liquid methanol to the MP2(fc) level of theory with a quite large cluster set (81 geometries). In addition, we investigate the influence of the two empirical parameters, a_{mf} and b_{xv}, on calculated thermochemical properties, e.g. constant pressure heat capacity C_p.

2. Computational methods and details

2.1. The QCE model

Since the QCE model has been described in detail previously [20,21,36], only a brief outline will be given first. Three approaches will be described then to determine the empirical parameters a_{mf} and b_{xv} of this model.

2.1.1. Outline of the model

The QCE model is based on statistical thermodynamics to evaluate the canonical partition function (Q) of the system. The difference in the evaluation of Q relative to the ideal gas approximation is the use of two empirical parameters, a_{mf} and b_{xv}, which are included in the model. These two parameters are used to describe the intercluster interaction (a_{mf}) and to take into account the smaller available volume for translation (b_{xv}).

The required data for this model are: the rotational symmetry number of the molecule or cluster (σ); the principal moments of inertia (I_A, I_B, I_C), the vibrational frequencies of normal modes (v_j) and the total energy (E_{tot}, sum of the electronic energy and the nuclear repulsion) of the cluster. The zero point vibrational energy (ZPVE) either can be added to E_{tot} or be included in the vibrational partition function [36]. From these calculated properties the partition function (q_i) for cluster i can be obtained. The cluster partition function q_i can be factored as

$$q_i = q_{i,elec}\, q_{i,trans}\, q_{i,rot}\, q_{i,vib} \tag{1}$$

where the terms at the right hand side are electronic partition function $q_{i,elec}$ (Eq. (2)), the translational partition function $q_{i,trans}$ (Eq. (5)), the rotational partition function $q_{i,rot}$ (Eq. (8)) and the vibrational partition function $q_{i,vib}$ (Eq. (9)), respectively. These partition functions can be expressed as follows:

$$q_{i,elec} = e^{-\Delta E_i/k_bT} \tag{2}$$

where ΔE_i is the energy difference of the ith cluster and the separated component molecules (methanol in the present case), i.e.

$$\Delta E_i = E_{i,clust} - k(i)a_{mf}/V_m - k(i)E_{ref} \tag{3}$$

$k(i)$ is the number of molecules in the ith cluster; a_{mf} is the mean field parameter to estimate the cluster–cluster interaction. This second term on the right side containing the a_{mf} parameter and expressing the intercluster interactions is linearly proportional with the density of the liquid or vapor and with the number of molecules in the cluster. E_{ref} denotes the energy of one of the separated molecules constituting the cluster. We choose to add the zero point vibrational energy to E_{tot},

$$E_{i,clust} = E_{i,tot} + ZPVE_i \tag{4}$$

By analogy, E_{ref} also contains this additional term. All the E_{tot} should be the BSSE corrected total energies.

$$q_{i,trans} = \frac{V - V_{excl}}{\Lambda_i^3} \tag{5}$$

where Λ_i is the thermal de Broglie wavelength (Eq. (7)) of the ith cluster with molecular mass m_i. The quantity V_{excl} is the volume filled out by the clusters which can be calculated using the appropriate van der Waals radii of the atoms or using the volume determined quantum mechanically from the electron density,

$$V_{excl} = b_{xv} \sum_i n_i N_A V_i \tag{6}$$

where V_i is the cluster volume and V means the total volume of the system. If the system contains 1 mole monomer units, V is the molar volume (V_m). Thus the $V - V_{excl}$ represents the available free space for translation and this free space depends on the b_{xv} parameter. The thermal de Broglie wavelength is expressed as follows:

$$\Lambda_i = h \Big/ \sqrt{(2\pi m_i k_B T)} \tag{7}$$

$$q_{i,rot} = \frac{1}{\sigma \hbar^3} \sqrt{8\pi (k_B T)^3 I_{A,i} I_{B,i} I_{C,i}} \tag{8}$$

The σ is the symmetry number, i.e. the number of ways the molecule or cluster can be oriented which are indistinguishable from each other, and I_A, I_B, I_C with indices i are the principal moments of inertia for the ith cluster.

$$q_{i,vib} = \prod_{j=1}^{3N-6} (1 - e^{-h\nu_j/k_BT})^{-1} \tag{9}$$

where v_j is the vibrational frequency of the jth normal mode.

Equality of the chemical potential μ_i of each cluster i in equilibrium and renormalization to a total number of molecules to one mol lead to

$$1 = \sum_{i=1}^{c} k(i) q_i \left(\frac{n_1}{q_1}\right)^{k(i)} N_A^{k(i)-1} \tag{10}$$

where N_A is the Avogadro-number and summation is over all the "c" number of cluster forms. The mol number of the ith cluster can thus be expressed as

$$n_i = q_i \left(\frac{n_1}{q_1}\right)^{k(i)} N_A^{k(i)-1} \tag{11}$$

The right hand side of Eq. (10) is strictly monotonically increasing as a function of n_1 in the interval [0,1], so that n_1 can be determined numerically easily to satisfy the equation for value 1.0. This n_1 then determines the $q_{i,trans}$ through V_{excl} (Eq. (5)) in the next iteration. Thus, an iterative process will lead to the values of n_i in the equilibrium. The convergence is fast, one can reach the equilibrium within a few cycles. Because the main focus is on the cluster distribution rather than the quality of the volume prediction by the model we used the experimental densities [37] to calculate the molar volume of the liquid or vapor at different temperatures. Consequently, there was no need to solve Eq. (13) (discussed in the next session) for V but only for the empirical parameter a_{mf}. Note that this parameter has no effect on the cluster distribution! This consideration reduces the parameters which have to be fitted to experimental data and simplifies the model.

2.1.2. Determination of the model parameters a_{mf} and b_{xv}

We have required two conditions to be satisfied in applying the model and in determining the parameters: The calculated pressure (Eqs. (12) and (13)) should be equal to the standard pressure (101,325 Pa) and the boiling point should be equal with the experimental boiling point (337.632 K) at that pressure. The latter was satisfied by setting equal the calculated Gibbs free energies (Eq. (14)) of the two phases at the experimental boiling point. It is possible to obtain this equality by a correct choice of the two empirical parameters a_{mf} and b_{xv}, while keeping the pressure at the standard pressure as detailed later in this section. The pressure for the system is given as partial derivative of the canonical partition function:

$$p = kT\left(\frac{\partial \ln Q}{\partial V}\right)_T \tag{12}$$

After the substitution of the q_i values in Eq. (12) and noting that $q_{i,rot}$ and $q_{i,vib}$ do not depend on the volume of the system, one obtains the following expression (Eq. (13)):

$$\begin{aligned} p &= kT\left(\frac{\partial \ln Q}{\partial V}\right)_T = kT\left(\frac{\partial \sum_{i=1}^{c} N_i[\ln q_{i,elec} + \ln q_{i,trans}]}{\partial V}\right)_T \\ &= kT\left(\frac{\partial \sum_{i=1}^{c} N_i\left[\ln e^{-\Delta E_i/kT} + \ln \frac{V - V_{excl}}{\Lambda_i^3}\right]}{\partial V}\right)_T \\ &= kT\left(\frac{\partial \sum_{i=1}^{c} N_i\left[\ln e^{-(E_i - a_{mf}k(i)/V - k(i)E_1)/kT} + \ln \frac{V - V_{excl}}{\Lambda_i^3}\right]}{\partial V}\right)_T \\ &= kT\sum_{i=1}^{c} N_i\left[\frac{-a_{mf}k(i)}{kT}\frac{1}{V^2} + \frac{1}{V - V_{excl}}\right] \\ &= \sum_{i=1}^{c} N_i\left[-a_{mf}k(i)\frac{1}{V^2} + \frac{kT}{V - V_{excl}}\right] \end{aligned} \tag{13}$$

The Stirling formula does not have to be applied here. Once the partition function Q is known, the Gibbs free energy could be calculated (Eq. (14)) for a given p, T and V. A is the Helmholtz thermodynamics function.

$$G = A + pV = -kT\ln Q + pV \tag{14}$$

where

$$Q = \prod_{i=1}^{c} \frac{q_i^{N_i}}{N_i!} \tag{15}$$

A FORTRAN77 program code was written for evaluating the canonical partition function (Q) and the value of G from the available molecular properties. The following fitting procedure for the two empirical parameters a_{mf} and b_{xv} was used: To determine G for the vapor phase at the boiling temperature a stochastic search has been carried out with random values of a_{mf} and b_{xv}. It was found that b_{xv} has a negligible effect on G in the case of vapor phase but that G is more sensitive to the value of a_{mf}. Because of this a_{mf} dependence, the simple way is to search for a_{mf} by satisfying Eq. (13) and using an approximate value of b_{xv} for determining the Gibbs free energy. Then the same procedure (stochastic search) was used to find a_{mf} and b_{xv} for fixed G and p (1 atm).

Three different approaches (models) for the determination of these two parameters have been used. In *model 1* both a_{mf} and b_{xv} first were fitted at the boiling point of liquid MeOH, a_{mf} (bp) and b_{xv} (bp). It was further assumed that for different temperatures, a_{mf} and b_{xv} are constant for the liquid [a_{mf} (lq) = a_{mf} (bp)] and vapor phase [b_{xv} (vapor) = b_{xv} (bp)], respectively. Thus, optimization at the various temperatures was done only for a_{mf} (vapor) and b_{xv} (lq) by requesting the pressure of the system to be equal to the standard pressure, p = 101,325 Pa. In *model 2*, irrespective of the temperature a constant value of $a_{mf} = a_{mf}$ (bp) was used at all temperatures for both the liquid as well as the vapor phase; similarly, for the vapor phase b_{xv} was kept constant, b_{xv} (vapor) = b_{xv} (bp). For the liquid phase, a temperature-dependent scaling based on the density at the boiling point (ρ_{Tb}) and the respective temperature ρ_{Tb}/ρ_T was applied to b_{xv}, b_{xv} (lq) = b_{xv}(bp) × ρ_{Tb}/ρ_T. Finally, in *model 3*, a_{mf} was optimized for both the liquid and vapor phase and b_{xv} was determined as in *model 2*, b_{xv} (lq) = b_{xv}(bp) × ρ_{Tb}/ρ_T and b_{xv} (vapor) = b_{xv} (bp). Similar to *model 1*, in *model 3* the system was required to be at standard pressure, p = 101,325 Pa.

2.2. Computation of molecular properties

B3LYP/6-31G(d)-optimized cluster structures up to $(MeOH)_8$ were taken from Ref. [15] and further optimized by second order Møller–Plesset perturbation theory [38] using the 6-31+G(d,p) basis set (MP2(fc)/6-31+G(d,p) [39,40]). Some of these structures collapsed upon optimization into identical geometries, resulting in 81 unique clusters. Because of the diffuse functions we have used tight convergence criterion for the wave function convergence and very small integral cutoffs both for SCF and MP2. The 1E-5 Hartree/Bohr geometry convergence criteria were requested. The final frequency analysis was requested via the NVIB = 2 keyword where the wave function and the gradient are evaluated by performing the displacements in both negative and positive Cartesian directions. The optimized structures are available as Supplementary data. Molecular volumes were evaluated by using the 0.001 e/bohr^3 electron density envelope. To consider the basis set superposition error, the BSSE were evaluated with the 6-311++G(d,p) basis set at the MP2(fc) level. No scaling factors were used for the calculated frequencies. Programs used were GAMESS [41] and Gaussian 09 [42].

3. Results and discussion

In the first part, thermochemical quantities, Gibbs free energies G, molar entropies S_m, and constant pressure heat capacities C_p, resulting from the three approaches for determining the empirical parameters a_{mf} and b_{xv} of the QCE model outlined in the previous section, will be presented. In the second part, cluster structures and cluster distributions at various temperatures will be discussed.

3.1. Thermochemical parameters

The parameters a_{mf} and b_{xv}, calculated Gibbs free energy G, deviation Δp from the standard pressure as well as intercluster interaction energies E_{cl-cl} computed from a_{mf} (Eq. (3)), obtained by applying *models 1–3* are presented in Tables 1–3, respectively. A plot of the Gibbs free energy vs. temperature calculated by *model 1* is shown in Fig. 1. The regression lines for the liquid and vapor phase intersect as requested at the experimental boiling point, T = 337.632 K. Analogous plots resulting from applying *model 2* or *model 3* are provided in Figs. S1 and S2 of the Supplementary data. *Model 1* in which b_{xv} (lq) was optimized at the various temperatures, results in a linear temperature dependence of b_{xv} (Fig. 2). Since in both *models 1* and *2* for the liquid phase constant a_{mf} (lq) = a_{mf} (bp) were used, cluster–cluster interaction energies in the liquid phase obtained by these two models are equal (Tables 1 and 2). Similarly, in *model 3* for the vapor phase the same values of a_{mf} and b_{xv} as in *model 1* were used. Hence, both models result in identical Gibbs free energies and intercluster interaction energies for the vapor phase (Tables 1 and 3).

Calculated molar entropies S_m (Eq. (16)) and constant pressure heat capacities C_p (Eq. (17)) are compared with the corresponding experimental data [43–45] in Table 4.

$$\left(\frac{\partial G_m}{\partial T}\right)_p = -S_m \tag{16}$$

$$\left(\frac{\partial H}{\partial T}\right)_p = C_p \tag{17}$$

From the data presented in Table 4 it can be clearly seen that *model 1* gives slightly better agreement with experiment for the liquid phase than *model 2* while *model 3* gives quite poor results, especially for the liquid phase. These findings indicate that the parameter b_{xv} should be optimized in case of liquid phase for the different temperatures. Less sensitivity of the calculated thermochemical parame-

Table 1
Calculated Gibbs free energy G, deviation Δp from standard pressure, and cluster–cluster interaction energies E_{cl-cl} ($N_A a_{mf}/V_m$ based on Eq. (3)) at various temperatures T according to *model 1*.[a]

T/K	ρ/kg m^{-3}	b_{xv}	$a_{mf}/10^{-24}$ J m^3	G/kJ mol^{-1}	Δp/Pa	E_{cl-cl}/J mol^{-1}
298.15	786.327	1.32249295	1.08003512	−64.9152	−0.4	15,961
308.15	776.911	1.33572471	1.08003512	−66.0101	−0.3	15,770
318.15	767.395	1.34907807	1.08003512	−67.1283	0.4	15,577
328.15	757.725	1.36254939	1.08003512	−68.2704	0.0	15,381
337.632	748.359	1.37541310	1.08003512	−69.3763	0.77	15,191
337.632	1.22079	1.37541310	6.47030000	−69.3764	−0.02	148.5
343.15	1.18534	1.37541310	5.16270000	−70.6906	−0.02	115.0
353.15	1.13815	1.37541310	3.97030000	−73.1119	0.03	84.9
363.15	1.10016	1.37541310	3.37820000	−75.5614	0.00	69.9
373.15	1.06600	1.37541310	2.92800000	−78.0283	0.01	58.7

[a] a_{mf} constant for the liquid and b_{xv} constant for the vapor phase.

Table 2
Calculated Gibbs free energy G, deviation Δp from standard pressure, and cluster–cluster interaction energies E_{cl-cl} ($N_A a_{mf}/V_m$ based on Eq. (3)) at various temperatures T according to *model 2*.[a]

T/K	ρ/kg m^{-3}	b_{xv}	$a_{mf}/10^{-24}$ J m^3	G/kJ mol^{-1}	Δp/Pa	E_{cl-cl}/J mol^{-1}
298.15	786.327	1.30900093	1.08003512	−65.0504	−97,379,690	15,961
308.15	776.911	1.32486575	1.08003512	−66.1199	−75,064,381	15,770
318.15	767.395	1.34129460	1.08003512	−67.2077	−51,370,913	15,577
328.15	757.725	1.35841205	1.08003512	−68.3129	−25,972,273	15,381
337.632	748.359	1.37541310	1.08003512	−69.3763	0.8	15,191
337.632	1.22079	1.37541310	1.08003512	−69.2527	4712.0	24.8
343.15	1.18534	1.37541310	1.08003512	−70.5997	3364.7	24.1
353.15	1.13815	1.37541310	1.08003512	−73.0501	2196.1	23.1
363.15	1.10016	1.37541310	1.08003512	−75.5139	1631.6	22.3
373.15	1.06600	1.37541310	1.08003512	−77.9913	1231.8	21.6

[a] a_{mf} and b_{xv} only fitted to the boiling point of the liquid; b_{xv} for the liquid phase scaled by density and constant b_{xv} for the vapor phase.

Table 3
Calculated Gibbs free energy G, deviation Δp from standard pressure, and cluster–cluster interaction energies E_{cl-cl} ($N_A a_{mf}/V_m$ based on Eq. (3)) at various temperatures T according to *model 3*.[a]

T/K	ρ/kg m^{-3}	b_{xv}	$a_{mf}/10^{-24}$ J m^3	G/kJ mol^{-1}	Δp/Pa	E_{cl-cl}/J mol^{-1}
298.15	786.327	1.30900093	0.81153307	−61.0823	−0.1	11,993
308.15	776.911	1.32486575	0.86801507	−63.0240	0.2	12,675
318.15	767.395	1.34129460	0.93131656	−65.0627	0.1	13,432
328.15	757.725	1.35841205	1.00291413	−67.2146	−0.1	14,283
337.632	748.359	1.37541310	1.08003512	−69.3763	0.77	15,191
337.632	1.22079	1.37541310	6.47030000	−69.3764	−0.02	148.5
343.15	1.18534	1.37541310	5.16270000	−70.6906	−0.02	115.0
353.15	1.13815	1.37541310	3.97030000	−73.1119	0.03	84.9
363.15	1.10016	1.37541310	3.37820000	−75.5614	0.00	69.9
373.15	1.06600	1.37541310	2.92800000	−78.0283	0.01	58.7

[a] Parameter a_{mf} optimized for both liquid and vapor phase; b_{xv} for the liquid phase scaled by density and constant b_{xv} for the vapor phase.

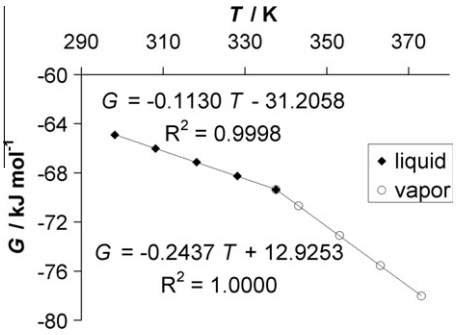

Fig. 1. Plot of the calculated Gibbs free energy of the liquid and vapor phase vs. temperature according to *model 1*.

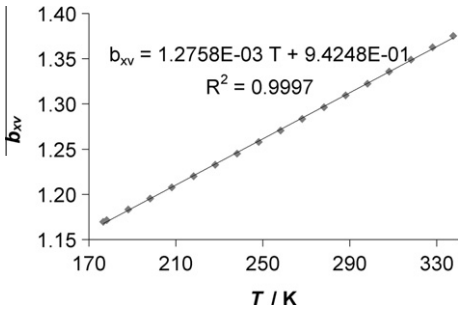

Fig. 2. Temperature dependence of the parameter b_{xv} as obtained from *model 1*.

ters is observed towards a_{mf}. Hence, this parameter can be considered as constant without compromising either the accuracy of thermodynamic quantities or cluster distribution. Since *models 1* and *3* both use the same parameters a_{mf} and b_{xv} for the vapor phase, identical results S(vapor) and C_p(vapor) are obtained. For the vapor phase, *model 2* gives better agreement with experimental data than *model 1* or *model 3*. Apparently, optimization in the vapor phase of a_{mf} while keeping b_{xv} constant leads to less agreement with exper-

Table 4
Calculated by the three models (*m1*, *m2*, and *m3*) and experimental heat capacities C_p and molar entropies S_m at different temperatures for the liquid and vapor phase (data in italics).

T/K	C_p (*m1*)	C_p (*m2*)	C_p (*m3*)	C_p (*exp*)[a]
298.15	71.5	52.2	337.9	81.4 (81.1)
308.15	73.8	53.9	349.3	83.4 (83.2)
318.15	76.2	55.7	360.6	85.4 (85.4)
328.15	78.6	57.4	371.9	87.3 (87.9)
337.632	80.9	59.1	382.7	89.2 (90.5)
337.632	*93.1*	*44.8*	*93.1*	*47.1*
	S_m (*m1*)	S_m (*m2*)	S_m (*m3*)	S_m (*exp*)[b]
298.15	108.3	106.1	187.5	127.19
308.15	110.7	107.9	198.9	129.9
318.15	113.0	109.6	210.2	132.6
328.15	115.4	111.4	221.5	135.3
337.632	117.7	113.0	232.3	137.9
337.632	*238.8*	*243.7*	*238.8*	*245.2*

[a] Experimental data of C_p for liquid phase from Refs. [43] and [44] (in parentheses); for vapor from Ref. [45].
[b] Experimental data of S_m for liquid phase from Ref. [43]; for vapor from Ref. [45].

iment than keeping both parameters constant, a_{mf}(vapor) = a_{mf}(bp) and b_{xv}(vapor) = b_{xv}(bp). It should also be noted that the dependence of the heat capacities on cluster size but separately for individual methanol clusters, ring, lasso, and chain, has been calculated previously [30]. As an explanation for the observed discrepancies with experimental data, neglect of anharmonic contributions to vibrational frequencies has been put forward.

3.2. Cluster distribution and structures

According to the results presented in the previous section, for the liquid phase best agreement with experimental thermochemical data could be achieved when using *model 1*. Hence, the following discussion will be based on this model.

The calculated cluster distributions based on *model 1* for five different temperatures in the range room temperature to boiling point of liquid methanol are presented in Fig. 3. Detailed cluster distributions (mol fraction of monomers bound in a given cluster form or, equivalently, monomer-normalized cluster distribution [36]) for liquid methanol in the temperature range between freezing and boiling point are provided in Table S1 of the Supplementary data. The corresponding vapor phase data are given in Table S2 together with the cluster volumes and energies. Fig. 3 clearly shows that only the cyclic $(MeOH)_5$ and $(MeOH)_6$ clusters are significant in the liquid, ca. 30% $(MeOH)_5$ and 60% $(MeOH)_6$ at room temperature. Thus, our present calculations corroborate the results of Ludwig [30] and are in line with Pauling's proposal of the structure of liquid methanol [10]. The fraction of smaller clusters, especially cyclic $(MeOH)_5$ structures, increases at the expense of cyclic $(MeOH)_6$ by getting closer to the boiling point. In contrast, lowering the temperatures leads to a substantial increase of the cyclic $(MeOH)_6$ clusters; at the freezing temperature approximately 90% of the methanol molecules are in this cyclic hexamer form (Fig. S3 in the Supplementary data).

In analogy to Boyd and Boyd we have adopted the following symbolic notation for the individual clusters [15]: The letters "*u*" and "*d*" indicate the "up" or the "down" position of the methyl group. Parentheses denote cyclic structures; in case of systems containing a ring and branches from that ring, after the parentheses the chains attached to the ring indicated by "*u*" or "*d*", followed by the number of the position where the chain is attached to the ring. The "*dc*" or "*uc*" means that the chain consists of more than one methanol molecule. The chain u/d position is determined relative to the plane of the OH-network, where the (O–H...O) sequence follows the clockwise direction. The notation (CH...O) followed by a number indicates a chain connecting back to the ring with a weak hydrogen-bond at the position of the ring numbered with the same number. Such a weak (CH...O) interaction closes a ring; the smallest example was described for the trimer [18]. The letter "*e*" in equivalent position with the "*u*" or "*d*" means the equatorial position rather than clear up or down. In case of the chain consisting of 8 methanol molecules there was no observable reference in the structure to determine the relative position so it was only marked as chain (8). The letter "*e*" before a symbolic structure means the enantiomer form. To illustrate this symbolic notation, the structure of the CH...O bonded methanol trimer, *due(CH...O)1*, is shown in Fig. 4.

Counterpoise (CP) corrected MP2/6-311++G(d,p) binding energies per monomer (Eq. (18)) of cyclic *n*-mers (n = 3–8) and the dimer are plotted in Fig. 5. This binding energy levels off at the hexamer as also found by Ludwig [30] and Boyd [15]. Beyond this ring size (or the heptamer) no further increase of the hydrogen-bond strength originating from the cooperativity effect can be observed. A maximum binding energy of ca. 30 kJ mol^{-1} per monomer is obtained.

$$\Delta E_{bind,m} = 1/n * [E(\text{cluster}) - nE(\text{monomer})] \quad (18)$$

In cyclic heptamers and octamers the ring is bent (Fig. 6) with the simultaneous formation of some weaker C-H...O hydrogen-bonds. This is in contrast to HF/6-31+G(d,p) calculations which yield flat rings for the lowest energy structures of $(MeOH)_n$, n = 3–8 [19].

4. Conclusion

In this work the quantum cluster equilibrium (QCE) model of Weinhold was applied with the direct use of experimental liquid

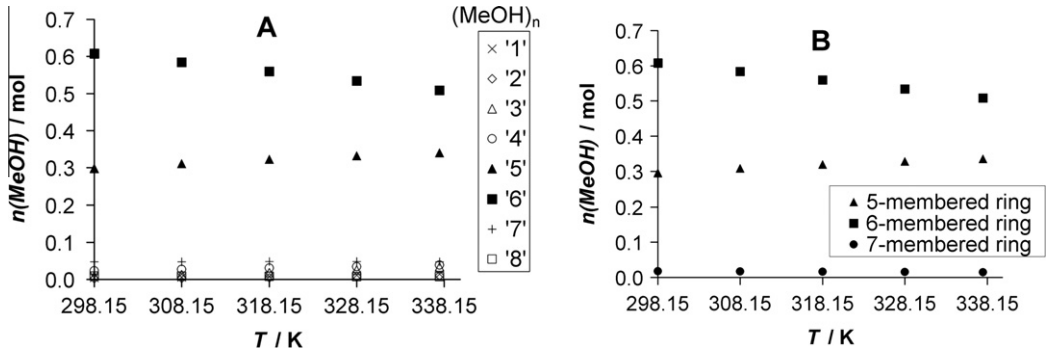

Fig. 3. Temperature dependence of the calculated (*model 1*) distribution of methanol molecules between: (A) clusters of different size irrespective of their structures; and (B): for cyclic pentamers (▲), hexamers (■), and heptamers (●).

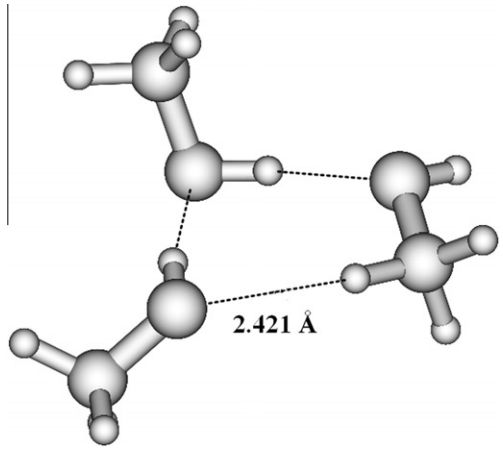

Fig. 4. Structure of the CH...O bonded methanol trimer with the symbolic notation *due(CH...O)1*.

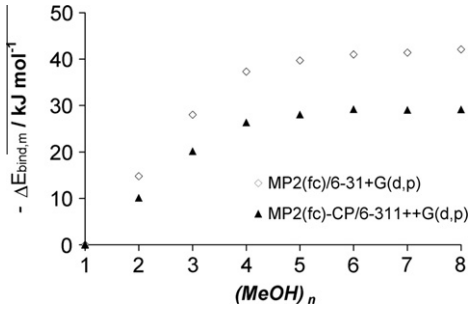

Fig. 5. MP2/6-311++G(d,p) counterpoise-corrected binding energy per monomer, $\Delta E_{bind,m} = 1/n * [E(\text{clust}) - nE(\text{monomer})]$ for lowest energy structures of clusters of different size (cyclic structures for $n \geqslant 3$).

and vapor phase volumes, i.e. *V* was not used in the parameter fit but included as a raw data. The model has been applied for a large cluster set of methanol molecular clusters up to $(MeOH)_8$. Cluster geometries were obtained by second order Møller–Plesset calculations [MP2(fc)/6-31+G(d,p)]; for cluster energies MP2(fc)/6-311++G(d,p) single point calculations including counterpoise corrections, were performed. The preferred clusters up to $(MeOH)_6$ are cyclic structures where the OH hydrogen-bonded network tends to be in a plane. For the $(MeOH)_7$ and $(MeOH)_8$ clusters bent structures with some additional weaker C–H...O hydrogen bonds were found. The dominant cluster in liquid methanol is the cyclic hexamer, even at the boiling point, ca. 50%, followed by the cyclic pentamer, ca 35%. At lower temperatures the amount of *cyclo*-$(MeOH)_6$ increases up to ~90% at the freezing point.

Three approaches to determine the two empirical parameters (a_{mf}, b_{xv}) of the QCE model in combination with the experimental liquid and vapor phase volumes have been used. In previous work only one pair of these two parameters were used for all the temperatures. While calculated thermodynamic properties are quite insensitive to the value of a_{mf}, it was found that the fitting at different temperatures of the parameter b_{xv} for the standard pressure condition significantly affects the results. Especially, for the liquid phase, a_{mf} can be considered as constant. For the vapor phase from our finding the best is to keep these two parameters constant.

Based on the present MP2 results, we also conclude that the computationally less demanding B3LYP procedure – as applied previously for a QCE study of liquid methanol [30] – is sufficiently reliable for this purpose.

Acknowledgement

Financial support by "Wissenschaftlich-technische Zusammenarbeit Österreich – Ungarn" (HU 4/2009, AT-23/2008) and Science, Please! Research Team on Innovation (SROP-4.2.2./08/1/2008-0011) are gratefully acknowledged.

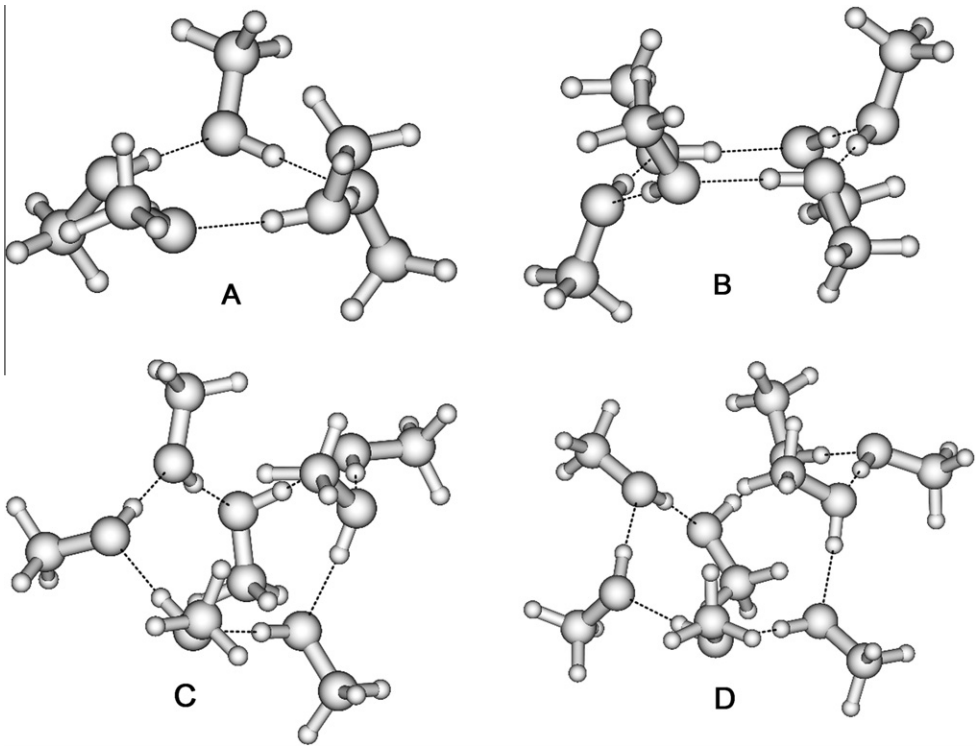

Fig. 6. Minimum energy structures of cyclic $(MeOH)_n$ clusters, $n = 5–8$, (A–D), respectively.

Appendix A. Supplementary data

Supplementary data associated with this article can be found, in the online version, at doi:10.1016/j.theochem.2010.07.003.

References

[1] M.P. Allen, D.J. Tildesley, Computer Simulation of Liquids, Oxford University Press, 1987.
[2] D.L. Cheung, L. Anton, M.P. Allen, A.J. Masters, Comput. Phys. Commun. 179 (2008) 61.
[3] B.D. Todd, D.J. Searles, Chem. Modell. 4 (2006) 324.
[4] M. Sprik, J. Phys. Condens. Matter. 12 (2000) A161.
[5] B.J. Alder, D.M. Ceperley, E.L. Pollock, Acc. Chem. Res. 18 (1985) 268.
[6] G. Malenkov, J. Phys. Condens. Matter. 21 (2009) 283101/1.
[7] F. Paesani, G.A. Voth, J. Phys. Chem. B 113 (2009) 5702.
[8] A.D. Buckingham, J.E. Del Bene, S.A.C. McDowell, Chem. Phys. Lett. 463 (2008) 1.
[9] G.G. Malenkov, J. Struct. Chem. 47 (2006) S1.
[10] L. Pauling, The Nature of the Chemical Bond, Cornell University Press, Ithaca, NY, 1960.
[11] W. Jorgensen, J. Am. Chem. Soc. 103 (1981) 341.
[12] M. Haughney, M. Ferrario, I. McDonald, J. Phys. Chem. 91 (1987) 4934.
[13] M. Valdez-Gonzalez, H. Saint-Martin, J. Hernandez-Cobos, R. Ayala, E. Sanchez-Marcos, I. Ortega-Blake, J. Chem. Phys. 127 (2007) 224507.
[14] J. Handgraaf, T.S. van Erp, E.J. Meijer, Chem. Phys. Lett. 367 (2003) 617.
[15] S.L. Boyd, R.J. Boyd, J. Chem. Theory Comput. 3 (2007) 54.
[16] J. David, D. Guerra, A. Restrepo, J. Phys. Chem. A 113 (2009) 10167.
[17] O. Mo, M. Yanez, J. Elguero, J. Chem. Phys. 107 (1997) 3592.
[18] M. Mandado, A.M. Graña, R.A. Mosquera, Chem. Phys. Lett. 381 (2003) 22.
[19] M.M. Pires, V.F. DeTuri, J. Chem. Theory Comput. 3 (2007) 1073.
[20] F. Weinhold, J. Chem. Phys. 109 (1998) 367.
[21] F. Weinhold, J. Chem. Phys. 109 (1998) 373.
[22] S.B.C. Lehmann, C. Spickermann, B. Kirchner, J. Chem. Theory Comput. 5 (2009) 1640.
[23] S.B.C. Lehmann, C. Spickermann, B. Kirchner, J. Chem. Theory Comput. 5 (2009) 1650.
[24] R. Ludwig, F. Weinhold, T.C. Farrar, Ber. Bunsen-Ges. Phys. Chem. 102 (1998) 197.
[25] R. Ludwig, F. Weinhold, T.C. Farrar, Ber. Bunsen-Ges. Phys. Chem. 102 (1998) 205.
[26] R. Ludwig, F. Weinhold, T.C. Farrar, Mol. Phys. 97 (1999) 479.
[27] M. Huelsekopf, R. Ludwig, J. Mol. Liq. 85 (2000) 105.
[28] M. Huelsekopf, R. Ludwig, J. Mol. Liq. 98–99 (2002) 163.
[29] P. Borowski, J. Jaroniec, T. Janowski, K. Wolinski, Mol. Phys. 101 (2003) 1413.
[30] R. Ludwig, ChemPhysChem 6 (2005) 1369.
[31] R. Ludwig, ChemPhysChem 6 (2005) 1376.
[32] K.N. Rankin, R.J. Boyd, J. Comput. Chem. 22 (2001) 1590.
[33] J. Ireta, J. Neugebauer, M. Scheffler, J. Phys. Chem. A 108 (2004) 5692.
[34] A. Dkhissi, R. Blossey, Chem. Phys. Lett. 439 (2007) 35.
[35] G. Murdachaew, C.J. Mundy, G.K. Schenter, J. Chem. Phys. 132 (2010) 164102.
[36] B. Kirchner, Phys. Rep.-Rev. Sec. Phys. Lett. 440 (2007) 1.
[37] E.W. Lemmon, M.O. McLinden, D.G. Friend, Thermophysical Properties of Fluid Systems, National Institute of Standards and Technology, Gaithersburg, MD 20899. Available from: <http://webbook.nist.gov> (retrieved January 7, 2010).
[38] C. Møller, M.S. Plesset, Phys. Rev. 46 (1934) 618.
[39] P.C. Hariharan, J.A. Pople, Theor. Chim. Acta 28 (1973) 213.
[40] T. Clark, J. Chandrasekhar, G.W. Spitznagel, P.v. Rague Schleyer, J. Comput. Chem. 4 (1983) 294.
[41] M.W. Schmidt, K.K. Baldridge, J.A. Boatz, S.T. Elbert, M.S. Gordon, J.H. Jensen, S. Koseki, N. Matsunaga, K.A. Nguyen, S. Su, T.L. Windus, M. Dupuis, J.A. Montgomery, J. Comput. Chem. 14 (1993) 1347.
[42] M.J. Frisch, G.W. Trucks, H.B. Schlegel, G.E. Scuseria, M.A. Robb, J.R. Cheeseman, G. Scalmani, V. Barone, B. Mennucci, G.A. Petersson, H. Nakatsuji, M. Caricato, X. Li, H.P. Hratchian, A.F. Izmaylov, J. Bloino, G. Zheng, J.L. Sonnenberg, M. Hada, M. Ehara, K. Toyota, R. Fukuda, J. Hasegawa, M. Ishida, T. Nakajima, Y. Honda, O. Kitao, H. Nakai, T. Vreven, J.A. Montgomery Jr., J.E. Peralta, F. Ogliaro, M. Bearpark, J.J. Heyd, E. Brothers, K.N. Kudin, V.N. Staroverov, R. Kobayashi, J. Normand, K. Raghavachari, A. Rendell, J.C. Burant, S.S. Iyengar, J. Tomasi, M. Cossi, N. Rega, J.M. Millam, M. Klene, J.E. Knox, J.B. Cross, V. Bakken, C. Adamo, J. Jaramillo, R. Gomperts, R.E. Stratmann, O. Yazyev, A.J. Austin, R. Cammi, C. Pomelli, J.W. Ochterski, R.L. Martin, K. Morokuma, V.G. Zakrzewski, G.A. Voth, P. Salvador, J.J. Dannenberg, S. Dapprich, A.D. Daniels, O. Farkas, J.B. Foresman, J.V. Ortiz, J. Cioslowski, D.J. Fox, Gaussian 09, Revision A.02, Gaussian Inc., Wallingford, CT, 2009.
[43] H.G. Carlson, E.F. Westrum Jr., J. Chem. Phys. 54 (1971) 1464.
[44] T.S. Khasanshin, T.B. Zykova, Inzh.-Fiz. Zhur. 56 (1989) 991.
[45] L.V. Gurvich, V.S. Iorish, V.S. Yungman, O.V. Dorofeeva, in: D.R. Lide (Ed.), Handbook of Chemistry and Physics, 87th ed., CRC Press, Taylor & Francis, Boca Raton, USA, 2006–2007, pp. 5–49.

THE JOURNAL OF PHYSICAL CHEMISTRY A

ARTICLE

pubs.acs.org/JPCA

Coordination of Methanol Clusters to Benzene: A Computational Study

Gergely Matisz,[†,‡] Anne-Marie Kelterer,[§] Walter M. F. Fabian,[‡] and Sándor Kunsági-Máté*[,†]

[†]Department of General and Physical Chemistry, University of Pécs, Pécs, H-7624, Hungary

[‡]Institute of Chemistry, Karl-Franzens University Graz, Heinrichstr. 28, Graz, A-8010, Austria

[§]Institute of Physical and Theoretical Chemistry, Graz University of Technology, Stremayrgasse 9/I, A-8010 Graz, Austria

Supporting Information

ABSTRACT: Benzene−methanol cluster structures were investigated with theoretical chemistry methods to describe the microsolvation of benzene and the benzene-methanol azeotrope. Benzene−methanol (MeOH) clusters containing up to six methanol molecules have been calculated by ab initio [MP2/6-311++G(d,p)//MP2/6-31+G(d,p) + BSSE correction] method. The BSSE was found quite large with this basis set, hence, different extrapolation schemes in combination with the aug-cc-pVxZ basis sets have been used to estimate the complete basis set limit of the MP2 interaction energy [ΔE(MP2/CBS)]. For smaller clusters, $n \leq 3$, DFT procedures (DFTB+, MPWB1K, M06-2X) have also been applied. Geometries obtained for these clusters by M06-2X and MP2 calculations are quite similar. Based on the MP2/CBS results, the most stable $C_6H_6(MeOH)_3$ cluster is characterized by a hydrogen bonded MeOH trimer chain interacting with benzene via $\pi\cdots$H−O and O$\cdots$H−C(benzene) hydrogen bonds. Larger benzene−MeOH clusters with $n \geq 4$ consist of cyclic $(MeOH)_n$ subclusters interacting with benzene by dispersive forces, to be denoted by $C_6H_6 + (MeOH)_n$. Interaction energies and cooperativity effects are discussed in comparison with methanol clusters. Besides MP2/CBS calculations, for selected larger clusters the M06-2X/6-311++G(d,p)//M06-2X/6-31+G(d,p) procedure including the BSSE correction was also used. Interaction energies obtained thereby are usually close to the MP2/CBS limit. To model the benzene−MeOH azeotrope, several structures for $(C_6H_6)_2(MeOH)_3$ clusters have been calculated. The most stable structures contain a tilted T-shaped benzene dimer interacting by $\pi\cdots$H−O and O$\cdots$H−C (benzene) hydrogen bonds with a $(MeOH)_3$ chain. A slightly less negative interaction energy results for a parallel displaced benzene sandwich dimer with a $(MeOH)_3$ chain atop of one of the benzene molecules.

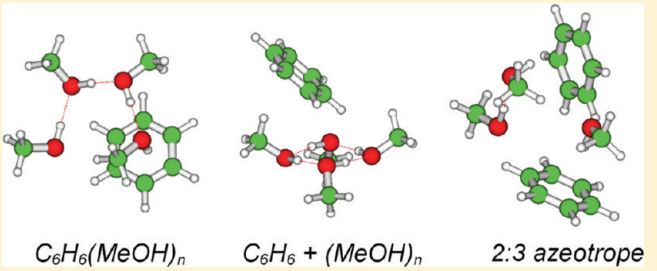

Downloaded via UNIV OF PECS on November 24, 2022 at 08:15:50 (UTC).
See https://pubs.acs.org/sharingguidelines for options on how to legitimately share published articles.

INTRODUCTION

The structures and energetics of weakly bound complexes between π-systems and solvents capable of forming hydrogen bonds have attracted much interest.[1−3] Water and alcohols as prototypes for such solvents themselves are known to form clusters of various sizes and structures. For instance, Pauling has proposed that liquid methanol mainly is composed of cyclic hexamers.[4] The very existence of such clusters forms the basis for the description of thermodynamic properties of the liquid phase by the quantum cluster equilibrium model (QCE).[5−12] Even interaction of nonfunctionalized aromatic molecules with alcohols or their clusters can induce significant changes in their hydrogen bond topology.[3] Besides the O−H$\cdots$O hydrogen bond present in water or alcohol clusters, weak nonconventional O−H$\cdots\pi$, C−H$\cdots\pi$, and C−H$\cdots$O hydrogen bonds have been identified as important in molecular recognition, supramolecular chemistry, the 3D-structure of biological macromolecules, and for clusters of aromatic molecules microsolvated by water or alcohols.[13−15] In view of the importance of such weak interactions, a number of experimental and computational studies on clusters between aromatic molecules and water[16−23] or alcohols, mostly methanol,[24−34] have been published. In addition to clusters of the type $Ar(H_2O)_n$ or $Ar(MeOH)_n$, ternary benzene−$(H_2O)_n$−$(MeOH)_m$[35,36] and (benzene)$_2$−$(MeOH)_3$ clusters[33] have been investigated. The molecular formula of these latter clusters formally corresponds to the composition of the benzene−methanol azeotrope for which recently a unit structure $[(C_6H_6)_2]_4[(MeOH)_4]_3$ has been proposed.[28] Finally, preferential solvation of anthracene in binary alcoholic solutions has been investigated.[37]

Calculations on benzene − methanol complexes $C_6H_6(MeOH)_n$, $n \leq 3$, mostly have been done by density functional theory;[25,38] larger systems were treated by Monte Carlo simulations using the OPLS force field [e.g., $C_6H_6(MeOH)_4$][39] or semiempirical (PM3) methods [e.g., $(C_6H_6)_2(MeOH)_3$].[33] Second order Møller−Plesset calculations are available for fluorobenzene−$(MeOH)_n$, n = 1,2 and p-difluorobenzene−MeOH.[24] Although strong hydrogen bonds usually are

Received: February 7, 2011
Revised: August 10, 2011
Published: August 12, 2011

 © 2011 American Chemical Society

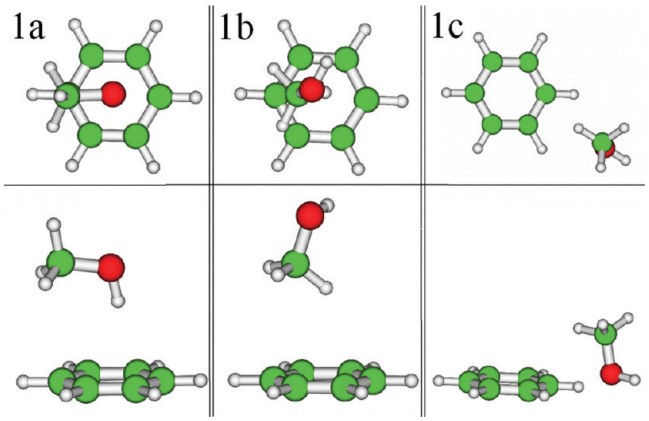

Figure 1. M06-2X/6-31+G(d,p) optimized structures of C_6H_6-$(MeOH)_1$ showing O−H···π (**1a**), C−H···π (**1b**), and O···H−C-(benzene) (**1c**) hydrogen bonds.

reasonably well described by the more popular density functionals,[40] questionable results might be obtained for C−H···O or C−H···π interactions.[41−43] In view of the importance of clusters between aromatic molecules and alcohols as models for microsolvation, we found it worthwhile to investigate computationally larger benzene−methanol clusters $C_6H_6(MeOH)_n$ than done previously, up to n = 6. Moreover, different theoretical levels, tight-binding DFT and DFT using various functionals as well as ab initio procedures (MP2), have been applied. Finally, complexes of the type $[(C_6H_6)_2(MeOH)_3]$, corresponding to the molar composition of the benzene−methanol azeotrope have been treated. These clusters are described with regard to structure, interaction energy and cooperativity effect in this work.

COMPUTATIONAL DETAILS

The initial structures for benzene−methanol complexes $C_6H_6(MeOH)_n$, n = 1−3, were generated by packing optimization.[44] In each case, 2000 structures resulted from placing the methanol molecules randomly within a sphere with r = 10 Å and one benzene at the center of that sphere. These randomly generated structures were then first optimized by the self-consistent charge tight-binding density functional method[45] with inclusion of dispersion corrections (SCC-DFTB+).[46] Further optimization was done by density functionals developed for the correct description of weak intermolecular interactions (MPWB1K[47] and M06-2X[48,49]) and ab initio methods (MP2[50] in the frozen core approximation) using the 6-31+G(d,p) basis set. Based on the results for these species, larger clusters $C_6H_6(MeOH)_n$, n = 2−6, were constructed from $C_6H_6(MeOH)_1$ by successively adding methanol molecules according to the methanol dimer geometry, r(O···H) = 1.8895 Å, α(C−O···H) = 110.3[51] and subsequent optimization. In these clusters, thereafter denoted by $C_6H_6(MeOH)_n$, interaction between the benzene ring and the methanol molecules occurs via O−H···π and (benzene)-C−H···O hydrogen bonding. In other words, cyclic structures comprised of methanol molecules connected by O−H···O hydrogen bonds and the aromatic ring, that is, rings consisting of π(benzene)···H−O···(H−O)$_{n-1}$···H−C (benzene) hydrogen bonds, are formed. A second type of structures, thereafter denoted by C_6H_6 + $(MeOH)_n$, consists of a benzene molecule placed above cyclic $(MeOH)_n$ subclusters obtained previously by MP2/6-31+G(d,p) optimizations.[51] BSSE-corrected[52] interaction energies for these clusters were obtained by MP2/6-311++G(d,p)//MP2/6-31+G(d,p) calculations. The complete basis set (CBS) limit has been evaluated using Martin's extrapolation scheme,[53] originally proposed for CCSD(T) energies, combined with the aug-cc-pVxZ (x = 2−4) basis sets,[54] eq 1 (N corresponds to x in the aug-cc-pVxZ basis sets).

$$E_{corr}(N) = A + B/(N + 1/2)^4 + C/(N + 1/2)^6 \quad (1)$$

The term for N = 5 has been reported to be rather small,[53,54b] hence, we have restricted the calculations to $N \leq 4$. For a number of weakly interacting systems, including the benzene dimer and the hydrogen bonded benzene−water cluster, it has been shown that an analogous CBS extrapolation scheme can also be used for the MP2 procedure.[55] These authors also proposed a modified formulation of the CBS limit for small basis sets (N = 2, 3), eq 2

$$E_{CBS,N} = [E_N(N + 1/2)^3 - E_{N-1}(N - 1/2)^3]/[(N + 1/2)^3 - (N - 1/2)^3] \quad (2)$$

Alternatively, eq 3, where x is the largest angular momentum of the given basis set, has been proposed[56] to estimate the MP2 CBS limit.

$$E(\mathrm{MP2,CBS}) = E(\mathrm{MP2},x) + \text{constant} \times x^{-3} \quad (3)$$

Here we used each one of these schemes.

Programs used were Packmol,[57] DFTB+,[58] GAMESS-US 2009 R3,[59] Gaussian 09,[60] NWChem 6.0,[61] Hyperchem 7.0,[62] and MOLDEN[63] for visualization.

RESULTS AND DISCUSSION

First we will describe structural features obtained by various computational procedures (tight-binding DFT, DFT, and MP2) for $C_6H_6(MeOH)_n$, n = 1−3, clusters. The corresponding interaction energies (DFTB+, MPWB1K, M06-2X, and MP2) are given in Table S1. In the second section, the energetics obtained by MP2 calculations for benzene−methanol clusters up to six methanol molecules will be discussed. In section three, results for $[(C_6H_6)_2(MeOH)_3]$ clusters will be presented.

Structural Features. For the first member of this series, $C_6H_6(MeOH)_1$, in principle, three types of noncovalent interaction, namely, O−H···π (**1a**), C−H···π (**1b**), and (benzene)C−H···O (**1c**) hydrogen bonding, Figure 1, are possible. Pribble et al.[38] have performed B3LYP/6-31+G(d) calculations on $C_6H_6(MeOH)_1$ showing the O−H···π type of interaction. In their calculated structure, the methanol molecule was pulled off the 6-fold axis of benzene. Our DFTB+ calculations result in a similar structure for **1a** with O−H binding to a carbon atom rather than to the center of the aromatic ring. No complex of type **1b**, that is, C−H···π interaction was found by MP2 optimizations; instead, this structure collapsed to **1a**. In the case of (benzene)C−H···O hydrogen bonding, both DFTB+ and MPWB1K calculations resulted in structures with one such interaction; in contrast, M06-2X and MP2 yielded a largely symmetric structure **1c** with two (benzene)C−H···O hydrogen bonds with r(H···O) = 2.51 Å (M06-2X) and r(H···O) = 2.67 Å (MP2). The oxygen atom of the methanol molecules lies approximately in the plane of the benzene ring (Figure 1c). In larger clusters, n = 2 and 3, slight deviations from

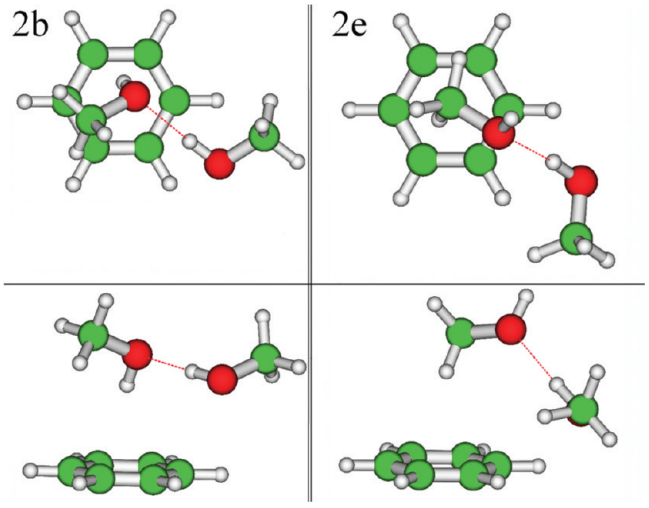

Figure 2. MP2/6-31+G(d,p) optimized structures of $C_6H_6(MeOH)_2$.

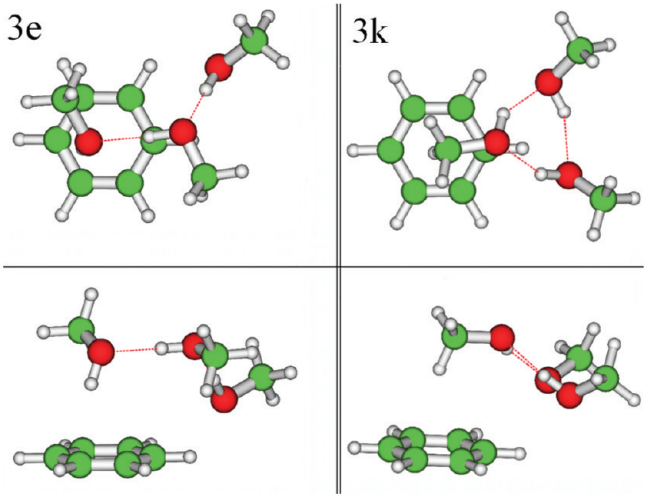

Figure 3. MP2/6-31+G(d,p) optimized structures of $C_6H_6(MeOH)_3$.

this symmetric C−H···O hydrogen bonding occurred. Moreover, the methanol involved in this type of hydrogen bond is pulled off the benzene plane (see Figure 2 for $n = 2$ and Figure 3 for $n = 3$).

Irrespective of the computational procedure used, structure **1a**, characterized by a O−H···π hydrogen bond, is the most stable cluster. Experimentally, formation of such a $C_6H_6(MeOH)_1$ involving interaction between the OH group of methanol and the π-system of benzene had been inferred from the observed red shift of the OH stretching vibration of $\Delta\nu = -43$ cm^{-1} compared with free methanol,[38] much smaller than that resulting from O−H···O hydrogen bonds ($\Delta\nu = -107$ cm^{-1} in the gas phase methanol dimer[64]) but still significant. Calculated shifts are close to this experimental value: $\Delta\nu = -33$ cm^{-1} (B3LYP[38]), -10 cm^{-1} [MP2/6-31+G(d)],[24] and -24 cm^{-1} [MP2/6-31+G(d,p)].

For $C_6H_6(MeOH)_2$ two main types, for example, **2b** and **2e** in Figure 2, can be distinguished at the MP2 level. The first type is characterized by a π···H−O···H−O···H−C(benzene), the second one by a π···H−CO···H−O···H−C(benzene) hydrogen bonding pattern; the notation *type 1* and *type 2* will be used in the following. Common to the lower energy clusters is formation of cyclic structures with participation of the benzene ring. Similar to $C_6H_6(MeOH)_1$ (**1c**), in the $C_6H_6(MeOH)_2$ clusters only one O···H−C(benzene) hydrogen bond is obtained by DFTB+ and MPWB1K. In contrast, nearly symmetric hydrogen bonds between the methanol oxygen and two benzene hydrogens result for **2b** with M06-2X [r(CH···O) = 2.78 and 2.84 Å] and MP2 [r(CH···O) = 2.92 and 2.95 Å]. Again, a shift of one methanol away from the center of the benzene ring toward a carbon atom in *type 1* complexes is found by DFTB+ calculations. Clusters of the *type 1*, that is, those involving a π···H−O hydrogen bond are more stable than clusters of *type 2*. The observed increased red shift of the OH stretching frequency, $\Delta\nu = -76$ cm^{-1} for π···H−O, and $\Delta\nu = -175$ cm^{-1} for O···H−O hydrogen bonds has been attributed to a cooperative strengthening of both hydrogen bonds.[38] Calculations also reveal this effect, $\Delta\nu = -57$ cm^{-1} (B3LYP[38]) and $\Delta\nu = -72$ cm^{-1} [MP2/6-31+G(d,p)] for π···H−O; $\Delta\nu = -189$ cm^{-1} (B3LYP[38]) and $\Delta\nu = -207$ cm^{-1} [MP2/6-31+G(d,p)] for O···H−O hydrogen bonds.

Similar to $C_6H_6(MeOH)_2$ clusters, two types (*type 1* or *type 2*) of structures containing either a π···H−O···H−O···H−O···H(benzene) or a π···H−C···H−O···H−O··· H−C(benzene) hydrogen bonding pattern, were found for $C_6H_6(MeOH)_3$, see **3e** and **3k** in Figure 3. At the MP2 level *type 1* structure **3e** is the most stable one. M06-2X calculations yield *type 2* structure **3c** as the lowest energy cluster. The lowest *type 2* MP2 structure **3k** actually corresponds to a cyclic $(MeOH)_3$ subcluster weakly interacting with benzene, that is, a cluster of the type benzene + $(MeOH)_3$ (see below). In both *type 1* and *type 2* series, two benzene hydrogens form an approximately symmetric hydrogen bond to the oxygen atom of methanol. For instance, in **3e** MP2/6-31+G(d,p) calculations yield r(CH···O) = 2.64 and 2.54 Å. The experimental shift, $\Delta\nu = -5$ cm^{-1}, of the benzene C−H stretches observed in C_6H_6-$(MeOH)_3$ has been attributed to the interaction between the terminal methanol of the $(MeOH)_3$ chain with the C−H bonds of benzene.[25] In our calculations, a shift of -9 cm^{-1} has been found for conformer **3e**.

Addition of the third methanol molecule results in an even further strengthening of the π···H−O and the O···H−O hydrogen bonds, as evidenced by the respective experimental (-92, -246, and -292 cm^{-1})[38] and MP2/6-31+G(d,p) calculated frequency shifts, $\Delta\nu = -84$, -277, and -341 cm^{-1} in **3e**.

In the free methanol trimer, a cyclic arrangement of the methanol molecules has been observed experimentally with a single OH stretch band red-shifted by 219 cm^{-1} with respect to the methanol monomer.[64] In contrast, experiments clearly show that the $C_6H_6(MeOH)_3$ cluster contains a linear arrangement of the three methanol molecules;[38] a cyclic structure results only by participation of the benzene ring. Interestingly, larger benzene−methanol clusters, $C_6H_6(MeOH)_n$, $n \geq 4$, apparently consist of the benzene molecule interacting with cyclic methanol subclusters $(MeOH)_n$, because only red shifts of the OH stretch characteristics for strong O−H···O hydrogen bonds could be observed.[38] So far structural features of the C_6H_6 + $(MeOH)_n$ clusters with $n \geq 4$ have only be described on the basis of force field calculations.[39] For instance, for C_6H_6 + $(MeOH)_4$ mainly interaction of one methyl group of the cyclic $(MeOH)_4$ subcluster on a single side of benzene had been predicted. Later, alternative structures with benzene interacting edge-on with the $(MeOH)_n$ cavity, were proposed.[38] In the following, both possibilities for benzene−methanol clusters with $n = 3 - 6$, namely, those characterized by π···H−O···[H−O]$_{n-1}$···H−C(benzene) hydrogen bonds ($C_6H_6(MeOH)_n$, **3e** and **4a**−**6a** in Figure 4), as

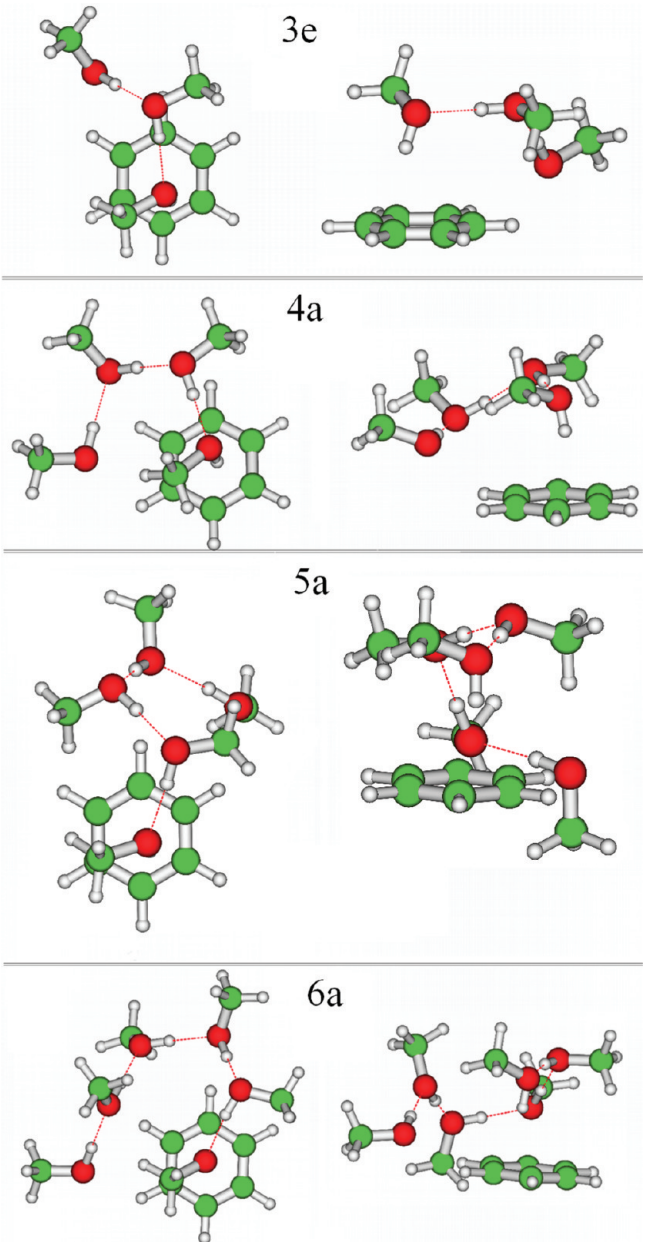

Figure 4. MP2/6-31+G(d,p) lowest energy structures of $C_6H_6(MeOH)_n$, $n = 3-6$ clusters with O−H···π hydrogen bonds (**3e**, **4a**−**6a**).

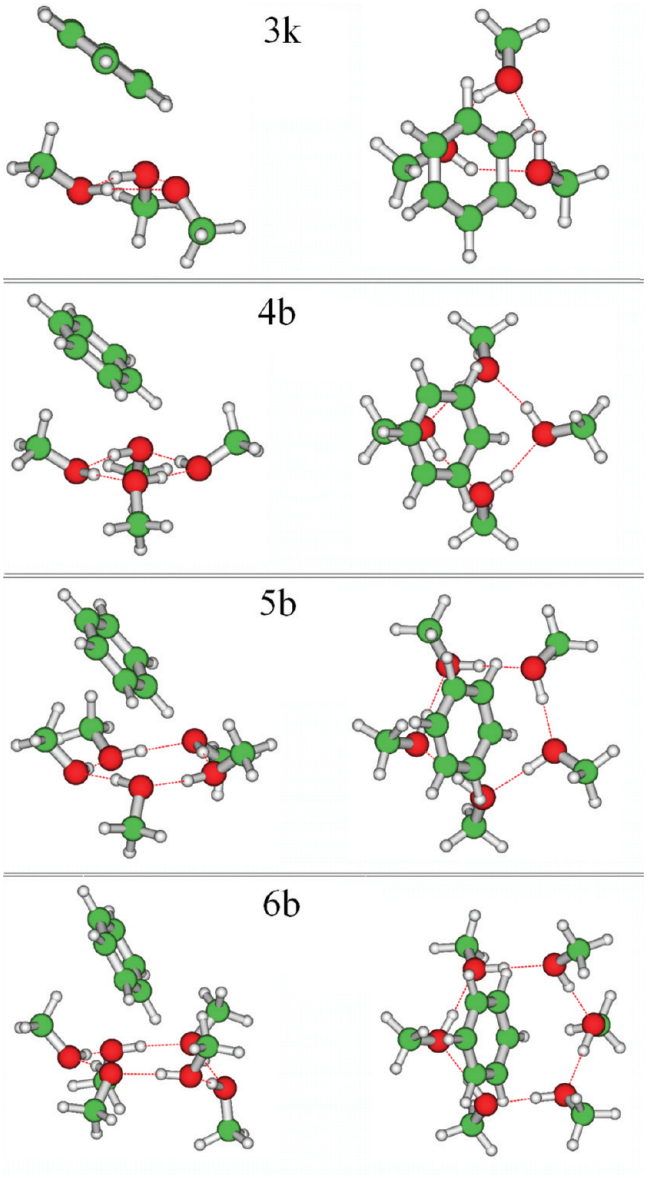

Figure 5. MP2/6-31+G(d,p) lowest energy structures of C_6H_6 + $(MeOH)_n$, $n = 3-6$ clusters with C−H···π hydrogen bonds between benzene and $(MeOH)_n$ subclusters (**3k**, **4b**−**6b**).

well as clusters consisting of one benzene molecule interacting with $(MeOH)_n$ subclusters (C_6H_6 + $(MeOH)_n$, **3k** and **4b**−**6b** in Figure 5), will be discussed. In **4a**, the OH group of the first methanol molecule in the $(MeOH)_4$ chain is shifted off the center of the benzene ring toward one carbon atom [r(C···HO) = 2.44 Å]; the benzene C−H in *para* position to this carbon atom makes a close contact to the third methanol molecule [r(C−H···O)] = 2.53 Å. The distance of the fourth MeOH to the adjacent benzene C−H bond is 2.67 Å. According to the MP2 calculations, in the C_6H_6 + $(MeOH)_n$ species the structure of the cyclic methanol subclusters is largely unchanged compared with the corresponding free $(MeOH)_n$ rings. Interaction with the benzene molecule occurs via a (methanol) C−H···π dispersive bond on one side of benzene. The benzene ring is tilted with respect to the normal to the $(MeOH)_n$ plane, pointing with one single C−H bond toward it, Figure 5. For instance, in **4b**, one of the C−H bonds of the methanol methyl groups is nearly symmetrically placed atop the benzene ring; the distances to the six benzene carbon atoms are in the range 2.83−2.98 Å. The closest benzene C−H···O distance is 2.52 Å.

Energetic Aspects of $C_6H_6(MeOH)_n$ and C_6H_6 + $(MeOH)_n$ Clusters. The following discussion of the energetic aspects of these clusters is largely based on the MP2/6-31+G(d,p) structures of these $C_6H_6(MeOH)_n$, $n = 1-6$, and C_6H_6 + $(MeOH)_n$, $n \geq 3$ clusters. Energies were calculated by M06-2X and MP2 using the 6-311++G(d,p) basis set. In addition, MP2 calculations were also performed with the aug-cc-pVxZ basis set, with x = 2−4 for $n \leq 3$ and 2−3 for $n = 4-6$ and extrapolated to the CBS limit. Unless very large basis sets are used, for example, aug-cc-pV5Z, correcting for basis set superposition error is essential. Hence, this correction has been applied to all the calculated interaction energies. The corresponding BSSE-corrected

Table 1. M06-2X/6-311++G(d,p), and MP2 Calculated Interaction Energies Including BSSE Corrections and Different CBS Extrapolation Schemes

	M06-2X	MP2							
			aug-cc-pVNZ			I[a]	II[b]		III[c]
$E_{WW+BSSE}$	6-311++G(d,p)	6-311++G(d,p)	$N = 2$	$N = 3$	$N = 4$	$N = 2-4$	$N = 3$	$N = 4$	$N = 2-4$
water−benzene	−16.5	−10.3	−12.7	−14.1	−14.5	−14.7	−14.9	−14.8	−14.7
1a	−19.0	−12.8	−16.7	−18.8	−19.3	−19.6	−19.9	−19.8	−19.6
1c	−12.1	−7.9	−10.0	−10.9	−11.2	−11.4	−11.4	−11.5	−11.3
2b	−53.5	−40.2	−47.6	−51.7	−53.1	−54.0	−54.0	−54.3	−53.7
2e	−39.8	−33.9	−39.3	−42.6	−43.9	−44.7	−44.5	−44.7	−44.3
3e	−97.6	−74.5	−85.7	−92.7	−95.1	−96.7	−96.8	−97.2	−96.2
3k	−99.2	−73.8	−83.8	−90.5	−92.9	−94.7	−94.4	−95.1	−93.9
4a	−137.0	−107.5	−122.8	−132.7			−138.4		
4b	−150.4	−119.5	−134.9	−145.6			−151.8		
5a	−175.1	−138.7	−157.8	−170.5			−177.8		
5b	−195.9	−157.4	−177.4	−191.6			−199.7		
6a	−221.3	−175.7	−197.1	−212.8			−221.8		
6b	−236.0	−192.6	−214.9	−231.7			−241.4		
7a		−92.0	−108.8	−118.0			−123.3		
7d		−89.5	−106.0	−114.7			−119.3		

[a] CBS extrapolation using eq 1. [b] CBS extrapolation using eq 2 with $N = 3$ and $N = 4$. [c] CBS extrapolation using eq 3.

interaction energies obtained by M06-2X/6-311++G(d,p), MP2/6-311++G(d,p), as well as MP2/CBS calculations, are given in Table 1. The BSSE corrections to MP2/6-311++G(d,p) results are quite large resulting in a significant reduction of the interaction energies. Previous MP2/6-31+G(d,p) studies[24,65] of benzene containing clusters have indicated an underestimation of interaction energies when BSSE corrections were used. This apparently is also the case when using the 6-311++G(d,p) basis set. Weak O−H···π hydrogen bonding interactions have been thoroughly studied computationally in the benzene−water cluster, including a comparison between MP2 and CCSD(T) BSSE corrections to interaction energies.[55,66−69] These calculations will serve as benchmark for evaluation of the procedures used here (Table 1). Depending on the geometry and extrapolation scheme used MP2/CBS values between −16.3 to −14.5 kJ mol^{-1} have been reported; CCSD(T)/CBS benzene−H_2O interaction energies are −14.0[55] and −13.7[70] kJ mol^{-1}. Dispersion corrected DFT (B3LYP-DCP/6-31+G(d,p))[66] and M06-2X calculations[69] yielded −13.4 and −14.2 kJ mol^{-1}, respectively. Compared with these data, our M06-2X and MP2 interaction energies obtained with the 6-311++G(d,p) basis set are slightly over- and underestimated (−16.5 and −10.3 kJ mol^{-1}, Table 1). The MP2/CBS benzene − H_2O interaction energies, −14.7 to −14.9 kJ mol^{-1} (Table 1) are in good agreement with those discussed above. Moreover, the different extrapolation schemes, eqs 1−3, yield nearly identical results. Most importantly, MP2/CBS interaction energies obtained by eq 2 with $N = 3$, that is, the aug-cc-pVDZ and aug-cc-pVTZ basis sets, only marginally differ from those using $N = 4$, that is, the aug-cc-pVTZ and aug-cc-pVQZ basis sets. Hence, we expect that the MP2/CBS interaction energies for the larger clusters where aug-cc-pVQZ calculations were not feasible, can be estimated with sufficient accuracy by eq 2 with $N = 3$.

Similar results also hold for the benzene−methanol clusters. Especially, MP2/6-311++G(d,p) calculations significantly underestimate interaction energies. MP2/CBS results are quite insensitive to the extrapolation scheme used. When applying Martin's extrapolation scheme, eq 1, for BSSE-corrected, as well as uncorrected interaction energies the BSSE error in the CBS limit is below 2%; eq 2 with $N = 3$ results in an error of only ∼5%. Hence, for the following discussion MP2/CBS interaction energies resulting from eq 2 with $N = 3$ will be used because MP2/aug-cc-pVQZ calculations were not feasible for the larger clusters. Treating electron correlation at a higher level [MP4, CCSD(T) aug-cc-pVDZ basis set] yields interaction energies for **1a** of ΔE_{int} = −15.7 (MP4) and −14.4 [CCSD(T)] kJ mol^{-1}; for **1c** of ΔE_{int} = −14.4 (MP4) and −9.0 [CCSD(T)] kJ mol^{-1}.

M06-2X/6-311++G(d,p) generally yields results closer to the MP2/CBS limit than MP2/6-311++G(d,p) calculations (Table 1). The mean M06-2X BSSE error compared to the uncorrected values is ∼13% and the BSSE-corrected M06-2X results are within 1.5 kJ mol^{-1} of the MP2/CBS limit obtained by eq 2, $N = 3$. However, as already seen in $C_6H_6(MeOH)_1$ clusters (cf. **1a** with **1b**), the M06-2X functional apparently overestimates the stability of the C−H···π interaction compared to MP2 (cf. **3e** with **3k**). Hence, for **3k** a larger difference M06-2X versus MP2/CBS of ∼5 kJ mol^{-1} is found (Table 1). Previous extensive calculations on uracil dimers are in line with this finding. Using CCSD(T)/CBS results as reference, the stability of stacked dimers was slightly overestimated compared with hydrogen-bonded structures.[71] For the clusters containing three methanol molecules ($n = 3$) both $C_6H_6(MeOH)_3$ and C_6H_6 + $(MeOH)_3$ have comparable interaction energies with a slight preference for the former structure involving π···H−O and O···H−C-(benzene) hydrogen bonds, ΔE_{int} = −96.8 versus −94.4 kJ mol^{-1}. For larger clusters, $n \geq 4$, structures resulting from interaction of benzene with cyclic methanol n-mers $(MeOH)_n$, **4b**−**6b**, clearly are more stable than their $C_6H_6(MeOH)_n$ counterparts **4a**−**6a** (Figure 6).

The magnitude of the O−H stretch frequency shifts have been interpreted in terms of significant cooperative strengthening of

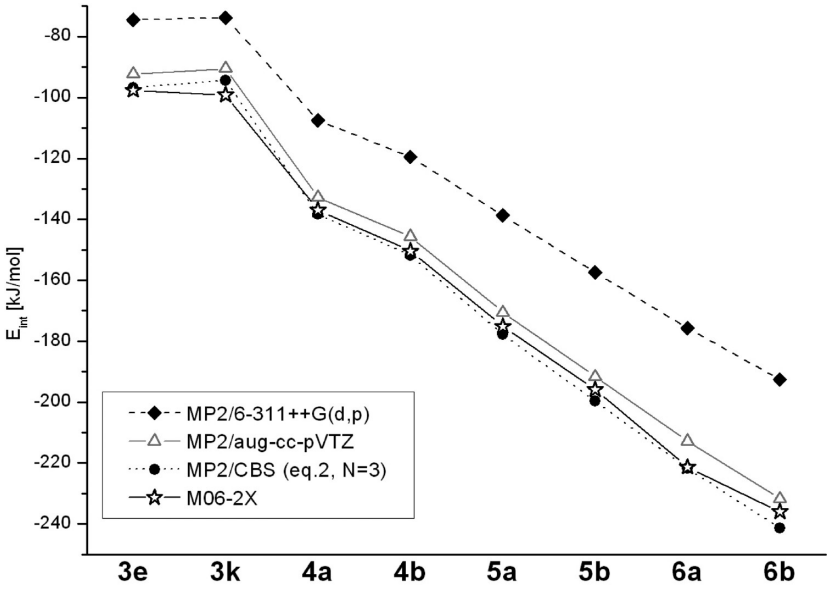

Figure 6. BSSE-corrected interaction energies (MP2/6-311++G(d,p), M06-2X/6-311++G(d,p), MP2/CBS (eq 2, $N = 3$)) for $C_6H_6(MeOH)_n$, n = 3−6 clusters with O−H···π hydrogen bonds (**3e**, **4a**−**6a**) and $C_6H_6 + (MeOH)_n$, n = 3−6 clusters with C−H···π hydrogen bonds between benzene and $(MeOH)_n$ subclusters (**3k**, **4b**−**6b**).

Table 2. BSSE-Corrected Cooperativity Energy per Hydrogen Bond, ΔE_{coop}/Hydrogen Bond (kJ mol^{-1})

$MeOH_n$	ΔE_{coop}/hydrogen bond			$C_6H_6(MeOH)_n$	ΔE_{coop}/hydrogen bond		
N	I[a]	II[b]	III[c]	n	I[a]	II[b]	III[c]
2	0.0	0.0	0.0	2	0.3	0.4	0.4
3	0.1	−0.1	−0.3	3	−3.3	−4.3	−4.5
4	−6.1	−7.9	−8.1	4	−5.3		−7.1
5	−7.8	−9.9	−9.5	5	−6.2		−8.6
6	−8.9	−11.0	−11.3	6	−7.6		−10.2

[a] MP2(fc)/6-311++G(d,p). [b] MP2/CBS, eq 1. [c] MP2/CBS, eq 2, $N = 3$.

the π···H−O and O···H−O bonds in $C_6H_6(MeOH)_2$ compared with those in $C_6H_6(MeOH)_1$ and $(MeOH)_2$. In the following, the cooperativity on interaction energies of cyclic $(MeOH)_n$ n-mers[51] and $C_6H_6(MeOH)_n$ clusters of the π···H−O···[H−O]$_{n-1}$···H−C(benzene) type, ΔE_{coop}, will be discussed. The BSSE-corrected interaction energy of the methanol dimer is ΔE_{int} = −20.3 [MP2/6-311++G(d,p)[51]], −24.2 (MP2/CBS, eq 1), and −23.8 kJ mol^{-1} (MP2/CBS, eq 2, $N = 3$). Cyclic $(MeOH)_n$ n-mers contain n O−H···O hydrogen bonds, thus, $\Delta E_{coop} = \Delta E_{int}[(MeOH)_n] - n \times \Delta E_{int}[(MeOH)_2]$. In $C_6H_6(MeOH)_n$ clusters in addition to $n - 1$ H−O···H hydrogen bonds, one π···H−O and one O···H−C(benzene) interaction occur. Exactly one of these interactions is present in **1a** (π···H−O) and **1c** [O···H−C(benzene)]. Thus, for all presented clusters ΔE_{coop} is given by $\Delta E_{coop} = \Delta E_{int}[C_6H_6(MeOH)_n] - (n - 1) \times \Delta E_{int}[(MeOH)_2] - \Delta E_{int}$(**1a**) − ΔE_{int}(**1c**). The MP2/6-311++G(d,p) BSSE-corrected interaction energies for these two nonconventional hydrogen bonds in $C_6H_6(MeOH)_1$ are −12.8 (**1a**) and −7.9 (**1c**) kJ mol^{-1}; the corresponding MP2/CBS values are −19.6 and −11.4 kJ mol^{-1} (eq 1); and −19.9 and −11.4 kJ mol^{-1} (eq 2, $N = 3$), Table 1. The cooperativity per hydrogen bond, ΔE_{coop}/hydrogen bond is larger (more negative) in the $C_6H_6(MeOH)_3$ cluster than in $(MeOH)_3$, Table 2. In contrast, for $n \geq 4$ the cyclic methanol n-mers have stronger cooperativity, because ΔE_{coop}/H-bond is larger (more negative) than in the $C_6H_6(MeOH)_n$ clusters. Thus, for $n \geq 4$ clusters of the type $C_6H_6 + (MeOH)_n$ will be preferentially formed. Despite the increased red shift of both OH stretching frequencies in $C_6H_6(MeOH)_2$ (see above), the value of ΔE_{coop}/hydrogen bond does not indicate any cooperativity in forming this structure. Most probably, this discrepancy between conclusions inferred from ΔE_{coop}/hydrogen bond versus $\Delta\nu$ is due to the distortion from the optimal geometry for O···H−C(benzene) hydrogen bonding. Whereas in $C_6H_6(MeOH)_1$ (**1c** in Figure 1) the oxygen atom of the methanol molecule lies in the plane of the benzene ring, the methanol molecule interacting with the benzene C−H bonds in $C_6H_6(MeOH)_2$ is significantly pulled off this plane (**2b** in Figure 2).

$[(C_6H_6)_2(MeOH)_3]$ Clusters. By a combination of resonant two-photon ionization, resonant ion-dip infrared and IR-UV hole-burning spectroscopies two structural isomers of $[(C_6H_6)_2(MeOH)_3]$ clusters have been identified[33] and possible structures suggested based on semiempirical (PM3) calculations. In the construction of these models it had been assumed that the T-shaped structure of the benzene dimers[72−74] will be largely retained in these two isomers.[33] In one of these isomers (Isomer B), the top benzene of the tee interacts with the $(MeOH)_3$ chain via a π···H−O hydrogen bond (and possibly also by a O···H−C(benzene) hydrogen bond to the same benzene ring). In the second isomer (Isomer A), a π···H−O to the stem and a O···H−C(benzene) hydrogen bond to the top benzene, respectively, of the benzene dimer was suggested.[33] Besides this T-shaped structure of the benzene dimer, the parallel displaced arrangement of the two benzene molecules is nearly isoenergetic.[75−77] Hence, besides several structures similar to Isomer A, Figure 7**a**−**c**, with nearly equal interaction energies also a parallel displaced sandwich dimer of benzene with a $(MeOH)_3$ chain atop one of the benzene rings, Figure 7**d**, were

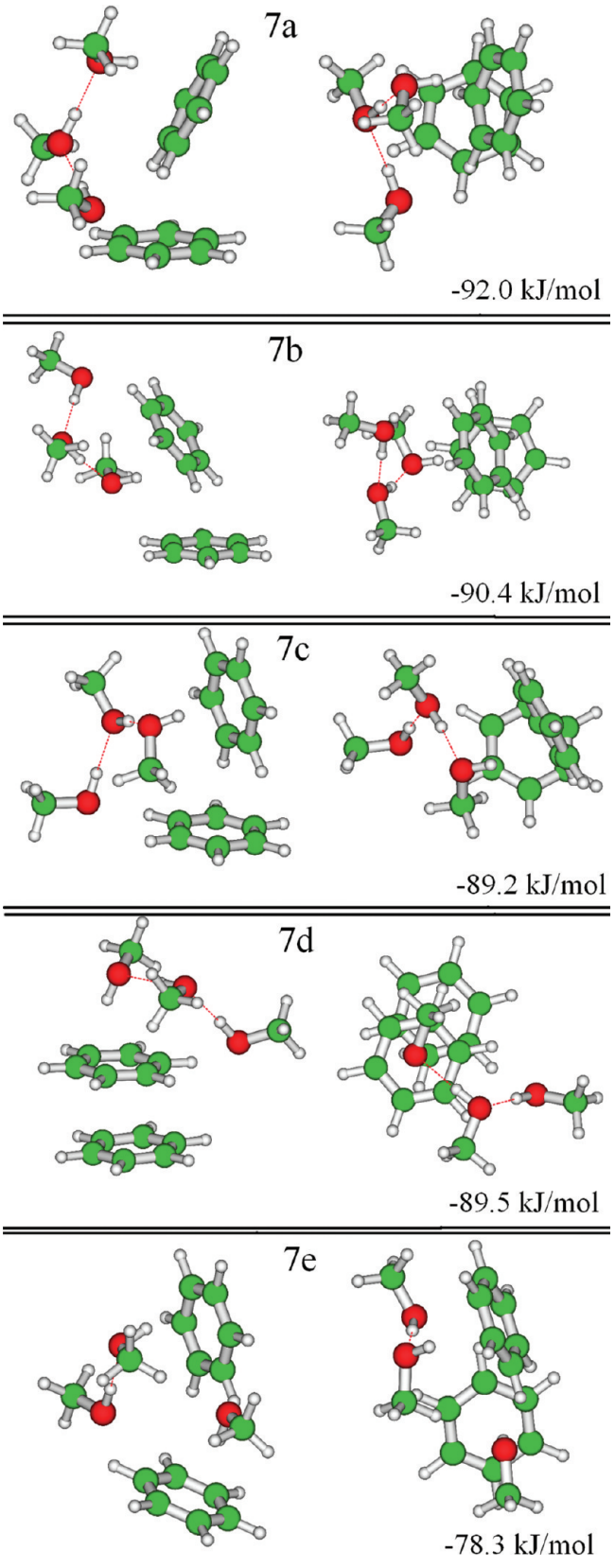

Figure 7. MP2/6-31+G(d,p) lowest energy structures of $(C_6H_6)_2$-$(MeOH)_3$ clusters and BSSE-corrected interaction energies..

found. In contrast, no $[(C_6H_6)_2(MeOH)_3]$ cluster corresponding to Isomer B could be obtained. Benzene and methanol form a binary azeotrope in the mole ratio 2:3 with a minimum boiling point at 55.76 °C at 678 mm Hg.[28] Recently, a unit-structure for the azeotrope composed of four benzene sandwich dimers and three cyclic methanol tetramers, $[(C_6H_6)_2]_4[(MeOH)_4]_3$, has been proposed.[28] Structure **7d** closely resembles a simplified model for this proposed structure. Besides $\pi\cdots$H−O and O···H−O hydrogen bonds benzene−benzene $\pi\cdots\pi$ interactions are present in **7d**. This isomer actually can be considered as cluster **3e** with an additional $\pi\cdots\pi$ interaction between two parallel displaced benzene molecules. The MP2 calculated interaction energies for such an arrangement (structure "Daa" in ref [75b]) are −17.2 (aug-cc-pVTZ) and −20.6 kJ mol^{-1} (CBS limit).[75b] The CCSD(T) CBS limit for the DZ-TZ basis set[75b] was given as −9.6 kJ mol^{-1}. Also comparable to the benzene dimer in **7d** is structure "Bz2/D", for which the RI-MP2 and CCSD(T) CBS limits are given as −20.6 and −11.0 kJ mol^{-1}, respectively.[55] Using the MP2/aug-cc-pVTZ BSSE-corrected interaction energy for **7d** and the corresponding data for **3e** and "Daa",[75b] the cooperativity in **7d** can be estimated as −2.3 kJ mol^{-1}.

The relatively compact structure **7e** with the maximum number of O−H···π and C−H···O hydrogen bonds and one O−H···O hydrogen bond has a lower interaction energy than all the other $[(C_6H_6)_2(MeOH)_3]$ clusters. The benzene−benzene interaction is broken in **7e** by one methanol shifted between the two tee benzenes and therefore exhibits less dispersion interaction. Furthermore, one O−H···O has also been broken, thus contributing to the lowering of the interaction energy.

CONCLUSION

Ab initio (MP2), tight-binding self-consistent charge DFT with dispersion correction (SCC-DFTB+) and DFT methods using various functionals (MPWB1K, M06-2X) were used to investigate benzene−methanol clusters $C_6H_6(MeOH)_n$, n = 1−6. Two different types of cluster structures were found. The first type consists of $(MeOH)_n$ chains connected through $\pi\cdots$H−O and O···H−C(benzene) hydrogen bonds to the benzene ring; thus, for $n \geq 2$ a cyclic cluster resulting from participation of the benzene ring, characterized by a $\pi\cdots$H−O···[H−O]$_{n-1}$···H−C(benzene) hydrogen bond pattern, was formed. The second type consists of cyclic $(MeOH)_n$ subclusters ($n \geq 3$) weakly interacting with the benzene molecule. For n = 3, both types have nearly the same interaction energy, with a small preference for the first type containing a $(MeOH)_3$ chain over the second type, benzene + cyclic $(MeOH)_3$ subcluster, ΔE_{int} [BSSE-corrected MP2/CBS//MP2/6-31+G(d,p), eq 2, N = 3] = −96.8 and −94.4 kJ mol^{-1}, respectively. For $n \geq 4$ there is a clear preference for the second type of clusters, C_6H_6 + $(MeOH)_n$, as found by experiment.[38] BSSE-corrected M06-2X/6-311++G(d,p) interaction energies usually are close to the MP2/CBS values.

In addition to structures of the molecular formula C_6H_6-$(MeOH)_n$, also isomeric $(benzene)_2$−$(MeOH)_3$ clusters, corresponding to the composition of the benzene−methanol azeotrope, were considered. Several structures closely resembling that of Isomer A,[33] containing a $(MeOH)_3$ chain connected by O−H···π and O···H−C(benzene) interactions to the stem and top benzene molecules, respectively, of a T-shaped benzene dimer, were found. In contrast, optimization of a structure corresponding to Isomer B resulted in a geometry consisting of a parallel displaced benzene sandwich dimer with a $(MeOH)_3$ chain atop one of the benzene molecules. The calculated

interaction energies [BSSE-corrected MP2/6-311++G(d,p)//MP2/6-31+G(d,p)] of these clusters are quite similar, ΔE_{int} = −89.2 to −92.0 kJ mol^{-1}. The BSSE-corrected MP2/CBS interaction energies for clusters **7a** (T-shaped benzene dimer) and **7d** (parallel displaced benzene dimer) are −123.3 and −119.3 kJ mol^{-1}. Cooperativity effects play a key role in the stabilization of the cluster geometries. Finally, it should be pointed out that the BSSE correction is both approximate and absolutely necessary. Only with very large basis sets, for example, aug-cc-pV5Z, this correction goes to zero. The relatively good performance of M06-2X, even with relatively small basis sets, may be attributed to the presence of weakly interacting molecules in the database used for parametrization of this functional. Calculations on the benzene dimer and its solvation are generally accurate to 4 kJ mol^{-1}. Hence, in any present day experiment, for example, in supersonic beams, all structures within this energy range can be expected to be present in the sample under investigation.

■ ASSOCIATED CONTENT

Supporting Information. Interaction energies (DFTB+, MPWB1K, M06-2X, MP2/6-31+G(d,p); Table S1); Cartesian coordinates of the optimized cluster geometries (MP2(fc)/6-31+G(d,p); DFTB+, MPWB1K/6-31+G(d,p), and M06-2X/6-31+G(d,p)) plot of MP2(fc)/6-31+G(d,p) optimized structures for **2a** versus **2b** and **2d** versus **2e** (Figure S1). This material is available free of charge via the Internet at http://pubs.acs.org.

■ AUTHOR INFORMATION

Corresponding Author

*Phone: + 36 72-503-600 (4208). Fax: + 36 72-503-635. E-mail: kunsagi@gamma.ttk.pte.hu.

■ ACKNOWLEDGMENT

Financial support by "Wissenschaftlich-Technische Zusammenarbeit Österreich—Ungarn" (HU 4/2009) and Developing Competitiveness of Universities in the South Transdanubian Region (SROP-4.2.1.B-10/2/KONV-2010-0002) projects are gratefully acknowledged. Generous computer time was provided at the IBM HPC supercomputer located at the Babes-Bolyai University in Cluj Napoca/Romania within the RO-14/2007 Intergovernmental projects.

■ REFERENCES

(1) Brutschy, B. *Chem. Rev.* **2000**, *100*, 3891–3920.
(2) Kim, K. S.; Tarakeshwar, P.; Lee, J. Y. *Chem. Rev.* **2000**, *100*, 4145–4185.
(3) Suhm, M. A. *Adv. Chem. Phys.* **2009**, *142*, 1–57.
(4) Pauling, L. In *The Nature of the Chemical Bond*; Cornell University Press: Ithaca, NY, 1960.
(5) Weinhold, F. *J. Chem. Phys.* **1998**, *109*, 367–373.
(6) Weinhold, F. *J. Chem. Phys.* **1998**, *109*, 373–384.
(7) Kirchner, B. *Phys. Rep.-Rev. Sec. Phys. Lett.* **2007**, *440*, 1–111.
(8) Ludwig, R.; Weinhold, F.; Farrar, T. C. *Mol. Phys.* **1999**, *97*, 479–486.
(9) Huelsekopf, M.; Ludwig, R. *J. Mol. Liq.* **2000**, *85*, 105–125.
(10) Huelsekopf, M.; Ludwig, R. *J. Mol. Liq.* **2002**, *98−99*, 163–171.
(11) Ludwig, R. *ChemPhysChem* **2005**, *6*, 1369–1375.
(12) Lehmann, S. B. C.; Spickermann, C.; Kirchner, B. *J. Chem. Theory Comput.* **2009**, *5*, 1640–1649.
(13) Desiraju, G. R.; Steiner, T. *The weak hydrogen bond in structural chemistry and biology*; Oxford University Press: Oxford, 1999.
(14) Jeffrey, G. A. *An introduction to hydrogen bonding*; Oxford University Press: Oxford, 1997.
(15) Nishio, M.; Hirota, M.; Umezawa, Y. In *The CH /π interaction: evidence, nature, and consequences*; Wiley-VCH: New York, 1998.
(16) Ahn, D. S.; Park, S. W.; Lee, S.; Kim, B. *J. Phys. Chem. A* **2003**, *107*, 131–139.
(17) Barth, H. D.; Buchhold, K.; Djafari, S.; Reimann, B.; Lommatzsch, U.; Brutschy, B. *Chem. Phys.* **1998**, *239*, 49–64.
(18) Gruenloh, C. J.; Carney, J. R.; Hagemeister, F. C.; Zwier, T. S.; Wood, J. T.; Jordan, K. D. *J. Chem. Phys.* **2000**, *113*, 2290–2303.
(19) Reimann, B.; Buchhold, K.; Barth, H. D.; Brutschy, B.; Tarakeshwar, P.; Kim, K. S. *J. Chem. Phys.* **2002**, *117*, 8805–8822.
(20) Sakai, M.; Daigoku, K.; Ishiuchi, S.; Saeki, M.; Hashimoto, K.; Fujii, M. *J. Phys. Chem. A* **2001**, *105*, 8651–8657.
(21) Tarakeshwar, P.; Choi, H. S.; Lee, S. J.; Lee, J. Y.; Kim, K. S.; Ha, T.-K.; Jang, J. H.; Lee, J. G.; Lee, H. *J. Chem. Phys.* **1999**, *111*, 5838–5850.
(22) Tarakeshwar, P.; Kim, K. S.; Djafari, S.; Buchhold, K.; Reimann, B.; Barth, H. D.; Brutschy, B. *J. Chem. Phys.* **2001**, *114*, 4016–4024.
(23) Prakash, M.; Samy, K. G.; Subramanian, V. *J. Phys. Chem. A* **2009**, *113*, 13845–13852.
(24) Buchhold, K.; Reimann, B.; Djafari, S.; Barth, H. D.; Brutschy, B.; Tarakeshwar, P.; Kim, K. S. *J. Chem. Phys.* **2000**, *112*, 1844–1858.
(25) Gruenloh, C. J.; Florio, G. M.; Carney, J. R.; Hagemeister, F. C.; Zwier, T. S. *J. Phys. Chem. A* **1999**, *103*, 496–502.
(26) Hagemeister, F. C.; Gruenloh, C. J.; Zwier, T. S. *J. Phys. Chem. A* **1998**, *102*, 82–94.
(27) Hu, Y.; Bernstein, E. R. *J. Phys. Chem. A* **2009**, *113*, 639–643.
(28) Jalilian, M. R.; Tayyari, S. F. *Spectrochim. Acta A* **2009**, *73A*, 828–832.
(29) Larsen, G.; Ismail, Z. K.; Herreros, B.; Parra, R. D. *J. Phys. Chem. A* **1998**, *102*, 4734–4741.
(30) Palmer, P. M.; Chen., Y.; Topp, M. R. *Chem. Phys. Lett.* **2000**, *321*, 62–70.
(31) Palmer, P. M.; Topp, M. R. *Chem. Phys. Lett.* **1998**, *292*, 307–316.
(32) Palmer, P. M.; Topp, M. R. *Chem. Phys. Lett.* **1998**, *286*, 113–120.
(33) Pribble, R. N.; Gruenloh, C.; Zwier, T. S. *Chem. Phys. Lett.* **1996**, *262*, 627–632.
(34) Saeki, M.; Ishiuchi, S.; Sakai, M.; Fujii, M. *J. Phys. Chem. A* **2001**, *105*, 10045–10053.
(35) Gruenloh, C. J.; Hagemeister, F. C.; Carney, J. R.; Zwier, T. S. *J. Phys. Chem. A* **1999**, *103*, 503–513.
(36) Hagemeister, F. C.; Gruenloh, C. J.; Zwier, T. S. *Chem. Phys.* **1998**, *239*, 83–96.
(37) Kunsági-Máté, S.; Iwata, K. *Chem. Phys. Lett.* **2009**, *473*, 284–287.
(38) Pribble, R. N.; Hagemeister, F. C.; Zwier, T. S. *J. Chem. Phys.* **1997**, *106*, 2145–2157.
(39) Garrett, A. W.; Severance, D. L.; Zwier, T. S. *J. Chem. Phys.* **1992**, *96*, 7245–7258.
(40) Rankin, K. N.; Boyd, R. J. *J. Comput. Chem.* **2001**, *22*, 1590–1597.
(41) Dkhissi, A.; Blossey, R. *Chem. Phys. Lett.* **2007**, *439*, 35–39.
(42) Murdachaew, G.; Mundy, C. J.; Schenter, G. K. *J. Chem. Phys.* **2010**, *132*, 164102.
(43) Ireta, J.; Neugebauer, J.; Scheffler, M. *J. Phys. Chem. A* **2004**, *108*, 5692–5698.
(44) Martínez, J. M.; Martínez, L. *J. Comput. Chem.* **2003**, *24*, 819–825.
(45) Elstner, M.; Porezag, D.; Jungnickel, G.; Elsner, J.; Haugk, M.; Frauenheim, T.; Suhai, S.; Seifert, G. *Phys. Rev. B* **1998**, *58*, 7260–7268.
(46) Elstner, M.; Hobza, P.; Frauenheim, T.; Suhai, S.; Kaxiras, E. *J. Chem. Phys.* **2001**, *114*, 5149–5155.

(47) Zhao, Y.; Truhlar, D. G. *J. Phys. Chem. A* **2004**, *108*, 6908–6918.
(48) Zhao, Y.; Truhlar, D. G. *Theor. Chem. Acc.* **2008**, *120*, 215–241.
(49) Zhao, Y.; Truhlar, D. G. *Acc. Chem. Res.* **2008**, *41*, 157–167.
(50) Møller, C.; Plesset, M. S. *Phys. Rev.* **1934**, *46*, 618–622.
(51) Matisz, G.; Fabian, W. M. F.; Kelterer, A.; Kunsági-Máté, S. *J. Mol. Struct.: THEOCHEM* **2010**, *956*, 103–109.
(52) Boys, S. F.; Bernardi, F. *Mol. Phys.* **1970**, *19*, 553–566.
(53) Martin, J. M. L. *Chem. Phys. Lett.* **1996**, *259*, 669–678.
(54) (a) Dunning, T. H. *J. Chem. Phys.* **1989**, *90*, 1007–1023. (b) Kendall, R. A.; Dunning, T. H.; Harrison, R. J. *J. Chem. Phys.* **1992**, *96*, 6796–6806.
(55) Min, S. K.; Lee, E. C.; Lee, H. M.; Kim, D. Y.; Kim, D.; Kim, K. S. *J. Comput. Chem.* **2008**, *29*, 1208–1221.
(56) (a) Molnar, L. F.; He, X.; Wang, B.; Merz, K. M. *J. Chem. Phys.* **2009**, *131*, 065102. (b) Halkier, A.; Helgaker, T.; Jørgensen, P.; Klopper, W.; Koch, H.; Olsen, J.; Wilson, A. K. *Chem. Phys. Lett.* **1998**, *286*, 243–252.
(57) Martínez, L.; Andrade, R.; Birgin, E. G.; Martínez, J. M. *J. Comput. Chem.* **2009**, *30*, 2157–2164.
(58) Aradi, B.; Hourahine, B.; Frauenheim, T. *J. Phys. Chem. A* **2007**, *111*, 5678–5684.
(59) Schmidt, M. W.; Baldridge, K. K.; Boatz, J. A.; Elbert, S. T.; Gordon, M. S.; Jensen, J. H.; Koseki, S.; Matsunaga, N.; Nguyen, K. A.; Su, S.; Windus, T. L.; Dupuis, M.; Montgomery, J. A. *J. Comput. Chem.* **1993**, *14*, 1347–1363.
(60) Frisch, M. J.; Trucks, G. W.; Schlegel, H. B.; Scuseria, G. E.; Robb, M. A.; Cheeseman, J. R.; Scalmani, G.; Barone, V.; Mennucci, B.; Petersson, G. A.; Nakatsuji, H.; Caricato, M.; Li, X.; Hratchian, H. P.; Izmaylov, A. F.; Bloino, J.; Zheng, G.; Sonnenberg, J. L.; Hada, M.; Ehara, M.; Toyota, K.; Fukuda, R.; Hasegawa, J.; Ishida, M.; Nakajima, T.; Honda, Y.; Kitao, O.; Nakai, H.; Vreven, T.; Montgomery, Jr., J. A.; Peralta, J. E.; Ogliaro, F.; Bearpark, M.; Heyd, J. J.; Brothers, E.; Kudin, K. N.; Staroverov, V. N.; Kobayashi, R.; Normand, J.; Raghavachari, K.; Rendell, A.; Burant, J. C.; Iyengar, S. S.; Tomasi, J.; Cossi, M.; Rega, N.; Millam, N. J.; Klene, M.; Knox, J. E.; Cross, J. B.; Bakken, V.; Adamo, C.; Jaramillo, J.; Gomperts, R.; Stratmann, R. E.; Yazyev, O.; Austin, A. J.; Cammi, R.; Pomelli, C.; Ochterski, J. W.; Martin, R. L.; Morokuma, K.; Zakrzewski, V. G.; Voth, G. A.; Salvador, P.; Dannenberg, J. J.; Dapprich, S.; Daniels, A. D.; Farkas, Ö.; Foresman, J. B.; Ortiz, J. V.; Cioslowski, J.; Fox, D. J. *Gaussian 09*, Revision A.02; Gaussian, Inc.: Wallingford, CT, 2009.
(61) Valiev, M.; Bylaska, E. J.; Govind, N.; Kowalski, K.; Straatsma, T. P.; Van Dam, H. J. J.; Wang, D.; Nieplocha, J.; Apra, E.; Windus, T. L.; de Jong, W. A. *Comput. Phys. Commun.* **2010**, *181*, 1477–1489.
(62) *Hyperchem(TM) Professional 7*; Hypercube, Inc.: Gainesville, Florida.
(63) Schaftenaar, G.; Noordik, J. H. *J. Comput.-Aided Mol. Des.* **2000**, *14*, 123–134.
(64) Huisken, F.; Kulcke, A.; Laush, C.; Lisy, J. M. *J. Chem. Phys.* **1991**, *95*, 3924–3929.
(65) Tarakeshwar, P.; Lee, S. J.; Lee, J. Y.; Kim, K. S. *J. Chem. Phys.* **1998**, *108*, 7217–7223.
(66) Lill, S. O. N. *J. Phys. Chem. A* **2009**, *113*, 10321–10326.
(67) Feller, D. *J. Phys. Chem. A* **1999**, *103*, 7558–7561.
(68) Molnar, L. F.; He, X.; Wang, B.; Merz, K. M. *J. Chem. Phys.* **2009**, *131*, 065102.
(69) Neves, A. R.; Fernandes, P. A.; Ramos, M. J. *J. Chem. Theory Comput.* **2011**, *7*, 2059–2067.
(70) Jurecka, P.; Sponer, J.; Cerny, J.; Hobza, P. *Phys. Chem. Chem. Phys.* **2006**, *8*, 1985–1993.
(71) Pitonak, M.; Riley, K. E.; Neogrady, P.; Hobza, P. *ChemPhysChem* **2008**, *9*, 1636–1644.
(72) Arunan, E.; Gutowsky, H. S. *J. Chem. Phys.* **1993**, *98*, 4294–4296.
(73) Scherzer, W.; Kraetzschmar, O.; Selzle, H. L.; Schlag, E. W. *Z. Naturforsch. A* **1992**, *47*, 1248–1252.
(74) Janowski, T.; Pulay, P. *Chem. Phys. Lett.* **2007**, *447*, 27–32.
(75) (a) Hobza, P.; Selzle, H. L.; Schlag, E. W. *J. Phys. Chem.* **1996**, *100*, 18790–18794. (b) Lee, E. C.; Kim, D.; Jurecka, P.; Tarakeshwar, P.; Hobza, P.; Kim, K. S. *J. Phys. Chem. A* **2007**, *111*, 3446–3457.
(76) Hill, J. G.; Platts, J. A.; Werner, H. *Phys. Chem. Chem. Phys.* **2006**, *8*, 4072–4078.
(77) Zhao, Y.; Truhlar, D. G. *J. Phys. Chem. A* **2005**, *109*, 4209–4212.